

**This thesis is submitted for the degree of Doctor of  
Philosophy**

**Production and Characterisation of  
Thermoelectrically Efficient Thin  
Films for Green Energy Applications**

**Becky Penhale-Jones**

**Supervisor: Professor Benjamin J. Robinson**

*Submitted: June 2024*

## **Declaration**

I have written this thesis independently, and no part of it has been previously submitted to any university. Any previously published information has been indicated appropriately in the text.

## **Acknowledgements**

Thanks to my supervisor Ben Robinson for getting me up to speed on all things quantum transport, and putting up with my clumsiness-related probe expenses.

Thanks also to Sam Jarvis for allowing me to use the Isolab AFM setup when mine went kaput, and for his and Charlie's help with the XPS measurements.

And finally, thanks to my friends and family (particularly my husband, Ian) for listening to my imposter syndrome-fuelled wobbles and reassuring me that I am capable of becoming Dr. Penhale-Jones (even if they will refuse to address me as such).

## Publications

O'Driscoll, L.J., Jay, M., Robinson, B.J., Sadeghi, H., Wang, X., **Penhale-Jones, B.**, Bryce, M.R., Lambert, C.J., 2023. Planar aromatic anchors control the electrical conductance of gold| molecule| graphene junctions. *Nanoscale Advances*.<sup>[1]</sup>

## Abstract

Molecular electronics focuses on using molecules or their monolayers as electrical devices. Within this, the field of molecular thermoelectronics hones in on using these same building blocks for improvement of thermoelectric properties, or conversion of waste heat into useful electricity. Specifically designing molecules enables fine tuning of these properties to produce devices that are capable of effectively harnessing previously wasted energy. For example, adding side chains to a molecular backbone will impact phonon transport within it, as well as changing the packing density once the molecule forms into a monolayer. Furthermore, altering where the electrodes in a junction contact these molecules and their monolayers will influence quantum interference (QI) effects. These characteristics consequently shift other properties of the materials such as electrical conductance and figure of merit (FOM). This, in turn, enables advancements in the devices utilising such materials to produce useful products with greater efficiency.

In this research, monolayers were formed via Langmuir-Blodgett (LB) deposition and self-assembled monolayers (SAMs) from specially designed molecules for improved QI and thermoelectric efficiency. Techniques including atomic force microscopy (AFM) and x-ray photoelectron spectroscopy (XPS) were used to determine whether these formed uniform monolayers with reasonable electrical conductance.

Graphene-coated AFM probes were wear-tested. Standard non-conductive AFM probes were coated in graphene via Langmuir-Schaefer (LS), in an attempt to prolong their lifetime. Conductive probes have been coated previously, with the conclusion that this improves conductance for tailored molecules in a junction. However, this study viewed the potential benefit of increased usability of the probes with minimal reduction in attainable detail.

Furthermore, tetrapodal molecules were investigated, building on previous work on the possibility of decoupling the electrical conductance of the molecular backbone from its anchors, creating stable yet conductive monolayers. The aim was to understand if varying the 'tail' group of the molecule influenced its interaction within the molecular junction, therefore changing its electrical conductance.

Finally, several dithiolenates were studied, with one anchor point and two thiol groups for substrate binding. Thiols have been extensively studied due to their affinity for gold, however, the role of dithiolenates is largely unknown. Two molecules were tested, both with protected and deprotected forms. Greater electrical conductance was anticipated for the deprotected forms than their protected counterparts.

This thesis concludes that LS and self-assembly produce good monolayers with the desired properties per their molecular design. As such, the techniques present promising methods for fabricating useful thermoelectrically efficient thin films.

## Contents

Declaration.....	2
Acknowledgements.....	3
Publications.....	4
Abstract.....	5
Contents.....	6
1. Introduction.....	9
2. Aims and Motivation.....	12
3. Theoretical Background.....	13
3.1. Electrical Transport.....	13
3.1.1. Atomic Structure.....	13
3.1.2. Crystalline Solids and Crystal Lattices.....	15
3.1.3. Classic Transport.....	20
3.1.4. Quantum Transport.....	21
3.2. Thermoelectric Properties.....	29
3.2.1. Thermal Conductivity and Current.....	29
3.2.2. The Seebeck Effect.....	31
3.2.3. Thermal Power Generation and Figure of Merit.....	33
3.2.4. Nanoscale Thermoelectricity.....	36
3.2.5. Molecular Junction Thermoelectricity.....	39
4. Experimental Background.....	42
4.1. Organic Electronics.....	42
4.2. Thin Films.....	47
4.3. Thermoelectricity.....	53
4.3.1. Seebeck Coefficient.....	53
4.3.2. Figure of Merit (FOM).....	56
4.4. Deposition Techniques.....	57
4.4.1. Self-Assembled Monolayers (SAMs).....	57

4.4.2.	Langmuir-Blodgett (LB) .....	62
4.5.	Characterisation techniques .....	69
4.5.1	Scanning Probe Microscopy .....	69
4.5.2	X-Ray Photoelectron Spectroscopy .....	73
4.6.	Applications .....	74
5.	Experimental Methods .....	77
5.1.	Langmuir Blodgett (LB) .....	77
5.2.	Self-Assembled Monolayers (SAMs) .....	78
5.3.	Quartz Crystal Microbalance (QCM) .....	79
5.4.	Preparation of Gold Samples .....	81
5.5.	Scanning Probe Microscopy (SPM) .....	82
5.5.1.	Imaging and Scratch Tests .....	83
5.5.2.	Electrical Conductivity .....	83
5.6.	X-Ray Photoelectron Spectroscopy (XPS) .....	85
6.	Results .....	86
6.1.	Graphene Coating Probes .....	86
6.1.1	Introduction .....	86
6.1.2	Coating via Langmuir-Schaefer .....	87
6.1.3	Wear Tests .....	90
6.1.4	Conclusions .....	112
6.2	Conductive Probe Testing .....	113
6.2.1	BOC8 molecules .....	113
6.2.2	Conclusions .....	115
6.3	Tetrapodal Molecules .....	116
6.3.1	Introduction .....	116
6.3.2	Molecular Design .....	116
6.3.3	Molecular Area .....	120
6.3.4	Electrical Conductivity .....	130

6.3.5	X-ray Photoelectron Spectroscopy .....	138
6.3.6	Conclusions .....	142
6.4	Dithiolenate Molecules .....	143
6.4.1	Introduction .....	143
6.4.2	Molecular Design .....	145
6.4.3	Molecular Area .....	146
6.4.4	Electrical Conductance .....	147
6.4.5	X-ray Photoelectron Spectroscopy .....	154
6.4.6	Conclusions .....	156
7.	Conclusions .....	158
	References.....	161



## 1. Introduction

In Richard Feynman's famous speech "There's Plenty of Room at the Bottom", he highlighted the possibility of the plethora of information that could be gained from studying things on a small scale.<sup>[2]</sup> This talk from 1959, alongside the invention of the scanning tunnelling microscope (STM) in 1981 and the Atomic Force Microscope (AFM) in 1986 opened up a world of nanoscale science that was previously predominantly undiscovered.<sup>[3]</sup>

Some of the methods described in Feynman's speech have since been made a reality, such as Molecular Beam Epitaxy (MBE), with STM also being a method he described. MBE can be described as a 'bottom-up' approach to creating nanomaterials, whereas lithography, for instance, is a 'top-down' methodology. Other examples of 'top-down' and 'bottom-up' techniques can be seen in Figure 1.1.<sup>[4]</sup>

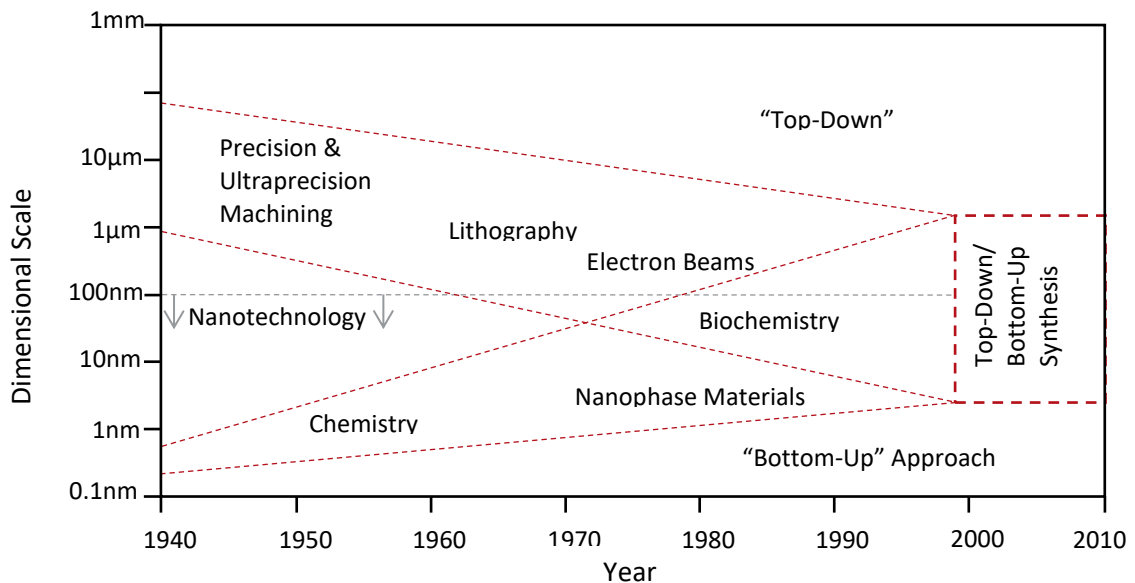


Figure 1.1 Approaches to nanotechnology, relating to Richard Feynman's speech "There's Plenty of Room at the Bottom". Generally, the approaches can be split into 'top-down' and 'bottom-up' and divided further within each umbrella.

In conjunction with Feynman's speech, Gordon Moore of Intel proposed what has now become known as Moore's Law, in 1965: in an integrated circuit, the number of transistors was predicted to double every two years.<sup>[5]</sup> This has broadly proven to be the case, possibly in a self-fulfilling prophecy, to the extent where the limit has almost been reached. The existing method for this employs optical lithography and silicon doping. Optical lithography, also termed photolithography, uses light for transference of a pattern onto a substrate. The substrate is initially covered entirely by a photoactive resist, with a mask over the top of this. Exposing this to ultraviolet light then removes material in the areas that were not protected by the mask (positive resist), or those that were (negative

resist); for silicon-based processes typically a positive resist is employed. In the case of silicon doping, impurities are added to influence the materials' electrical conductivity. The dopant used dictates whether the semiconductor is n-type, with more negative charge carriers, or p-type with more positive charge carriers.<sup>[6]</sup> These two combined enable the production of transistors with the desired composition and electrical conductivity when a voltage is applied. Progressing further than the current achievements encounters issues regarding cooling requirements and quantum interference.<sup>[7]</sup>

Climate change has increasingly moved to the forefront of public consciousness in recent years, with evidence of its impacts becoming more undeniable. To combat this, climate scientists agree that we must reduce global warming to no more than 1.5 °C greater than levels from 1900. We have already reached 1.1 °C, with greenhouse gas emissions continuing to increase due to fossil fuel use, agricultural methods, social factors and many more emitting practices. In a report recently published by the Intergovernmental Panel on Climate Change (IPCC), they declared with high confidence that concentrations of CO<sub>2</sub> in 2019 were higher than they have reached in the past 2 million years, whilst nitrous oxide and methane were at their highest level in 800,000 years. 79% of these emissions were concluded to be a result of energy, industry transport and buildings.<sup>[8]</sup>

As a result, suggestions have been made for converting to greener fuels and energy production such as hydrogen, nuclear, and renewables. This broaches the response via changing the energy used altogether; an alternative route to minimising climate change is to lessen the energy we use in the first place. This can be achieved by improving the efficiency of existing technology or by harnessing previously wasted energy. According to the IPCC, some such mitigations are not only technically viable but are becoming increasingly financially attractive and widely accepted by the public.<sup>[8]</sup>

Both improving technological efficiency and waste heat recovery are attainable by harnessing thermoelectric effects including the Seebeck effect, wherein a heat differential creates a voltage bias, and the Figure of Merit (FOM) which indicates the effectiveness of a thermoelectric material. Until around the 1990s, these effects were only investigated in bulk materials however, after that point nanomaterials began to delve deeper by utilising quantum transport to their advantage.<sup>[9]</sup> An FOM of greater than one has been achieved by bulk solid solutions involving Bi<sub>2</sub>Te<sub>3</sub>, Bi<sub>2</sub>Se<sub>3</sub>, and Sb<sub>2</sub>Te<sub>3</sub>; these are used in conventional thermoelectric generators. It's understood that an FOM over three is necessary to compete with the current large-scale commercial devices that use liquids and gases.<sup>[10]</sup> Typically such high values have been attained at elevated temperatures, however, ideally they will be reached in ambient conditions to be more practical.

One such example that utilises thermoelectric effects to improve overall device efficiency is incorporating thermoelectrically efficient thin films into solar photovoltaic modules. Thermoelectric layers can be added that simultaneously cool the module, increasing its efficiency due to their peak operating temperature often being lower than ambient temperature, whilst converting that obtained heat into further electricity.<sup>[11, 12]</sup> To use these thin films in a practical sense, it is prudent to incorporate them into electrical circuits.

## 2. Aims and Motivation

Returning to Feynman's speech, there is the idea of the 'bottom-up' approach which leaves room for switching from traditional semiconductors such as silicon, to molecular devices. The research featured in this thesis focuses on 'bottom-up' techniques, starting with single-molecule building blocks and transforming them into thin films. To create these thin films, molecular electronics are employed. For example, molecules can be tuned to have particular band gaps, exhibit certain electron transport, and therefore have enhanced electrical conductance, all the while limiting thermal conductance.<sup>[13]</sup> Several deposition methods have already been established for creating films for molecular electronics, many of which are based on techniques formed for inorganic materials that are now applied to organic materials. Some such methods include spin-coating, chemical vapour deposition, electrochemical methods, inkjet printing, spray-coating, sol-gel processing and physical vapour deposition which can in turn be categorised into thermal evaporation, MBE and sputtering. When dealing solely with organic materials, electrostatic layer-by-layer deposition, Langmuir-Blodgett (LB) deposition and self-assembly can be used.<sup>[6]</sup>

In this research, thermoelectric monolayers built from tailor-made molecules to create effective thin films for conversion of waste heat into electricity will be demonstrated, alongside characterisation via AFM using graphene-modified probes. First, LS was used to coat AFM probes with graphene, to investigate how this impacts their wear-resistance and coupling to self-assembled monolayers for conductive measurements. This altered the top contact used in molecular junctions, mimicking the integration into electrical circuits. Subsequently, these coated probes were used alongside uncoated probes to test the electrical conductance of monolayers of tetrapodal molecules. These aimed to enhance electrical conductance by employing constructive quantum interference through the molecular backbone whilst decoupling this from the anchors. Different groups within the anchors were tested for different interactions with the substrate and potential further enhancement of their electrical conductivity. Finally, a second series of molecules was studied in self-assembled monolayer form, this time with two thiol groups for attempted additional monolayer stability.

Further work is suggested to investigate the Seebeck coefficient of the materials created in order to determine their FOM for comparison to existing technology.

## 3. Theoretical Background

### 3.1. Electrical Transport

#### 3.1.1. Atomic Structure

The fundamental atomic structure relies on electron wave-particle duality in which Equation 3.1 (the De-Broglie formula) is true:

$$\lambda = \frac{h}{m_e v} \quad \text{Equation 3.1}$$

Where  $\lambda$  is the electron wavelength;  $m_e$  is the electron mass,  $v$  is the velocity; and  $h$  is Planck's constant,  $6.63 \times 10^{-34}$  J.<sup>[14]</sup>

This gives rise to the Rutherford-Bohr atomic structure, in which a small nucleus, comprised of protons and neutrons, is orbited by electrons in set orbits. These orbits can be concluded from Equation 3.2, due to them corresponding to electron wavelengths as an integer ( $n$ ) of the orbital circumference ( $r$ ):

$$2\pi r = n\lambda = \frac{nh}{m_e v} \quad \text{Equation 3.2}$$

$$m_e v r = \frac{nh}{2\pi} \quad \text{Equation 3.3}$$

Equation 3.3 demonstrates that angular momentum ( $m_e v r$ ) is quantised due to being an integer multiple of  $h/2\pi$ . As a result of this, electron orbits form: each Bohr shell is labelled by quantum number,  $n$ , and given a spectroscopic label (K, L, M, N etc.; where  $n=1,2,3,4$ ).<sup>[14]</sup>

This idea can be advanced to consider the wave behaviour of electrons, by including wavefunctions, which define the probability of an electron being in a specified position (in the form  $x, y, z$ ), at a given time. To find the electron's energy, Schrödinger's equation (Equation 3.4) is applied:

$$-\frac{\hbar^2}{2m_e} \nabla^2 \psi + V(x, y, z) \psi = E \psi \quad \text{Equation 3.4}$$

Where  $\hbar$  is the reduced Planck's constant ( $h/2\pi$ );  $\psi$  is the wavefunction,  $V(x, y, z)$  is the electron's potential energy function;  $E$  is electron energy. This can be solved to give the associated electron energies ( $E_n$ ) for a set of permissible wavefunctions ( $\psi_n$ ) when set boundary conditions are applied. Permitted wavefunctions for atoms are given by 1s, 2s,

2p, 3s... etc (where 1, 2, 3 and 4 are equivalent to the K, L, M and N from the Bohr model). In this atomic model, four quantum numbers apply:

- $n$  = principal; like that from Bohr shells.
- $l$  = angular momentum; varies from  $l=0,1,2,\dots,(n-1)$ . This decides what shape the orbital will be (e.g.  $l = 0$  is an s orbital and, therefore, spherical).
- $m$  = magnetic; varies from  $m = 0, \pm 1, \dots, \pm l$ . This dictates the orbital's special orientation within the subshells. For instance, when  $l = 1$  there are three p orbitals, corresponding to  $m = 0, +1$ , and  $-1$ .
- $s$  = spin; can be  $\pm 1/2$  for an electron, due to the Pauli exclusion principle.<sup>[14]</sup>

This effectively means an electronic orbital has acceptable energy, shape, direction, and occupancy combinations. Rydberg states in isolated atoms correspond to Bohr shells and combinations of the quantum numbers given above. The total number of electrons in an atom determines the occupation of these energy states, levels or orbitals, with the lowest energy level filled first. Beyond the occupied energy levels, the spacing between Rydberg states decreases until they converge to form the vacuum level ( $n=\infty$ ), beyond which the electron is free of the atom and electronic states are empty.<sup>[14]</sup>

Further to this, the highest occupied energy level is termed the valence band. This is also referred to as the Highest Occupied Molecular Orbital, or HOMO. The conduction band is that with the lowest unoccupied energy level, or Lowest Unoccupied Molecular Orbital (LUMO). These are termed the frontier orbitals and the space between the two is referred to as the 'HOMO-LUMO gap' with anything in between described as falling 'mid-gap'.<sup>[15]</sup> The location of this can be found using Ultraviolet-Visible spectroscopy (UV-Vis).

Beginning with the Drude-Lorentz free electron model for metals, it's understood that a metallic solid is formed from a 'sea' of electrons surrounding a closely packed lattice of cations, where the electrons have been ionised from the valence band of the atoms. That being said, it is more accurate to consider relating to quantum mechanics: the free electrons are confined within a potential well (like the particle-in-a-box theory), and the wavefunction boundary conditions are required to remove these constraints. Schrödinger's equation (Equation 3.4) is used to determine the applicable wavelengths.<sup>[14]</sup>

Given a one-dimensional (1D) box of length  $L$  the applicable wavelengths are given by  $\lambda_n=2L/n$ , in which  $n$  is the quantum number (and  $=1,2,3$ ), whilst the permitted wavevectors  $k_n=2\pi/L$  are from the relationship  $k_n=n\pi/L$ . The wavefunctions resulting from the particle-in-a-box model satisfy the following equation (Equation 3.5):<sup>[14]</sup>

$$\psi_n = \left(\frac{2}{L}\right)^{\frac{1}{2}} \sin\left(\frac{n\pi x}{L}\right) \quad \text{Equation 3.5}$$

$$E_n = \frac{n^2 h^2}{8mL^2} \quad \text{Equation 3.6}$$

Equation 3.6 gives the corresponding energy of the electronic level;  $E_n$  here only consists of kinetic energy, due to the potential energy being 0 within the box. Due to these formulae, there is a parabolic relationship between  $E_n$  and  $n$ , as well as  $E_n$  and  $k$ ; furthermore, the energy levels within the parabola are quantised. However, due to the size of  $L$  for a typical metal structure, the separation between energy levels is small when compared with thermal energy ( $k_B T$ ) and thus energy distribution can be considered continuous (see Figure 3.1).<sup>[14]</sup>

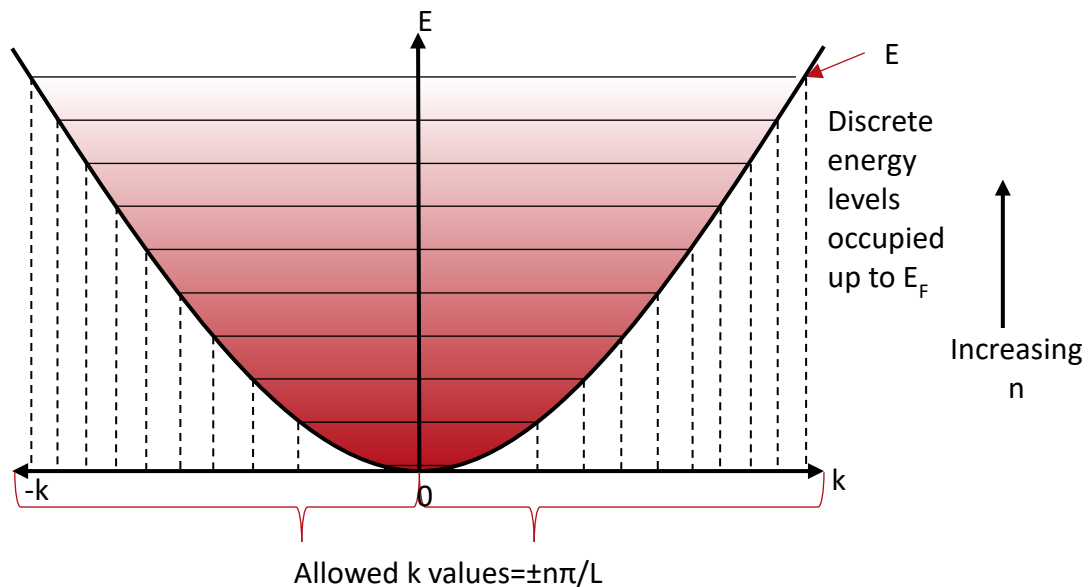


Figure 3.1 Permitted electron wavevectors ( $k$ ) and their energy ( $E$ ) levels within a confined potential well of length  $L$  demonstrate a parabolic relationship. The shaded regions contain electrons. The distribution of energy within this model can be considered to be continuous despite being in discrete levels, as the steps between levels are so small; this results from the length being so limited compared to the thermal energy present.

It is of note that as  $L$  decreases and the electron becomes more localised, the electron state energy increases; this influences bonding and quantum-confined systems.<sup>[14]</sup>

### 3.1.2. Crystalline Solids and Crystal Lattices

Properties of bulk solids result from considering the previously described relationships in three dimensions. Solids are built of 'unit cells' of repeating three dimensional (3D) arrangements with translational symmetry and can be moved by an integer of the lattice translation vector. Due to the repeating nature of unit cells, ionic cores form within crystals thus controlling the contained electrical potential. Relating to the electronic

behaviour previously described, this means that the wavefunctions that satisfy Schrödinger's equation are controlled by lattice recurrence. This is the basis for Bloch's theorem (Equation 3.7):

$$\psi(\mathbf{r}) = u_k(\mathbf{r})e^{i\mathbf{k}\cdot\mathbf{r}} \quad \text{Equation 3.7}$$

Where  $\mathbf{r}$  is the position and  $u$  is a periodic function for which  $u_k(\mathbf{r})=u_k(\mathbf{r}+\mathbf{T})$  for any translational vector  $\mathbf{T}$ . The wavefunctions that satisfy this are termed Bloch functions, and signify waves passing through a crystal, the shapes of which are altered by the crystal potential encountered at each atomic location. In a 1D lattice with interatomic spacing,  $a$ :

$$\psi(x) = u_k(x)e^{ikx} \quad \text{Equation 3.8}$$

For which  $u_k(x)=u_k(x+na)$  for any integer  $n$ . If periodic boundary conditions are applied to a chain of atoms of length  $L=Na$ :

$$\psi(Na) = \psi(0) \quad \text{Equation 3.9}$$

$$u_k(Na)e^{ikNa} = u_k(0) \quad \text{Equation 3.10}$$

$$k = \pm \frac{2n\pi}{Na} = \pm \frac{2n\pi}{L} \quad \text{Equation 3.11}$$

Equation 3.11 results from applying  $e^{(ikNa)}=1$  to Equation 3.10. From this it can be concluded that consecutive  $k$  values are separated by  $2\pi/L$ ; this is defined as the  $\mathbf{k}$ -space volume taken up by each wavevector state. For 3D structures this occurs in all dimensions, giving a  $\mathbf{k}$ -space volume of  $8\pi^3/V$  per wavevector state ( $V=L^3$ ). Moreover, Equation 3.11 also gives the number of wavevector states per energy band, when  $n$ 's upper limit is known.<sup>[14]</sup>

Diffraction effects result from lattice periodicity: each atom within a 1D atomic chain (with atomic spacing  $a$ ) reflects an electron wave passing through. These reflections will be constructive if  $m\lambda=2a$ , which describes an integer multiple of the De-Broglie wavelength of the aforementioned electron travelling through the atomic chain. In this case, the lattice contains electron waves travelling in opposite directions, with the combination of these forming a standing wave that corresponds to electron density distributions ( $|\psi(x)|^2$ ) consisting of all nodes (regions of low amplitude: where destructive quantum interference occurs) or all antinodes (high amplitude regions; constructive interference occurs) at the lattice sites  $x=a, 2a, 3a\dots$  etc. Two solutions result which differ in energy on account of opposing energies between electrons and positively charged ions, despite there being just one wavevector value. Band gaps are then created in the electron dispersion curves



at the points *where*  $k=\pm m\pi/a$  (see Figure 3.2).<sup>[14]</sup> Given that they are standing waves, the electron group velocity:

$$v_g = \frac{\partial \omega}{\partial k} = \frac{1}{\hbar} \frac{\partial E}{\partial k} \quad \text{Equation 3.12}$$

Equation 3.12 tends to zero at these points. This is evidence of the stark transformation from an electron in a free space (for which the dispersion relationship is parabolic:  $E \propto k^2$  for all values of  $k$ ) and that in a crystalline solid.<sup>[14]</sup>

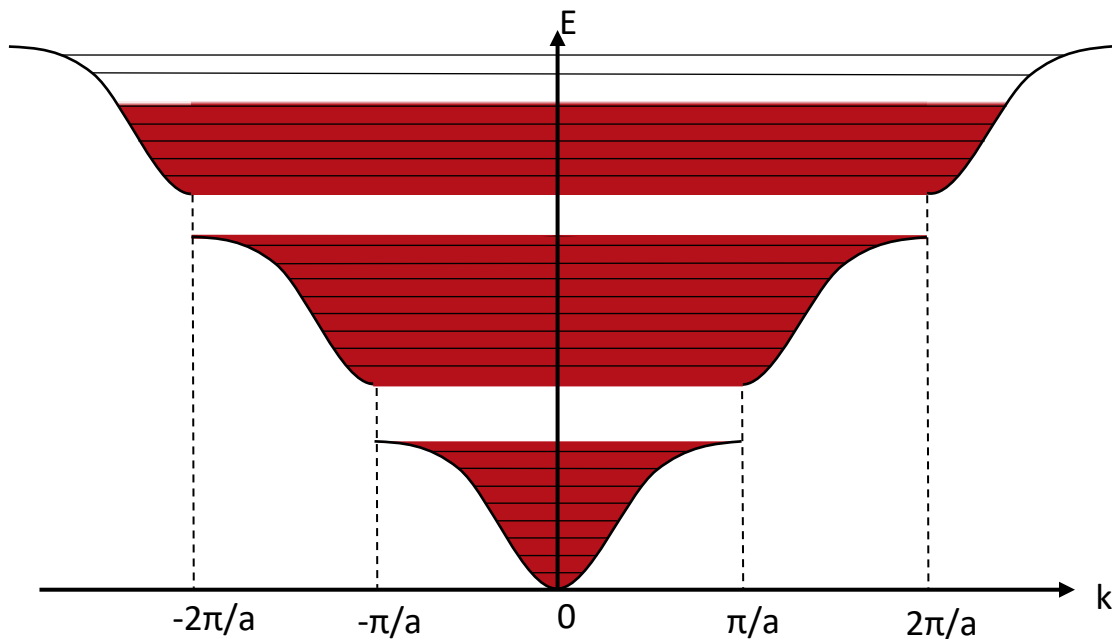


Figure 3.2 Shaded zones depict electron occupancy. The parabolic relationship between permitted electron wavevectors and their corresponding electron energy when confined to a 1D potential well is shown, wherein the potential varies over periods of  $a$ . The band gaps, where there is no electron occupancy, result from standing waves forming over electron density distributions, causing nodes and antinodes.

Brillouin zones are the  $k$  spaces between two diffraction conditions, hence for a 1D crystal, the first is between  $k=-\pi/a$  and  $k=+\pi/a$ . This means that any value of  $k$  outside of these bounds corresponds to an electron wave of wavelength less than  $2a$ . Any such wave cannot be defined by individual wave amplitudes due to the high special frequency, whilst waves of wavelength  $>2a$  can be identified. Within a  $k$ -space, an equivalent point within a Brillouin zone can be found for a value of  $k$  outside of it, by applying the relationship:

$$k' = k \pm \frac{2m\pi}{a} \quad \text{Equation 3.13}$$

Where  $2m\pi/a$  is the crystal's reciprocal lattice vector.

For 3D crystals, energy gap locations in electron dispersions are found by electron diffraction due to lattice planes. However, Brillouin zones are defined by complex surfaces in 3D  $k$ -space resulting from unit cell and atomic structures.<sup>[14]</sup>

Using Equation 3.13 the ends of the Brillouin zone are  $k=\pm\pi/a$ ; knowing that reciprocal lattice vector translation can be used to map endpoints onto one another, the total number of permitted  $k$  values is  $N$ . This, in conjunction with the Pauli Exclusion principle, can be used to conclude that the number of states per energy band is  $2N$ . When applied to 3D this is labelled  $N_u$  states per band, wherein  $N_u$  = number of unit cells per crystal. The number of valence electrons in a crystal is given by  $zN_u$  where  $z$  refers to the number of valence electrons per unit cell. In a solid, this means:

1. If  $z$  is even: one energy band is filled and the following is empty. The valence band is the highest filled band, with the conductance band referring to the next empty band. The result of this arrangement is the formation of an insulator, as there is insufficient energy (from an externally supplied voltage) to allow the electrons to 'jump' into the next available band (the conduction band). If the gap between the valence and the conduction bands is small enough, a semiconductor forms as opposed to an insulator.
2. If  $z$  is odd: the highest occupied energy band is half full. There are sufficient vacant sites sufficiently close to the highest occupied energy bands to allow electron movement; the material is a metal.<sup>[14]</sup>

These different materials are depicted in Figure 3.3.<sup>[14]</sup>

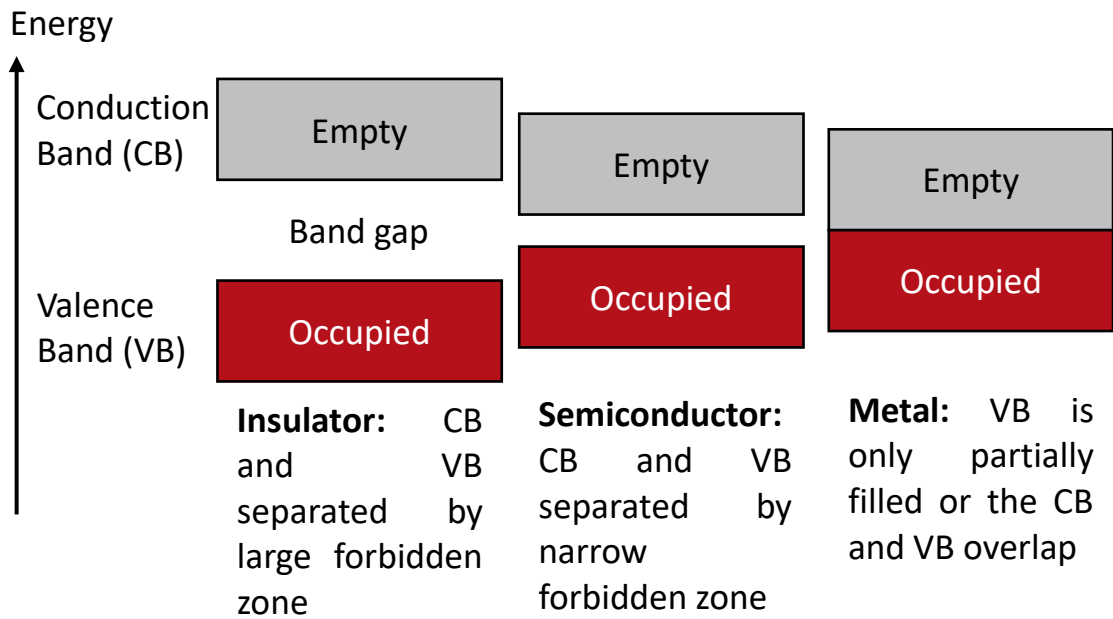


Figure 3.3 Band diagram for an insulator, a semi-conductor and a metal. The grey, empty box is the conduction band and the occupied red box is the valence band. For insulators, there is a significant gap between the two. This gap is smaller for semiconductors and is not present at all for metals.

A solid's highest occupied energy level is referred to as its Fermi level,  $E_F$ . The corresponding wavevector is:

$$E_F = \frac{\hbar k_F^2}{2m_e} \tag{Equation 3.14}$$

$$k_F = (3\pi^2 n_e)^{1/3} \tag{Equation 3.15}$$

$$E_F = \frac{\hbar(3\pi^2 n_e)^{2/3}}{2m_e} \tag{Equation 3.16}$$

Using the volume of  $k$ -space per state of  $8\pi^3/V$  from earlier, the volume of  $k$ -space occupied by  $N$  electrons is  $4N\pi^3/V$  when the Pauli Exclusion principle is accounted for. By equating this to the volume of a sphere in  $k$ -space, with a radius of  $k_F$  (for a Fermi sphere), Equation 3.15 is obtained. Substituting in  $n_e=N/V$  for electron density gives Equation 3.16.<sup>[14]</sup>

$N(E)dE$  is the density of states and is defined in a way that  $N_S = \int N(E)dE$  gives how many states there are per unit crystal volume in each energy band. From above, it's evident that the number of wavevector states per  $k$ -space unit volume is  $V/8\pi^3$ . Therefore, the number of states per band can be found from:

$$N_S = 2 \times \frac{V}{8\pi^3} \int dk \quad \text{Equation 3.17}$$

Where the factor of two accounts for two spin states per  $\mathbf{k}$  value. In 3D,  $d\mathbf{k}=4\pi k^2 dk$  and, therefore:

$$N_S = \frac{V}{4\pi^3} \int 4\pi k^2 \frac{dk}{dE} dE \quad \text{Equation 3.18}$$

When the bands are parabolic,  $E = \frac{\hbar^2 k^2}{2m_e}$ , meaning that  $\frac{dk}{dE} = \frac{m_e}{\hbar^2 k}$  so:

$$N(E) = \frac{4\pi(2m_e)^{3/2} E^{1/2}}{h^3} \quad \text{Equation 3.19}$$

The dependence on  $E^{1/2}$  ( $\propto k$ ) of the density of states (DOS) results from the increased volume of available phase space at larger energy values.

### 3.1.3. Classic Transport

According to Ohm's law, electron transport through a conductor sandwiched between two points is directly proportional to the voltage between them; where the proportionality constant is resistance (Equation 3.20). This considers electrons as classic particles. Kirchhoff developed this idea further, to introduce the total conductance when there are multiple conductors. He concluded that conductors in parallel were equal to the sum of the parts, whereas in series the reciprocal was taken (Equation 3.21 and Equation 3.22 respectively).<sup>[16]</sup>

$$I = \frac{V}{R} \quad \text{Equation 3.20}$$

$$G = G_1 + G_2 \dots \quad \text{Equation 3.21}$$

$$\frac{1}{G} = \frac{1}{G_1} + \frac{1}{G_2} \dots \quad \text{Equation 3.22}$$

$$G = \sigma \frac{A}{L} \quad \text{Equation 3.23}$$

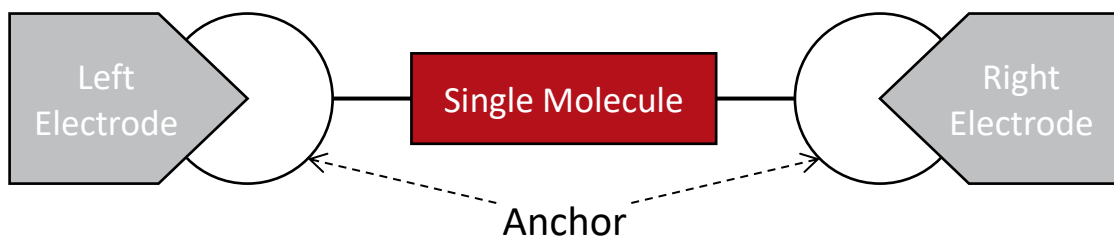
In the case of Equation 3.23,  $G$  is electrical conductivity,  $\sigma$  is the intrinsic conductivity of the material,  $A$  is the area and  $L$  is the length of the conductor. In Ohm's law,  $I$  is current,  $V$  is voltage and  $R$  is resistance.

In the region  $>3$  nm, Ohm's law, and by extension, Kirchhoff's law, no longer apply due to interference among charge carriers from scattering. At this point, QI effects take precedence and charge transport becomes phase coherent.<sup>[16]</sup> This is because the

charge carriers are nearing their De-Broglie wavelengths and, therefore, transport moves from diffusive to ballistic, meaning that the conductor's length overtakes that of the free mean path of electrons in the material.

### 3.1.4. Quantum Transport

A nanojunction consists of a nanoscale material (typically a molecule or monolayer) sandwiched between metal electrodes, as in Figure 3.4.<sup>[16]</sup> An electron is injected from one electrode, passes through the anchor points into the molecule and out the other side, to be collected by the other electrode. If the distance between the electrodes is less than a few nanometres, charge transport is phase coherent, meaning that frequency and waveform are identical. This allows for stationary interference in which two waves combine to make one, of greater, lower or the same amplitude. As a result, the electron travelling through the junction doesn't lose energy on its travels. In theory, the molecule in the junction forms a closed system, due to there being no electrons able to enter or leave and, therefore, it can be concluded that the energy levels of this isolated molecule are quantised.<sup>[15]</sup>



*Figure 3.4 A molecular junction, showing a molecule anchored between two electrodes. Electrons are injected in one side, through the left electrode, and pass along the junction to the right electrode on the other side. In the event the molecule featured is less than a few nanometres in length, frequency and waveform are identical due to phase coherency.*

The scattering approach typically describes coherent transport through nanojunctions. Within such junctions, the chemical potential,  $\mu$ , of the electrodes and the nanomaterial's energy level are what dictate carrier diffusion and transport. The electrodes here form electron reservoirs with a known chemical potential and temperature dependence. The scattering approach relates transmission and reflection probabilities through a sample using electron transport. The potential landscape through which the electron travels (the molecule, in a molecular junction) decides the shape of energy levels, due to the atomic nucleus.

Transmission coefficient ( $T(E)$ ) refers to how easily an electron wave, of energy  $E$ , can travel from left to right.<sup>[15]</sup>

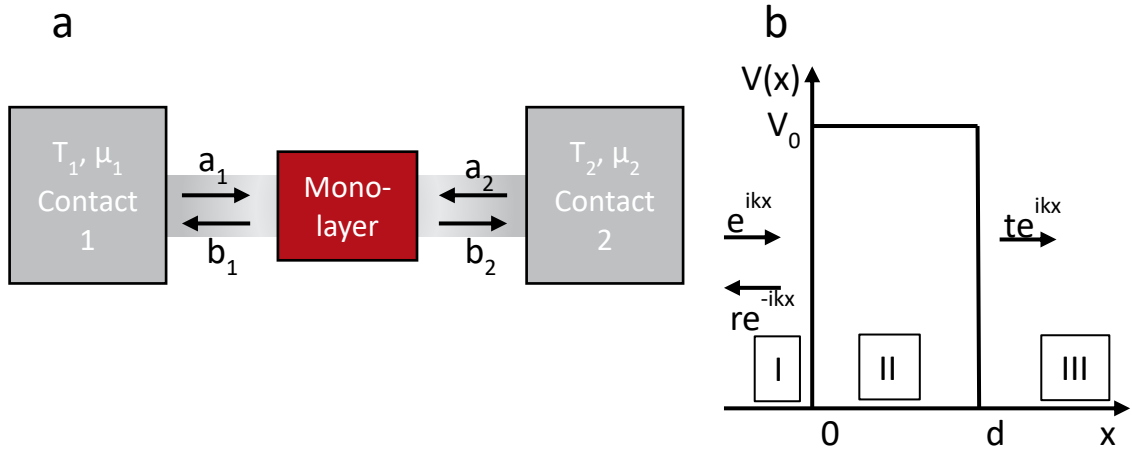


Figure 3.5 a depicts a nanojunction joined to two large junctions via two leads;  $T$  and  $\mu$  are temperature and chemical potential respectively. The two contacts are of known chemical potential ( $\mu$ ) and temperature dependence. Figure b gives the potential barrier of regular height and width, where  $e^{ikx}$  is an incoming planar wave that gets partially reflected and transmitted. The transmitted portion is given by  $te^{ikx}$  and reflected as  $re^{-ikx}$

Looking at a nanojunction such as that in Figure 3.5,<sup>[17]</sup> electrons are scattered once they've left the leads. An incoming electron planar wave, in the form  $e^{ikx}$ , is partially reflected by the barrier ( $re^{-ikx}$ , where  $r$  is the amplitude of the incident wave) and the rest is transmitted ( $te^{ikx}$ ); the likelihood of one electron reaching the second electrode can be denoted as  $|t|^2 = T(k)$ , with  $|t|$  corresponding to the modulus of the transmitted wave. From here, it can be concluded that in any given  $k$  state, the electrical current density is given by:

$$J_k = \frac{\hbar}{2m^*} \left[ \psi^* \frac{d\psi}{dx} - \psi \frac{d\psi^*}{dx} \right] = \frac{e}{d} v(k) T(k) \quad \text{Equation 3.24}$$

Here,  $v(k) = \frac{\hbar k}{m^*}$  is the group velocity of electrons in the  $k$  state;  $d$  is the material length;  $T(k)$  is the probability of an electron travelling from between electrodes. In this system, it's necessary to account for the sum of transport over all  $k$  states to encompass all electrons involved. It is, therefore, prudent to consider the Pauli exclusion principle through the introduction of the factor  $f_1(k)[1-f_2(k)]$ .  $f_{1,2}$  here refer to the Fermi distributions in the two Reservoir one and empty states of Reservoir two, which are considered for current flowing from one to two:

$$J_{1,2} = \sum_k \frac{e}{d} v(k) T(k) [f_1(k)(1 - f_2(k))] \quad \text{Equation 3.25}$$

$$J_{1 \rightarrow 2} = \frac{e}{h} \int_{-\infty}^{+\infty} T(E) [f_1(E)(1 - f_2(E))] dE \quad \text{Equation 3.26}$$

$$J_{2 \rightarrow 1} = \frac{e}{h} \int_{-\infty}^{+\infty} T(E) [f_1(E)(1 - f_2(E))] dE \quad \text{Equation 3.27}$$

$$I = J_{1 \rightarrow 2} - J_{2 \rightarrow 1} = \frac{2e}{h} \int_{-\infty}^{+\infty} T(E) [f_1(E)(1 - f_2(E))] dE \quad \text{Equation 3.28}$$

Between Equation 3.25 and Equation 3.26, the sum over  $k$  spaces is converted to the integral over all energy per  $k$  whilst adding the density of states per  $k$ . Equation 3.27 gives this relationship for electrons flowing in the opposite direction. Finally, Equation 3.28 demonstrates the resultant total current when deducting one from the other; otherwise known as the Landauer formula (Equation 3.29). It's used to relate transmission function ( $T(E)$ ) and electric transport; the factor of two is included to account for electron spin. As the system's temperature tends to zero, the fermi distributions  $f_{1,2}$  are step functions valued one below their chemical potential:  $\mu_1 = E_F + \frac{eV}{2}$  and  $\mu_2 = E_F - \frac{eV}{2}$ , otherwise it's zero. When  $T=0$  is reached, and the bias voltage is low, current,  $I=GV$  where  $G$  is conductance, which in turn:

$$G = \frac{2e^2}{h} T(E_F) \quad \text{Equation 3.29}$$

If a perfectly conductive channel on two levels is considered, there is an obvious maximum conductance:  $G_0$ . This is a fundamental constant relating electron charge and Planck's constant ( $h$ ):

$$G_0 = \frac{2e^2}{h} = 7.748 \times 10^{-5} S \quad \text{Equation 3.30}$$

This value is referred to as the conductance quantum and is often used when reporting the electrical conductance of nanodimensional junctions. It's also useful when describing that in a ballistic regime, conductance is quantised.<sup>[15]</sup>

The Landauer formula can be further manipulated to consider one-dimensional multiple-channel electron transport, working with the assumption that electron transport can be segmented into transverse and longitudinal parts. The longitudinal part is characterised by the continuous wave vector,  $k_l$  and by energy:

$$E_l = \frac{\hbar^2 k^2}{2m^*} \quad \text{Equation 3.31}$$

Meanwhile, the transverse part is quantised and, therefore, can be defined by the discrete index  $n$ , and transverse energies  $E_{1,2,n}$  which are also quantum channels. As a

result, the system's total energy is the sum of these two parts, and given that  $E_i$  is positive, there will be a finite number of usable channels for a specified total energy,  $E$ .

Referring back to the schematic in Figure 3.5, the multiple channels have operators  $a_{1,2\dots,j;n}$  and  $b_{1,2\dots,k;n}$  that describe how electrons coming in and out impact the sample, respectively per channel; these are related by the matrix  $\hat{S}$ .

$$\begin{pmatrix} b_{1,1} \\ b_{2,1} \\ \dots \\ b_{k,n} \end{pmatrix} = \hat{S} \begin{pmatrix} a_{1,1} \\ a_{2,1} \\ \dots \\ a_{j,n} \end{pmatrix} \quad \text{Equation 3.32}$$

$$\hat{S} = \begin{pmatrix} r & t' \\ t & r' \end{pmatrix} \quad \text{Equation 3.33}$$

$r$  and  $r'$  here are reflection amplitudes, whilst  $t$  and  $t'$  refer to transmission amplitudes for the potential.<sup>[18]</sup>

By introducing the matrix  $tt^\dagger$ , the formula is generalised, allowing for multiple channel considerations. This can be extracted from  $\hat{S}$ ; here, the eigenvalues of the matrix are the transmission coefficients of the multiple channel system ( $T_n(E)$ ), with values of one and zero. The eigenchannels/ conduction channels are formed of wavefunctions, and  $n$  is the index used for quantised electron motion in the transverse direction.

$$I(E_F, V, T) = \frac{2e}{h} \sum_n \int_{-\infty}^{+\infty} T_n(E) [f_1(E) - f_2(E)] dE \quad \text{Equation 3.34}$$

$$G = \frac{2e^2}{h} T \sum_n T_n(E_F) \quad \text{Equation 3.35}$$

Equation 3.35 gives the generalised Landauer formula for multiple-channel electrical conductance.<sup>[19]</sup>

For charge transport within a molecule, the number of electrons present depends on the molecule. When approaching the left and right electrodes, the metallic surfaces influence the molecule's properties. It is also the case that the electrodes act as reservoirs of charge carriers, with their chemical potentials ( $\mu$ ) being equivalent to their Fermi energy ( $E_F$ ) at zero temperature. When  $T$  (temperature) is more than zero, the Fermi-Dirac function describes the population of electrons as a function of energy and the thermal broadening of energy distribution:

$$f(E) = \frac{1}{e^{\left(\frac{E-\mu}{k_B T}\right)} + 1} \quad \text{Equation 3.36}$$



Here,  $\varepsilon$  is electron energy,  $k_B$  is Boltzmann constant,  $\mu$  is the chemical potential of the reservoir and  $T$  is temperature.<sup>[14]</sup>

At equilibrium, there is no current flow, due to the electrodes having even chemical potential. If a symmetrical bias voltage is applied,  $V_B$ , the chemical potential shifts by:

$$\mu_L = \varepsilon_F + \frac{eV_B}{2} \quad \text{Equation 3.37}$$

$$\mu_R = \varepsilon_F - \frac{eV_B}{2} \quad \text{Equation 3.38}$$

$\mu_{L,R}$  refer to the potentials of the left and right electrodes respectively. The result of this is that the left has occupied states whilst the right has empty ones, with charge transporting from left to right. Moreover, the energy range between the two chemical potentials is the bias window. When no molecular level falls within this window, electrons don't have sufficient energy to occupy or empty orbitals and thus transport is blocked. Increasing the bias voltage across the molecule junction will increase the bias window until the point where one of the electrodes aligns with a molecular level, allowing transport once again (see Figure 3.6).<sup>[17]</sup>

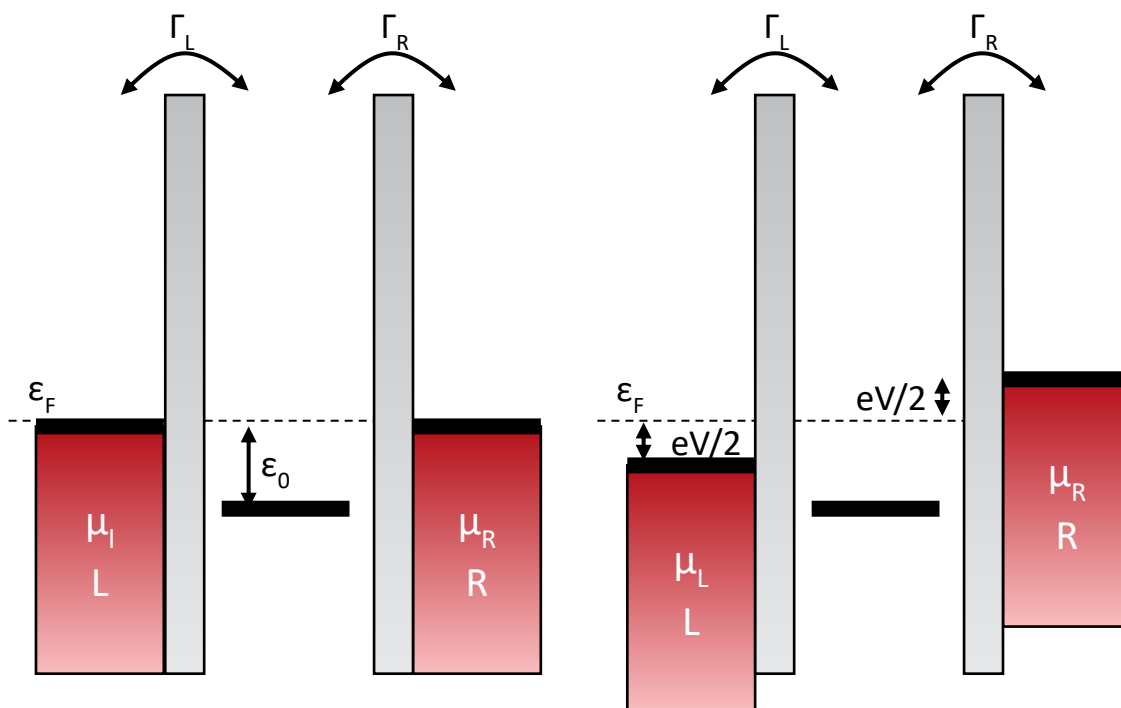


Figure 3.6 Depiction of chemical potential alignment and misalignment influencing electron transport. Increasing or decreasing the bias applied to the electrodes can cause the alignment or misalignments given. When the electrodes align with molecular levels, electron transport is possible.

Electrons can transport through molecules via scattering (including transmission) and tunnelling. The simplest model is for single-level resonant tunnelling; however, multiple orbitals can be involved in electron transport. In single-level tunnelling, the electrons

involved are those with energy closest to the electrodes' Fermi energy. The electrons that are released at the  $E_F$  tunnel through the HOMO-LUMO gap, which is typically a few electron volts, and hundreds of times higher than  $k_B T$  at room temperature; the gap protects the tunnelling electrons from scattering. The relative position of this to the HOMO and LUMO of the molecule in the junction, as well as coupling, are key to dictating the properties of the junction.<sup>[15]</sup>

When the energy of an electron tunnelling through a junction is close to  $E_F$ ,  $T(E)$  exhibits a resonance, and peaks (Figure 3.7).<sup>[15]</sup> Due to the proportional relationship between transmission and electrical conductance, conductance is found from the point at which the transmission curve is intercepted by the  $E_F$  of the electrode.<sup>[15]</sup>

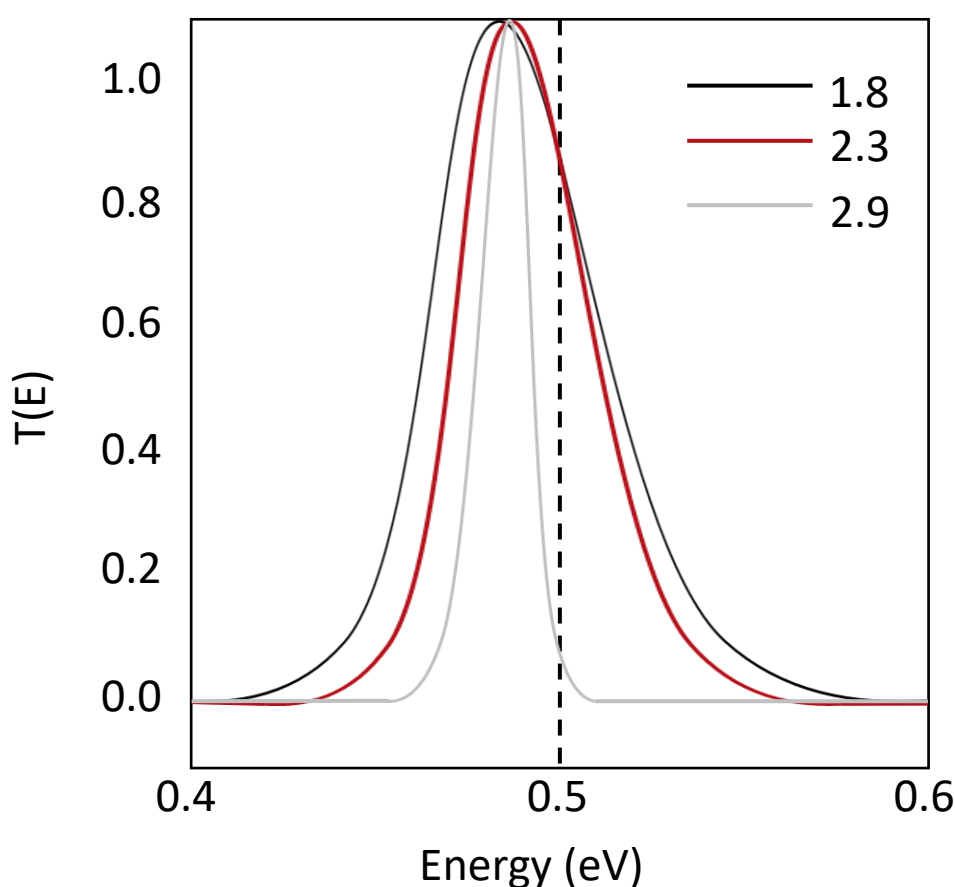


Figure 3.7 Transmission curve with quantum interference peaks occurring where the electron tunnelling energy is close to the Fermi energy; given by the dashed line. Where the Fermi energy intercepts the transmission curve is the point at which the material is conductive.

Separating the molecule and electrodes in a molecular junction causes coupling to weaken and, therefore, the resonance peak width reduces; the opposite is true if they are brought closer together.<sup>[15]</sup>

The Landauer formula (Equation 3.29) can be used to determine junction transport; the transmission for which requires adjustment to consider the electrode coupling strength on voltage.

This relationship is described by the Breit-Vigner formula:

$$T(E, V) = \frac{4\Gamma_l\Gamma_r}{[E - \epsilon_0(V)]^2 + [\Gamma_l - \Gamma_r]^2} \quad \text{Equation 3.39}$$

Plotting this gives the resonance peaks shown in Figure 3.7.<sup>[15]</sup>

So, conductance:

$$G = \frac{2e^2}{h} \times \frac{4\Gamma_l\Gamma_r}{[E - \epsilon_0(V)]^2 + [\Gamma_l - \Gamma_r]^2} \quad \text{Equation 3.40}$$

Equation 3.40 represents the generalisation of the molecular junction Landauer formula.

A key component of quantum transport is quantum interference (QI); it's the interaction between electron waves travelling through molecular orbitals in a molecular junction. QI can be constructive (CQI), where  $T(E)$  is large and the De-Broglie wave pattern has a large amplitude at the right electrode, or destructive (DQI), where the opposite is true; these lead to a change in conductance of the molecule in question; see Figure 3.8.<sup>[15, 16]</sup>

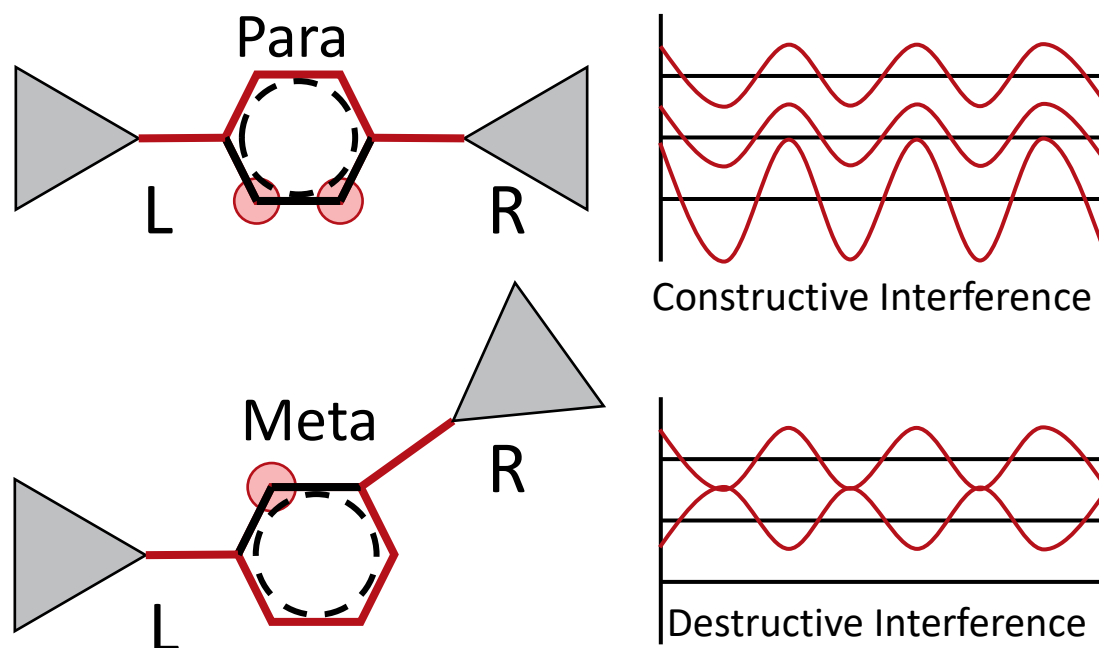


Figure 3.8 Transmission graph for a para- and meta-aligned molecule, alongside the waveforms for the resulting quantum interference. The para position causes constructive interference whereas the meta causes destructive interference.

Magoga and Joachim concluded that QI is caused by resonance within molecular orbitals, and suggested Kirchhoff's law be updated to include an interference term:<sup>[20]</sup>

$$G = G_1 + G_2 + 2\sqrt{G_1 G_2} \quad \text{Equation 3.41}$$

However, it was later surmised that this interference term varies depending on the molecule.

In classical systems, there is a linear dependence of conductance on the conductor length. However, when there is dominant coherent transport, as length increases conductance exponentially decreases.

$$G = G_0 e^{-\beta L} \quad \text{Equation 3.42}$$

Wherein  $\beta$  is the decay constant,  $G_0$  is contact conductance and  $L$  is conductor length.

It was subsequently proven that for series tunnelling:<sup>[21]</sup>

$$J = J_0 e^{-\beta_1 L_1 - \beta_2 L_2} \quad \text{Equation 3.43}$$

In which  $J$  is the current density, and notations 1 and 2 refer to the two molecular parts. QI impacts the overall transmission properties of a molecule. As such, it enables the prediction of current flow disruption and charge transport properties. Theorists have previously proposed multiple methods for estimating the effects of DQI:

- Atom-atom polarisability;
- Kekulé structures;
- Frontier orbital analysis;
- Bond orders.

Each of these can be applied to sets of molecules, however, none of them are universally applicable.<sup>[16]</sup>

It is understood that charge transport is influenced by molecular structure; unequal paths (such as those in meta rather than para-positioned branches from a  $\pi$ -system; see Figure 3.8) cause destructive interference and subsequent decrease in conductivity through the molecule. Including cross-conjugation in single-molecule systems has the same result. It has also been established that saturated  $\sigma$ -systems can exhibit significant DQI effects.

### 3.2. Thermoelectric Properties

Fundamentally, applying a temperature difference across two conducting or semiconducting materials or sides of the same material causes a charge differential. The opposite is also true. These phenomena are encompassed by the Seebeck and Peltier effects respectively.<sup>[22]</sup>

#### 3.2.1. Thermal Conductivity and Current

If a metallic material is heated from one end, the resultant current generation is defined by the Seebeck effect. According to Fourier's Law (Equation 3.44), a temperature gradient influences charge transport, in addition to the applied electric field ( $E$ ):

$$\bar{J}_q = -\kappa \nabla T \quad \text{Equation 3.44}$$

In which  $\bar{J}_q$  is temperature gradient induced electron movement, and  $\kappa$  is the material's 'resistance' to heat (thermal conductance). The negative relationship indicates that current flow is always in the opposite direction to a temperature gradient, as the heating of the electrons gives them more energy, therefore, allowing for greater movement.

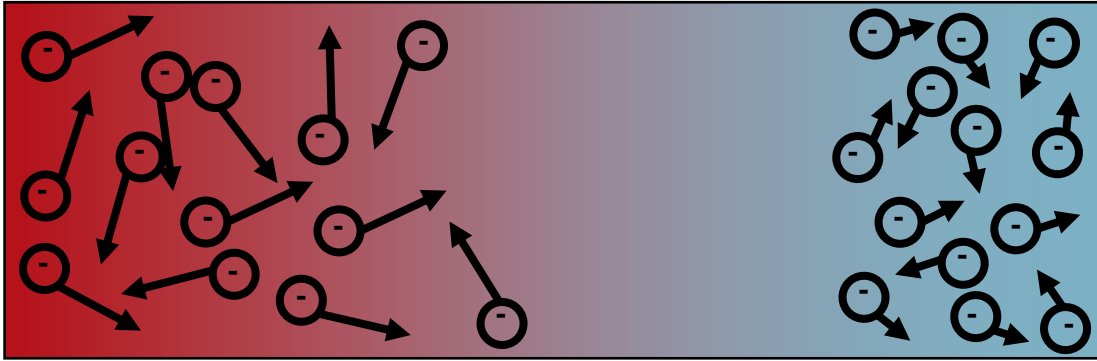


Figure 3.9 Electron density and motion resulting from the application of a temperature gradient. The electrons on the hot side have more energy and are therefore more dispersed; the opposite is true of the cold side. This causes electron transport from the hot to the cold side.

Considering the position  $x$  in the hot side of a material (shown in Figure 3.9),<sup>[17]</sup> collision time  $\tau$  (delay between scatterings), and equilibrium temperature electron thermal energy  $\varepsilon(T)$  within the Drude scattering model, an electron's final collision will be at  $x-v\tau$  with energy  $\varepsilon(T[x-v\tau])$ . In the other direction, electrons have less energy:  $\varepsilon(T[x+v\tau])$ . Summing these gives the total current density as:

$$j_q = nv^2\tau \frac{d\varepsilon}{dT} \left( -\frac{dT}{dx} \right) \quad \text{Equation 3.45}$$

Substituting the thermal electron mean square velocity into Equation 3.45 to relate it to 3D, and using electron specific heat  $c_v$  in place of  $n \frac{d\varepsilon}{dT}$  (as  $n=N/V$ ), gives:

$$j_q = \frac{1}{3} v_{th}^2 \tau c_v (-\nabla T) \quad \text{Equation 3.46}$$

$$\kappa = \frac{1}{3} v_{th}^2 \tau c_v \quad \text{Equation 3.47}$$

Equation 3.47 is gained by combining Equation 3.46 with Equation 3.44 and defines thermal conductance.

The Sommerfield electron theory requires electron speed from Equation 3.46 to be altered slightly, to encompass electron distribution and density of available states surrounding the Fermi energy  $E_F$ . By substituting the thermal electron velocity with Equation 3.48 and dividing by electrical conductivity, the Wiedemann-Franz law is concluded (Equation 3.49):

$$v_f^2 = \frac{2\varepsilon}{m^*} \quad \text{Equation 3.48}$$

$$\frac{\kappa}{\sigma} = \frac{\pi^2}{3} \left( \frac{k_b}{e} \right)^2 T \quad \text{Equation 3.49}$$

This is critical for thermoelectric design as it relates electrical and thermal conductivities ( $G$  and  $\kappa$  respectively) to one another.

### 3.2.2. The Seebeck Effect

As aforementioned, heating one end of a material causes electrons to travel from the hot to the cold end, given their increased energy (Figure 3.9). The opposite is, therefore, also true, with positive charges gathering at the cold end, and negative at the hot, thus producing an electric field. This is termed the Seebeck, or thermoelectric, effect. The size of the voltage difference depends on the temperature gradient (Equation 3.50):

$$E_{th} = -S\nabla T \quad \text{Equation 3.50}$$

Here,  $S$  is the Seebeck coefficient. Given that this is a non-equilibrium process, if the temperature gradient is removed, the charge carriers will redistribute, thus diminishing the electric field. As electric and thermal components are relevant when looking at total current density, the following is true:

$$j_{tot} = G(-\nabla V + E_{th}) \quad \text{Equation 3.51}$$

$$S = -\frac{\nabla V}{\nabla T} \quad \text{Equation 3.52}$$

$$S = -\frac{\Delta V}{\Delta T} \quad \text{Equation 3.53}$$

Substituting  $J_{tot}=0$  into Equation 3.51, Equation 3.52 can be concluded. When small temperature gradients are evaluated this can in turn be altered to Equation 3.53, in which  $\Delta T$  is the temperature gradient and  $\Delta V$  the resultant thermovoltage. The negative symbol indicates these two are operating in opposite directions.

In metals, both charge carrier types (electrons and holes) influence the thermoelectric voltage, meaning that their  $S$  is low given they are almost equal and opposite. Contrastingly, semiconductors are of interest due to their charge carrier duality causing high  $S$ .  $S > 0$  results from p-type materials, and  $S < 0$  from n-type. This, therefore, explains which charge carrier dictates transport within the material.

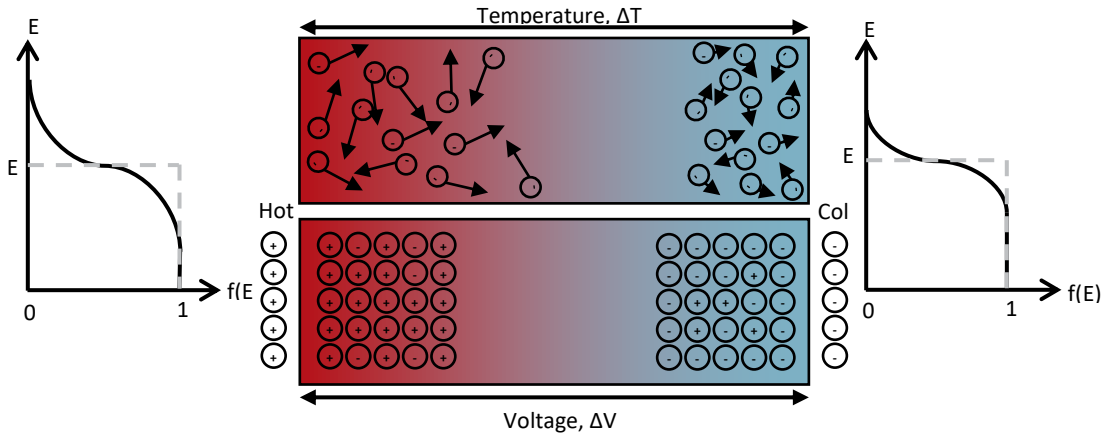


Figure 3.10 Fermi-Dirac distributions for electrons at either side of a thermoelectric material with a temperature gradient applied. A depiction of the charge carrier arrangement within the material is also shown. Again, the electrons in the hot side have more energy and hence spread to the cold side; this causes holes to be left on the hot side.

The Drude-Sommerfeld free electron model can be utilised to approximate electron movement in metals, by accounting for electron motion, but not phonons (scattering lattice vibrations), impurities or diffusion crystal defects. This works well for predicting the metal's Seebeck coefficient. From this model, assuming the Fermi-Dirac distribution given in Equation 3.54 and the 3D velocity of states from Equation 3.55, the average electron energy when  $T \rightarrow 0$  is given in Equation 3.56 (wherein  $E_{f0}$  is the fermi energy at  $T=0$ ).

$$f(E) = \frac{1}{1 + e^{\frac{E-E_f}{k_b T}}} \quad \text{Equation 3.54}$$

$$g(E) = \frac{m_e}{\pi^2 \hbar^3} \sqrt{2m_e E} = \frac{3}{2} \frac{n}{E_f} \sqrt{\frac{E}{E_f}} \quad \text{Equation 3.55}$$

$$E_{av}(T) \approx \frac{3}{5} E_{f0} \left[ 1 - \frac{5\pi^2}{12} \left( \frac{k_b T}{E_{f0}} \right)^2 \right] \quad \text{Equation 3.56}$$

In Figure 3.10 it's evident that the electrons on the hot side have more energy than those on the cold (as demonstrated by the Fermi-Dirac distributions on either side).<sup>[17]</sup> Considering the previously described Seebeck effect, under equilibrium conditions, average energy  $E_{av}$  (from Equation 3.56) needs balancing with the electric field (Equation 3.57).

$$-q\Delta V = e\Delta V \quad \text{Equation 3.57}$$

$$E_{av}(T) = \frac{\partial E}{\partial T} \Delta T = \frac{\pi^2 k_b^2 T}{2E_{f0}} = e\Delta V \quad \text{Equation 3.58}$$



$$S = -\frac{\Delta V}{\Delta T} = \frac{\pi^2 k_b^2}{2eE_{f0}} T \tag{Equation 3.59}$$

Molecular junction thermopower varies depending on the molecular scaled structural modification, like length, substitution, and spacer/anchor/electrode components. Equation 3.59 qualitatively explains the thermopower of large-area SAM-based molecular junctions.

Using Equation 3.59, the results shown in Table 3.1 and Figure 3.11 can be concluded:

Table 3.1 Common metal Ss which align with the relationships given in Equation 3.59.<sup>[23]</sup>

Material	S@20 K ( $\mu\text{V/K}$ )	S@300 K ( $\mu\text{V/K}$ )
Gold	1.79	1.94
Aluminium	-1.6	-1.8
Copper	1.7	1.84
Platinum	4.45	-5.28

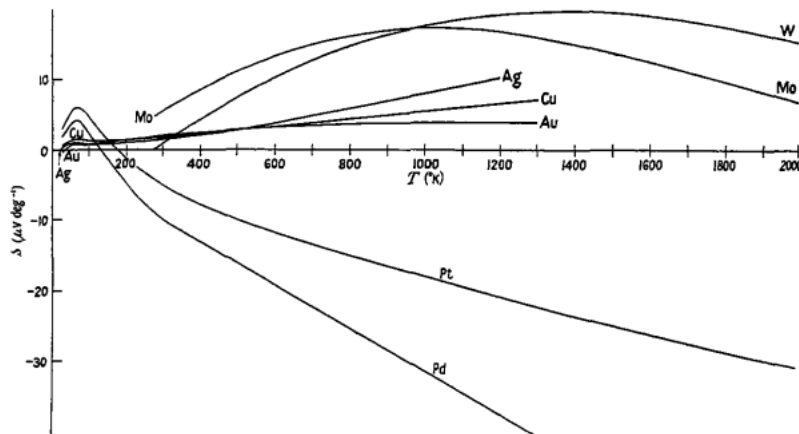


Figure 3.11 Common metal S coefficients obtained using the Drude-Sommerfeld free electron model which defines S as varying with temperature.<sup>[23]</sup>

### 3.2.3. Thermal Power Generation and Figure of Merit

The previously described properties of conductive materials lend them to being used for thermoelectric power generation. Particularly, the combination of n- and p-type materials, like the set-up in Figure 3.12.<sup>[17]</sup> The grey sections depict the electrical connection between the semiconductor legs, and the heat source and sink.

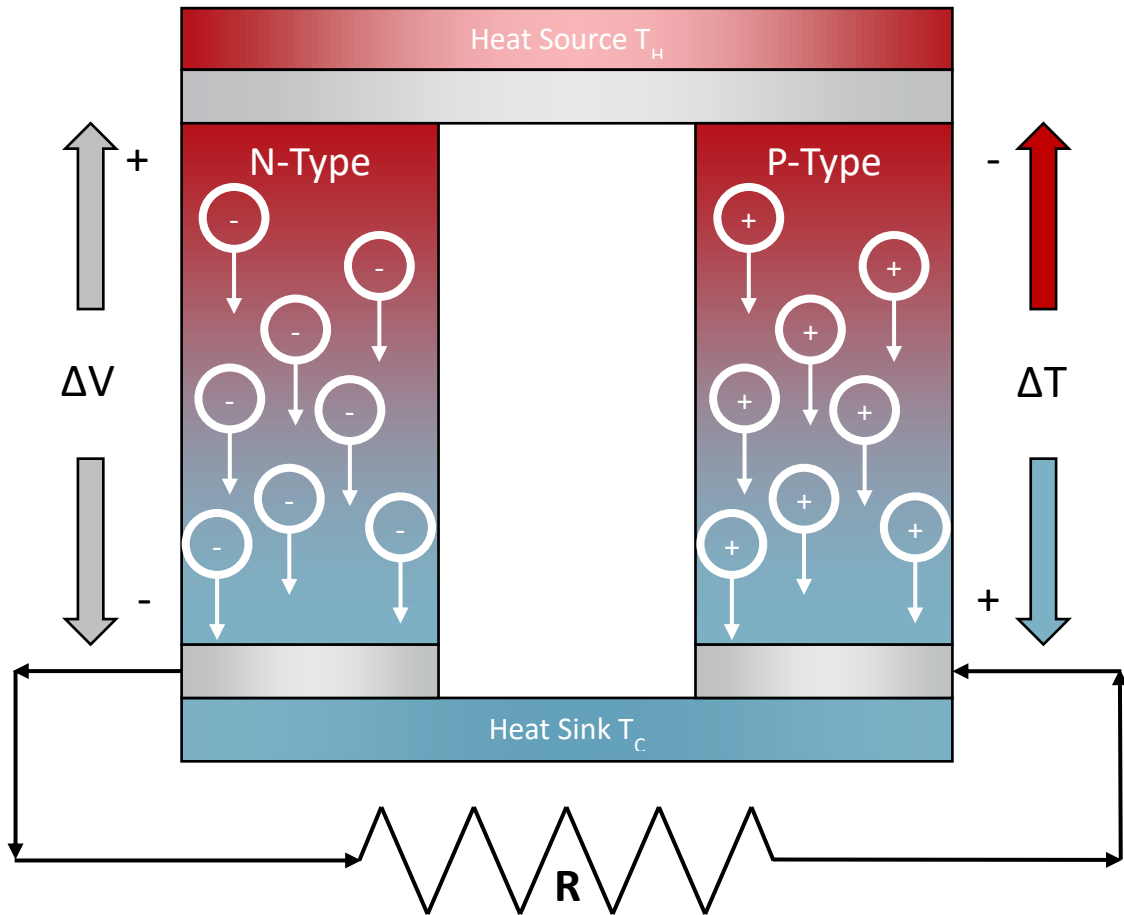


Figure 3.12 Thermoelectric generator consisting of n- and p-type materials. The legs are connected in series with a heat source and sink, where  $R$  the load, and the generated current,  $I$ , are shown by the arrows. Charge carrier movement due to applied temperature gradient is demonstrated also.

The resultant change in the electric field from the application of temperature gradient produces a potential difference, that causes a current:

$$\Delta E_{th} = (S_p - S_n)(T_H - T_C) \quad \text{Equation 3.60}$$

$$I = \frac{(S_p - S_n)(T_H - T_C)}{R_p + R_n + R} \quad \text{Equation 3.61}$$

In which  $S_n$  and  $S_p$  are the Seebeck coefficients of the semiconductor legs,  $T_H$  and  $T_C$  are the temperatures of the heat source and sink,  $R_n$  and  $R_p$  are the resistances of the legs and  $R$  is that of the load resistor. Power,  $W$ , dissipated by the load resistor can be described as:

$$W = I^2 R = \left[ \frac{(S_p - S_n)(T_H - T_C)}{R_p + R_n + R} \right]^2 R \quad \text{Equation 3.62}$$

As the Seebeck effect is non-equilibrium, the temperature differential must be maintained to keep generating the voltage, otherwise, Peltier cooling comes into effect and limits the

temperature gradient. Resultantly it's imperative to retain good heat flow to find the system's overall efficiency.

Peltier cooling can be written as in Equation 3.63, and the opposing heat flow as in Equation 3.64. In these equations,  $\kappa_n$  and  $\kappa_p$  are the thermal conductivities of the two semiconductor legs. The total heat current through both is given in Equation 3.65.

$$\dot{Q}_{Peltier} = \frac{S_p - S_n}{T_H} \quad \text{Equation 3.63}$$

$$\dot{Q}_h = (\kappa_n + \kappa_p)(T_H - T_C) \quad \text{Equation 3.64}$$

$$\dot{Q}_{total} = \frac{S_p - S_n}{T_H} + (\kappa_n + \kappa_p)(T_H - T_C) \quad \text{Equation 3.65}$$

The thermodynamic efficiency of such a system is given by  $\eta/\dot{Q}_{total}$ . By maximising the ratio of  $W: R$ , the highest efficiency can be obtained. With the system above, this occurs when the load resistance to internal resistance is:

$$\frac{R}{R_p + R_n} = \sqrt{1 + ZT} \quad \text{Equation 3.66}$$

In Equation 3.66,  $T$  is the average temperature across the system, and  $Z$  is the FOM. This can be further described by Equation 3.67.

$$Z = \frac{S^2 G}{k} \quad \text{Equation 3.67}$$

Wherein  $\kappa = \kappa_n + \kappa_p$  and is the thermal conductivity of the thermally connected branches;  $S = S_p - S_n$  and is the material's thermopower;  $G$  is the electrical conductance of the system. FOM is expressed with temperature, however, it's typically combined to be given as  $ZT$  to become dimensionless, but at a specific temperature. The system efficiency can be concluded to be a ratio of net power output to heat input, or:<sup>[24, 25]</sup>

$$\eta = \frac{(T_H - T_C)}{T_H} \frac{\sqrt{1 + ZT} - 1}{\sqrt{1 + ZT} + \frac{T_C}{T_H}} \quad \text{Equation 3.68}$$

From Equation 3.67 and Equation 3.68, it's evident that efficiency improves with heightened  $Z$ , which in turn is improved by increased heat flow. At the same time, electrical resistance and thermal conductance should be curtailed.<sup>[26, 27]</sup>

From Equation 3.67 it's evident that electrical conductance and Seebeck coefficient should be maximised whilst thermal conductance should be minimised to retain the temperature gradient. It can be rewritten to show Equation 3.69, in which  $k$  is given in

Equation 3.70. It is noted that the numerator of Equation 3.69 is often referred to as the power factor of a material.

$$ZT = \frac{S^2 G}{\kappa} T \quad \text{Equation 3.69}$$

$$\kappa = \kappa_e + \kappa_{ph} \quad \text{Equation 3.70}$$

As highlighted previously, the Wiedemann-Franz law (Equation 3.49) shows there is a correlation between electrical and thermal conductance and, therefore, one cannot be increased without increasing the other, and vice versa. The Wiedemann-Franz law can be re-arranged to in which  $L$  is the Lorentz number ( $2.44 \times 10^{-8} \text{W}\Omega\text{K}^{-2}$ ).

$$\frac{\kappa_e}{G} = LT \quad \text{Equation 3.71}$$

From Equation 3.69 to Equation 3.71 it's clear that phonon contribution thermal conductivity, or increasing  $S$  are the best ways to improve thermal efficiency. Practically,  $FOM$  needs to be greater than one with the ideal value greater than three.

#### 3.2.4. Nanoscale Thermoelectricity

Nanomaterials are likely to have good FOM and related properties due to having large surface areas for their total volume. In particular, they are effective at reducing the phonon component of thermal conductivity, as a result of their surfaces. This has been demonstrated for SiGe superlattices and other nanocomposites.<sup>[28, 29]</sup> Furthermore, it has been found that adding impurity atoms to nanostructures by allowing the materials caused shorter wavelength phonons to be scattered, thus showing another way for reducing phonon thermal conductivity.<sup>[30]</sup>

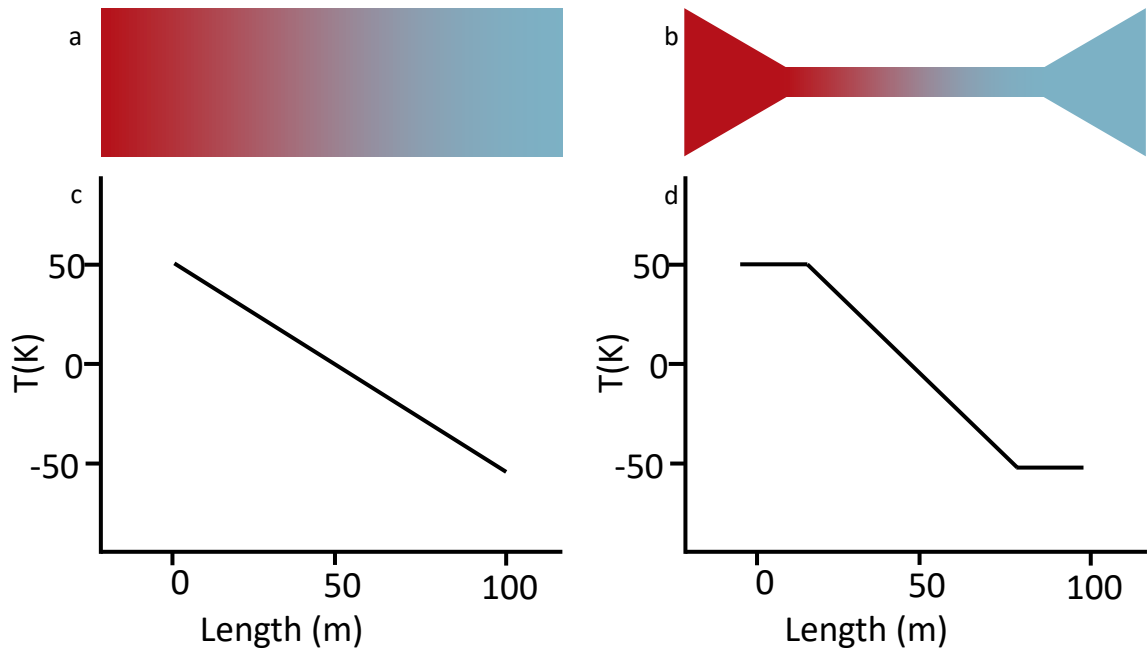


Figure 3.13 Heat transport in a bulk material (a) and nanomaterial (b) with their respective heat transport graphs (c & d). In the bulk material, there is a linear relationship between temperature and material length whereas for a nanoconstriction there is a steep decrease in temperature at the constriction point.

As shown in Figure 3.13,<sup>[17]</sup> heat travels differently when in a bulk material vs. nanoconstriction between two electrodes; in the bulk material, the heat drops away linearly from the hot side to the cold side. In the nanoconstriction, however, there is a sharp reduction in heat when the constriction is reached. Given the steep gradient, it can be assumed that electrons in this region have greater energy than those outside of it, causing them to flow to the cold side of the junction.

As described in the previous parts of Chapter 3.2, negative charge carriers gather at the cold side of the junction, creating an electric field. As such, Equation 3.28 can be adjusted to 'open-circuit' conditions by making it equal to zero. Furthermore, the distribution functions of the leads have been expanded for lead one.

$$0 = \frac{2e}{h} \int_{-\infty}^{+\infty} dET(E) \left[ \left( \frac{\partial f}{\partial \mu} \Big|_{\mu=\mu_1} \right)_{T_1} \Delta\mu_{1-2} + \left( \frac{\partial f}{\partial T} \Big|_{T=T_1} \right)_{\mu_1} \Delta T_{1-2} \right] \quad \text{Equation 3.72}$$

Using the approximations given in Equation 3.73 and Equation 3.74, Equation 3.72 can be expressed as in Equation 3.75.

$$\frac{\partial f}{\partial \mu} = -\frac{\partial f}{\partial E} \approx \delta(E - \mu) \quad \text{Equation 3.73}$$

$$\frac{\partial f}{\partial T} = -\frac{E - \mu}{T} \frac{\partial f}{\partial E} \quad \text{Equation 3.74}$$

$$\frac{\Delta\mu_{1-2}}{\Delta T_{1-2}} = \frac{1}{T(E)|_{\mu=\mu_1}} \int_{-\infty}^{+\infty} dET(E) \frac{E - \mu}{T_1} \frac{\partial f_1}{\partial E} \quad \text{Equation 3.75}$$

By expanding transmission function in a Taylor series by using the Sommerfield expansion, whilst considering that changing chemical potential causes diffusive charge flow ( $\Delta\mu_{1-2} = -q\Delta V_{1-2}$ ) it is possible to reach the Mott formula (Equation 3.76).<sup>[31]</sup>

$$s = -\frac{\Delta V}{\Delta T} = -\frac{\pi k_b^2 T}{3e} \left. \frac{\partial [\ln T(E)]}{\partial E} \right|_{E=\mu} \quad \text{Equation 3.76}$$

Equation 3.76 is the Mott formula for metals in a free electron model, without scattering. This form is only applicable when temperature variation is minimal, and far from transmission resonance, such that it can be assumed the transmission function is also minimal. It is evident from this relationship that by increasing the gradient on  $\ln T(E)$  near  $E=E_f$ , the Seebeck coefficient is maximised.<sup>[31]</sup>

A nanomaterial's thermoelectric properties are influenced by transport resonances. This is demonstrated by assuming a linear-response system and relating electrical current, heat flow, voltage difference and temperature difference (Equation 3.77).<sup>[32-34]</sup>

$$\begin{pmatrix} I \\ \dot{Q} \end{pmatrix} = \frac{1}{h} \begin{pmatrix} e^2 L_0 & \frac{e}{T} L_0 \\ e L_1 & \frac{1}{T} L_1 \end{pmatrix} \begin{pmatrix} \Delta V \\ \Delta T \end{pmatrix} \quad \text{Equation 3.77}$$

With phase coherent transport,  $L_n$  represents the sum of spin contributions (Equation 3.78), in which  $n=0,1,2\dots$

$$L_n = L_n^\uparrow + L_n^\downarrow \quad \text{Equation 3.78}$$

$$L_n^\sigma = \int_{-\infty}^{+\infty} dE (E - E_f)^n T^\sigma(E) \left( -\frac{\partial f}{\partial E} \right) \quad \text{Equation 3.79}$$

In Equation 3.79,  $\sigma$  represents the spin [ $\uparrow\downarrow$ ] of the electron with energy ( $E$ ).<sup>[35]</sup>

Using thermoelectric properties that can be determined experimentally, Equation 3.77 can be rewritten.<sup>[34]</sup> The parts are included in Equation 3.81 - Equation 3.84.

$$\begin{pmatrix} \Delta V \\ \dot{Q} \end{pmatrix} = \frac{1}{h} \begin{pmatrix} 1/G & S \\ \Pi & \kappa \end{pmatrix} \begin{pmatrix} I \\ \Delta T \end{pmatrix} \quad \text{Equation 3.80}$$

$$G = \frac{e^2}{h} \quad \text{Equation 3.81}$$

$$S = -\frac{\Delta V}{\Delta T} = \frac{1}{eT} \frac{L_1}{L_0} \quad \text{Equation 3.82}$$

$$\Pi = \frac{1}{e} \frac{L_1}{L_2} \quad \text{Equation 3.83}$$

$$\kappa = \frac{1}{hT} \left( L_2 - \frac{L_1^2}{L_0} \right) \quad \text{Equation 3.84}$$

From here, another expression for  $ZT$  can be determined:

$$ZT = \frac{L_1^2 G}{(L_0 L_2) - L_1^2} \quad \text{Equation 3.85}$$

Due to the contribution from phonons being minimal in such a system at room temperature,  $\kappa$  can be assumed to be equal to just  $\kappa_e$ .<sup>[36]</sup> This relationship underpins how electrical and thermal transports relate to one another and, therefore, adds difficulty to improving thermopower; this is exacerbated at the nanoscale.

### 3.2.5. Molecular Junction Thermoelectricity

Organic molecules are the logical next step in terms of improving FOM, due to their intrinsically low thermal conductivity which enables a near-constant temperature gradient to be maintained. Their small size also makes them ideal as they promote ballistic electron transport, meaning that the previously outlined thermoelectric theory applies.

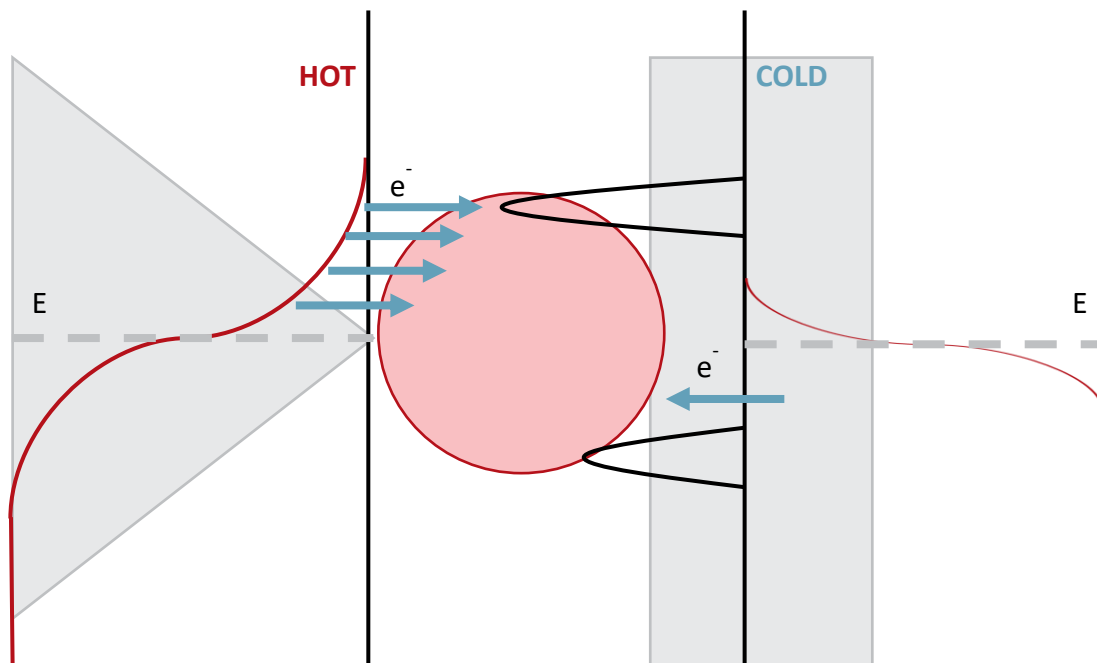


Figure 3.14 A molecular junction in which some electrons have energy greater than  $E_f$  and can, therefore, tunnel to the cold side via empty energy levels. The opposite phenomenon occurs much less because energy levels are filled up to  $E_f$ .

As shown in Figure 3.14,<sup>[37]</sup> electrons on the cold side typically have energy greater than the Fermi level, whilst electrons on the cold side are below it. The subsequent difference

in chemical potential causes electrons to tunnel between electrodes via empty molecular orbitals. Hence, this flow is more common from the hot to the cold side as there are more abundant empty orbitals in that direction.

Similarly to how hot point probes can determine whether a semiconductor material is n- or p-type, a material's  $S$  can be indicative of Fermi level location.<sup>[38, 39]</sup>

As previously outlined, applying a voltage to a molecular junction can cause electrons to tunnel from one electrode to another, via the bridging molecule. If  $E_{HOMO}$  and  $E_{LUMO}$  are assigned to the frontier orbitals' energy levels, the aforementioned relationship can be expressed in terms of a two-level system, both of which contribute to charge carrier transport. Assuming there are Lorentzian peaks in transmission function at both HOMO and LUMO:<sup>[38]</sup>

$$T(E) = \frac{\Gamma_1 \Gamma_2}{\Gamma^2 + (E - E_{HOMO})^2} + \frac{\Gamma_1 \Gamma_2}{\Gamma^2 + (E - E_{LUMO})^2} \quad \text{Equation 3.86}$$

$$S = -\frac{8\pi^2 k_b^2 T}{e} \frac{1}{(E_H - E_L)^2} \left( E_f - \frac{E_H + E_L}{2} \right) \quad \text{Equation 3.87}$$

In Equation 3.86  $\Gamma$  is the peak broadening caused by lead contact, in which  $\Gamma$  is the average of  $\Gamma_1$  and  $\Gamma_2$ . Equation 3.87 results from the Taylor expansion of Equation 3.86 when it's assumed the Fermi energy falls perfectly halfway between HOMO and LUMO peaks and, therefore, the difference between  $E_f$  and  $E_{H,L}$  is far greater than the sum of  $\Gamma_{1,2}$ . From Equation 3.87 it's clear that in molecular junctions, thermopower is not related to electrode coupling, however, this is only true when  $E_f$  is at the perfect mid-gap position. In contrast, electrical conductance does depend on coupling.<sup>[40]</sup>

Equation 3.86 also highlights two possible solutions for  $E_f$  at certain  $T(E)$  values; hence it is impossible to determine which is true. However, the sign associated with the  $S$  from Equation 3.87 is indicative of which side of the middle point in the HOMO-LUMO gap  $E_f$  falls.



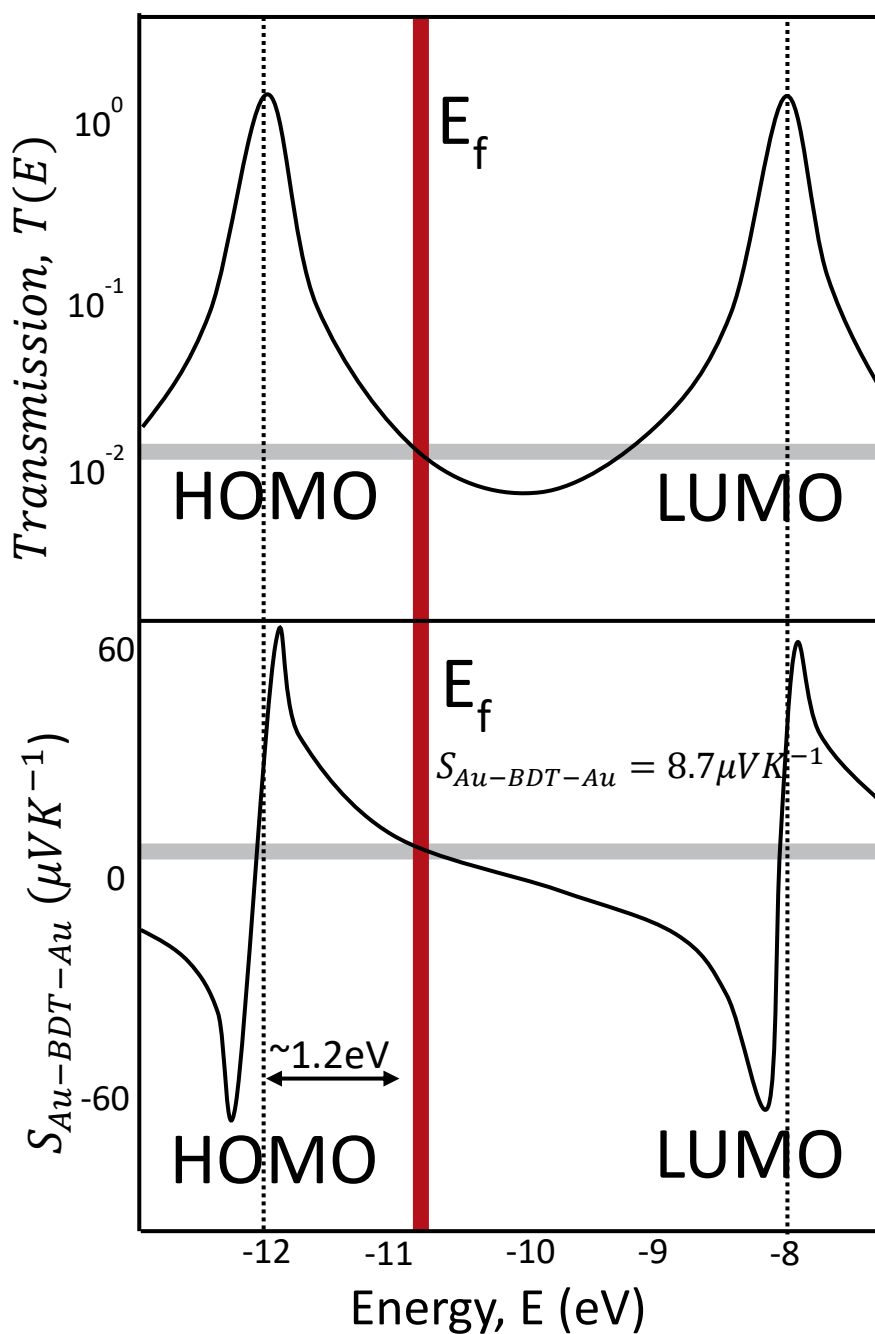


Figure 3.15 Depiction of the relationship between transmission and Seebeck, for benzenedithiol between gold electrodes. The red line highlights the Fermi energy. If this intersects the transmission graph at a steep gradient, it will correspond to a high  $S$ ; this also corresponds to high electrical conductance.

Figure 3.15 gives  $E_f$  relating to both  $T(E)$  and  $S$ ; electrical conductance can subsequently be found from the magnitude of  $T(E)$  at  $E_f$ .<sup>[41]</sup> Furthermore, thermal power can be found from the derivative of  $\ln T(E)$  at  $E_f$ .  $S$  is positive for HOMO-dominated molecules, and negative when they're LUMO-dominated.<sup>[40, 41]</sup> As is evident from Figure 3.15, it's helpful to have a steep gradient in  $T(E)$  close to  $E_f$  given that that will correspond to a high  $S$ .<sup>[15]</sup>

## 4. Experimental Background

### 4.1. Organic Electronics

Traditionally, electronic devices were formed by scaling down a bulk material as in the top-down methods defined in Richard Feynman's speech, per Chapter 1. It was later suggested that a bottom-up approach may be more suitable for the next stage in size reduction, to enable Moore's law to take effect. This gave rise to molecular electronics, in which molecules are specifically designed with electronic properties in mind.<sup>[6]</sup>

Kuhn and Mann are typically credited with being the first to perform molecular electronics-related experiments, in 1971. They used monolayers of cadmium salts of fatty acids for conductance measurements and found that increasing the number of layers subsequently exponentially decreased the conductivity. They theorised that this was a result of electron tunnelling through the layers.<sup>[42]</sup>

Shortly after this, in 1974, Aviram and Ratner published the first work on single-molecule electron transport. They created a junction using a  $\sigma$ -bonded methylene tunnelling bridge between a  $\pi$ -accepting and a  $\pi$ -donating system and applied a voltage.<sup>[43]</sup> Ratner stated in 2013 that he believed two things made their research seminal:

1. A calculation was suggested which led to the development of non-equilibrium Green's Functions.
2. It was proposed that single molecules could be used as electronic devices; they suggested two electrodes could be attached to a single molecule to form an electronic circuit. This has extensively been studied since, in the form of Break Junctions (BJs).<sup>[44]</sup>

Following these initial breakthroughs, the development of the Scanning Tunnelling Microscope (STM) at IBM in 1981 and the Atomic Force Microscope (AFM) in 1986 enabled scientists to directly measure the electrical conductance of single molecules for the first time.<sup>[44]</sup>

The late 1990s and early 2000s saw Mark Reed, James Tour and their research groups progressing on how to measure transport in single molecules, and how these results differ between species. They formed break junctions using the self-assembly of benzene-1,4-dithiol onto gold electrodes, which gave the junction gold-sulphur-aryl-sulphur-gold.<sup>[45]</sup>

Several key issues faced the field of molecular electronics in the beginning, including the requirement for collaboration across synthetic chemistry, theoretical physics and experimental physics, among others. Landauer, Büttiker, Meir and Wingreen, alongside non-equilibrium Green's functions, were pivotal in developing the understanding of the

theory behind molecular electronics; they enabled theoretical calculations to accurately predict the outcome of experiments. The acquisition of accurate single molecule conductance results was also initially problematic, though this was largely solved by the employment of electrochemical or mechanical BJJs, with the statistical analysis of large datasets being made possible.<sup>[46-48]</sup>

In 2003 research began into Quantum Interference (QI) effects within molecular electronics, which now forms the majority of research in this field. This was done by moving the thiol position between meta and para on a molecule, therefore raising the potential to decouple the electronic properties of a molecule from disordered electrodes. The molecule in question was bis-9,10-phenylethynylantracene at the core and thiol anchors protected by acetyl groups; see Figure 4.1.<sup>[49]</sup>

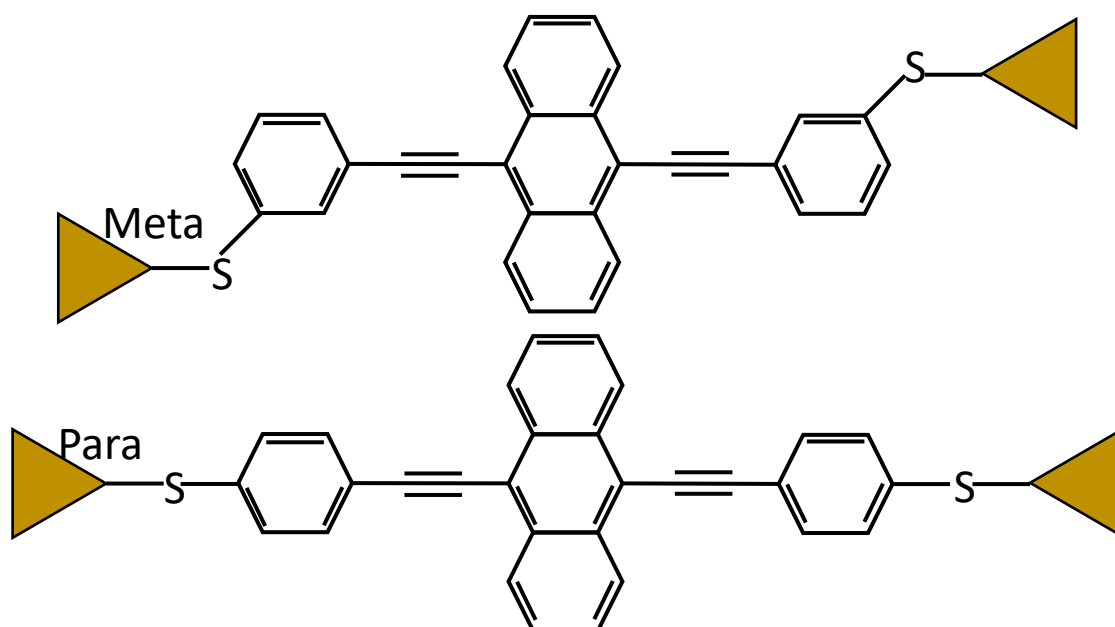


Figure 4.1 Molecular wires were used to investigate quantum interference effects when changing the thiol position between para and meta positions when including the molecule in a mechanical break junction. They found that electrical conductance was worse for the meta configuration than for the para.

It was concluded that the conductance of the molecule did indeed vary depending on the thiol position; the meta position resulted in lower electrical conductance than the para.<sup>[49]</sup>

The first key step in organic electronics and organic molecular electronics was the discovery of the photoconductivity of anthracene in 1906.<sup>[50]</sup> This was then followed by further studies of similar molecules into the 1950s, with phthalocyanine compounds being amongst the first studied for their relative stability.<sup>[51]</sup> In particular, charge transfer complexes were reported in 1954 to have low resistivity when combining perylene with iodine or bromine, regardless of the initial species being insulating.<sup>[52]</sup>

In 1963 Giulio Natta and his colleagues received the Nobel prize for chemistry for their work in developing the first organic semiconductor. They found that it was possible to tune its conductivity depending on the production method, with results in the range of  $7 \times 10^{-11}$  S/m to  $7 \times 10^3$  S/m. This and other similar works though thought-provoking, proved largely unusable due to being unable to dissolve such molecules in organic solvents. This was made possible by Jim Feast developing a soluble precursor which is processed to have excess groups from its synthesis removed to make the target molecule. Soluble conductive polymers could next be created therefore giving rise to the fabrication of useful devices into the 1980s. The benefit of such materials over their inorganic counterparts is that they are easily fabricated via cheaper methods including spin coating and roll-to-roll processing, as opposed to high-temperature deposition from vapour components typical of inorganic semiconductors.<sup>[6]</sup>

Organic molecules' sensitivity and selectivity lend them to molecular engineering from the bottom up, therefore making them ideal candidates for molecular engineering.<sup>[6]</sup>

In recent years, several review articles have been published highlighting achievements in the field of organic molecular electronics. The results of a plethora of organic thermoelectric materials research were summarised and it was concluded that there is further work required before the existing technology reaches a practical level of usefulness. It was recognised that key areas of study include tuning QI effects and thermoelectric properties via molecular design, particularly with the selection of molecular core, additional side groups and subsequently packing of molecules within a monolayer, altering energy levels and heteroatom effect. These aspects, alongside material doping, are proposed to be critical in designing effective materials with high charge transport, with that in the region of  $10^{20}$ - $10^{21}$  cm<sup>3</sup> leading to the greatest thermoelectric performance.<sup>[53]</sup>

Organic molecules and their monolayers have been previously investigated due to their relatively low toxicity, ease of fabrication and abundance of constituent elements compared to inorganic semiconductors, however, they often gave lower Seebeck coefficients ( $S$ ) and corresponding Figure of Merit (FOM) than researchers had hoped. Single-molecule junctions and Self-Assembled Monolayers (SAMs) are of particular interest in this field due to their Density of States (DOS) depending significantly on their molecular energy levels which can, in turn, be designed specifically with thermoelectric properties in mind.

Tanaka's review summarised how involving metal complexes had the potential to alter these results, by manipulating metal-ligand complexes and functions for transmission

function control and subsequently impact  $S$ . Such complexes can be separated into three categories:

1. Coordination (inorganic) complex junctions, in which metal-ion coordination stabilises the frontier orbitals.
2. Metal encapsulated junctions that surround the organic molecule therefore stabilising the frontier orbitals.
3. Organometallic junctions wherein hole transport through the HOMO is enhanced by disrupting the frontier orbitals resulting from the metal-carbon covalent bond.

These are depicted graphically in Figure 4.2.<sup>[54]</sup> Little has been done to verify the results experimentally, however, theoretical studies imply that an  $S$  of up to  $90 \mu\text{V/K}$  is attainable using these techniques.<sup>[54]</sup>

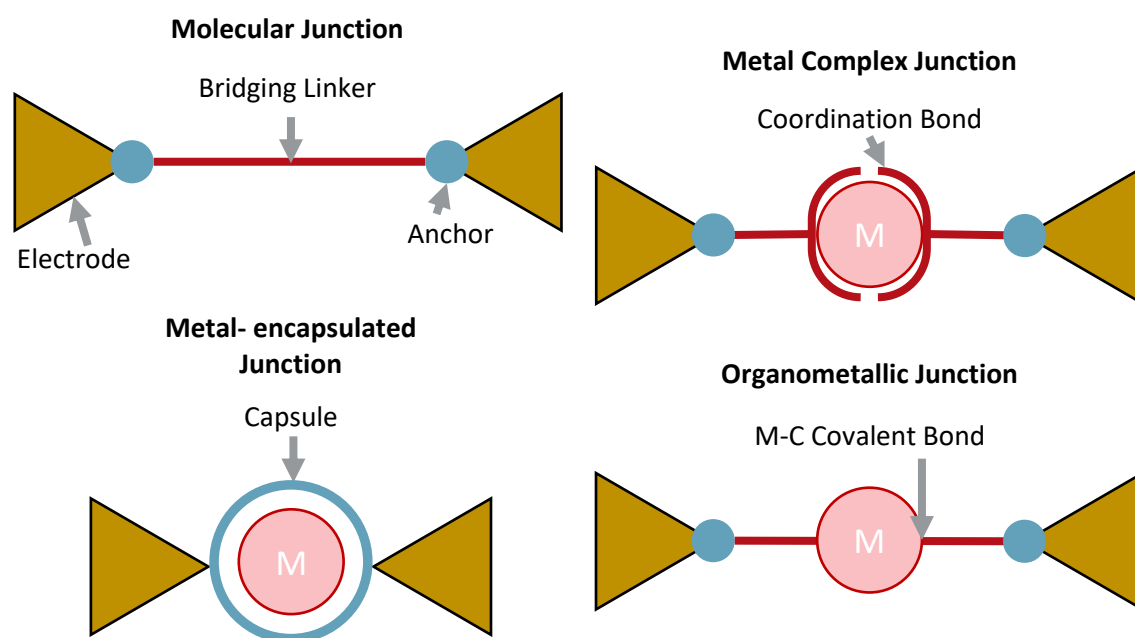


Figure 4.2 Different options for including metal complexes in molecular junctions are depicted. The top left image shows a standard molecular junction; the top right gives a metal complex junction with a coordination bond. The bottom left diagram shows a metal encapsulated junction whilst the bottom right image is of an organometallic junction.

Several researchers have attempted to tune molecules and their monolayers to consider these potential improvements. For example, a series of anthracene-based molecules that had been tuned per their QI effects were formed into SAMs on gold. Four molecules were tested; combinations included using different positions and combinations of nitrogen linkers and thiols. Both para and meta positions of these connections compared to the molecular backbone were tested. Following the production of the SAMs, Langmuir-Blodgett (LB) was employed for depositing a further monolayer on top of the existing SAM to create the linker to the top contact in a molecular junction. Porphyrins on

graphene were used for this 'slippery' linker, so termed due to the lack of covalent bonds between layers.<sup>[55]</sup>

This work concluded that adding the planar layer could improve the  $S$  of the junction by a maximum factor of two, though this was not the case for every molecule studied. It was surmised that this was due to the molecules' packing density; higher packing density perhaps lead to more overlapping  $\pi$ - $\pi$  interactions resulting in a shift of the HOMO and LUMO energies and therefore altering the Fermi energy and consequently the  $S$ . It was suggested that side groups could be added to the molecules to reduce this packing density and hopefully improve  $S$  further still.<sup>[55]</sup>

Furthermore, when looking at single-molecule junctions, the length of the molecule can dictate the mode of charge transport through the junction. For instance, it was found that molecules with length,  $L$ , shorter than 3 nm followed quantum transport effects and therefore broadly aligned with the relationship  $G \sim e^{-\beta L}$  due to transport being phase coherent. However, when the molecule length exceeded 3 nm, the relationship instead became  $G \sim 1/L$ , per classical transport thus relating to incoherent transport. This then means that molecules and their subsequent SAMs can be designed to have specific transport and QI effects, even at room temperature, enabling control of their charge transport related properties. Controlling their QI also has the potential for tuning other thermoelectric characteristics such as  $S$ .<sup>[56]</sup>

It has been concluded that one method for improving FOM is to reduce phonon transport, reducing the phonon component of thermal conductance. This can be done by adding side groups to molecules which cause a reduction in phonon transmission. Alternatively, QI can be manipulated to improve electron transport and therefore enhance electrical conductance. This is achieved by designing a molecule such that electrons in two separate paths are in phase with one another's wave functions.<sup>[57]</sup>

One review noted, however, that several challenges face this field of research, most notably how to experimentally determine FOM. The challenge of this is threefold: most experiments are executed under ambient conditions, leading to rapid heat dissipation; the actual temperature range is minimal, so measurement of it must be precise; and the junctions are physically tiny.<sup>[57]</sup>

Most recently, 2,5,8-triphenylbenzo[1,2-b:3,4-1 b':5,6-b'']trifuran (Ph<sub>3</sub>-BTF) was investigated for its potential to have a particularly high  $S$ . A large, undoped, single crystal was tested; it has been found to have a very largely negative  $S$ : up to -239 mV/K at 350 K. It is suspected this may be a result of its extremely tight packing density, with its  $\pi$ - $\pi$  stacking distance being 3.32 Å. However, as there is no carrier doping in this material,

the power factor remains low despite the giant  $S$  effect. There is great potential in this material to improve the electrical conductance and therefore increase the power factor and subsequent FOM, though further research is necessary to improve electrical conductance whilst maintaining the high  $S$ .<sup>[58]</sup>

#### **4.2. Thin Films**

Thin films have been of interest for many years due to their difference in performance from bulk materials, particularly at interfaces; however, thin films often suffer from more defects than their counterparts. Currently, transition metal oxide (TMO) films and metal-organic framework (MOF) films are being studied for use in solar cells, energy storage and other thermoelectric applications.<sup>[59-66]</sup>

TMOs have been of interest for a long time due to their uses as semiconductors, ionic conductors, plasmonics and ferroelectrics. Though these uses have been widely studied in the bulk material form, challenges arise when researching their thin films, but this is where the greatest opportunity lies for energy and electrical applications. Critically, there's great potential for large films made with minimal resources that are simultaneously more stable and have lower toxicity and more tuneable parameters. One example of a series of materials that have been investigated as thin film TMOs are tungstates; these demonstrate promise as photoanodes within electrochemistry for water splitting.<sup>[67]</sup> The main issue for specifically thin film TMOs is defects, as they degrade properties and are hard to rectify. Methods have been studied for mitigating these issues at practical growth temperatures. A summary of the findings can be found in Table 4.1.<sup>[60]</sup>

Table 4.1 Assessment of methods for mitigating TMO thin film problems, such as defects, to enable use in energy and electrical applications.

Method	Advantages	Disadvantages
<b>MBE adsorption-controlled growth</b>	Easy by Pulsed Laser Deposition (PLD). Thermodynamics provides automatic composition control.	Otherwise unreachable. In multi-material heterostructural growth, materials with different adsorption-controlled growth windows and substrate temperature complicate synthesis.
<b>Hybrid growth process</b>	Enables highly stoichiometric films.	Metalorganic source limited. High vapour pressure and room temperature liquid phase preferred.
<b>Interval growth in PLD</b>	Film homogeneity and crystallinity improved without growth rate compromise.	Potential for reduced point defect formation but not enhanced “beneficial” dislocation formation. May not allow a significant reduction in growth temperatures.
<b>Amorphous phase epitaxy</b>	Relatively straightforward.	Growth-induced stacking faults are likely. The method is largely new for defect mitigation.
<b>Liquid-assisted growth</b>	Uses vapour deposition methods. High quality attainable, cf. standard methods, enables growth temperature reduction. Swift growth (with 1 $\mu\text{m}/\text{min}$ ) standard (> 1 order of magnitude faster than alternatives). Monocrystalline quality.	Undesirable melt residues on the film surface after growth. Accessible eutectics are not universal in film compositions.
<b>Vertically aligned nanocomposites</b>	Vapour methods applicable. Far higher functionalities in many functional oxides.	Need materials which grow together whilst phase separated in the composite. One of the sole function’s phases could reach greater crystal quality.
<b>Laser-heated substrates with localised high-temperature heating</b>	Atomically smooth substrates with chemically controllable surfaces, specific to substrate heating for reduced contamination and greater refractory oxide growth at low vapour pressure with $T_{\text{sub}} < 2,000$ °C achievable.	Needs specialised hardware.

MOFs have great porosity and subsequently great adsorption capabilities. That paired with the potential for tuning chemical properties and alterable metal nodes and organic linkers leads to these being an area of research interest. As with all technologies, MOFs have their disadvantages, namely their stable form being as polycrystalline micro-powders with limited processability, though this can be alleviated by depositing them onto substrates. The prominent approaches presently used for the deposition of MOFs are demonstrated in Figure 4.3. It was concluded that such films are suited for use in microelectronics, catalysis and gas separation. In particular, cyclodextrin can be used in



thin film form for desalination.<sup>[68]</sup> It has been highlighted that whilst solution-based methods have widely agreed effectiveness, there is a motivation for developing a process using a more environmentally conscious approach that still enables careful control of their structure; liquid- and gas-based solutions are progressing towards this aim but further work is required at present.<sup>[61]</sup>

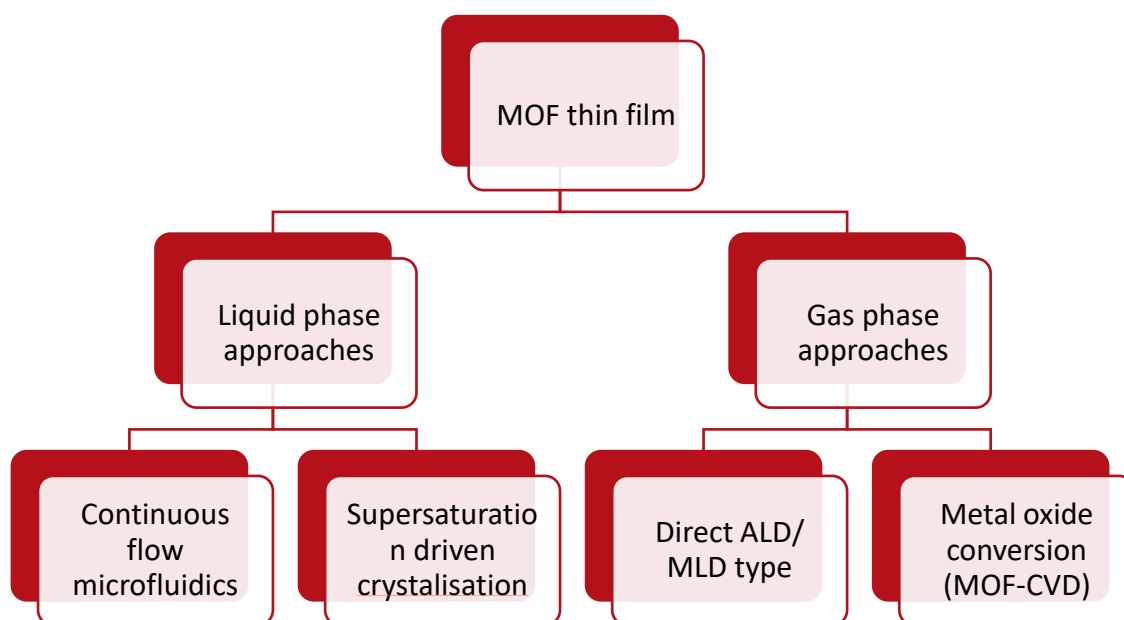
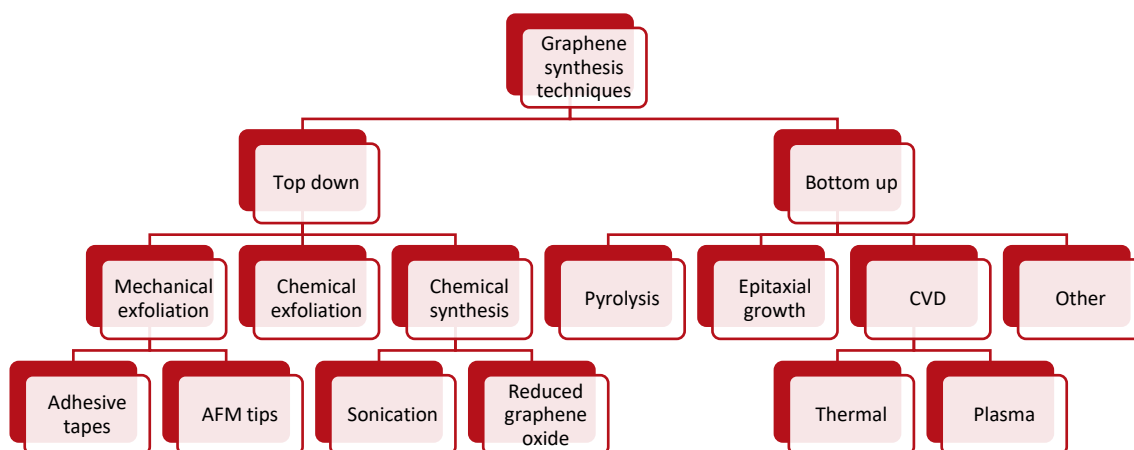


Figure 4.3 Diagram of different methods for forming MOF thin films for use in catalysis, gas separation and microelectronics.<sup>[61]</sup>

One of the most famous thin films in recent years is graphene.<sup>[64]</sup> Graphene is the thinnest known 2D material at around 0.34 nm thick. It consists of six covalently bonded carbon atoms, in a honeycomb structure, but in two dimensions. This material is useful for energy storage, optoelectronic, medical and electronic applications. This is due to its great charge mobility (120,000 cm<sup>2</sup>/Vs), high surface area, good thermal conductivity (5,000 W/mK), high Young's modulus (1 TPa), intrinsic mechanical properties, enhanced optical transmittance, and transparency that's tuneable by the number of layers. Graphene is inexpensive, lightweight, efficient, high-performance, and flexible. It has been used for supercapacitors, Li-ion battery electrodes, oxidation catalysts, and solar cell electrodes (as both the anode and cathode). It's a semi-metallic, zero bandgap semiconductor with conduction and valence bands that meet at Dirac points, where charge carriers can form straight dispersion cones. Graphene lends itself to solar cells as a result of its 97.7% transparency in the visible light region with <0.1% reflectance. Because of this, it has been used in organic, dye-sensitised and perovskite solar cells; and used as both the electron transport layer (ETL) and the hole transport layer (HTL).<sup>[69]</sup>

Graphene is also often utilised in conjunction with other materials as composites and multi-layered structures. This enables materials to be developed with an amalgamation of properties, or greater results of properties already displayed by graphene. For example, growing graphene on SiC and using Teflon as a smooth conforming coating creates a superhydrophobic material. Graphene and graphene oxide have also been found to exhibit properties desirable for application in fuel cells, energy storage devices, and at almost every layer within a dye-sensitised solar cell (DSSC).<sup>[70]</sup> Originally, graphene sheets were obtained via scotch tape peeling,<sup>[71]</sup> however, further techniques for obtaining it can be seen in Figure 4.4.<sup>[70]</sup> This figure is split into ‘top-down’ and ‘bottom-up’ approaches, in line with the descriptions given in Chapter 1.



*Figure 4.4 Methods for synthesising graphene sheets. These have been separated into ‘top-down’ and ‘bottom-up’ methods per the definitions given earlier in this thesis. The original method used for obtaining graphene was the ‘scotch tape’ method, here described as ‘adhesive tapes’.*

Graphene oxide is also of particular interest, and both graphene and graphene oxide can be functionalised for further property modification. A summary of some of these functionalisations can be seen in Table 4.2.<sup>[72]</sup> These functionalisations have been investigated due to the requirement for expanding the properties of graphene and graphene oxide, to then broaden the potential applications.<sup>[72]</sup>

Table 4.2 Summary of functional groups coupled with graphene and graphene oxide with their results and applications; this aims to broaden the use of these materials.

Modification Type	Modified Group	Modification Agent	Interaction Type	Property	Application
Covalent Functionalisation	-C=C-	4-Propargyloxydiazobenzenetetrafluoroborate	Diazotization	Water soluble	Biosensors
	-COOH	SOCl <sub>2</sub>	Esterification	Conductive	Conducted membrane
	-OH	2-Bromoisobutryl bromide, NaN <sub>3</sub> , HC≡C-PS	Esterification	Good solubility	Polymer composites
	-OH	N <sub>2</sub> H <sub>4</sub> , DNA	Addition esterification	Good solubility	Biosensors
Non-covalent Functionalisation	Carbon six-membered ring	Tetrapyrrene derivative	$\pi$ - $\pi$	Stable and dispersed, conductive	Sensors
	Carbon six-membered	Sulfonated styrene-ethylene/butylene-styrene copolymer	Co-polymerisation	Conductive	Nanocomposites
	-COOH	SDBS	Ion interaction	Stably dispersed, conductive	Packaging
	-COOH	Amine-terminated polymers	Ion interaction	Stable and dispersed, good solubility	-
	-OH	DXR	Hydrogen bond interaction	Stable and dispersed, good solubility	Drug carriers
	-OH	DNA	Hydrogen bond interaction	Stable and dispersed, good solubility	Biomedicine
	-COO-	Hydrazine	Electrostatic interaction	Stably dispersed	-
Element Doping	-C-	B, P, and N	-	Band structure change	Electronic devices

Graphdyne (GDY) is an umbrella term for graphyne, graphdiyne, and graphyne-n, all of which are similar to graphene in that they are carbon monolayers, however, they have hybridised sp- and sp<sup>2</sup>-bonded atoms. It contains some carbines (carbon triple bonds) between hexagons. The most interesting of this group is graphdiyne which displays the following properties:<sup>[69]</sup>

- Bandgap 0.44-1.47 eV;
- Electron mobility  $\sim 10^5$  cm<sup>2</sup>/Vs;
- Young's modulus 0.25 TPa;
- Single layer GDY has bandgap 0.46 eV at  $\Gamma$  point;
- Electron mobility is an order of magnitude higher than hole mobility, at  $10^5$  cm<sup>2</sup>/Vs at room temperature.

GDY nanoribbons were investigated; it was found that they resulted in lower thermal conductance than graphene. Moreover, using density functional theory (DFT), tight-binding and non-equilibrium green's functions, it looks to be that Ab stacking of bilayer  $\alpha$ -GDY nanoribbons is the most stable configuration, whilst changing the edge type of the layers alters properties such as band gap and  $S$ .<sup>[73]</sup>

Furthermore, carbon nanotubes (CNTs) present another interesting alternative due to their mechanical and electrical characteristics. They are made up of graphene sheets that have been rolled into tubes. CNTs can have single wall thickness (SWNT) with a diameter of c. 1.4 nm or multiwall (MWNT) with a diameter of 10-20 nm.<sup>[74]</sup> These structures are noteworthy due to the orientation of how the graphene sheet joins onto itself determining whether the tube formed behaves metallically or as a semiconductor. As a result of their favourable properties, SWNTs specifically may be used as nanowires and nanoscale electronics. For instance, applications for these materials may include chemical sensors, advanced composite materials and field-effect transistors. However, challenges face SWNTs regarding their manipulation into useful devices; methods such as inkjet printing have been proposed to overcome this.<sup>[75]</sup> Moreover, researchers have had to develop ways to prevent CNTs from aggregating into larger structures by dispersing them in solution. This enables introduction of CNTs into practical applications.<sup>[76]</sup>

Another material of interest is black phosphorous (BP), which displays intrinsic semiconductor characteristics but is difficult to create monolayers of due to complicated manufacturing and low availability. Its benefits include a tunable direct bandgap when in thin films (depending on layer stacking; the monolayer form has a direct bandgap of 2 eV however, this decreases as more layers are added) and the potential for application in highly efficient, relatively cheap, solar cells. It is predicted that a Power Conversion Efficiency (PCE) of 20% is attainable with this material, though this has yet to be proven experimentally.<sup>[69]</sup> The usefulness of layered BP has been commented on, with the methods of production and possible uses also assessed; some examples of which are given in Table 4.3.<sup>[77]</sup>

Table 4.3 Summary of conclusions from the review article on black phosphorus (SnSe) separated into desirable characteristics, suitable manufacturing techniques and possible uses.

Useful Characteristics	Manufacturing Techniques	Potential Applications
<ul style="list-style-type: none"> <li>• Very low thermal conductance;</li> <li>• Small electron mass;</li> <li>• Highly light absorbent and over a large range;</li> <li>• Very anisotropic;</li> <li>• Good mechanical properties;</li> <li>• Oxidation resistant;</li> <li>• Improvable by doping;</li> <li>• Eco-friendly;</li> <li>• Non-toxic;</li> <li>• Earth-abundant;</li> <li>• Chemically stable;</li> <li>• Possible to transition from indirect to direct band gap.</li> </ul>	<ul style="list-style-type: none"> <li>• Top-down methods:               <ul style="list-style-type: none"> <li>○ Ball milling;</li> <li>○ Micromechanical cleavage;</li> <li>○ Liquid exfoliation;</li> <li>○ Electrochemical exfoliation;</li> </ul> </li> <li>• Bottom-up methods:               <ul style="list-style-type: none"> <li>○ Chemical Vapour Deposition (CVD);</li> <li>○ Physical Vapour Deposition (PVD);</li> <li>○ Atomic Layer Deposition (ALD);</li> <li>○ Molecular Beam Epitaxy (MBE);</li> <li>○ Wet chemical syntheses;</li> <li>○ Print SnSe.</li> </ul> </li> </ul>	<ul style="list-style-type: none"> <li>• Ultrafast photonics;</li> <li>• Electronic components;</li> <li>• Photodetectors;</li> <li>• Solar cells;</li> <li>• Photocatalysts;</li> <li>• Solar-driven water evaporators;</li> <li>• Alkali-ion barriers (for batteries);</li> <li>• Supercapacitors;</li> <li>• Gas sensors;</li> <li>• Biomedical applications (like biosensors).</li> </ul>

### 4.3. Thermoelectricity

#### 4.3.1. Seebeck Coefficient

Thermoelectric generators (TEGs) have been investigated as a means of reducing electricity use and thus making energy consumers more sustainable. This is largely achieved by altering materials' FOM, which in turn relies on having a high  $S$ , high electrical conductivity and low thermal conductivity. It was previously understood that  $S$  was a bulk material property, however, research has found that when reducing bulk materials from three dimensions to two,  $S$  is no longer independent of size. Due to the mean free paths of electrons being extended in 2D materials, electron energies remain elevated due to not being thermalised by the bulk lattice.<sup>[78]</sup>

It has been demonstrated that  $S$  is chain-length dependent, and this dependency is dictated by energy offset ( $\Delta E$ ) as well. They concluded that the location of the accessible energy level was the deciding factor as to whether the  $S$ -to-chain-length relationship is influenced by  $\Delta E$ . Aryl molecules' accessible energy is confined to the backbone and thus this is what dictates the response of the backbone's electronic structure when the molecular length is varied and in turn, dominates the dependence of  $S$  on molecular length. With alkyl molecules, however, it is the anchor which holds the accessible energy and resultantly the impact of length on  $S$  depends on transmission peak intensity as opposed to  $\Delta E$ .<sup>[79]</sup>

Further to this, in simple organic molecules,  $\Delta E$  also overcomes any molecular orbital changes. In essence, if molecular orbital broadening,  $\Gamma$ , is altered, the result is only seen if  $\Delta E$  is small, for example in molecules with small HOMO-LUMO gaps. The effect of  $\Gamma$

is also inhibited by van der Waals contacts due to molecules with these only having marginal  $\Gamma$ .<sup>[79]</sup>

It has been found that there is a relationship between the  $S$  and charge carrier mobility ( $S \propto \mu^{0.2}$ ) when looking at conducting polymers, such as poly(3,4-ethylenedioxythiophene) (PEDOT). It was concluded that this relationship is a consequence of two contributors to  $S$ ; namely,  $\pi$ -orbital widening near the band edge impacts the material's electronic structure and its charge transport behaviour. Transitioning from quasi 1D to 2D hopping was seen when the crystallinity of the films rose, more so in the pyridine-treated samples with longer PEDOT chains. This allowed for greater charge transport and ensuing improvement in thermoelectric properties.<sup>[80]</sup>

Semiconductors are often selected for thermoelectrically based research due to their intrinsically low charge carrier concentration and subsequent high  $S$ , though this is paired with low electrical conductivity; metals exhibit the opposite properties. In the past, it has only been possible to deposit semiconductor thin films via Radio Frequency (RF) sputtering, inhibiting scale-up of manufacturing and, therefore, reducing industrial application. They are further impaired by being typically more expensive and having more complicated charge carrier transport mechanisms than alternative materials. To overcome these difficulties, researchers looked at Direct Current (DC) sputtering of metallic thin films and principally, the influence of process conditions including background pressure and discharge current. It was found that it was domain size rather than film thickness which influenced  $S$ , and as such, it was the impact of process conditions on domain size which gave rise to changes in thermoelectric properties. It was found that the domain size decreased with decreased discharge current and increased background pressure, and it was desirable to have a smaller domain size to increase the deviation of the  $S$  of the films from that of the bulk material.<sup>[81]</sup>

In a previous study it was found to be possible to achieve  $S$ s of  $-310 \mu\text{V/K}$  at  $90^\circ\text{C}$ , and  $-191.6 \mu\text{V/K}$  at room temperature when using a one-step thermal evaporation procedure to form thin films of bismuth antimony telluride (BST). This was a development on prior works which found that orientating the crystals along (001) planes led to enhanced thermoelectric properties. It was concluded that the high  $S$  values obtained resulted from the combination of the heat treatment used, the nanocrystallinity of films, and the introduction of Te and In dopants.<sup>[82]</sup>

$\text{TiO}_2$  has been investigated for use in thermoelectric devices, due to its relatively low cost, chemical stability, and non-toxic nature. A further benefit of this material is its high transparency lending it to a non-disruptive application on glass, such as windows. That

being said, TiO<sub>2</sub> displays a comparatively low FOM when compared with other thermoelectric materials. To overcome this disadvantage, they attempted to use nanostructuring. Whilst successful in creating films with a nanorod structure through hydrothermal methods, it was concluded that the  $S$  derived from the films was similar to that of the bulk material and worse than reported values for similar films; the highest  $S$  reported in this work was  $\sim -200 \mu\text{V/K}$ .<sup>[83]</sup>  $S$  of  $\sim -380 \mu\text{V/K}$  has previously been reported for TiO<sub>2</sub> films formed via solid-state reaction with TiN. The research also investigated the impact of adding different amounts of N dopant and identified that other than TiO<sub>2</sub> without doping, higher dopant concentration led to greater  $S$ .<sup>[84]</sup> Moreover, further research doped TiO<sub>2</sub> with boron via pulsed current sintering and discovered that  $S$  was greatest in magnitude when doped with 1 mol% B<sub>2</sub>O<sub>3</sub>, to an absolute value of  $\sim -550 \mu\text{V/K}$ . However, they concluded the best FOM resulted from doping with 0.5 mol% TiB<sub>2</sub> due to the influence of decreased electrical resistivity and thermal conductivity.<sup>[85]</sup>

Single molecules for use as thermoelectric junctions are an emerging idea, based on them having conductive pi-electronic systems that are manufacturable on a large scale with chemically tunable properties. In some cases, these have been predicted to have  $S$  values as high as  $-56 \mu\text{V/K}$  in the case of a fullerene pair or a range of  $-280 \mu\text{V/K}$  to  $230 \mu\text{V/K}$  for metalloporphyrins. As such, organic molecules are of great interest as thermoelectric devices. An  $S$  of  $-7 \mu\text{V/K}$  to  $-11.4 \mu\text{V/K}$  (with the negative sign indicating LUMO dominance in the charge transport) has been obtained by employing STM BJJs with OPE3 derivatives (phenylene, 2,5-dimethoxyphenylene & 9,10-anthracenyl). However, such molecules are inhibited by their low energy conversion efficiency and instability. It has been concluded that for a molecule to have suitable FOM, an ability to host side groups and modification of anchor groups is required. This structure would also preferably prevent phonon transport without preventing electron transport, meaning a strong molecular backbone is favoured.<sup>[86]</sup>

In one case, OPE3 was chosen as the backbone due to its synthetic versatility, highly-conjugated structure and the fact it has been widely studied previously; conductivity values for the backbone are already widely understood, therefore, any variance from this can be attributed to the anchor/ side groups. Density Functional Theory (DFT) was used to compute the binding energies of OPE3 derivatives on Au, whilst electronic transport properties were determined through the use of non-equilibrium Green's function theory based on the Density Functional based Tight-Binding method (DFTB). It was found experimentally that both OPE3 and its derivatives displayed negative  $S$ , meaning conductance is LUMO-dominated. It was also found that  $S$  dropped on the introduction of the side groups OPE3-Ph(OMe)<sub>2</sub> and OPE3-An compared to OPE3-Ph, without much

impact on the electrical performance. It was also noted that a greater temperature difference could be applied to OPE3-An, implying higher thermal stability.<sup>[86]</sup>

Similarly, Destructive Quantum Interference (DQI) effects have been investigated through different placements of functional groups on an anthracene backbone, on molecules used to form SAMs. Cross-plane transport was also examined regarding the effect on the thermoelectric properties of the SAMs. It has previously been proven that chemical modification of molecules can be used to alter the molecules' electrical conductivity by varying their connection to the electrode. It was concluded that the  $S$  of the SAMs using thioether/thiolates anchor groups on the anthracene backbone did vary with the location of the functional group; it was connectivity dependent, with up to a 50% difference in values depending on the location of the thioether groups. Likewise, the electrical conductance of the same molecules varied by a factor of  $\sim 16$  depending on functional group location.<sup>[87]</sup>

Typical TEGs are not eco-friendly in parts and as such, alternative materials are being investigated. In previous research, P-type  $\text{Cu}_{2+x}\text{Zn}_{1-x}\text{SnS}_4$  and  $\text{Cu}_{2+x}\text{Zn}_{1-x}\text{SnSe}_4$  were used alongside n-type  $\text{Al}_y\text{Zn}_{1-y}\text{O}$  as they are relatively cheap, plentiful and sustainable. It was concluded that the used devices are of comparable power density per cost to typical TEGs, whilst being much more environmentally friendly.  $S$  in the range  $-39 \mu\text{V/K}$  at  $50^\circ\text{C}$  to  $-54 \mu\text{V/K}$  at  $300^\circ\text{C}$  was obtained. Power density an order of magnitude higher than similarly sustainable materials investigated elsewhere was also achieved.<sup>[88]</sup>

#### 4.3.2. Figure of Merit (FOM)

Mesoporous structures typically exhibit low thermal conductivity, resulting from the pores acting as effective phonon scatterers. Combining this property with a high  $S$  and high electrical conductivity leads to an enhanced FOM. The use of ZnO as the mesoporous structure, doped with Ti was investigated. It was found that whilst increasing the Ti dopant concentration to 1.5 at% caused little change in the crystallinity and pore structure, it did impact the thickness and porosity of the films, making them increase. This in turn meant that carrier concentration was enhanced, enabling greater electrical conductivity. Whilst the  $S$  for this film did suffer as a result of the doping, the increase in electrical conductivity resulted in an overall increase of a magnitude of almost 1.5 in mesoporous ZnO power factor ( $S^2G$ ; the numerator in the FOM equation).<sup>[89]</sup>

It has been attempted to create Si-Ge-based materials via two methods to compare the impact of the fabrication technique on the resultant FOM. The methods employed were nanostructuring and modification of the electronic structure. It was concluded that by



altering the electronic configuration, they were able to obtain an FOM of  $>1.88$  for Si-Ge<sub>873K</sub> at 873 K.<sup>[90]</sup>

Altering grain size within a material is one way in which to influence the overall FOM of a material, due to grain boundaries inhibiting electron transport. Sintering of samples to increase grain size has been attempted, to try and improve the temperature range over which an FOM of  $\sim 1.5$  for Mg<sub>3</sub>(Sb, Bi)<sub>2</sub> could be reached; previously this has only been possible at  $\sim 700$  K. The results were enhanced average FOM with grain size increased by a factor of 7.<sup>[91]</sup>

#### **4.4. Deposition Techniques**

##### **4.4.1. Self-Assembled Monolayers (SAMs)**

Self-assembled monolayers (SAMs) form when molecules spontaneously adsorb onto a substrate material from air or solution, into highly ordered monolayers. They are held in place due to chemisorption, where a chemical bond is formed between molecule and substrate. It's required that the substrate has few imperfections, to produce the best possible monolayer.

The molecules in question are comprised of a functional 'tail' group, molecular spacer and 'head' group; per Figure 4.5. It is the spacer group (typically an alkyl chain) which causes the molecules to form ordered monolayers, due to van der Waals forces between them.<sup>[92]</sup>

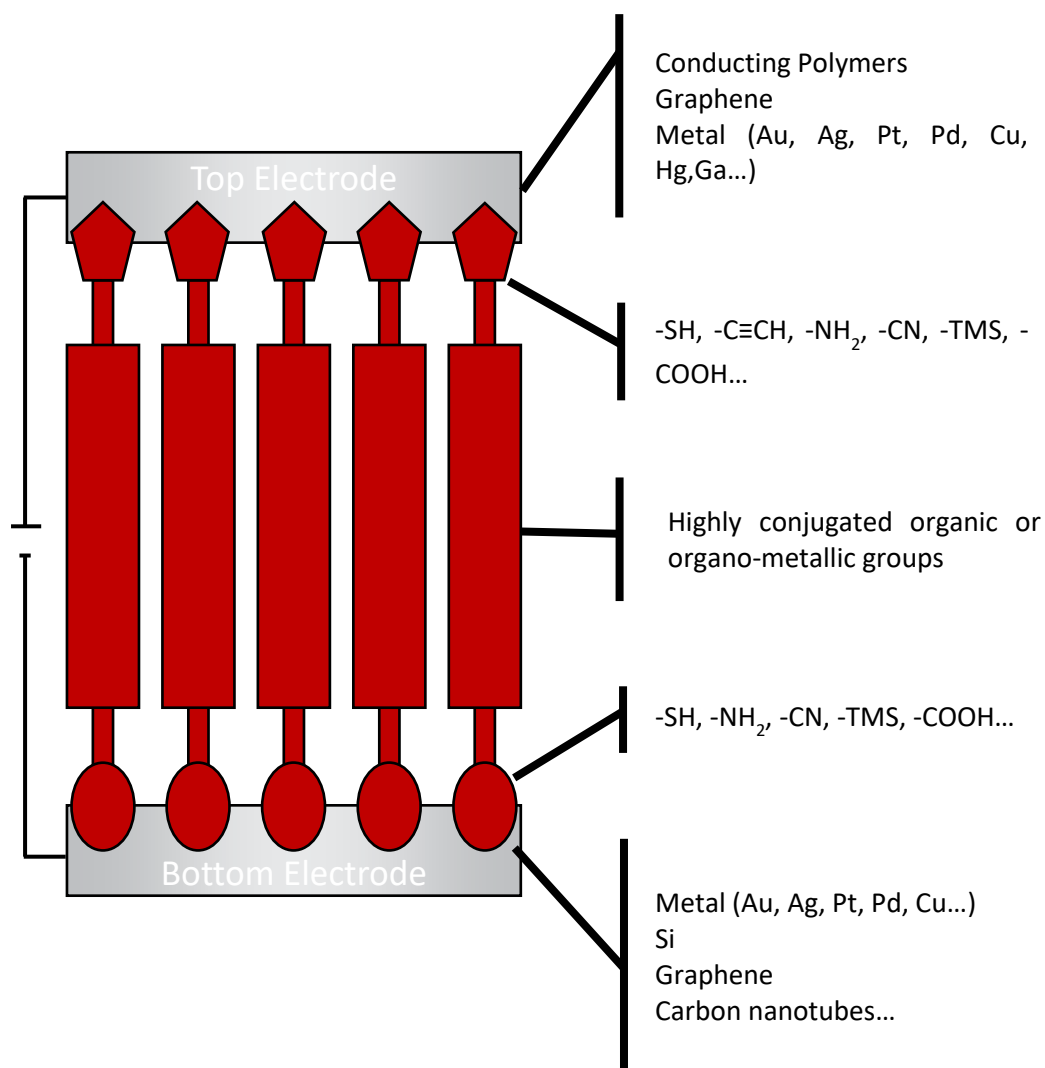


Figure 4.5 A SAM sandwiched between two electrodes. The head group, molecular backbone and tail groups are all shown, with common examples of functional groups also given.<sup>[93]</sup>

It has been concluded that SAM formation occurs in two stages: adsorption and organisation. Adsorption is initiated by molecules transitioning from the bulk to the interface between solid and liquid phases. This is achieved via convective and diffusive transport. As adsorption takes place, the molecules must subsequently organise themselves to form a crystalline 2D structure on the substrate. This stage seems to be broken down further into three stages, much like those witnessed when compressing a monolayer in LB deposition; quasi-gas, -liquid and -solid stages are observed. If the temperature of the deposition is below the triple point, the quasi-liquid phase of deposition may be bypassed. It is generally assumed that adsorption for self-assembly follows the Arrhenius relation for temperature dependence;<sup>[94]</sup> the equation is given in Equation 4.1 below. Here,  $k$  is the rate constant,  $T$  is absolute temperature,  $A$  is the pre-exponential factor,  $E_a$  is activation energy and  $R$  is the universal gas constant.<sup>[95]</sup>

$$k = Ae^{\frac{-E_a}{RT}}$$

Equation 4.1

In recent years, other functional groups have become the focus, as thiols face a multitude of issues. For example, oxidation of the thiol to disulphides and unintended electrical conductance effects. A suggested replacement has been amine, due to the nitrogen lone pair. Though the bonding between nitrogen and gold isn't as strong as that with sulphur, there is still expected to be strong electronic coupling.<sup>[93]</sup>

The thickness of SAMs is dictated by the length of the molecular spacer group between the 'head' and 'tail' groups. It has also been found that increasing the chain length of the molecular backbone can increase the adsorption rate.<sup>[94]</sup>

Since SAMs are formed using readily available and straightforward equipment, and with little outside interference, the fabrication costs are minimal. Furthermore, minimal material is required to form monolayers over large surface areas (like in LB), hence the method is appealing for industrial applications.<sup>[93]</sup>

The earliest systematic research into SAMs was in 1946 by William Zisman; he and his colleagues generated samples by submerging a metal or metal oxide substrate into an adsorbate solution containing, for example, alkylamines or carboxylic acids. The resulting films were found to be autophobic, with similar interfacial properties to Langmuir-Blodgett (LB) films (explained further in Chapter 4.4.2). What differentiated the new films from those produced by LB was that the driving force behind the deposition was ligating chemical interactions between the polar groups and substrates, meaning there is a chemical bond between the molecule and substrate as opposed to just a physical bond as observed in LB deposits.<sup>[96]</sup>

These studies also discovered that the interfacial characteristics of the films were changeable by altering the functional groups. Problems arose from these films, however, making them largely impractical. Namely, difficulties in obtaining clean enough substrate material and the relatively low stabilities of the films due to their low adsorption (in the region of 5-15 kcal/mol).<sup>[96, 97]</sup>

Following this research, it was reported in 1983 by Nuzzo and Allara that dialkylsulphide adsorbates formed on gold.<sup>[98]</sup> This initiated further research into sulphur-metal-based SAM interactions, which later discovered other organosulphur compounds like thiols and alkyl sulphides formed SAMs on the surfaces of gold, silver and copper, among other metals.<sup>[97, 99]</sup> Subsequently, the focus in recent years has been on alkane-thiol-gold systems due to four reasons outlined here:<sup>[97, 100, 101]</sup>

1. Gold is relatively inert and, therefore, forms no oxide under ambient conditions. However, silver and copper form an oxide layer that often prevents the adsorption of the organosulphur film;
2. In “hard-soft” acid-base theory, both sulphur and gold are considered ‘soft’, meaning the interaction between the two is specific and highly favoured. This relationship prevents other ‘hard’ groups such as alcohols interfering, meaning that molecules deposited in this way can be designed with ‘hard’ groups, without fear of them attaching in place of the sulphur;
3. Van der Waals forces between the alkyl chains within the alkanethiol adsorbate backbones stabilise the monolayer, due to the close packing enabled by trans-extended chains being thermodynamically favoured in densely packed monolayers;
4. The chemical simplicity of the alkanethiols enables easy organic synthesis variation.

The reaction by which alkanethiols form SAMs on gold is demonstrated in Equation 4.2.<sup>[101]</sup>



Crystal orbital overlap population, crystal orbital Hamiltonian population and fragment molecular orbital techniques have been used to gain an understanding of the nature of S-Au in such systems. They concluded that whilst it might be assumed that the connection is  $\sigma$ -bond dominant, it depends on the binding position within the gold crystal lattice. If the S contacts directly to the Au atom,  $\sigma$ -bonding is dominant. Contrastingly, if the S bonds at a hexagonal close packed or face centred cubic site, or somewhere in between (termed a bridge site),  $\pi$ -bonding is present.<sup>[102]</sup>

SAMs are particularly useful when it’s required to modify the properties of metal electrodes, due to the ease of changing the functional tail group. As a result of the self-assembly, the films created can self-heal.<sup>[101]</sup> Furthermore, the dense and stable structure of SAMs lends them well to being used as corrosion protection and wear prevention, as well as chemical and biochemical sensors. Piezoelectric surfaces have also been modified with SAMs by altering the tail group and thus changing the proton donor/ acceptor properties.<sup>[103]</sup>

It’s possible to tune the electrical properties of 2D materials by contacting them with SAMs. This is referred to as “contact doping” or “charge transfer doping” and relies on the SAM having a different fermi level to the 2D material it is doping. It is possible to do

this either by depositing the 2D material onto the SAM, or vice versa. In the case of 2D materials on SAMs, the 2D materials are physically in contact with the SAM. In this case, the dipole moment of the SAM is dictated by the functional group on it, thus impacting the 2D material's Fermi level shift. This combination of SAM and 2D material influences the charge impurity-blocking efficiency, carrier density, work function, and/or field-effect mobility of the 2D material. For SAMs on 2D materials, physisorption or chemical reaction is what causes the bond between the two. This again results in a change in the Fermi level due to the dipole moment. The doping of the 2D material is further influenced by unreacted SAM linker groups.<sup>[104]</sup>

Guatam and Barile have worked on coupling ferrocene to carbon electrodes, which has led to an understanding of the role of SAM defect sites on electron transfer to the ferrocene molecules. They discovered that when ZnO is used to block the defect sites, SAM linker lengths have a direct influence on electron transfer. The conclusion drawn from this was that electron transfer is defect-driven on ferrocene-modified SAMs when using carbon electrodes, compared to the alkyl linker tunnelling mechanism typical of SAMs on gold electrodes.<sup>[105]</sup>

More recently, SAMs have been used in the production of metal halide perovskites (MHPs), which demonstrate potentially useful optoelectronic properties. Self-assembly was the chosen technique due to its ease of control of how the nanocrystals (NCs) align, alongside their shaping and dimensionality. These MHP NCs lend themselves to SAMs as they have low formation energy, easy ion transport and rapid anion exchange. By using self-assembly, the NCs formed close-packed structures with long-range order, thus enabling manipulation of the material's charge transport and electrical conductivity.<sup>[106]</sup>

SAMs have also been employed within the nanocomposite of PDINH/TiO<sub>2</sub>/Bi<sub>2</sub>WO<sub>6</sub>. Initially, monolayers of PDINH were formed into organic supramolecular carriers via self-assembly. The TiO<sub>2</sub> layer was subsequently bonded to this with quasi-hydrogen bonds through utilisation of sulphuric acid treatment. In a separate step, Bi<sub>2</sub>WO<sub>6</sub> was also self-assembled, however, this process included hydrothermal synthesis. The overall monolayer consisted of predominantly PDINH but with side chains of TiO<sub>2</sub> and Bi<sub>2</sub>WO<sub>6</sub>. The final structure exhibited good performance as a solar photocatalyst for organic pollutant photodegradation, without need for a cocatalyst.<sup>[107]</sup>

#### 4.4.2. Langmuir-Blodgett (LB)

In 1773 Benjamin Franklin discovered that dropping a teaspoon of oil into a pond caused waves in the water to smooth over a large distance.<sup>[108]</sup> Lord Rayleigh later found that the oil molecules were spreading into a single monolayer. Following this, Agnes Pockels developed a method for determining the surface tension of the water, by using a button, some string and a pivot balance. This then led to the understanding that the molecules described by Lord Rayleigh forming the monolayer were interacting with the water they sat atop and subsequently altering the surface tension. She later found that the area of these films could be controlled by barriers, causing the films to expand and compress.<sup>[109]</sup>

Irving Langmuir extended the research to note that the molecules seemed to spread on the water surface due to a hydrophilic and hydrophobic part of the oil molecules. He found that given a small enough surface area of water, the molecules aligned such that the hydrophobic tails stood straight up out of the water, whilst the molecules remained closely packed atop the water. He discovered that the area occupied by each molecule was then dictated by the 'head' of the molecule, whilst the thickness of the film formed was due to the length of the carbon chain 'tail'. Langmuir also concluded that passing a substrate through the film suspended on water would result in that film being deposited on the substrate, but dependent on which way the substrate was passed through the film.<sup>[110, 111]</sup> This work won Langmuir the Nobel Prize for Chemistry in 1932.

This was expanded upon by Katherine Blodgett, to create multilayer films of nanometre thickness; by dropping and raising a substrate through the monolayer to build up layers. The alternating up and downwards depositions were labelled Y films; if the layers were built up only by dropping the substrate through the film, they were termed non-alternating X-films.<sup>[112]</sup>

Films created via LB deposition are built from surfactants, which are surface active materials that form monolayers at the interface between two phases (typically gas and liquid, but can be between two liquid phases). Surfactants have hydrophilic and -phobic parts, meaning that they align as described by Langmuir: with the hydrophilic head atop the liquid phase and the hydrophobic tail in the air. It is Coulomb forces that hold the hydrophilic part in place whilst van der Waals forces connect the hydrophobic tails. This is what causes the molecules to remain at the interface, as they have two types of bonding within one structure. However, if the molecule is not correctly balanced, it will not interact as desired with the subphase: a too-short tail will cause the molecule to dissolve, whilst a too-small head may cause a thicker multilayer to form if a layer forms at all.<sup>[113]</sup>

Monolayers form as a result of molecules wanting to reduce their free energy. The layer sits atop the bulk phase, or sub-phase (which is usually water), where molecules are surrounded by fewer molecules than when in the bulk phase and hence have lower free energy. Equilibrium of the system, and molecular activation energies, are reached at the surface when as many molecules diffuse from surface to bulk as vice versa; see Figure 4.6.<sup>[114]</sup>

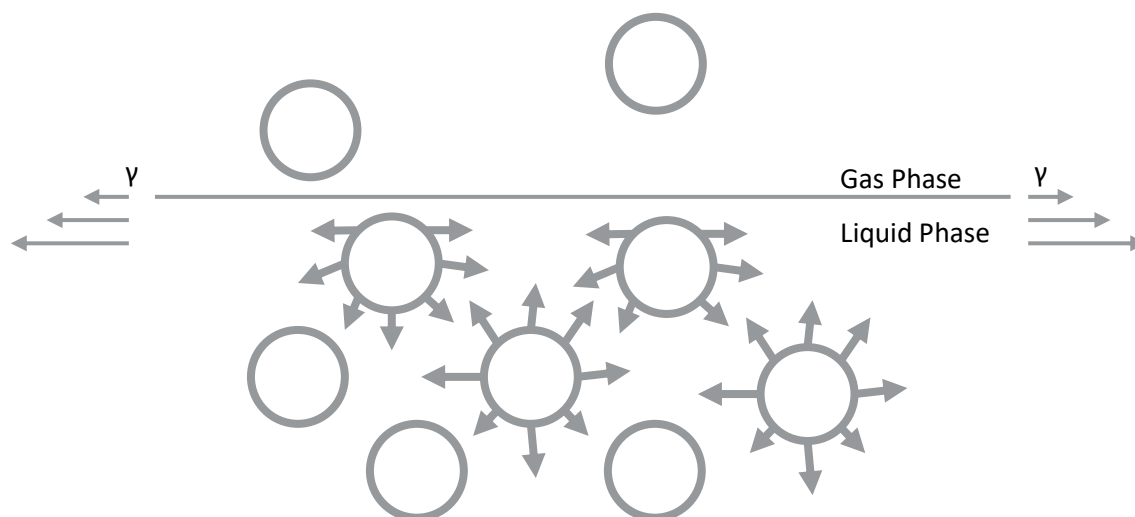


Figure 4.6 Forces acting on molecules in the bulk phase and at the gas-liquid interface in a Langmuir-Blodgett experiment.

Surface tension,  $\gamma$ , is acting on the surface molecules here. This can be related to free energy ( $G$ ) and surface area ( $A$ ) as defined in Equation 4.3. In particular, when the liquid considered is pure and in thermodynamic equilibrium, surface pressure can be expressed as Helmholtz free energy per unit area (Equation 4.4);  $F^S$  is surface excess free energy.

$$\gamma = \left( \frac{\partial G}{\partial A} \right)_{T,P} \quad \text{Equation 4.3}$$

$$\gamma_0 = \frac{F^S}{A} \quad \text{Equation 4.4}$$

For LB experiments, surface pressure is measured to monitor the formation of the monolayer. How surface pressure varies relates to the difference between the surface tension of the pure liquid ( $\gamma_0$ ) and that of the film ( $\gamma_f$ ) (see Equation 4.5).

$$\Pi = \gamma_0 - \gamma_f \quad \text{Equation 4.5}$$

Here, the parameter  $\Pi$  has the dimension  $\text{mNm}^{-1}$  and is used to see how the monolayer is forming.<sup>[114]</sup>

When compressing monolayers atop a subphase, as carried out by Pockels, monolayers transition through 2D phases similar to those experienced by bulk materials; namely quasi-gas, -liquid and -solid phases. This evolution can be monitored through the use of the surface pressure as described above. Compressing monolayers causes higher intermolecular forces to act, which paired with a smaller surface area causes the surface tension to change. Plotting this surface pressure change ( $\Pi$ ) against an occupied area produces an isotherm. An example of this can be seen in Figure 4.7.<sup>[114]</sup>

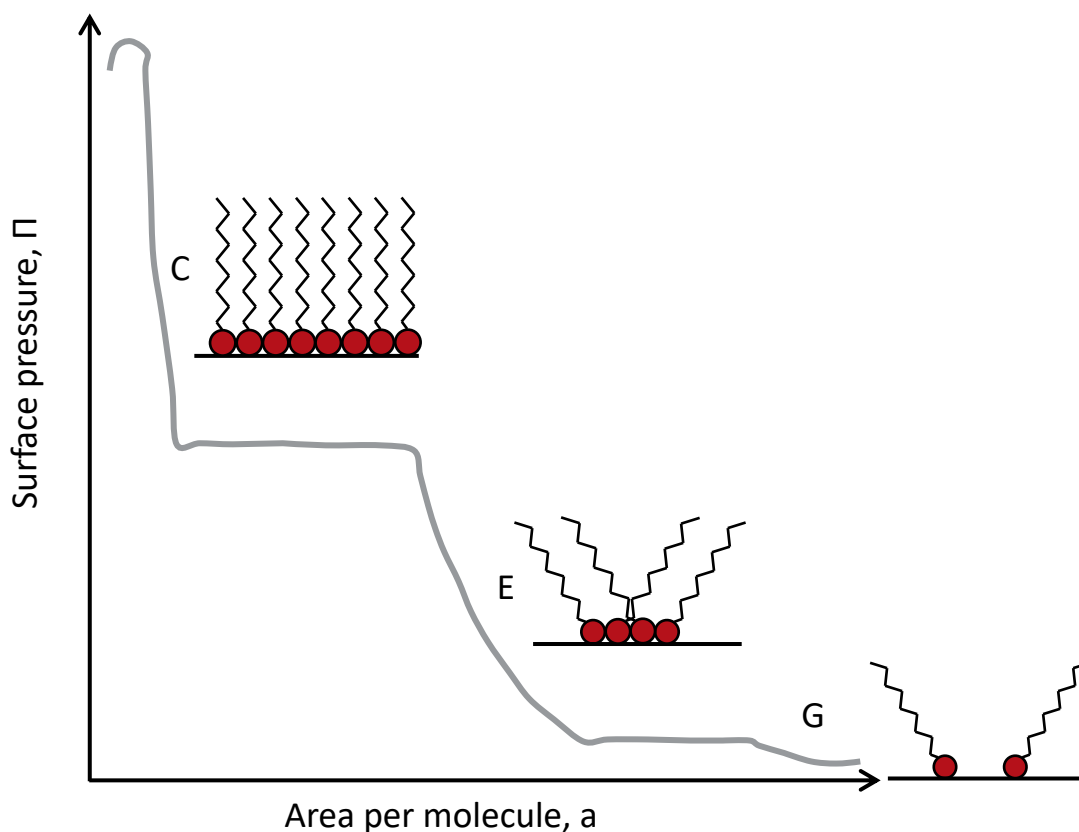


Figure 4.7 Example isotherm for a long chain organic molecule, showing surface pressure vs. area per molecule. The arrangement of molecules on the surface is also shown. C represents the condensed, or solid, phase; E is the expanded monolayer (liquid) phase, and G is the gaseous state. The monolayer undergoes these changes due to compression on the subphase surface.

From this information, the area per molecule can be obtained by applying the following equation:

$$a = \frac{AM}{cN_A V} = \frac{A}{cN_A V} \quad \text{Equation 4.6}$$

In which  $A$  is film area,  $M$  is molecular weight,  $C$  is spreading solution concentration (mass/ unit volume),  $c$  is solution-specific molar concentration,  $V$  is volume and  $N_A$  is Avogadro's constant.



When in the 'gas' phase, molecules barely interact and exert negligible force on one another. When in the 'liquid' (expanded) phase, the molecules are randomly arranged but have weak interactions. Beyond this point, 'solid' (compressed) phases form, with molecules closely packing to form an ordered monolayer. Here, the area per molecule should roughly align with the size of the hydrophilic 'head'.<sup>[114]</sup> Compressing a monolayer beyond the 'solid' phase causes it to collapse.

As discovered by Blodgett, passing a substrate through the monolayer causes it to deposit; held in place via physisorption (due to molecular interactions such as van der Waals forces). This is best carried out in the 'solid' phase so it is helpful to complete a full isotherm to find at what surface pressure this phase is reached, and subsequently, carry out the deposition accordingly. To measure the surface pressure in real-time, a Wilhelmy plate, made from either clean-leaf platinum or filter paper, is used. This measures the surface tension of the subphase at equilibrium before adding the monolayer and monitors the change as the molecule is added and the surface area is reduced. It works by measuring the capillary force on the plate from the subphase.

Depositions can fall into X, Y, or Z as aforementioned; these are depicted in Figure 4.8. X depositions are made by dropping the substrate down through the monolayer, whilst Z depositions form by bringing the substrate up through the monolayer.

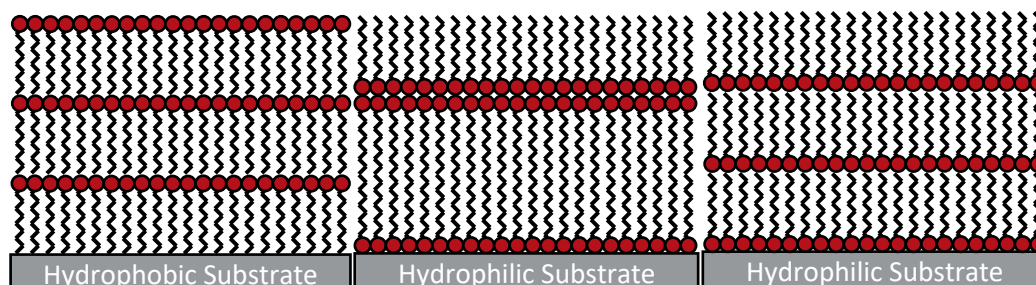


Figure 4.8 X, Y and Z depositions respectively. X and Z depositions require layers to be deposited the same way each time, whereas Y depositions alternate layers.<sup>[114]</sup>

If the monolayer does not closely pack or is too rigid, Langmuir-Schaefer (LS) deposition can be used instead, where the substrate material is 'stamped' onto the monolayer (Figure 4.9).<sup>[114]</sup>

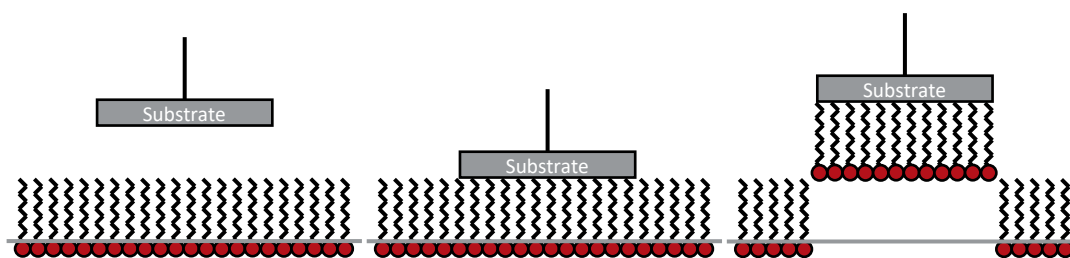


Figure 4.9 Horizontal Langmuir-Schaefer monolayer deposition. Rather than passing the substrate material through the monolayer, it is 'stamped' onto.

It has been found previously that using SAMs on gold electrodes can cause defects within the films formed, as the molecule etches into the gold. In the case of depositing 1,4-bis(1H-pyrazol-4-ylethynyl) benzene, this results in gold-pyrazolate complexes forming and, therefore, prevents well-ordered monolayers from forming. Resultantly, LB has been used in place of self-assembly to ensure the monolayers that formed were of the highest possible quality. It was found in this study that the subphase pH influenced the degree of deprotonation of the film deposited atop it, which in turn influenced the electrical properties of the monolayer. Pure water and NaOH were used as the subphases to influence pH, which yielded conductances of  $1.19 \times 10^{-4} G_0$  at pH=11 and  $0.27 \times 10^{-4} G_0$  at pH=5.6 when using a gold STM tip. These are notably higher than conductances observed with other similar molecules, see Table 4.4.<sup>[115]</sup>

Table 4.4 Conductance values obtained for molecular wires deposited via LB deposition; determined via contact mode in AFM.

Molecular Structure	Conductance ( $G_0$ )	Monolayer Thickness (nm)
	$0.26 \times 10^{-5}$ (pH = 5.6)	$1.81 \pm 0.05$
	$1.75 \times 10^{-5}$ (pH = 11.4)	$1.95 \pm 0.05$
	$1.20 \times 10^{-5}$	$1.49 \pm 0.04$
	$1.37 \times 10^{-5}$	$1.77 \pm 0.05$
	$3.90 \times 10^{-5}$	$2.02 \pm 0.05$
	$5.17 \times 10^{-5}$	$1.70 \pm 0.05$
	$6.20 \times 10^{-5}$	$1.6 \pm 0.1$
	$2.7 \times 10^{-5}$ (pH = 5.6)	$1.4 \pm 0.1$
	$11.9 \times 10^{-5}$ (pH = 11.0)	$1.6 \pm 0.1$

Further recent research has used LB to form films for use in molecular junctions (MJs) to overcome problems relating to poor contact between single molecules; including chemical degradation at device operating temperature, polymerization problems, high resistance to contact, and multiple conductance values being achieved by single

molecules due to binding geometry variability. LB films of a 1,4-bis(pyridylethynyl) benzene derivative (Figure 4.10) have been used,<sup>[116]</sup> in which the electrical contact is made via the pyriyl moiety and amplified by methyl(thiomethyl) anchor groups. The molecule used was designed such that the pyridyl groups were able to form N-Au  $\sigma$ -contacts whilst forming  $\pi$ -contacts between it and features on the surface of the electrode. The anchor groups also formed strong physical contact with the electrode through S-Au bonds, however, the electronically decoupled nature of the anchor groups (due to the methyl linkers) prevented extra electron transfer pathways from forming and, therefore, inhibited resultant QI. It was concluded that the molecule worked as intended.<sup>[116]</sup>

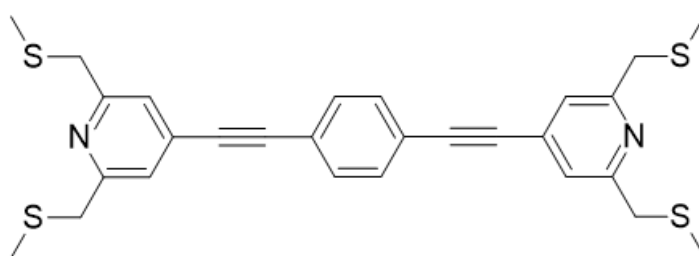


Figure 4.10 1,4-bis(pyridylethynyl) benzene, used to investigate LB films for use in molecular junctions.

LB typically results in well-ordered monolayers but only uses weak physisorption onto the substrate, whereas electrografting forms stronger bonds to the substrate, however, with disordered films. Therefore, hybridised LB deposition with electrografting by simultaneously oxidatively electrografting octadecylamine (ODA) and alcohol onto gold whilst using LB deposition on an aqueous subphase has been attempted. These monolayers were formed by part submerging a gold electrode in an LB trough, alongside a saturated calomel electrode (SCE) and carbon paper counter electrode. These in turn were electrically connected, creating an electrochemical cell within the trough. The ODA monolayer was then deposited onto a pH 9 subphase within the trough, a chronoamperometry of  $E=+0.85$  V/SCE was applied, and the gold was raised from the trough until it was fully outside the subphase. A control was carried out in which the two stages were carried out separately (LB deposition carried out, and subsequent emersion of the gold with monolayer deposition into the electrochemical cell followed by electrolysis). Characterisation via AFM, X-ray photoelectron spectroscopy (XPS), infrared (IR) spectroscopy, measurement of water contact angles, grazing incidence diffraction (GIXD) and electrochemistry found that the hybrid deposition created locally organised monolayers covalently bonded to the gold substrate, with nanometric pinholes. It was concluded that these pinholes are likely a result of the covalent bonds to the substrate preventing the rearranging of molecules on the surface after the

deposition has taken place. It was suggested that these monolayers would be suitable for sensors and biosensors.<sup>[117]</sup>

LB deposition has been used to form thin films of  $\text{Na}_3\text{V}_2(\text{PO}_4)_3(\text{NVP})\text{-MnO}_2$  nanocomposites for implementation in hybrid energy storage applications. In one study, different ratios of NVP:  $\text{MnO}_2$  were investigated for their effectiveness as part of an aqueous half-cell. NVP was selected in this case due to its potential for high specific energy density, thermal stability, and discharge capacity, however, low electrical conductivity and lagging sodium transport through the core were required to be mitigated. Ball milling has been used to gain nanosized particles to increase NVP defects for this purpose. The combination with  $\text{MnO}_2$  was due to its improved  $\text{Na}^+$  storage and pseudo-capacitor behaviour, which enables hybrid energy storage and, therefore, the nanocomposite structure can be used for batteries and supercapacitors. Ten layers of the nanocomposite were built up by drawing the substrate up through the LB film, to reach the desired electrode thickness. It was confirmed that varying the ratio of NVP:  $\text{MnO}_3$  indeed varied the hybrid energy storage properties of the electrode, with the 3:1 ratio giving an electrode with a high specific capacity, good cyclic stability and good rate capability. The proof of concept was subsequently demonstrated by employing an aqueous half-cell with the chosen electrode, which demonstrated the capability to integrate it into a solid-state thin film battery in the future. It was also noted that the use of an ITO/PET substrate enables flexible applications.<sup>[118]</sup>

Conjugated polymers (CPs) have received particular interest due to their suitability for use in solar cells, LEDs and flexible displays among other photoelectric applications, resulting from their electroluminescence, high quantum efficiency, enhanced mechanical and thermal properties, and conductivity. In particular, polyfluorene CPs are an attractive prospect due to their emission in the blue light region of the electromagnetic spectrum. The C-9 position of the fluorine group leads to greater control of electrical and optical properties compared with its counterparts. In contrast, poly(p-phenylene vinylene)s (PPV), polythiophene (PT)s, polyfluorene (PF)s and poly(p-phenylene)s (PPP), and their respective derivatives have similar properties but emit more in the green to the blue part of the spectrum. However, issues have arisen as a result of macromolecules folding and unfolding during the formation of larger structures. In a study it was concluded that LB can be used to mitigate these issues, by ensuring that the molecules being used are co-spread with other surfactants, or chemically functionalised for improved suitability.<sup>[119]</sup>

1D nanowires of lead halide perovskites (LHPs) have been developed, resulting in enhanced optoelectronic properties compared to the bulk material. However, these

structures are highly ionic and have low dissociation energy and, therefore, suffer from environmental impacts. To mitigate these effects, surface modification of the colloidal CsPbBr<sub>3</sub> nanowires, with polystyrene-block-poly(4-vinylpyridine) (PS-P4VP) has been used. This resulted in improved photoluminescent emission and better colloidal stability in water. In turn, a modified LB technique was employed to form monolayers from the nanowires; it was found that using optimised LB deposition caused monolayers to form which displayed a strong dielectric effect.<sup>[120]</sup>

## 4.5. Characterisation techniques

### 4.5.1 Scanning Probe Microscopy

The Nobel Prize for Physics was awarded to Gerd Binnig and Heinrich Rohrer for their invention for imaging atoms on a surface; the scanning tunnelling microscope (STM). From here, other scanning probe microscopes (SPM) have been developed, such as the atomic force microscope (AFM).<sup>[121]</sup> Unlike other microscopic methods (some examples of which are featured in Figure 4.11), AFM relies on forces between the probe and sample, rather than bombarding a surface with light or electrons. This allows a 3D image to be built up, given that the height of the sample can also be seen from the results. The discovery of the AFM following the STM allowed for non-conductive samples to be investigated.<sup>[122]</sup> Per Table 4.5,<sup>[122]</sup> the scale at which different microscopes can image varies along with the cost of operation and other properties.

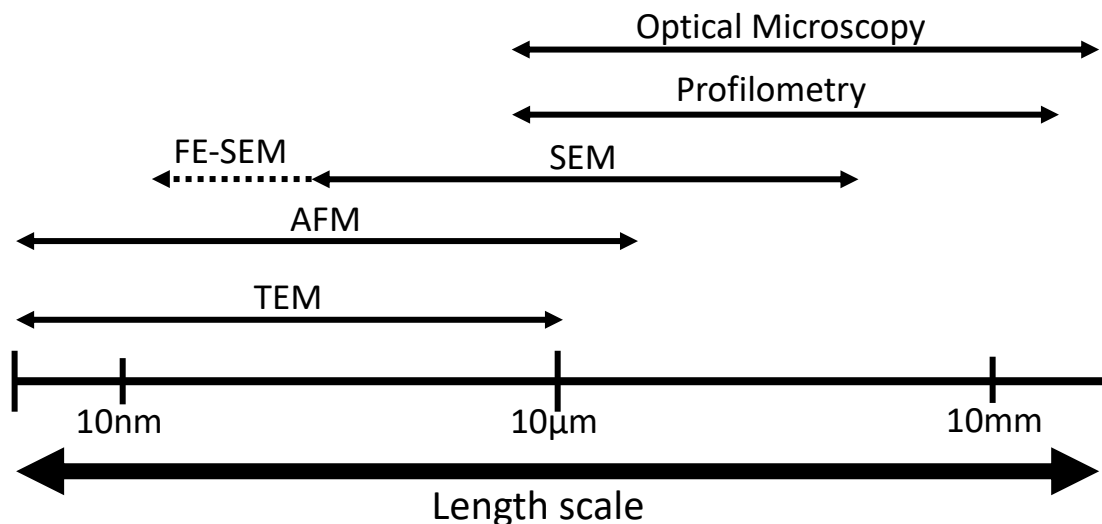


Figure 4.11 Optical and electron microscopy techniques and the scales they can be used to observe.<sup>[122]</sup>  
This research has focussed on AFM.

*Table 4.5 Comparison of common SPM methods and their properties. This demonstrates the key differences between the different modes.*

	<b>AFM</b>	<b>SEM</b>	<b>TEM</b>
<b>Sample Preparation</b>	Little or none	Little to a lot	Little to a lot
<b>Resolution</b>	0.1nm	5nm	0.1nm
<b>Relative Cost</b>	Low	Medium	High
<b>Sample Environment</b>	Any	Vacuum/ Gas	Vacuum
<b>Depth of Field</b>	Poor	Good	Poor
<b>Sample Type</b>	Conductive/ Insulating	Conductive	Conductive
<b>Time for Image</b>	2-5 Minutes	0.1 – 1 Minute	0.1 – 1 Minute
<b>Maximum Field of View</b>	100µm	1mm	100nm
<b>Maximum Sample Size</b>	Unlimited	30mm	2mm
<b>Measurements</b>	3D	2D	2D

In essence, AFM works by scanning a tip over the material surface using a piezoelectric transducer, with a sensor in place to measure the force between the two. A feedback loop is then used to ensure this force is kept constant whilst the surface is scanned to form an image.<sup>[122]</sup>

AFMs all consist of a cantilever spring with a sharp tip, a way of sensing the deflection of this, a feedback system to monitor and control this deflection, a scanning system that moves the sample beneath the probe tip (or vice versa), and a display system to show the results as a topographical image (Figure 4.12).<sup>[121]</sup>

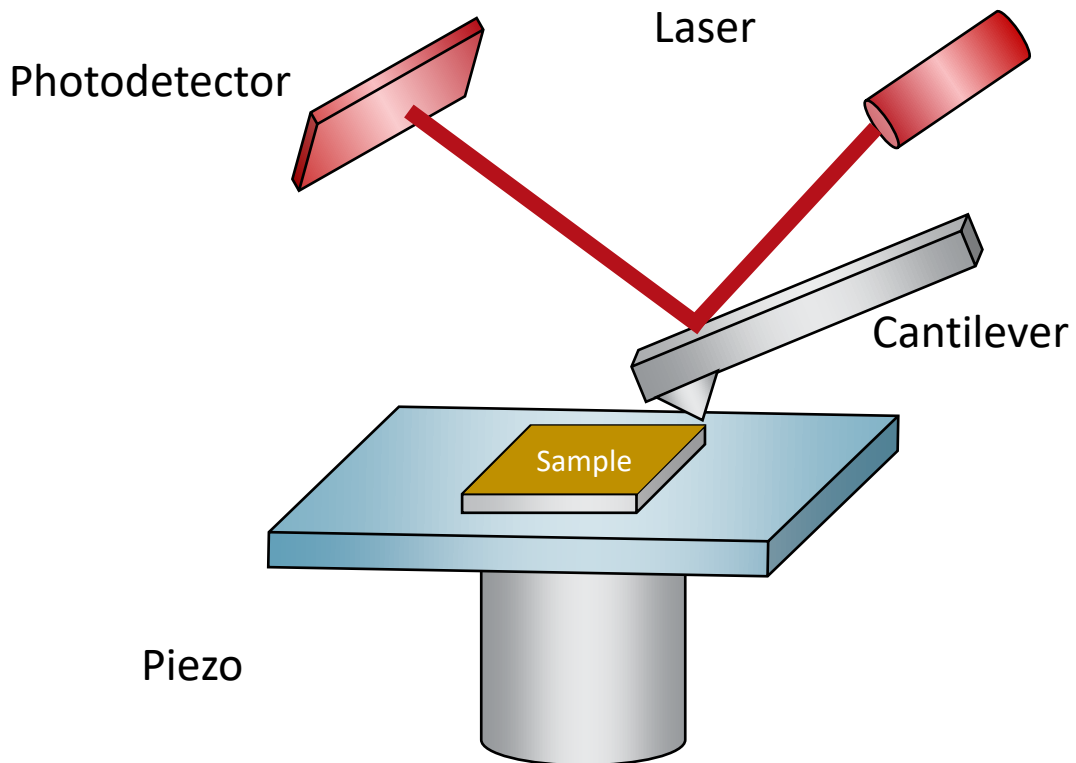


Figure 4.12 AFM system setup. The piezo scanner brings the probe tip into contact with the sample, with a feedback loop used to control the distance between the two. A photodetector and laser are employed to sense cantilever deflection to create the 3D image of the surface.

AFM can be used in air, in a vacuum, or in liquid. Liquid use is typically applied to biological samples such as monitoring DNA that has been edited to display antibacterial behaviours.<sup>[123]</sup> Vacuum AFM can be used for work that is highly sensitive to contamination, for instance, measuring van der Waals forces between an extreme ultraviolet photomask and the AFM tip.<sup>[124]</sup> Ambient AFM is often used for measurements in more 'real-life' conditions.

Within AFM there are different working modes. One such mode is termed 'Contact mode', in which the AFM probe is in direct contact with the sample being investigated. This is a common mode used, with the probe tracing closely over the surface for an accurate topographical measurement. Non-contact mode, on the other hand, is used when direct interaction could damage the sample. This instead relies on the probe being kept a constant distance away from the sample surface.<sup>[125]</sup>

Recently, Peak Force Tapping mode has instead been employed in order to prevent destruction of the sample, whilst enabling collection of thermoelectric and electrical data. Instead of the probe constantly scanning over the surface, in this mode the probe contacts the sample at a point before drawing away and re-contacting elsewhere. These point measurements are then reconstructed to give the sample's topography. It was reported that using tapping mode in conjunction with thermoelectric and contact modes

was a successful means of measuring sample properties similar to those obtained through typical contact modes, without causing destruction to the organic samples. Furthermore, this approach enabled recording of additional nanomechanical properties.<sup>[126]</sup>

Within AFM research it is necessary to select the probe based on the sample to be investigated. For example, a thicker cantilever may be used if the sample is hard, stable, or if the AFM will be used in non-contact mode. For organic samples, softer probes are recommended. Typical AFM probes are made from silicon however, many are coated on the backside (for laser alignment), frontside (for differing interaction with the sample), or both. Aluminium coatings are used mostly for non-contact modes in air, however are not suited to liquid measurements. Gold coatings can be used in liquid settings as they don't de-laminate as aluminium coated probes do. Platinum coating on the frontside enable conductive measurements to be taken. Diamond probes can be used for indentation into hard samples, and doped diamond probes can be used for conductive measurements.<sup>[127]</sup> See Table 4.6 for some examples of probes and their specifications from NuNano Ltd (industry partner).<sup>[128]</sup>

Table 4.6 Examples of AFM probe dimensions and applications.

Probe Type	Tip Apex (nm)	Cantilever Thickness ( $\mu\text{m}$ )	Coating	Application
<b>Scout 350</b>	5	4.5	None	Non-contact and tapping modes in air, hard samples.
<b>Scout 70</b>	5	2.5	None	Non-contact and soft tapping modes in air for softer samples.
<b>Scout 350 RAI</b>	5	4.5	Backside aluminium	Non- contact and tapping modes in air
<b>Scout 350 RAu</b>	5	4.5	Backside gold	Non- contact and tapping modes in air and liquid.
<b>Spark 70</b>	18	2.5	Front and backside platinum	Electrical contact and non-contact modes.



Typically available probes are fabricated from silicon or silicon nitride with a stiffness ranging from 0.01-100 N/m. All metal probes have been suggested as a method for expanding this range to enable greater measurement of nano- and microtribological samples. Nickel probes were created with stiffnesses of 20 N/m and 2,800 N/m via electrodeposition.<sup>[129]</sup>

Alternatively, existing probes are being coated with new materials to alter their characteristics. One such example was coating probes with noble metals to improve their wear resistance. It was found that coating silicon probes in a platinum-iridium layer gave them improved scratch resistance, making the probes ideal for contact mode measurements.<sup>[130]</sup>

Another probe coating that has been developed as of late is graphene. This will be discussed further in Chapter 6.1.

#### 4.5.2 X-Ray Photoelectron Spectroscopy

X-ray photoelectron spectroscopy (XPS) utilises the photoelectric effect, where electrons are emitted upon absorption of electromagnetic radiation, to determine bonding within a sample. In these measurements, a sample is bombarded with X-rays of known kinetic energy, and electrons are subsequently ejected and their energy is measured. A single wavelength of X-ray is used to be able to determine the kinetic energy of the electrons released, via Equation 4.7.

$$E_k = h\nu - E_b + \Phi \quad \text{Equation 4.7}$$

Here,  $E_k$  is kinetic energy;  $h$  is Planck's constant;  $\nu$  is the incident photons' frequency;  $E_b$  is the binding energy and  $\Phi$  is the spectrometer work function which is intrinsic to the specific instrument used.  $h\nu$  represents photon energy.

Energy levels for atoms differ from one another when measured under vacuum, therefore it's possible to use the electron energies detected to conclude sample composition, including bonding environments.<sup>[92, 131]</sup> See Figure 4.13 for a diagrammatical representation.<sup>[92]</sup>

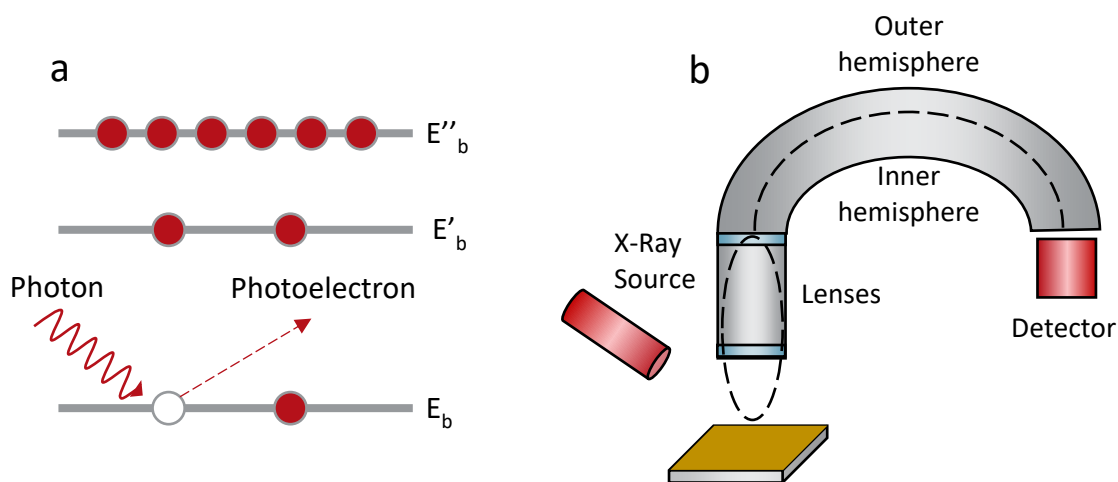


Figure 4.13 Working principals of XPS. a) gives the photoelectric effect as it occurs within the sample; a photon contacts an electron and causes a photoelectron to be emitted. b) depicts the layout of a hemispherical XPS spectrometer X-rays are emitted and contact electrons causing them to be released. These are then directed towards a detector which collects the data ready for analysis.

Due to the lack of damage caused by X-rays, this method is typically used for organic materials.<sup>[6]</sup>

### 4.6. Applications

Lee and Wu summarised energy harvesting techniques for thermoelectric materials and the thin films that show promise in each sector. This is given in Table 4.7.<sup>[132]</sup> With this in mind, it has been suggested that further research is required into improving manufacturing routes for these materials, removing toxic elements, increasing the devices' efficiency, improving the lifetimes of wearable technology, and developing integrated energy storage.<sup>[132]</sup>

Table 4.7 Summary of methods for producing energy and the 2D thermoelectric materials that may be employed.

Energy Harvesting Technique	Working Theory	Desirable Characteristics	2D Materials of Interest
<b>Photovoltaic Cells</b>	Electron–hole pairs generated upon light illumination are separated and collected at the two terminals under an electrical field.	<ul style="list-style-type: none"> <li>• Absorption spectra close to the solar spectrum;</li> <li>• Strong light-matter interaction;</li> <li>• Long exciton and charge diffusion length;</li> <li>• Long carrier lifetime;</li> <li>• High charge mobility;</li> <li>• Optical transparency;</li> <li>• High absorption coefficient.</li> </ul>	<ul style="list-style-type: none"> <li>• Graphene;</li> <li>• TMDs;</li> <li>• BP;</li> <li>• MXene;</li> <li>• 2D perovskite;</li> <li>• 2D polymer.</li> </ul>
<b>Thermoelectric Energy Harvesting</b>	An electrical output is generated with a temperature gradient across the materials.	<ul style="list-style-type: none"> <li>• High Seebeck coefficient;</li> <li>• High electrical conductivity;</li> <li>• Low thermal conductivity;</li> <li>• Wide operation temperature range.</li> </ul>	<ul style="list-style-type: none"> <li>• Graphene;</li> <li>• TMDCs;</li> <li>• Tellurides;</li> <li>• Tellurene;</li> <li>• BP.</li> </ul>

In particular with photovoltaic cells, the benefit of integrating thermoelectric materials is twofold: by attaching a TEG to the back of an existing PV cell, it is possible to continue electricity generation from the cell overnight. Generation occurs throughout the day also, as the external air acts as the heat sink, compared to the solar cell being heated by the sun. During the night hours, radiative heat is released from the earth and thus the solar cell acts as the heat sink. This method attained power generation up to  $50 \text{ mW/m}^2$  and an open circuit voltage ( $V_{oc}$ ) of 100 mV with a clear night sky. It was suggested that this would be particularly helpful for off-grid communities as it reduces the need for batteries, and improves the efficiency of their solar installations.<sup>[133]</sup>

The second benefit of this combination is that TEGs affixed to the back of solar cells can cool the module, resulting in improved efficiency. In such a setup in South Korea, researchers were able to improve the overall solar cell efficiency by 11.21%, with a daily increase in electricity production of 8.3%.<sup>[134]</sup>

In terms of energy harvesting, TEGs can be utilised as Passive Radiative Coolers (PRCs), which use thermal radiation to pass excess heat to cooler spaces. This could be useful for thermal power plants, smart windows, energy-efficient buildings and optoelectronic devices. They require high reflectance in the solar spectrum (0.3-2.5  $\mu\text{m}$ ) and high emissivity in the atmospheric transmittance range (8-13  $\mu\text{m}$ ). PRCs work passively, as suggested by the name, so don't require energy to create their cooling effect. By ensuring the devices have high emissivity in the atmospheric range, PRCs will pass heat from earth objects straight into space (which sits at  $\sim 3 \text{ K}$ ). Night-time PRCs have been developed previously, as these negate solar radiation effects, however, these do not aid with daytime cooling. Polymer-based PRCs seem promising however, they're held back by a high tendency to degrade, as a result of peeling and oxidation.<sup>[135]</sup> A PRC has previously been combined with a TEG to produce  $90.74 \text{ mW/m}^2$  throughout the day.<sup>[136]</sup>

Additionally, low emissivity coatings on windows could be used for temperature regulation in homes; it has been outlined that transparent and conductive oxides (TCOs) can be formed from existing broad bandgapped metal oxides by adding dopants. This can introduce holes, allowing for potentially large improvements in their electrical conductivity. Such devices could be useful for transparent resistors, non-volatile memory and thermoelectric devices. The most commonly applied TCOs are ITO ( $\text{In}_2\text{O}_3: \text{Sn}$ ), AZO ( $\text{ZnO}: \text{Al}$ ) and FTO ( $\text{SnO}_2: \text{F}$ ). To be most effective, these coatings need to have high transmittance in the visible light spectrum, whilst displaying high reflectance in the infrared spectrum, thus allowing people to see through them whilst aiding with

temperature regulation. The required characteristics for this are transmittance between 380-750 nm and reflectance >750 nm.<sup>[137]</sup>

The final key application of thermoelectric materials is as wearable technology; the devices these materials have been affixed to would be charged in part by body heat. Double-chain TEGs have been fabricated through screen printing. The resulting devices consisted of n-type and p-type thermoelectric inks deposited onto polymeric substrates, forming thermocouples and constructing two independent chains. Consequently, the gap between the two chains was covered by a layer of silk fibroid, forming a functional layer for sensing water vapour presence and temperature. The maximum voltage output achieved by the devices was 3.3 V, however, it was revealed that when coupled with capacitors, the devices were capable of powering a commercial calculator from human body heat alone.<sup>[138]</sup>

## 5. Experimental Methods

### 5.1. Langmuir Blodgett (LB)

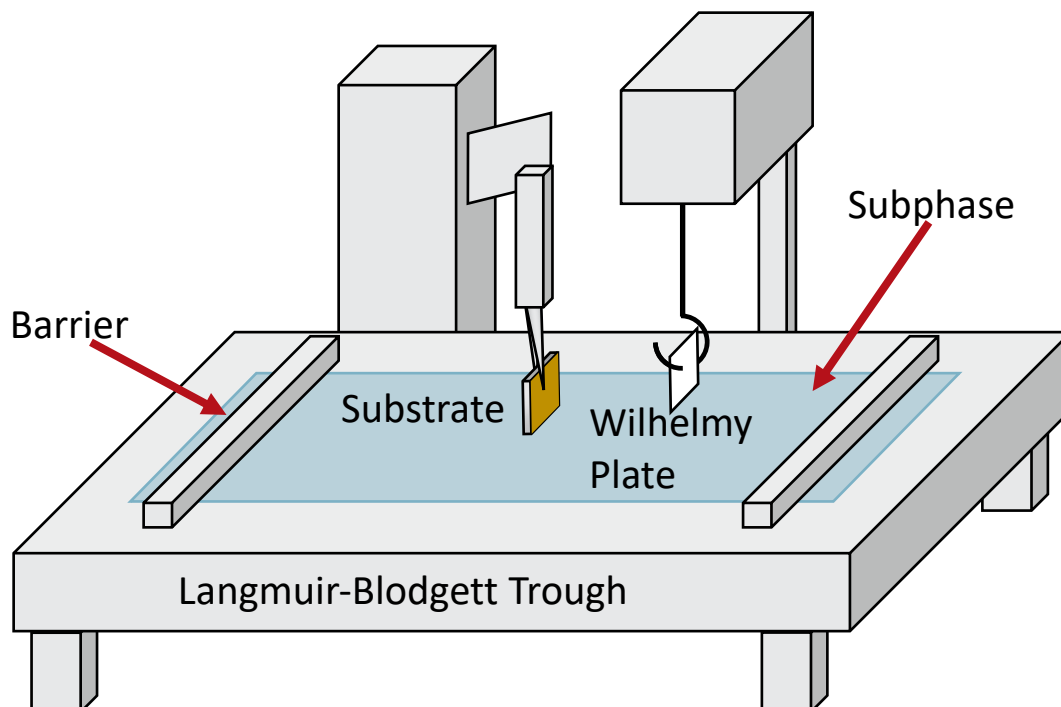


Figure 5.1 Schematic of the setup used for LB experiments. The apparatus consists of a hydrophobic LB trough filled with a subphase. In these experiments the subphase was water. This is topped by hydrophobic barriers which sit atop the subphase, but with the meniscus touching the barriers; these compress to push the monolayer into the quasi-solid state. A Wilhelmy plate was employed for monitoring surface tension. The trough dimensions are 364 x 75 x 4 mm.

For this research, a Biolin Scientific KSV Nima 2003 Langmuir-Blodgett trough was used (see Figure 5.1). It was thoroughly cleaned with IPA and ethanol before being filled with pure water until menisci formed at the edges of the trough and against the compression barriers, and a known volume of the molecule was subsequently applied to the surface via a micro syringe. Given that the molecules were typically dissolved in a solvent, they were left for a period of ~20 minutes to allow the solvent to evaporate before experiments were carried out. Filter paper (Whatman, grade 1; approximately 1 cm x 2 cm) that had been saturated with pure water was used as the Wilhelmy plate.

The barriers were controlled via computer monitoring to close until a point where a closely packed monolayer formed, before passing a substrate through the monolayer. The closing rate used was typically 7.5 mm/min.<sup>[17]</sup>

For the Atomic Force Microscope probes coated in graphene, Langmuir Schaefer deposition as described in Chapter 4.4.2 was used. Further detail is given in Chapter 6.1.2.

## 5.2. Self-Assembled Monolayers (SAMs)

In this research, SAMs were prepared by submerging a well-cleaned gold substrate (on silicon) per Chapter 5.4, in a 1 mMol solution of the target molecule and leaving the SAM to form over minutes or hours, at room temperature. The length of time required varies depending on the molecule. The sample was subsequently rinsed with the same solvent(s) the molecule was dissolved in, and dried with nitrogen to remove physisorbed molecules; see Figure 5.2.

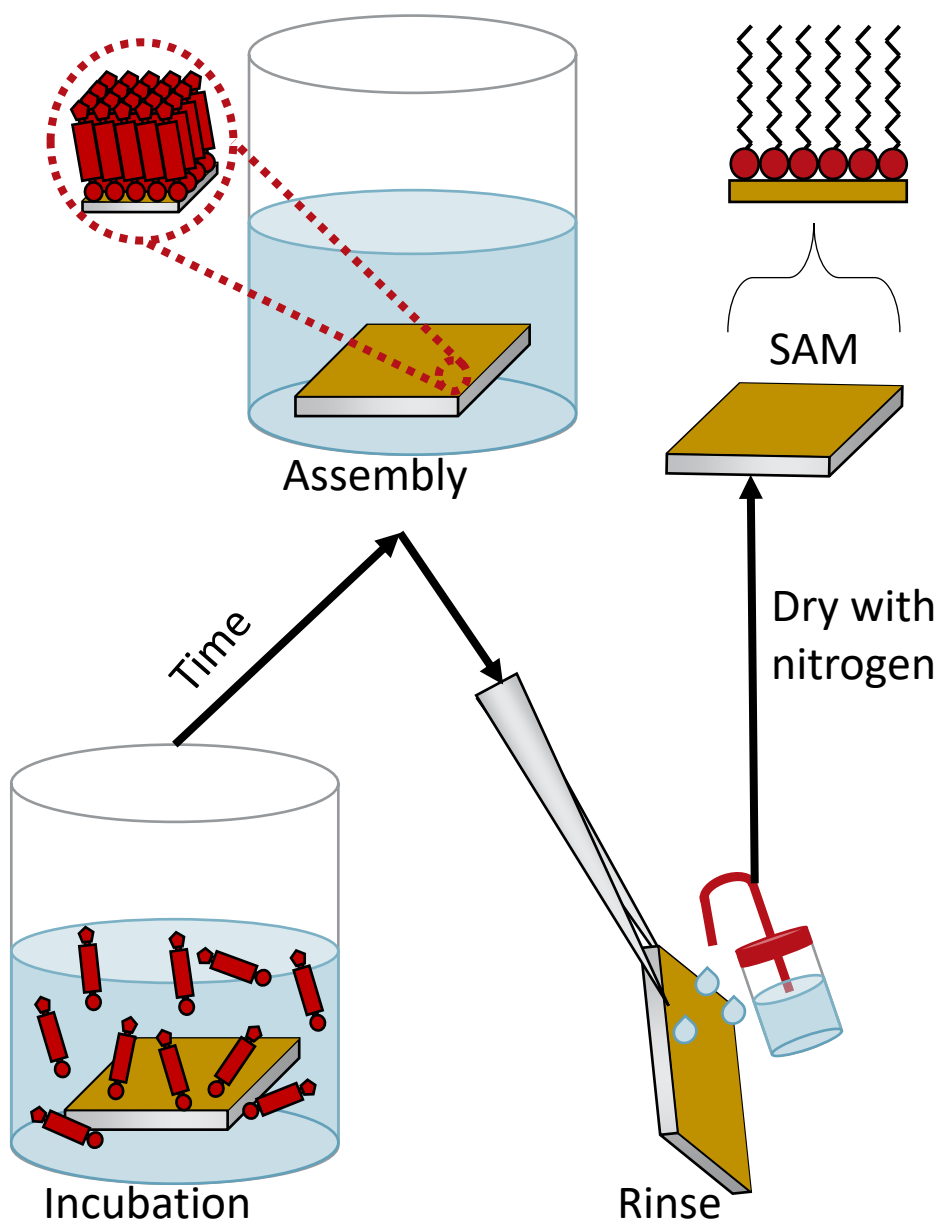


Figure 5.2 Method for creating samples via self-assembly. A substrate is left in a solution containing the target molecule for a set period. This is then removed, rinsed and studied.<sup>[93]</sup>

Solvents play a critical role in the formation of SAMs. Ethanol is often used in the case of thiols deposited on gold, as it is non-toxic, low cost and able to dissolve a wide range

of molecules. For alkanethiols, nonpolar solvents have faster results than polar solvents like ethanol but result in less well-organised monolayers. Nucleophilicity also impacts solvent choice; for such molecules, a solvent that won't react with the nucleophile should be chosen. Moisture content also plays a role, with anhydrous toluene being shown to extract moisture to aid the formation of crystalline monolayers. Ultimately, the solvent selected should be capable of fully dissolving the molecule in it, to enable the monolayer deposition to be carried out.<sup>[139]</sup> In this research, for the tetrapodal molecules a solution of 1:5 ethanol: toluene was used to ensure the molecules fully dissolved; this combination aimed to allow the molecule to dissolve well whilst maintaining ordered monolayers. The dithiolene molecules were dissolved in tetrahydrofuran (THF) initially, with NaOMe added to deprotect as required. This solution required sonicating for 1 hour to ensure the solution had fully homogenised.

### 5.3. Quartz Crystal Microbalance (QCM)

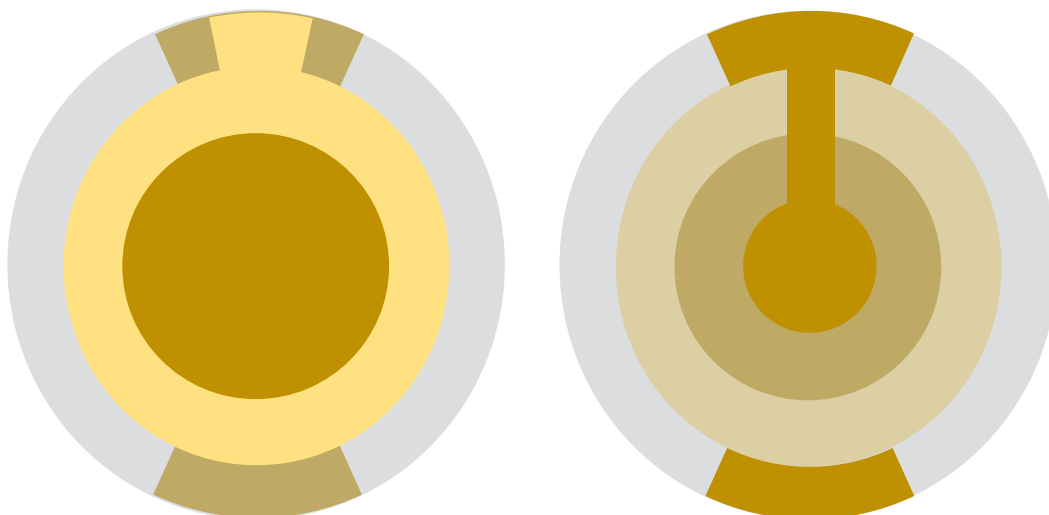


Figure 5.3 Crystals used for QCM; front and back. The translucent region is AT-cut quartz crystal, whilst the gold regions are electrodes on which the SAM forms.

Quartz Crystal Microbalance (QCM) is used for the real-time characterisation of SAMs. It includes an AT-cut quartz crystal, with gold electrodes mounted onto it (see Figure 5.3). The AT-cut nature of the crystal causes it to oscillate out of the plane when a frequency is applied. QCMs are used to determine the mass of a SAM that has been deposited onto the crystal, by using the Sauerbrey equation (Equation 5.1).<sup>[140]</sup> This method relies on SAMs forming on the gold substrate material provided by the QCM crystal; this typically limits the research to molecules that feature functional groups with an affinity for gold, such as thiols.

$$\Delta f = \frac{-2 \times f_0^2}{A \times \sqrt{\rho \times \mu}} \times \Delta m$$

Equation 5.1

Where  $f$  is frequency,  $f_0$  is the resonant frequency of the crystal,  $A$  is the crystal area,  $\rho$  is the density of quartz and  $\mu$  is the shear modulus of quartz. The Sauerbrey equation assumes that the film that forms is rigid, thin and coupled to the crystal's surface. In the case of biomolecules in liquid and other hydrated systems, the application of this equation leads to an underestimation in the film mass; viscoelastic modelling can be used instead.<sup>[141]</sup> Given that no such molecules were studied in this research, this is considered beyond the scope of this work.

For this research, predominantly, an Open QCM Q<sup>-1</sup> was used to measure the frequency and dissipation of SAM growth on 5MHz resonant frequency crystals; only the frequency was noted and utilised. Figure 5.4 depicts a SAM forming on a crystal, with the resulting change in frequency and dissipation over time given in the graph below.

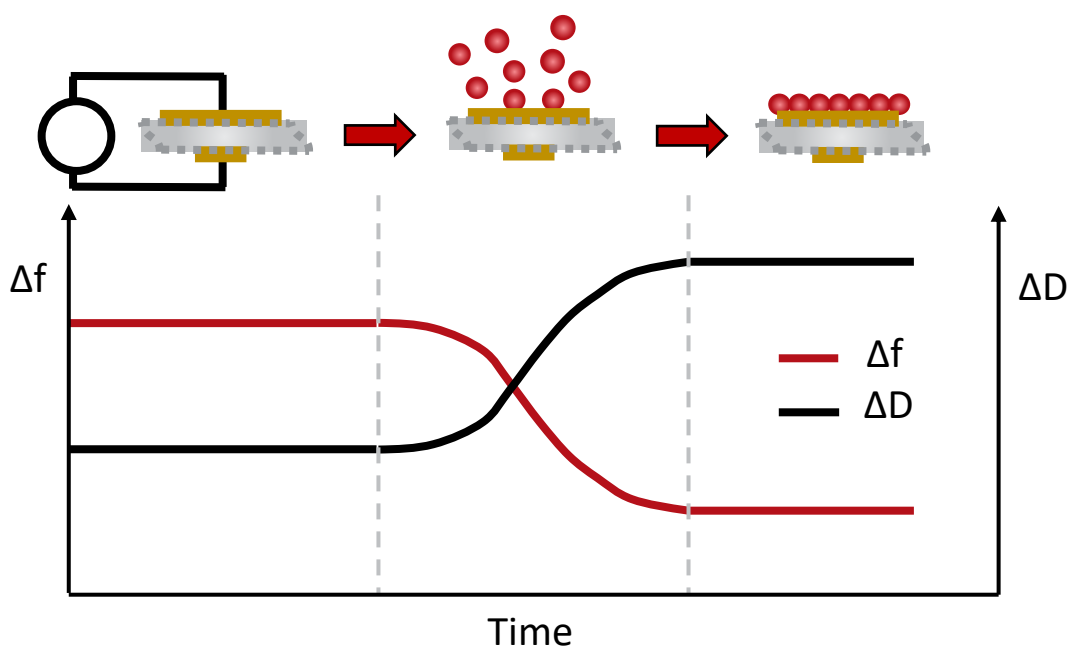


Figure 5.4 Graph produced when taking measurements with QCM; the black line is dissipation, or how well the sample is adhered to the surface. The red line is frequency, which steadily drops as the molecules align on the substrate until it plateaus once the monolayer has fully formed. The diagram above the graph shows a SAM forming on a crystal.<sup>[141]</sup>

The resonant frequency was measured before any deposition occurred to obtain the baseline resonant frequency after the crystal had been cleaned by first plasma-cleaning for 10 minutes in a Henniker Plasma HPT-100 plasma oven, next submerging in dimethyl formaldehyde (DMF) heated to 100 °C for 2 hours, then left in room temperature DMF overnight. Following this, the crystals were rinsed first with ethanol and then with IPA, before being baked in a (Thermo Scientific Vacutherm VT 6025) vacuum oven at 35 °C overnight. The crystal was subsequently submerged in a given solution for set periods before being rinsed with solvent to remove physisorbed molecules, blown with nitrogen, and placed in the Open QCM Q<sup>-1</sup> measurement port. Each measurement was recorded



after being allowed to stabilise for 20 minutes. This was carried out until the frequency stopped changing, meaning that a complete SAM had formed. In many cases, only an initial measurement and a final measurement the following day were taken, as the deposition time was not important.

From the Sauerbrey equation (Equation 5.1) it is possible to convert from new frequency to mass deposited to the area per molecule deposited. Using Equation 5.2 and Equation 5.3 it is possible to rearrange the Sauerbrey equation to give molecular area (Equation 5.4).

$$A_{molecule} = \frac{A'}{n} \quad \text{Equation 5.2}$$

$$n = \frac{\Delta m \times N_A}{M_w} \quad \text{Equation 5.3}$$

$$A_{molecule} = \frac{-2 \times f_0^2 \times M_w}{\Delta f \times \sqrt{\rho \times \mu} \times N_A} \quad \text{Equation 5.4}$$

In the above equations,  $A'$  = the surface area of the electrode,  $n$  = number of molecules deposited (from Avogadro's relation),  $M_w$  = molecular weight and  $N_A$  = Avogadro's constant.

By substituting values for the constants in the above equation, it can be simplified to Equation 5.5.

$$A_{molecule} = \frac{-2 \times f_0^2 \times M_w}{\Delta f \times 5.32 \times 10^{33}} \quad \text{Equation 5.5}$$

The constants substituted are:<sup>[142]</sup>

- $\rho = 2.648 \text{ gcm}^{-3} \times \frac{\text{m}^{-3}}{\text{cm}^{-3}} = 2.648 \times 10^6 \text{ gm}^{-3}$
- $\mu = 2.947 \times 10^{11} \text{ gcm}^{-1}\text{s}^{-2} \times \frac{\text{m}^{-1}}{\text{cm}^{-1}} = 2.947 \times 10^{13} \text{ gm}^{-1}\text{s}^{-2}$
- $N_A = 6.022 \times 10^{23} \text{ mol}^{-1}$

It is noted that the change in frequency will always be negative as mass is added to the crystal. Therefore, the area will be positive due to the negative signs from the numerator and denominator subsequently cancelling one another out.

#### 5.4. Preparation of Gold Samples

For the experiments carried out which utilise template stripped gold as the substrate, the method for production of this was as follows:<sup>[143, 144]</sup>

1. Sonicate silicon wafer in acetone, followed by methanol and finally isopropanol.

2. Plasma clean this with oxygen.
3. Thermally grow 200 nm of 99.8% purity evaporated gold on the surface of the silicon.
4. Cut approximately 0.5 cm x 1 cm pieces of silicon (cleaned as above).
5. Use Epotek 353nd epoxy adhesive to stick these pieces of silicon to the gold from above.
6. Cure for 40 minutes on a hot plate at 140 °C.
7. Remove the smaller piece of Si from the larger, and the Au will come away with it.
8. Use Atomic Force Microscopy (AFM) to spot-check the surface in several places to ensure the Au is sufficiently flat; the roughness should not exceed 0.1 nm.

Figure 5.5 shows how the layers form, and which parts are then used for creating samples.

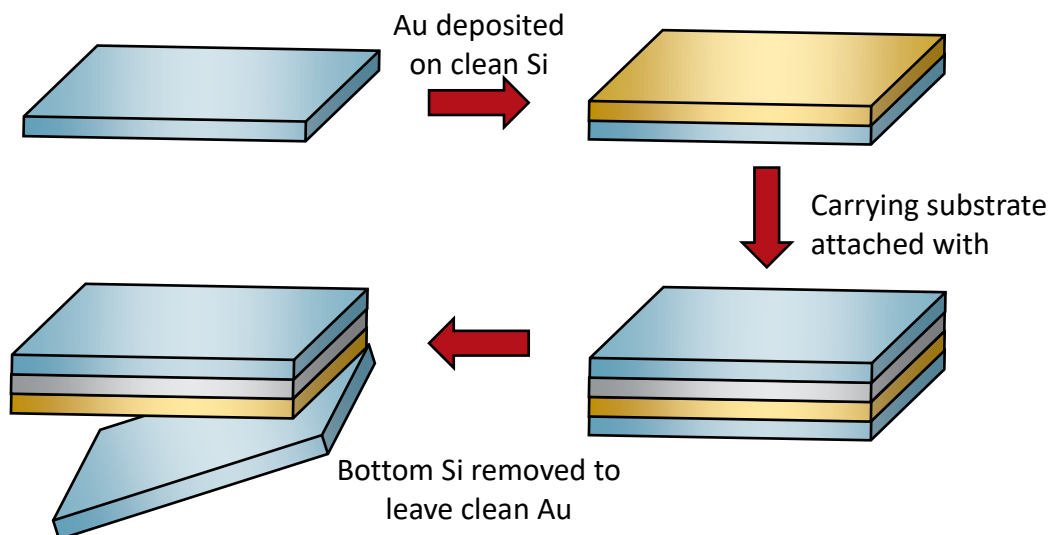


Figure 5.5 Formation of template-stripped gold samples for thin film deposition. Initially, gold is deposited onto silicon, with a further silicon layer then attached to the top. When it's ready to be used, the bottom silicon layer is cleaved off, leaving a clean and flat layer of gold ready to be used as a substrate. The films are deposited onto the Au that is exposed in the final sample (bottom left).

### 5.5. Scanning Probe Microscopy (SPM)

For this research, a Bruker MultiMode 8 was used, connected to a Nanoscope V controller. For imaging, PeakForce QNM (Quantitative Nanoscale Mechanical) or Scan Assyst were used; for causing the scratches for scratch tests, contact mode was employed, and for electrical conductivity measurements, contact mode was modified to include multiple input channels.

### 5.5.1. Imaging and Scratch Tests

As well as gaining a topographical image of the surface of a material, it's possible to gain an idea of how thick the monolayer is using AFM to perform a nanoscratch. It is simply necessary to contact the probe (Scout probes from NuNano Ltd. were used) with the surface for several scans, pressing hard enough to remove the monolayer whilst leaving the substrate intact. The height difference between the area with and without the monolayer can then be found, with the height of the molecule used being the difference between the two. If the length of the molecule is known, the angle at which it has been deposited can then be found.

To process the raw data produced by the microscope, the free software Gwyddion was used. In the case of topographical measurements, several steps were taken; the functions used and their purposes are given in Table 5.1.<sup>[145]</sup>

*Table 5.1 Gwyddion settings and their uses for analysing AFM images.*

Function	Purpose
<b>Plane Level</b>	Removes the plane from the raw data, using all image data points.
<b>Facet Level</b>	Similar to above, but in patches rather than for the whole image.
<b>Flatten Base</b>	Facet and polynomial levelling are used to flatten the base vs. any peaks present.
<b>Remove Scars</b>	Removes horizontal scanning errors.
<b>Step Line Correction</b>	Adjusts for misaligned heights in horizontal portions.
<b>Fix Zero</b>	Moves the value for 0 on the gradient legend.
<b>Profiles</b>	Gives the 3 <sup>rd</sup> .dimensional view, to show the height difference of where the molecule has been removed from the substrate.

To find the height difference from the scratch test, the profile function was selected, and the thickness was increased so that an average difference was taken across the entire scratch. The difference between the normal height (of substrate plus molecule) and that where the molecule had been removed (so only the substrate remains) was then taken; this is the height of the molecule.

### 5.5.2. Electrical Conductivity

To record conductivity measurements via cAFM (conductive Atomic Force Microscopy), a conductive probe (Pt coated Multi75E-G from Budget Sensors unless otherwise stated) and probe holder were used, alongside a low noise Femto DLCPA-200 I/V converter. Within the setup, the gold substrate onto which the monolayer had been deposited acted as a bottom electrode, whilst the probe (of around 3 Nm<sup>-1</sup> spring constant and 75 Hz resonant frequency) acted as the top electrode. A spot of silver paint was used to ensure

electrical contact between the monolayer and sample holder. See Figure 5.6 for a diagram of the equipment used.

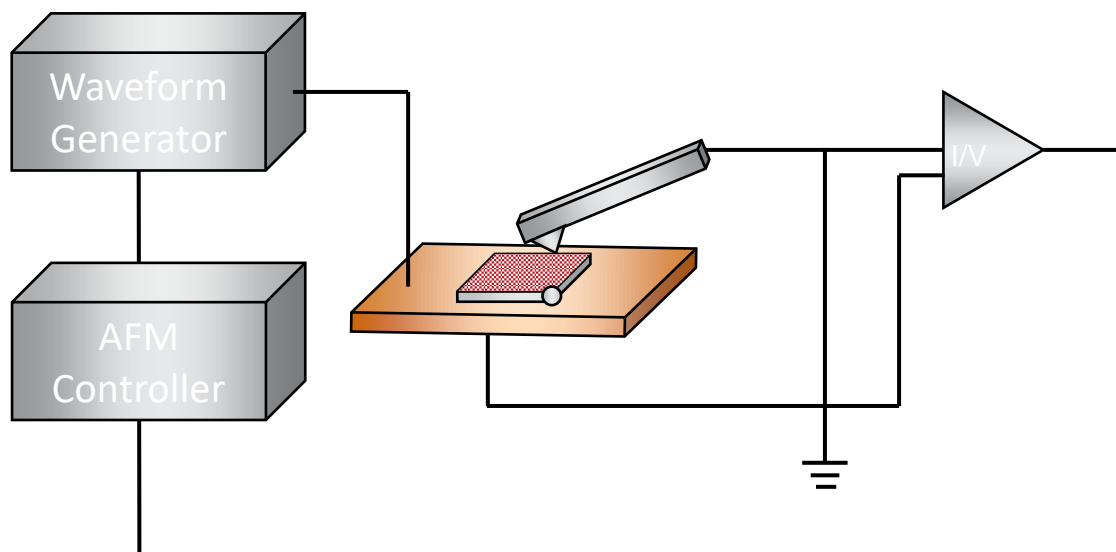


Figure 5.6 Setup for conductive AFM measurements. A Bruker Multimode was used in conjunction with a Femto I/V converter and waveform generator.

A triangular waveform was transmitted through the sample from an Agilent 33500B, with the peak-to-peak voltage (VPP) typically reaching up to 1 VPP but with some molecules requiring this to be increased. This was then passed through an I/V converter (the Femto device; with sensitivity typically set to  $10^9$  V/A) before reaching the AFM controller. The signal conducted through this loop was subsequently measured and viewed using Nanoscope software. Within the software, the input and output signals were viewed side-by-side.

For electrical measurements, the scan size for the AFM software was set to zero, to gain measurements of a single point. Multiple measurements were acquired in multiple spots to build a picture of the conductivity of the overall film.

Conductance per molecule was determined using Equation 5.6; wherein  $r$  is the contact radius,  $F$  is the applied force from the probe,  $R$  is the probe tip radius and  $1/Y$  is as shown in Equation 5.7. In Equation 5.7,  $\nu_{1,2}$  are the Poisson ratio of materials, and  $E_1$  and  $E_2$  are Young's modulus of the probe (around  $10^{11}$  Pa) and the molecular layer respectively.

$$r = \left( F \times R \times \frac{1}{Y} \right)^{\frac{1}{3}} \quad \text{Equation 5.6}$$

$$\frac{1}{Y} = \frac{3}{4} \left( \frac{1 - \nu_1^2}{E_1} + \frac{1 - \nu_2^2}{E_2} \right) \quad \text{Equation 5.7}$$

In this research, it is assumed that: force is  $1 \times 10^{-8}$  N; probe tip radius is  $3 \times 10^{-8}$  m;  $\nu_1$  is 0.33,  $\nu_2$  is 0.33;  $E_1$  is  $1 \times 10^9$  N/m<sup>2</sup> and  $E_2$  is  $1 \times 10^{11}$  N/m<sup>2</sup>.

From here, the number of molecules in the junction is easily determined by dividing the calculated area by the cross-sectional area of the molecule in question. This was then applied to find the conductance per molecule.

### **5.6. X-Ray Photoelectron Spectroscopy (XPS)**

For this thesis, all XPS measurements were carried out using Kratos AXIS Supra, to determine the binding of different functional groups to the gold substrate used throughout. The device software was utilised to assign which peaks in the spectra aligned with which binding.

## 6. Results

### 6.1. Graphene Coating Probes

#### 6.1.1 Introduction

Chapter 1 discusses the difficulty of progressing from a single molecule to a thin film, and ending with a top contact in an electrical circuit for practical purposes.

To measure the electrical properties of thin films in a laboratory setting, it is typically necessary to contact two electrodes to either side of the film, particularly in techniques such as SPM and break junctions. In methods such as cAFM, a sharp probe acts as the top electrode, with a current able to flow from the probe tip through the sample under investigation into the sample holder; the second electrode. In most cases, these conductive probe tips are formed of silicon that has been coated in metal, however, these coatings tend to diminish over time due to friction and high currents. Previously this has been overcome by instead coating the probes in diamond. However, this is expensive and causes lower resolution in the images produced as a result of the tip having a larger apex. This is also the case with solid metal probes.<sup>[146]</sup> Furthermore, these probes are limited to a few tip apexes, spring constants and resonant frequencies, as well as being sold by only a few manufacturers. With diamond probes, in particular, the high stiffness of the probes can cause damage to the sample over time and reduce tip sharpness from particle adhesion.<sup>[147]</sup>

Moreover, previous methods for integrating graphene into circuits have included single-layer-graphene (SLG) bottom electrodes, SLG nanogaps, and layers of graphene integrated between the top contact and monolayer. All of these, however, resulted in unreliable or poorly functioning solutions. By instead graphene-coating the SPM probe, it is possible to recreate the junction large area device geometry in an SPM whilst maintaining a graphene contact.<sup>[148]</sup>

It has also been suggested that graphene coating these precise probes could be a suitable alternative due to its favourable physical, mechanical and electrical characteristics. Ample research has been carried out into using chemical vapour deposition (CVD) to coat probes thus, with promising results of greater electronic coupling and improved wear resistance.<sup>[149-153]</sup>

As an alternative to CVD, solution-processed sheets of graphene have been created to coat the probes, relying on van der Waals forces to physisorb graphene to the probe. Though the results of this research were promising in terms of successfully coating the probes, it was noted that this method does not enable control of the number of layers of graphene involved in the coating.<sup>[154]</sup>

Sputtering and liquid phase exfoliation have also been attempted for the graphene-coating of nanoprobes, with some success. Of the techniques mentioned, exfoliation has been the most promising in terms of cost and replicability. Moreover, in the case of all the techniques, graphene-coated probes resulted in better wear resistance as well as chemical, thermal and mechanical stability than their uncoated counterparts.<sup>[147]</sup>

This research employed Langmuir-Schaefer (LS) deposition for coating probes in graphene in an attempt to overcome these issues, with the intention of creating an improved top contact for junctions and potentially real-life applications.

### **6.1.2 Coating via Langmuir-Schaefer**

Based on the results seen previously with CVD and other experimental methods, for this research, LS deposition was utilised for coating conductive Budget Sensors Multi75E-G Pt probes and non-conductive NuNano Scout 70 probes with graphene; both for use in AFM measurements. For this purpose, cleaning was carried out as highlighted in Chapter 5.1. 200  $\mu\text{L}$  of 0.1 mg/mL graphene in Dimethylformamide solution was then dispersed over the trough (each drop  $\sim$ 5-10  $\mu\text{L}$ ) and 20 minutes allowed for solvent evaporation. After this, the closing rate of the barriers was set to 7.5 mm/min,<sup>[17]</sup> and an isotherm was performed to find the target surface pressure (see Figure 6.1). The process was then carried out a second time, but the target was set to a surface pressure within the 'solid' region of the isotherm.

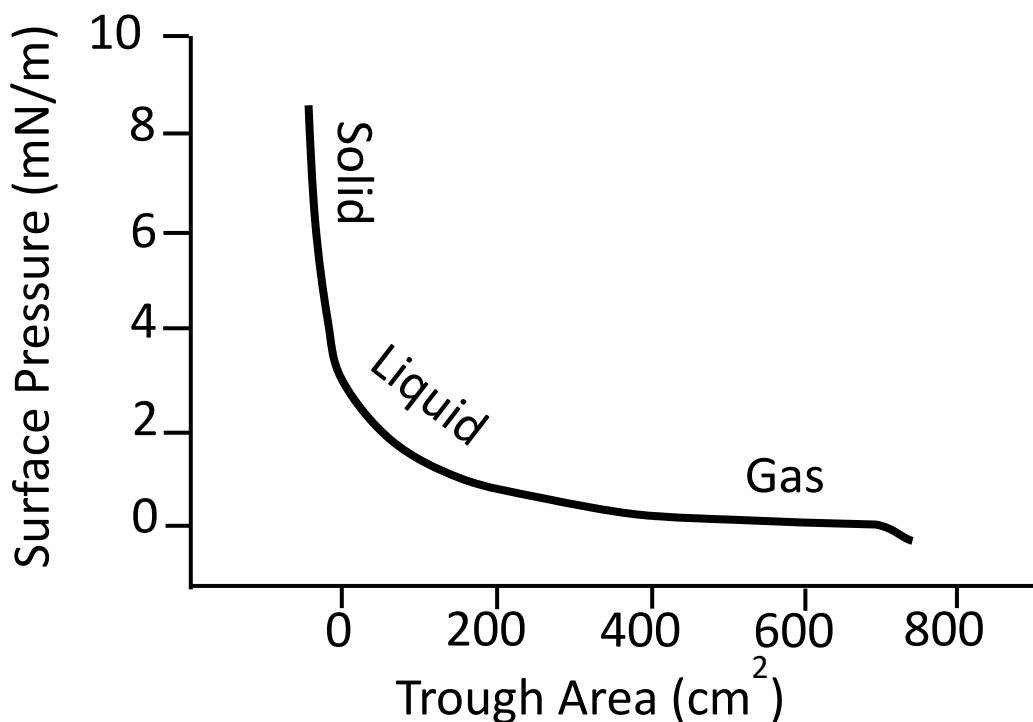


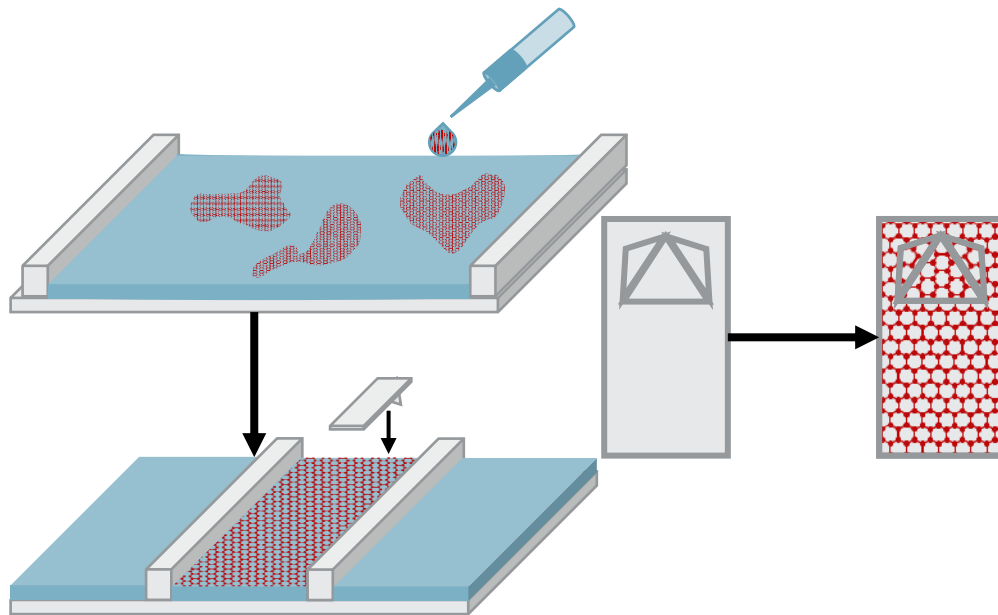
Figure 6.1 The isotherm for compressing a monolayer of graphene.<sup>[17]</sup> The region of best alignment, in the 'solid' phase, is from approximately 4 mN/m to 8 mN/m.

The low surface pressure region, from 750 cm<sup>2</sup> to 200 cm<sup>2</sup> trough area, is the 'gaseous' state for the graphene, where flakes are dispersed evenly on the surface and are not exerting much force on one another. Between here and 0 cm<sup>2</sup> the monolayer passes into the liquid phase, where the flakes begin to join together for some longer-range order regions. Beyond this, the monolayer is packed into the solid phase, in the honeycomb structure typical of graphene sheets. It is in this region that the LS deposition was carried out.

Unlike the polar molecules usually used for LB depositions, graphene does not form monolayers with a hydrophilic head in the subphase and hydrophobic tails neatly aligned in the air above the subphase surface; the flakes remain planar to the water surface.

The previously mentioned probes were attached to a silicon wafer using carbon tape, before being manually stamped into the graphene monolayer (Figure 6.2). The probes were softly blown with compressed air before being placed in a vacuum oven overnight at around 80 °C and 10<sup>-2</sup> mBar.





*Figure 6.2 Graphene coating of probes via LS deposition. Initially, graphene is spread atop water to create a monolayer. Barriers are compressed to cause the graphene flakes to pack together. An AFM probe is 'stamped' onto the monolayer, and graphene transfers from the water onto the probe.*

Figure 6.3 shows an SEM image of the probes coated in graphene. As can be seen from the image, the graphene coating adheres well to the probe and slightly increases the tip apex. This may be due to a particularly large flake of graphene depositing onto the probe.

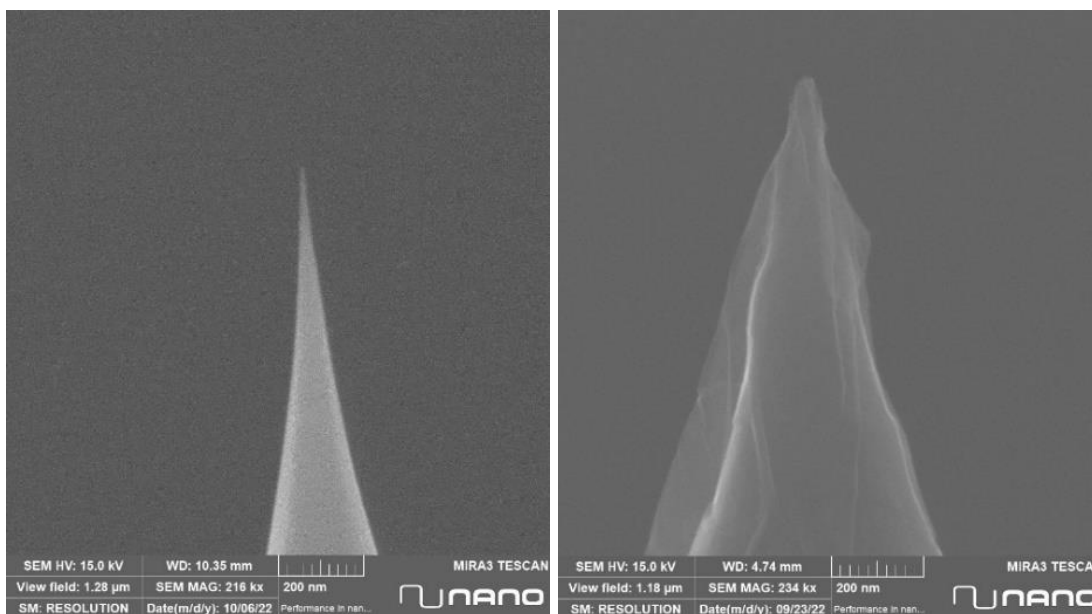


Figure 6.3 SEM images of a standard probe (left) and graphene-coated probe (right). Industry partner NuNano Ltd performed SEM imaging. It is suspected that the graphene coating may be a multilayer due to its thickness. The scale bar is 200nm.

### 6.1.3 Wear Tests

#### 6.1.3.1 Phase 1

To test how the graphene coating reacted to repeated friction experiments, non-conductive AFM probes from NuNano Ltd. were coated via LS (as in Chapter 6.1.2) and subsequently subjected to extensive wear testing. The same conditions were also applied to non-graphene-coated probes to compare the impact of the coating against a control group. The first set of testing was carried out in Nanoscope modes Scan Assyst (tapping), and Contact Mode with deflection setpoints of 0.2 V, 1 V, 5 V and 10 V. The second set of tests used Scan Assyst only.

For the initial tests, 1,700 scans were executed, with images collected at each stage. The Nanoscope settings used in each mode are given in Table 6.1.

Table 6.1 Nanoscope settings for probe wear testing. The same settings were used for both coated and uncoated probes, with both also subjected to a total of 1,700 scans. \*Each was selected for one set of tests.

	Scan Assyst Mode	Contact Mode
<b>Scan Size</b>	10 $\mu\text{m}$	10 $\mu\text{m}$
<b>Scan Rate</b>	10 Hz	10 Hz
<b>Samples/ Line</b>	64	64
<b>Feedback Gain</b>	100	100
<b>LP Deflection BW</b>	40 kHz	20 kHz
<b>Peak Force Amplitude</b>	20 nm	-
<b>Peak Force Frequency</b>	2 kHz	-
<b>Lift Height</b>	10.3 nm	-
<b>Peak Force Setpoint</b>	67.89 nN	-
<b>Deflection Limit</b>	25 V	-
<b>Noise Threshold</b>	0.5 nm	-
<b>Proportional Gain</b>	-	20
<b>Deflection Setpoint</b>	-	0.2/1/5/10 V*

Once wear tests had been carried out, the used probes were transported to the industry partner NuNano Ltd., who carried out SEM imaging on each probe.

The following tables summarise the results gained from the first set of wear tests. See Table 6.2 for discussion of the results.

Table 6.2 Summary of tests carried out in the initial phase of wear testing. References are given to the following results tables, with commentary given.

Table reference	Test depicted	Observations
Table 6.3	Scan Assyst Mode (IsoLab)	The quality of the image acquired with the non-graphene-coated probe degraded with time, as more scans are executed. However, when using the graphene-coated probe it is evident that the degradation was minimised, if not negated. From the SEM images, it is also clear that the tip was worn down more when uncoated. Though the tip radius, or apex, appears to have been increased by enveloping it in graphene, per the SEM image, it does look to have protected the tip and resulted in a smaller tip apex compared to the non-coated probe after being worn down.
Table 6.4	Contact mode; deflection setpoint of 0.2 V	There is little difference between graphene-coated and non-coated probes when it comes to the low deflection setpoint contact mode scanning. This is unsurprising, given that there is also little difference between the image obtained first and last with the uncoated probe. The SEM images support this further, showing little difference in tip apex between the two probes and neither shows obvious signs of wear, though the graphene-coated probe appears to have collected less contamination.
Table 6.5	Contact mode; deflection setpoint of 1 V	This table shows little difference in the images obtained with the graphene-coated probe, however, there is perhaps a slight degradation in image resolution with the uncoated probe. The tip apex does not appear to have been affected.
Table 6.6	Contact mode; deflection setpoint of 5 V	As with the previous experiments carried out in contact mode, this table demonstrates that increasing the deflection setpoint to 5 V made little difference to the images obtained via AFM. However, using the higher deflection setpoint appears to have caused the uncoated probe to distort, either due to picking up other particles from the surface of the calibration grid or due to being worn away. This seems to have occurred slightly with the coated probe too, though to a much lesser extent.
Table 6.7	Contact mode; deflection setpoint of 10 V	Similarly, to the images obtained at a setpoint of 5 V, those acquired at 10 V show little change in the actual images, however, the tip appears to have gathered particles from the sample surface. This looks to be worse for the uncoated probe than for the coated probe.
Table 6.8	Scan Assyst Mode (A54)	For these results, an AFM setup from a different lab was employed. All of the settings utilised were the same, and the equipment was of the same specifications. The difference between the two setups lies in the room in which they are housed; with IsoLab being a far more isolated environment and therefore likely to yield more accurate measurements. Resultantly, the wear in the AFM images in this table was not as clear as in the first. Furthermore, the SEM images obtained for these probes show more material was picked up by both probes, particularly the graphene-coated probe.

Table 6.3 AFM and SEM images of wear testing of graphene-coated and uncoated AFM probes, carried out in Scan Assyst mode in IsoLab. SEM images from NuNano Ltd. NG = non-graphene-coated. G= graphene-coated. The scale for each image is from 0-1µm; the size of the AFM scans is 10 µm. The scale of the SEM images is 200nm.







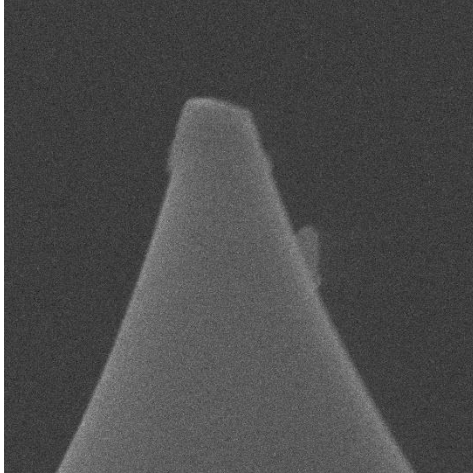

NG – spring constant = 2.6 N/m		G – spring constant = 3.1 N/m
	Scan 1	
	Scan 850	
	Scan 1700	
 SEM HV: 15.0 kV    WD: 4.83 mm    MIRA3 TESCAN View field: 1.46 µm    SEM MAG: 190 kx    200 nm SM: RESOLUTION    Date(m/d/y): 10/06/22    Performance in nan...	SEM image	 SEM HV: 15.0 kV    WD: 4.97 mm    MIRA3 TESCAN View field: 1.37 µm    SEM MAG: 202 kx    200 nm SM: RESOLUTION    Date(m/d/y): 09/23/22    Performance in nan...
Estimated tip apex: 90 nm		Estimated tip apex: 50 nm

Table 6.4 AFM and SEM images of wear testing of graphene-coated and uncoated AFM probes, carried out in contact mode with a deflection setpoint of 0.2V. SEM images from NuNano Ltd. NG = non-graphene-coated. G= graphene-coated. The scale for each image is from 0-1µm; the size of the AFM scans is 10 µm. The scale of the SEM images is 200nm.







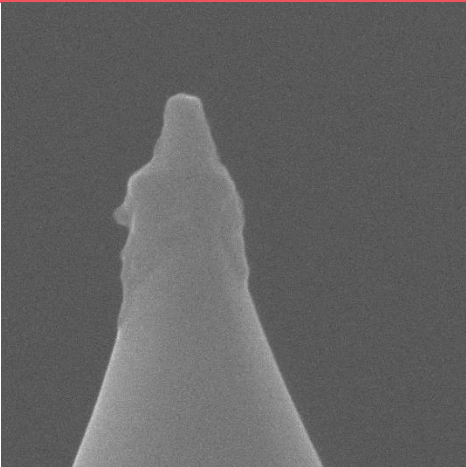
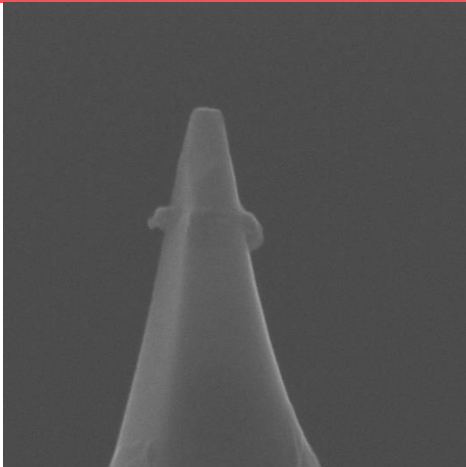
NG – spring constant = 1.7 N/m	Scan 1	G – spring constant = 3.4 N/m	
		Scan 850	
			
	Scan 1700		
 <p data-bbox="311 1865 778 1921">SEM HV: 15.0 kV    WD: 10.08 mm    MIRA3 TESCAN View field: 1.25 µm    SEM MAG: 221 kx    200 nm SM: RESOLUTION    Date(m/d/y): 10/06/22    Performance in nan...</p>		SEM image	 <p data-bbox="960 1865 1428 1921">SEM HV: 15.0 kV    WD: 4.91 mm    MIRA3 TESCAN View field: 1.04 µm    SEM MAG: 267 kx    200 nm SM: RESOLUTION    Date(m/d/y): 09/23/22    Performance in nan...</p>
<p data-bbox="368 1921 715 1966">Estimated tip apex: 45 nm</p>	<p data-bbox="1018 1921 1364 1966">Estimated tip apex: 40 nm</p>		

Table 6.5 AFM and SEM images of wear testing of graphene-coated and uncoated AFM probes, carried out in contact mode with a deflection setpoint of 1V. SEM images from NuNano Ltd. NG = non-graphene-coated. G= graphene-coated. The scale for each image is from 0-1µm. The size of the scans is 10 µm. . The scale of the SEM images is 200nm.







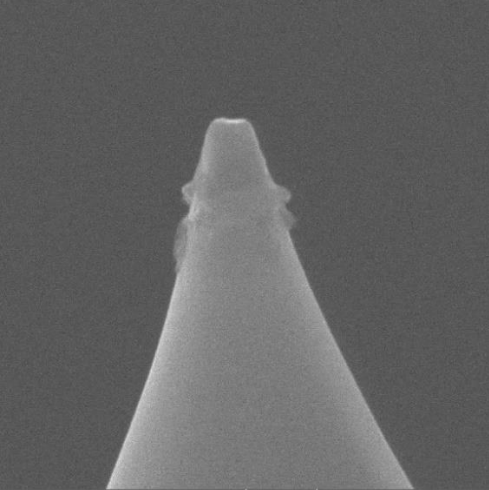

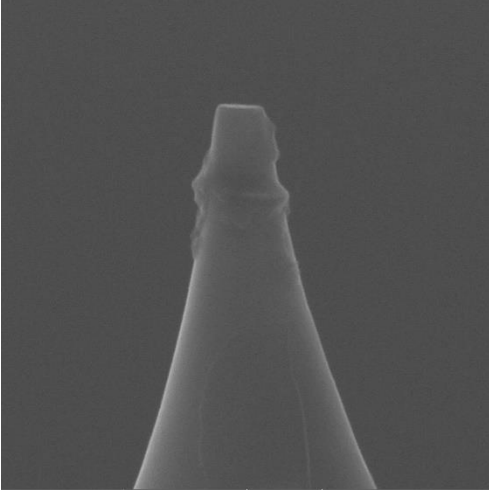

NG – spring constant = 1.9 N/m		G – spring constant = 3.4 N/m
	Scan 1	
	Scan 850	
	Scan 1700	
 SEM HV: 15.0 kV    WD: 10.07 mm    MIRA3 TESCAN View field: 1.38 µm    SEM MAG: 201 kx    200 nm SM: RESOLUTION    Date(m/d/y): 10/08/22    Performance in nan... 	SEM Image	 SEM HV: 15.0 kV    WD: 4.87 mm    MIRA3 TESCAN View field: 1.31 µm    SEM MAG: 212 kx    200 nm SM: RESOLUTION    Date(m/d/y): 09/23/22    Performance in nan... 
Estimated tip apex: 70 nm		Estimated tip apex: 80 nm

Table 6.6 AFM and SEM images of wear testing of graphene-coated and uncoated AFM probes, carried out in contact mode with a deflection setpoint of 5V. SEM images from NuNano Ltd. NG = non-graphene-coated. G= graphene-coated. The scale for each image is from 0-1µm. The size of the scans is 10 µm. . The scale of the SEM images is 200nm.







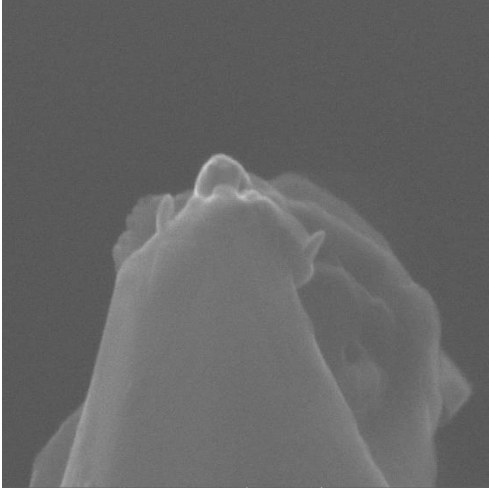
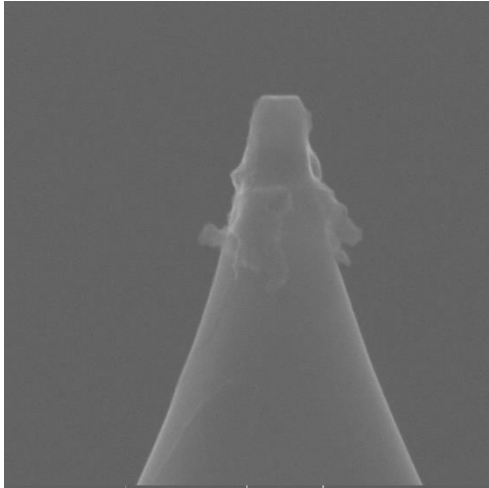
NG – spring constant =2.1 N/m		G – spring constant = 3.8 N/m
	Scan 1	
	Scan 850	
	Scan 1700	
 SEM HV: 15.0 kV    WD: 10.04 mm    MIRA3 TESCAN View field: 1.31 µm    SEM MAG: 212 kx    200 nm SM: RESOLUTION    Date(m/d/y): 10/08/22    Performance in nan... <b>NUNANO</b>	SEM Image	 SEM HV: 15.0 kV    WD: 4.92 mm    MIRA3 TESCAN View field: 1.27 µm    SEM MAG: 217 kx    200 nm SM: RESOLUTION    Date(m/d/y): 09/23/22    Performance in nan... <b>NUNANO</b>
Estimated tip apex: 100 nm		Estimated tip apex: 70 nm



Table 6.7 AFM and SEM images of wear testing of graphene-coated and uncoated AFM probes, carried out in contact mode with a deflection setpoint of 10V. SEM images from NuNano Ltd. NG = non-graphene-coated. G= graphene-coated. The scale for each image is from 0-1 $\mu$ m. The size of the scans is 10  $\mu$ m. . The scale of the SEM images is 200nm.







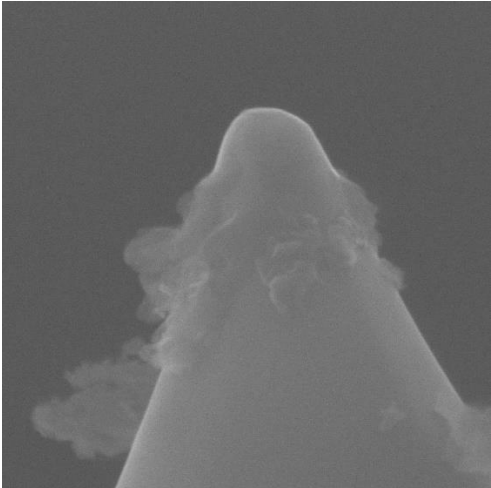
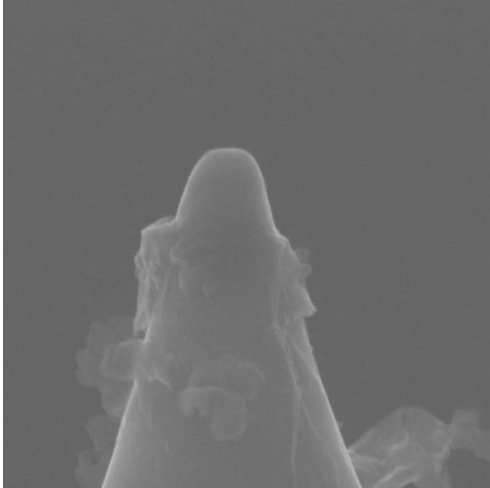






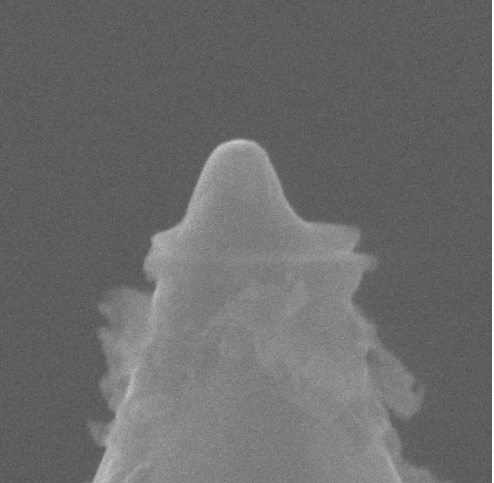
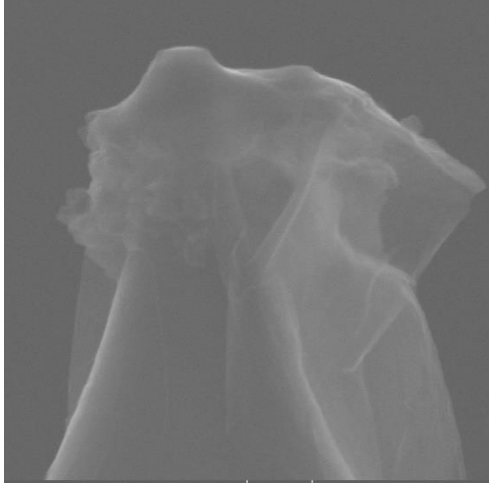
NG – spring constant =2.6 N/m		G – spring constant = 3.8 N/m
	Scan 1	
	Scan 850	
	Scan 1700	
 SEM HV: 15.0 kV    WD: 10.39 mm    MIRA3 TESCAN View field: 1.31 $\mu$ m    SEM MAG: 211 kx    200 nm SM: RESOLUTION    Date(m/d/y): 10/06/22    Performance in nan...	SEM Image	 SEM HV: 15.0 kV    WD: 5.19 mm    MIRA3 TESCAN View field: 1.27 $\mu$ m    SEM MAG: 219 kx    200 nm SM: RESOLUTION    Date(m/d/y): 09/23/22    Performance in nan...
Estimated tip apex: 120 nm		Estimated tip apex: 100 nm

Table 6.8 AFM and SEM images of wear testing of graphene-coated and uncoated AFM probes, carried out in Scan Assyst mode on the AFM in A54. SEM images from NuNano Ltd. NG = non-graphene-coated. G= graphene-coated. The scale for each image is from 0-1µm. The size of the scans is 10 µm. . The scale of the SEM images is 200nm.

NG – spring constant =1.4 N/m		G – spring constant = 2.7 N/m
	Scan 1	
	Scan 850	
	Scan 1700	
 <p data-bbox="264 1892 759 1951"> <small>SEM HV: 15.0 kV    WD: 10.43 mm    MIRA3 TESCAN</small>  <small>View field: 1.20 µm    SEM MAG: 231 kx    200 nm</small>  <small>SM: RESOLUTION    Date(m/d/y): 10/08/22    Performance in nan...</small> </p>	SEM Image	 <p data-bbox="914 1892 1409 1951"> <small>SEM HV: 15.0 kV    WD: 4.91 mm    MIRA3 TESCAN</small>  <small>View field: 1.43 µm    SEM MAG: 187 kx    200 nm</small>  <small>SM: RESOLUTION    Date(m/d/y): 09/23/22    Performance in nan...</small> </p>
Estimated tip apex: 100 nm		Estimated tip apex: undetermined

The overall trend of these wear tests appears to show that a greater deflection setpoint results in greater degradation of the probe tip. This is particularly evident when looking at the uncoated probes. There appears to be something depositing onto the probes in the scans with a greater deflection setpoint, particularly in the case of the uncoated probes; further testing is required to identify exactly what is happening.

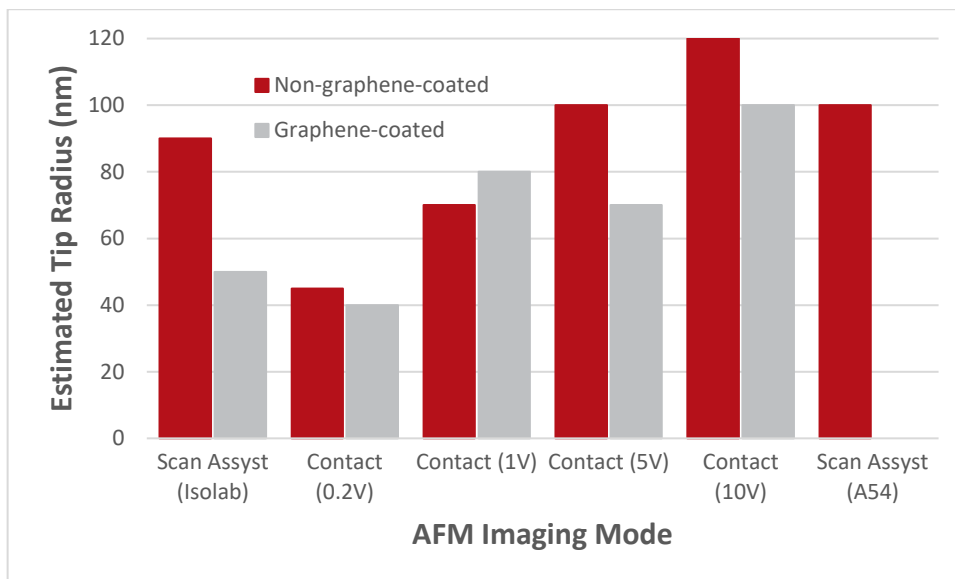


Figure 6.4 Comparison of tip apexes for graphene-coated and non-graphene-coated AFM probes after having been subjected to wear tests. Measured via SEM by industry partner NuNano Ltd; errors for the measurements are unknown.

As can be seen from Figure 6.4, the tip apexes of graphene-coated probes are typically smaller than those of the non-graphene-coated counterparts when the probe tips have been extensively used.

### 6.1.3.2 Phase 2

After the first tests had been carried out, further investigation was completed for which SEM images of the probe tips were gathered before coating, after coating, and after testing. Again, the same conditions were applied to both graphene-coated and uncoated probes for comparison. This time, far fewer scans were completed by each probe, always in Scan Assyst (tapping) mode. See Table 6.9 for the settings used.

Table 6.9 Settings used in Scan Assyst on AFM for the second set of probe wear tests. The parameters applied to both graphene-coated and uncoated probes.

Scan Assyst Settings		
Scan Size	5	μm
Scan Rate	0.5	Hz
Samples/ Line	256	
Lines	256	
Feedback Gain	100	
Noise Threshold	0.5	nm
Peak Force Amplitude	20	nm
Peak Force Frequency	2	kHz
Lift Height	40	nm
Peak Force Setpoint	14.34	nN
Deflection Limit	24.58	V
LP Deflection BW	40	kHz
Z Limit	5.27	μm

Details of how many scans were carried out for each probe, and their spring constants are given in Table 6.10.

Table 6.10 Details regarding the number of scans carried out per probe for the second phase of wear testing on AFM. NB: probe 8 was damaged for the graphene-coated probes, hence there is no spring constant data available.

Probe	No. Scan	Spring constant	
		Graphene-coated (N/m; ±10%)	Uncoated (N/m; ±10%)
1	1	3.5723	1.347
2	5	1.4178	1.4676
3	10	1.4009	1.2631
4	1	1.2927	1.5456
5	5	1.6483	1.5257
6	10	1.2291	1.4769
7	1	1.3429	1.3677
8	5	-	1.1831
9	5	1.3745	1.3505
10	10	1.2919	1.1857

Industry partner NuNano Ltd provided the probes for these tests and also carried out the SEM imaging.

From the before and after coating images (to Table 6.19) it is evident that a thicker layer of graphene was applied to the probes this time than previously. This has the negative impact of expanding the tip apex, therefore making the probes less appropriate for highly detailed work.

It is noted that measurements were not acquired for Probe 8 due to the cantilever getting broken during the graphene coating process. Nine coated and nine uncoated probes were tested in total: three pairs underwent one scan, three pairs five scans and three pairs ten scans. The graphene-coated Probe 9 lost its cantilever during or after testing and as such final images are not given for it. All estimated tip apexes are given in nm.

Table 6.11 Results for “Probe 1”, subjected to one full scan on AFM in ScanAsyst mode. The top row depicts the uncoated probe whilst the bottom shows the graphene-coated probe. Tip apex measurement has been carried out in the SEM software. Each image is 700nm viewfield. SEM imaging was carried out by industry partner NuNano Ltd.

0° 	90° 			0° 	90° 
Estimated tip apex: 6 nm	Estimated tip apex: 10 nm			Estimated tip apex: 60 nm	Estimated tip apex: 63 nm
<b>Initial SEM image</b>		<b>SEM image post-coating</b>		<b>Final SEM image</b>	
0° 	90° 	0° 	90° 	0° 	90° 
Estimated tip apex: 4.5 nm	Estimated tip apex: 4.8 nm	Estimated tip apex: 15.5 nm	Estimated tip apex: 11 nm	Estimated tip apex: 19.1 nm	Estimated tip apex: 21.4 nm

Table 6.12 Results for "Probe 2", subjected to five full scans on AFM in ScanAsyst mode. The top row depicts the uncoated probe whilst the bottom shows the graphene-coated probe. Tip apex measurement has been carried out in the SEM software. Each image is 700nm viewfield. SEM imaging was carried out by industry partner NuNano Ltd.

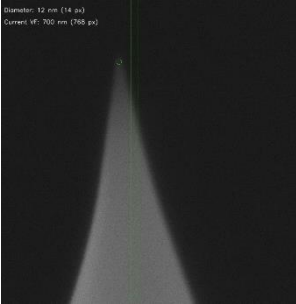
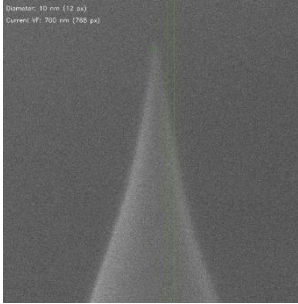

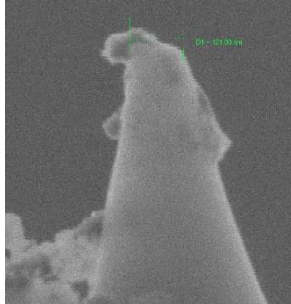
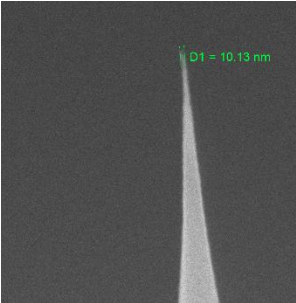
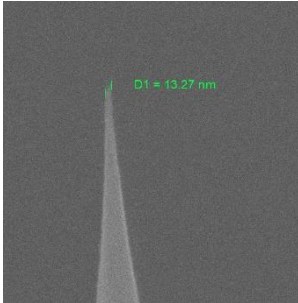
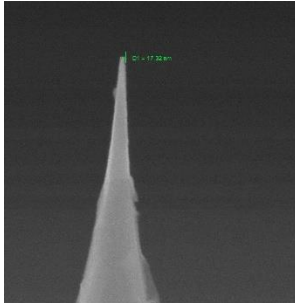
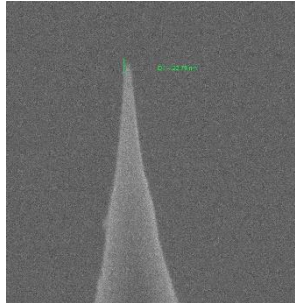
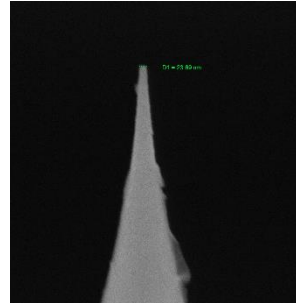
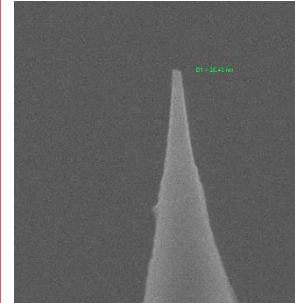
0° 	90° 		0° 	90° 	
Estimated tip apex: 6 nm	Estimated tip apex: 5 nm		Estimated tip apex: 73 nm	Estimated tip apex: 61 nm	
<b>Initial SEM image</b>		<b>SEM image post-coating</b>		<b>Final SEM image</b>	
0° 	90° 	0° 	90° 	0° 	90° 
Estimated tip apex: 5.1 nm	Estimated tip apex: 6.6 nm	Estimated tip apex: 8.6 nm	Estimated tip apex: 11.4 nm	Estimated tip apex: 11.8 nm	Estimated tip apex: 13.2 nm

Table 6.13 Results for “Probe 3”, subjected to ten full scans on AFM in ScanAsyst mode. The top row depicts the uncoated probe whilst the bottom shows the graphene-coated probe. Tip apex measurement has been carried out in the SEM software. Each image is 700nm viewfield. SEM imaging was carried out by industry partner NuNano Ltd.

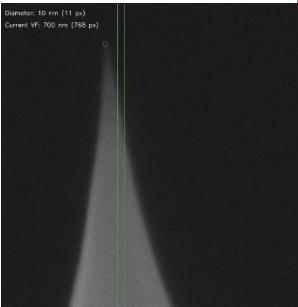


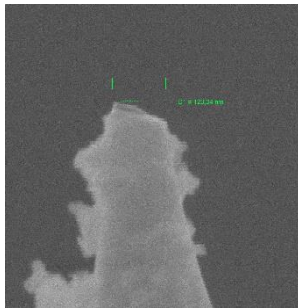
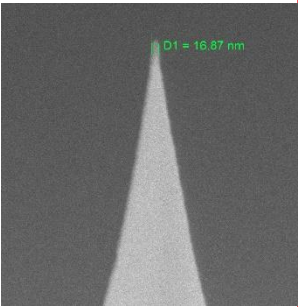
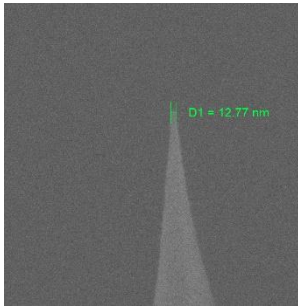
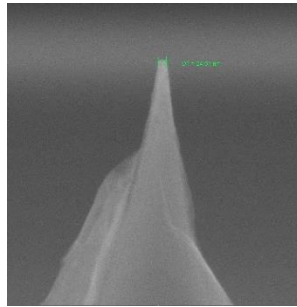
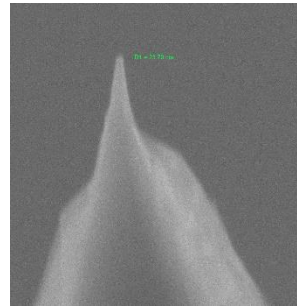
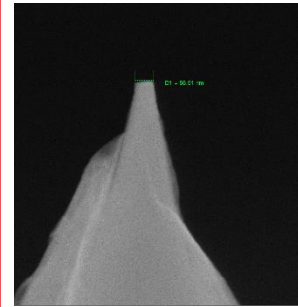
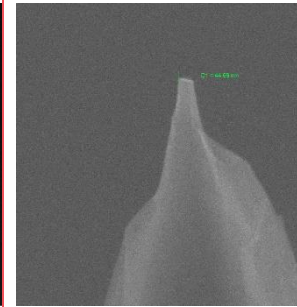
0° 	90° 			0° 	90° 
Estimated tip apex: 5 nm	Estimated tip apex: 6 nm			Estimated tip apex: 71 nm	Estimated tip apex: 61 nm
<b>Initial SEM image</b>		<b>SEM image post-coating</b>		<b>Final SEM image</b>	
0° 	90° 	0° 	90° 	0° 	90° 
Estimated tip apex: 8.4 nm	Estimated tip apex: 6.4 nm	Estimated tip apex: 12.3 nm	Estimated tip apex: 11.9 nm	Estimated tip apex: 28.3 nm	Estimated tip apex: 22.3 nm



Table 6.14 Results for “Probe 4”, subjected to one full scan on AFM in ScanAsyst mode. The top row depicts the uncoated probe whilst the bottom shows the graphene-coated probe. Tip apex measurement has been carried out in the SEM software. Each image is 700nm viewfield. SEM imaging was carried out by industry partner NuNano Ltd.

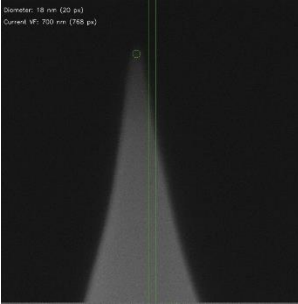
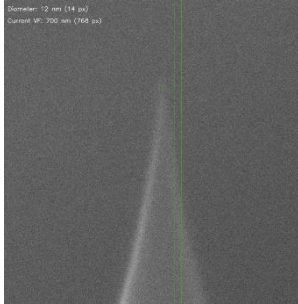
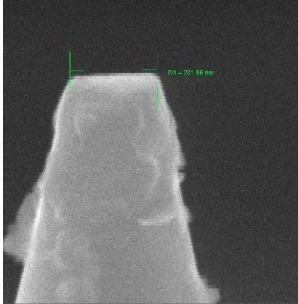
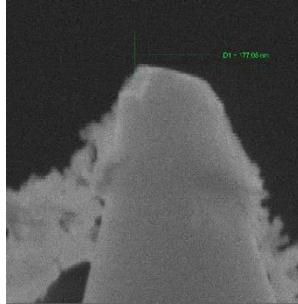
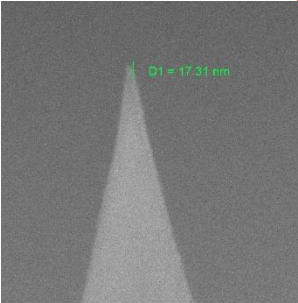
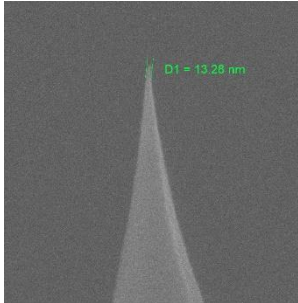
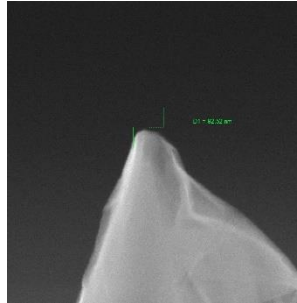
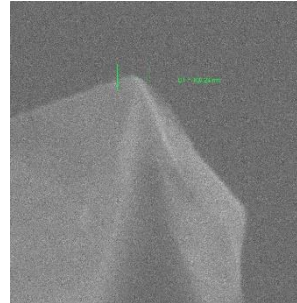
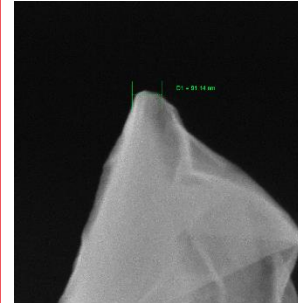
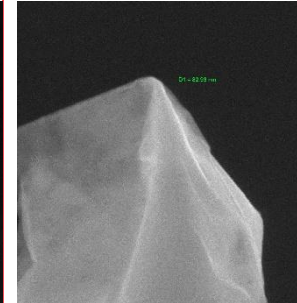
0° 	90° 		0° 	90° 	
Estimated tip apex: 9 nm	Estimated tip apex: 6 nm		Estimated tip apex: 101 nm	Estimated tip apex: 89 nm	
<b>Initial SEM image</b>		<b>SEM image post-coating</b>		<b>Final SEM image</b>	
0° 	90° 	0° 	90° 	0° 	90° 
Estimated tip apex: 8.7 nm	Estimated tip apex: 6.6 nm	Estimated tip v: 46.3 nm	Estimated tip apex: 50.1 nm	Estimated tip apex: 45.6 nm	Estimated tip apex: 41.5 nm

Table 6.15 Results for “Probe 5”, subjected to five full scans on AFM in ScanAsyst mode. The top row depicts the uncoated probe whilst the bottom shows the graphene-coated probe. Tip apex measurement has been carried out in the SEM software. Each image is 700nm viewfield. SEM imaging was carried out by industry partner NuNano Ltd.

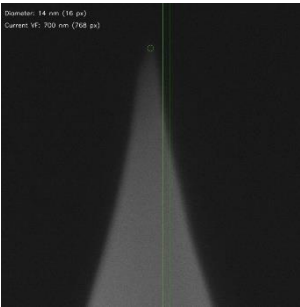
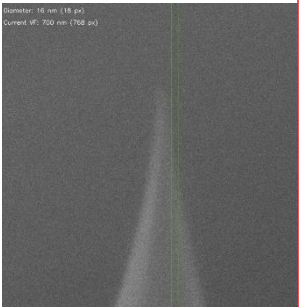

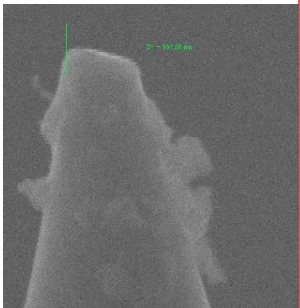
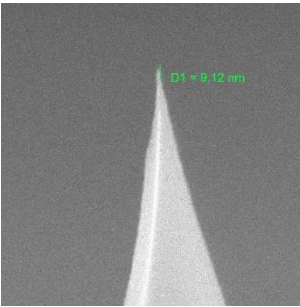
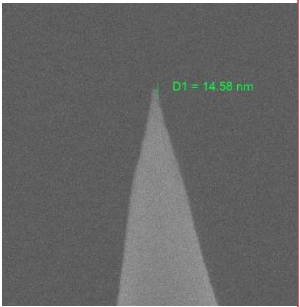
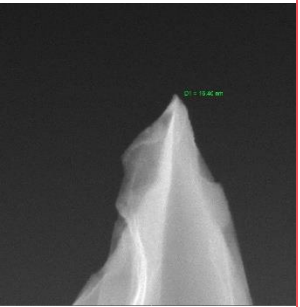

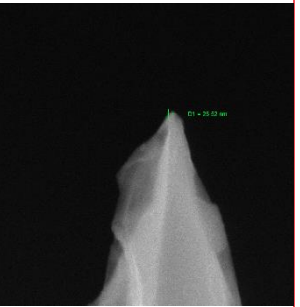
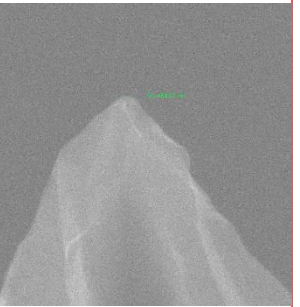
0°  Diameter: 14 nm (16 ps) Current: 700 nA (768 ps)	90°  Diameter: 16 nm (18 ps) Current: 700 nA (768 ps)			0°  D1 = 108.50 nm	90°  D1 = 105.00 nm
Estimated tip apex: 7 nm	Estimated tip apex: 8 nm			Estimated tip apex: 99 nm	Estimated tip apex: 82 nm
<b>Initial SEM image</b>		<b>SEM image post-coating</b>		<b>Final SEM image</b>	
0°  D1 = 9.12 nm	90°  D1 = 14.98 nm	0°  D1 = 19.46 nm	90°  D1 = 11.94 nm	0°  D1 = 12.8 nm	90°  D1 = 44.6 nm
Estimated tip apex: 4.5 nm	Estimated tip apex: 7.3 nm	Estimated tip apex: 8.2 nm	Estimated tip apex: 25.5 nm	Estimated tip apex: 12.8 nm	Estimated tip apex: 44.6 nm

Table 6.16 Results for “Probe 6”, subjected to ten full scans on AFM in ScanAsyst mode. The top row depicts the uncoated probe whilst the bottom shows the graphene-coated probe. Tip apex measurement has been carried out in the SEM software. Each image is 700nm viewfield. SEM imaging was carried out by industry partner NuNano Ltd.

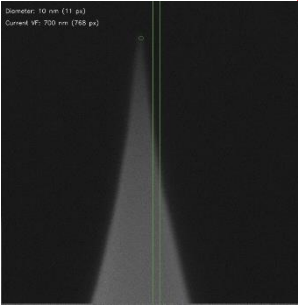
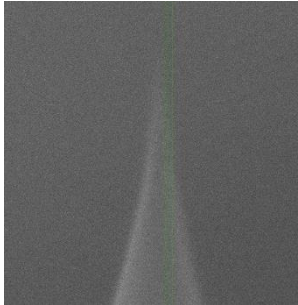

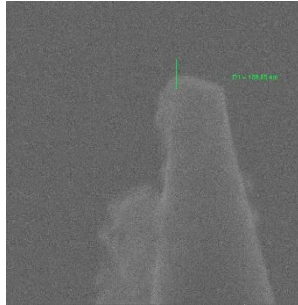
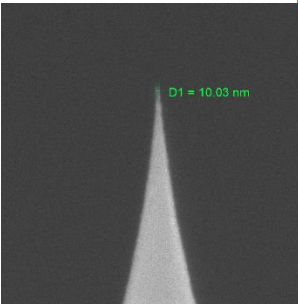
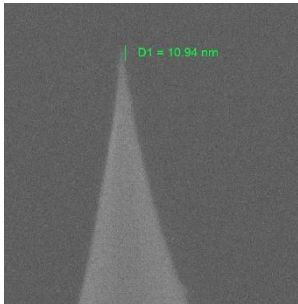
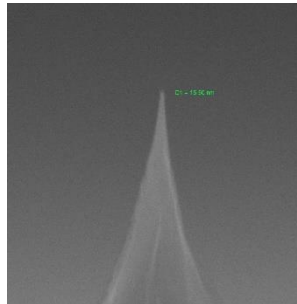
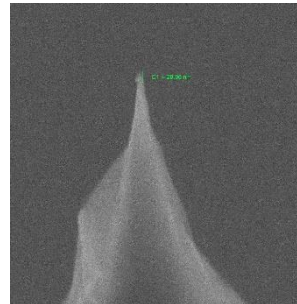
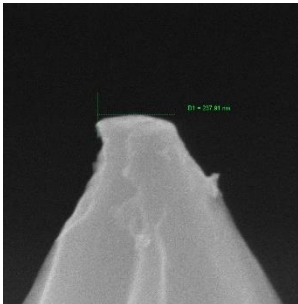
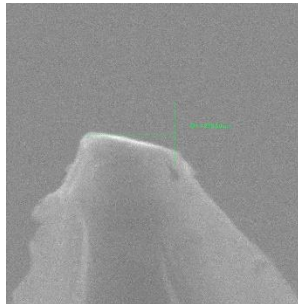
0° 	90° 			0° 	90° 
Estimated tip apex: 5 nm	Estimated tip apex: 5 nm			Estimated tip apex: 53 nm	Estimated tip apex: 54 nm
<b>Initial SEM image</b>		<b>SEM image post-coating</b>		<b>Final SEM image</b>	
0° 	90° 	0° 	90° 	0° 	90° 
Estimated tip apex: 5 nm	Estimated tip apex: 5.5 nm	Estimated tip apex: 7.8	Estimated tip apex: 10.5 nm	Estimated tip apex: 119 nm	Estimated tip apex: 137.6 nm

Table 6.17 Results for “Probe 7”, subjected to one full scan on AFM in ScanAsyst mode. The top row depicts the uncoated probe whilst the bottom shows the graphene-coated probe. Tip apex measurement has been carried out in the SEM software. Each image is 700nm viewfield. SEM imaging was carried out by industry partner NuNano Ltd.

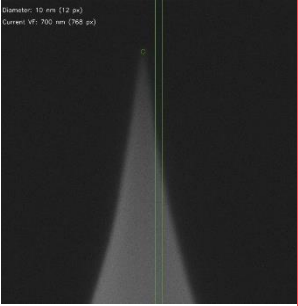
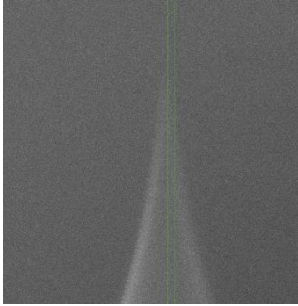
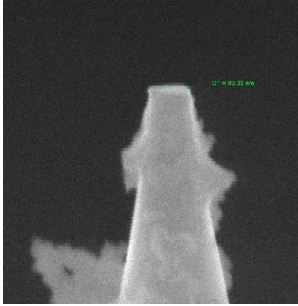
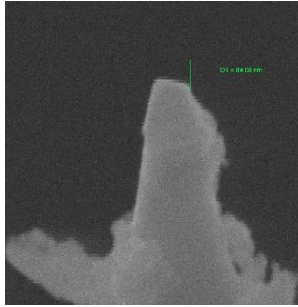
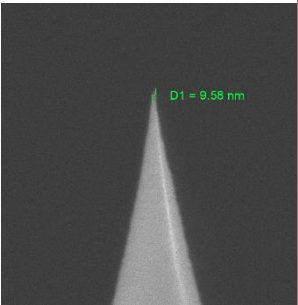
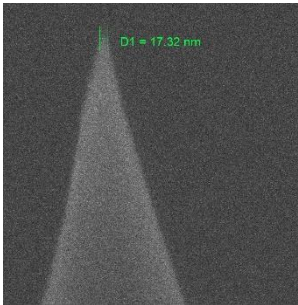

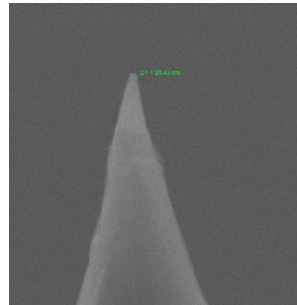

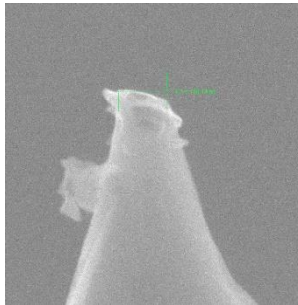
0° 	90° 			0° 	90° 
Estimated tip apex: 5 nm	Estimated tip apex: 5 nm			Estimated tip apex: 47 nm	Estimated tip apex: 42 nm
<b>Initial SEM image</b>		<b>SEM image post-coating</b>		<b>Final SEM image</b>	
0° 	90° 	0° 	90° 	0° 	90° 
Estimated tip apex: 4.8 nm	Estimated tip apex: 8.7 nm	Estimated tip apex: 6.8 nm	Estimated tip apex: 13.2 nm	Estimated tip apex: 62.4 nm	Estimated tip apex: 74.1 nm

Table 6.18 Results for "Probe 9", subjected to five full scans on AFM in ScanAsyst mode. The top row depicts the uncoated probe whilst the bottom shows the graphene-coated probe. Note that the cantilever was broken after testing for the graphene-coated probe, hence there are no images of it after it had been used. Tip apex measurement has been carried out in the SEM software. Each image is 700nm viewfield. SEM imaging was carried out by industry partner NuNano Ltd.

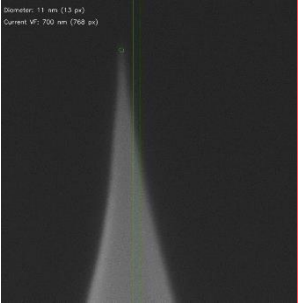
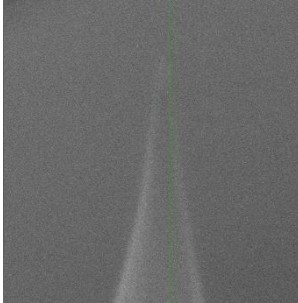
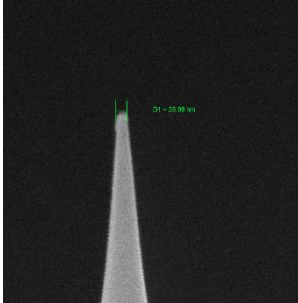
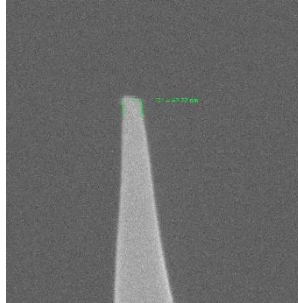
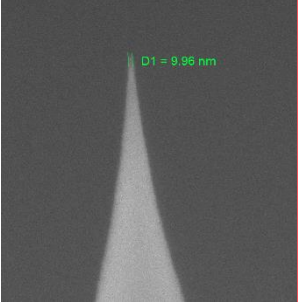
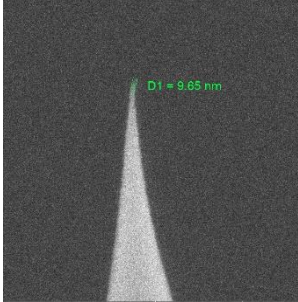

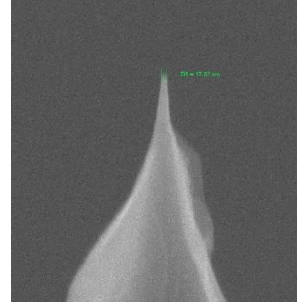
0° 	90° 			0° 	90° 
Estimated tip apex: 5 nm	Estimated tip apex: 7 nm			Estimated tip apex: 13 nm	Estimated tip apex: 24 nm
<b>Initial SEM image</b>		<b>SEM image post-coating</b>		<b>Final SEM image</b>	
0° 	90° 	0° 	90° 		
Estimated tip apex: 5 nm	Estimated tip apex: 4.8 nm	Estimated tip apex: 7.8 nm	Estimated tip apex: 8.7 nm		

Table 6.19 Results for "Probe 10", subjected to ten full scans on AFM in ScanAsyst mode. The top row depicts the uncoated probe whilst the bottom shows the graphene-coated probe. Tip apex measurement has been carried out in the SEM software. Each image is 700nm viewfield. SEM imaging was carried out by industry partner NuNano Ltd.

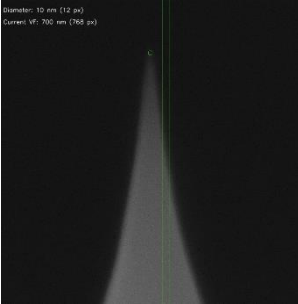
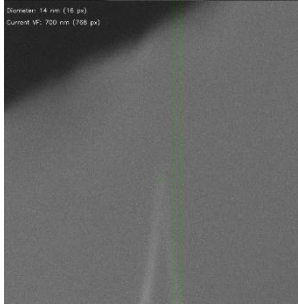

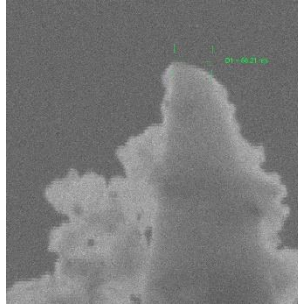
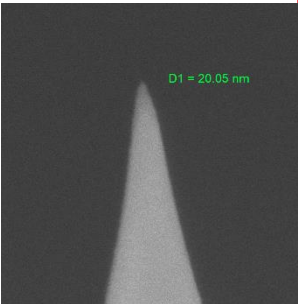

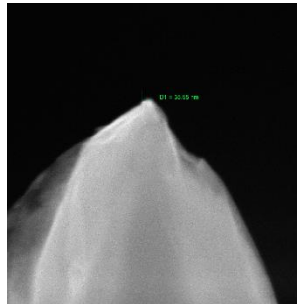
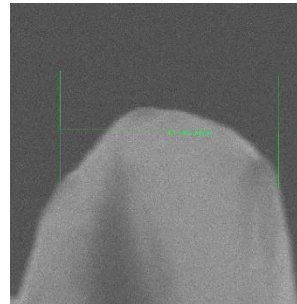
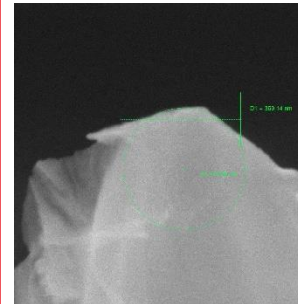
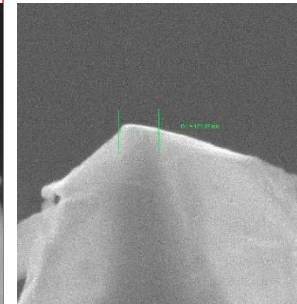
0° 	90° 			0° 	90° 
Estimated tip apex: 5 nm	Estimated tip apex: 5 nm			Estimated tip apex: 54 nm	Estimated tip apex: 44 nm
<b>Initial SEM image</b>		<b>SEM image post-coating</b>		<b>Final SEM image</b>	
0° 	90° 	0° 	90° 	0° 	90° 
Estimated tip apex: 10 nm	Estimated tip apex: 8.2 nm	Estimated tip apex: 17.8 nm	Estimated tip apex: 335.7 nm	Estimated tip apex: 184.6 nm	Estimated tip apex: 62 nm

Table 6.20 Summary of tip apex results for uncoated probes subjected to wear testing on AFM; the results given are as measured from SEM imaging performed by industry partner Nu Nano Ltd.

Probe	No. scans undertaken	Average tip radius before coating (nm)	Average tip radius after test scans (nm)	Difference between before and after testing (nm)
1	1	8±2	61.5±1.5	53.5
2	5	5.5±1	67±6	61.5
3	10	5.5±1	66±5	60.5
4	1	7.5±1.5	95±6	87.5
5	5	7.5±1	90.5±8.5	83
6	10	5±0	53.5±0.5	48.5
7	1	5±0	44.5±2.5	39.5
9	5	6±1	18.5±5.5	12.5
10	10	5±0	49±5	44
<b>Averages:</b>		6.1±2.9	60.6±42.1	54.5

As is evident from Table 6.11 to Table 6.19 and the summary of results in Table 6.20, there is a definite increase in tip apex after scanning has been carried out. This implies that the tips are wearing out as expected, with the greatest difference occurring with Probe 4, despite it only performing one full scan. There does not seem to be a trend for more scans meaning more wearing, however, this may be more obvious with a larger sample size.

Table 6.21 Summary of tip apex results for graphene-coated probes subjected to wear testing on AFM; the results given are as measured from SEM imaging performed by industry partner Nu Nano Ltd.

Probe	No. scans undertaken	Average tip apex before coating (nm)	Average tip apex after coating (nm)	Average tip apex after test scans (nm)	Difference caused by graphene coating	Difference caused by testing (nm)
1	1	4.7±0.15	13.3±2.3	20.3±1.1	8.6	7
2	5	5.9±0.7	10±1.4	12.5±0.7	4.1	2.5
3	10	7.4±1	12.1±0.2	25.3±3	4.7	13.2
4	1	7.7±1	48.2±1.9	43.6±2	40.5	-4.6
5	5	5.9±1.4	16.9±8.7	28.7±15.9	11	11.8
6	10	5.3±0.3	9.2±1.4	128.3±9.3	3.9	119.1
7	1	6.8±1.9	10±3.2	68.3±5.9	3.2	58.3
9	5	4.9±0.1	8.3±0.5	-	3.4	-
10	10	9.1±0.9	176.3±158.5	123.3±61.3	167.2	-53
<b>Averages:</b>		6.4±1.7	33.8±25.5	56.3±43.8	27.4	19.3

Looking again at Table 6.11 to Table 6.19, this time comparing with the summary for graphene-coated probes in Table 6.21, it is evident that the graphene coating significantly increased the tip apex for these tests. This is likely to be due to larger graphene flakes coating the probes, and perhaps forming multilayers rather than monolayers. There is scope for future work on fine tuning the dipping part of the LS

process in order to coat the probes more evenly. However, the average increase in tip apex observed after scanning is smaller than that seen in the uncoated probes. This implies that the graphene coating is indeed minimising the amount of wear undergone by the probes, though further testing is required to confirm this. Furthermore, it appears as with the first wear tests that the graphene-coated probes attract less contamination through use than the uncoated probes.

#### **6.1.4 Conclusions**

It was expressed in Chapter 2 that this research aimed to create an improved top contact for AFM junctions when investigating SAMs. The intention was to create a longer lasting probe without decreasing resolution, that provides a cheaper alternative to diamond probes. Graphene was suggested as a coating for existing probes to achieve this, however previous research has used CVD to deposit it.<sup>[146, 147, 149-154]</sup> Results were gathered using sharp non-conductive AFM probes from industry partner NuNano Ltd. These were subsequently coated with a monolayer of graphene via LS deposition. Initially, extensive wear tests were carried out on both coated and uncoated probes, with their SEM images taken after use. This work showed promise as there was evidence the graphene-coating may have been protecting the probes from wear as well as minimising detritus picked up by the probe that would lessen resolution of scans executed by them. A second set of probes were tested over less scans and only in ScanAssyst mode, this time with SEM images taken before and after graphene-coating, as well as after the wear tests had been performed. These results appeared to show that the coating was a multilayer of graphene rather than a monolayer, and as such the tip apexes of the probes were significantly increased. There did appear however, to be a reduction in the wear effects on the coated probes. Further work on this is suggested, with a larger sample size investigated.

This presents interesting practical potential, as improving the lifetime of these probes in this way provides evidence for LS-deposited graphene coatings could be used on a larger scale to improve the lifetimes of electrical components utilising thin film layers.

It was also expressed in the opening chapter of this thesis that this same method would be applied to conductive probes in an attempt to improve coupling between SAMs and their top contact. This is investigated further in the following results chapters.

Additional further work is suggested, not only for the non-conductive probes in a larger sample size and more automated LS coating, but also for wear testing of conductive probes. This could give conclusions on whether graphene-coating improves probe lifetime in electrical and contact AFM modes.



## 6.2 Conductive Probe Testing

### 6.2.1 BOC8 molecules

There has been extensive research done into molecular junctions (MJs),<sup>[41]</sup> with various methods for altering electron transport through them attempted.<sup>[155]</sup> In such junctions, gold is typically used as the top electrode, however, it has been suggested to use graphene instead.<sup>[156]</sup> In these cases, planar aromatic head groups for the molecule in the junction are ideal, due to the potential for  $\pi$ -interactions with the graphene. It has previously been observed that in MJs with graphene, increasing the number of aromatic rings also increases both binding energy<sup>[157]</sup> and cross-plane conductance.<sup>[158]</sup> It was proposed to attempt similar research but with planar aromatic head groups within Au|SAM|Pt and Au|SAM|graphene junctions.

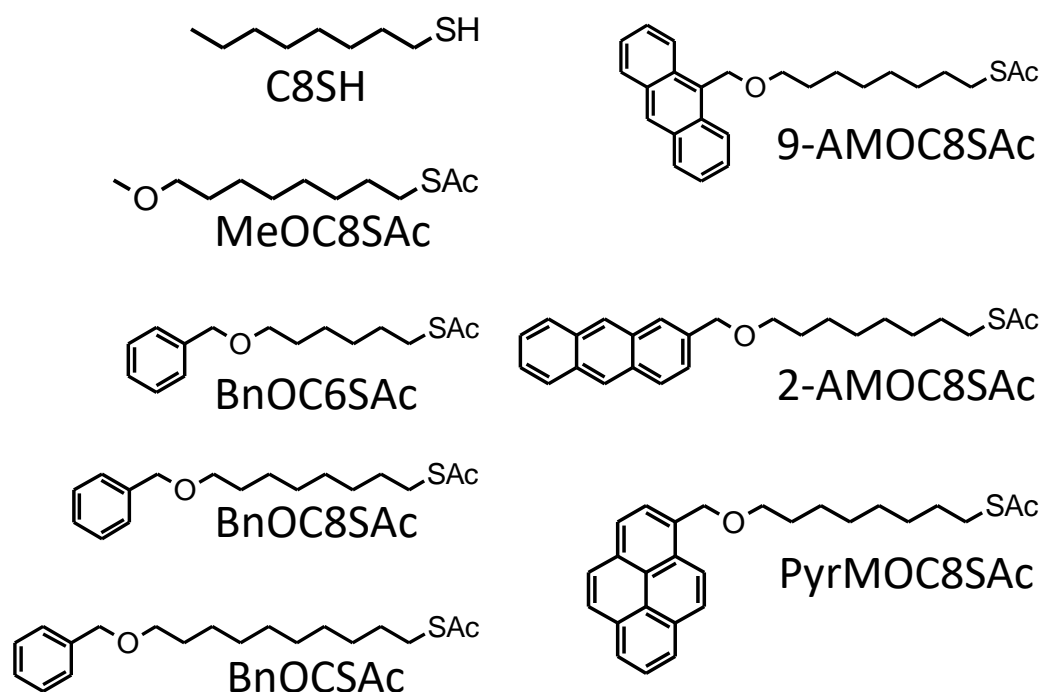


Figure 6.5 Molecules analysed with graphene probes. Each molecule (besides commercial octanethiol) consists of a linear alkyl chain with an ether functional group at one end, and an acetyl-protected group at the other. The naming convention is the nature of the ether-linked head, the length of the alkyl chain (CX) and the terminal functional group. E.G. BnOC8SAc for the octyl chain headed by a benzyl ether and tailed by thioacetate.

As such, research was carried out into a series of molecules with varying head groups (octane with no head, MeO, BnO, 9-AMo, 2-AMo, and PyrMO) and varying alkyl chain lengths (C6, C8 and C10) (Figure 6.5).<sup>[1]</sup> In each case, the backbone of the molecule was an alkyl chain, but with an ether at one end and an acetyl-protected thiol at the other. This was designed such that deprotection would occur during monolayer formation, allowing the thiol to arrange on the gold substrate and the alkyl/ aryl head would then be left to contact the AFM probe. Alkyl chains were chosen despite their typically low single-

molecule electrical conductance, due to their ease of chemical synthesis, likelihood to form ordered monolayers, and potential for flexibility enabling better probe contact. It was also concluded that low conductance is of less importance in this case due to such a multitude of molecules being contacted within the junction formed. The intention of the variation of designs in this series was to investigate how electrical conductance is influenced by how the aromatic anchor is presented, in terms of size and shape.

SAMs of each molecule were formed on template stripped gold substrates (per Chapter 5.4) using the methods outlined in Chapter 5.2 The method for QCM from Chapter 5.3 was used for monitoring assembly and determining molecular area, the nanoscratch method outlined in Chapter 5.5.1 was employed for gaining molecule height and cAFM measurements per Chapter 5.5.2 were used to determine the monolayers' electrical conductances. cAFM measurements were gathered using both standard Pt conductive probes and graphene-coated probes (per Chapter 6.1.2).

*Table 6.22 Conductance per molecule obtained for each molecule studied, gathered via statistical analysis of AFM data. The results are given for graphene-coated and uncoated probes. The errors for these data are unknown.*

<b>Molecule</b>	<b>Log(<math>G_{Pt}(S)</math>)</b>	<b>Log(<math>G_{Graphene}(S)</math>)</b>	<b><math>G_{Graphene}/G_{Pt}</math></b>
<b>C8S</b>	<b>-6.58</b>	<b>-6.31</b>	<b>1.86</b>
<b>MeOC8S</b>	<b>-7.81</b>	<b>-7.82</b>	<b>0.98</b>
<b>BnOC8S</b>	<b>-8.94</b>	<b>-8.62</b>	<b>2.09</b>
<b>9-AMOC8S</b>	<b>-8.89</b>	<b>-8.28</b>	<b>4.07</b>
<b>2-AMOC8S</b>	<b>-9.25</b>	<b>-9.13</b>	<b>1.32</b>
<b>PyrMOC8S</b>	<b>-10.29</b>	<b>-9.58</b>	<b>5.13</b>

It was concluded that as the size of the aromatic head increases, the electrical conductance decreases; seemingly contradicting previous research.<sup>[159]</sup> However, the aromatic heads in this work differ from the previous studies as they are coplanar to the electrode surface due to tilting with respect to the probe; the electrode pathway is therefore extended as the head group increases in size when it is done so lengthwise. In the case of 9-AMOC8S, the same pattern is not followed, as the head group increases in width rather than length, so the same conductance path extension is not observed.

A further observation from this series was that for the changing head groups, as the number,  $n$ , of aromatic rings increased, the ratio of conductance with the Pt probe compared to the graphene-coated probe ( $G_{graphene}/G_{Pt}$ ) approximately followed the trend  $n+1$ . This was taken to mean that larger head groups are better coupled to graphene probes than Pt probes, as anticipated. This was suspected to be a result of  $\pi$ - $\pi$  interactions between the aromatic head groups and the graphene probe coating; these

interactions are not present with the Pt probe contact. Moreover, it was suggested that the atomically flat nature of the graphene coating may enable more flexibility with relation to the SAM, compared with the sharper Pt probe.

C8S and 2-AMOC8S were outliers in this regard, both displaying smaller conductance with the graphene-coated probe than the uncoated probe. This may be explained for C8S as it being unable to form into a SAM as readily as the other molecules, resulting from the lack of ether link and shorter alkyl chain. In the case of 2-AMOC8S, the anthracene unit within the structure may be causing a large difference in molecule shape and thus monolayer packing compared to the other aromatic structures.

Furthermore, with the different alkyl chain lengths, the expectation was for their conductances to follow the relationship given in Equation 6.1.

$$G \propto e^{-\beta L}$$

Equation 6.1

Where  $G$  is electrical conductance,  $\beta$  is the molecular backbone's tunnelling decay constant and  $L$  is the molecular length; these have been determined here via Density Functional Theory (DFT) calculations. For the Pt probe results,  $\beta=5.6 \text{ nm}^{-1}$  which is slightly below the typical value for alkanethiols and alkanedithiols in metallic junctions ( $8\text{-}10 \text{ nm}^{-1}$ )<sup>[160]</sup> and for the graphene-coated probes  $\beta=3.5 \text{ nm}^{-1}$  which aligns well with literature for metal| molecule| graphene junctions.<sup>[161]</sup>

### 6.2.2 Conclusions

The overall conclusions from this work were that experimental results, supported by DFT modelling, showed that aromatic head groups are good for graphene contacts, providing the aromatic groups are planar to the electrode. If they couple with  $\pi$ - $\pi$  interactions to the graphene they don't negatively impact electrical conductivity. It was also found that altering the molecular length through the series did indeed follow the relationship outlined above, in the case of both graphene-coated and uncoated conductive AFM probes.

Future molecules for these types of junctions should be designed to have large aromatic heads that will lie parallel to the graphene, to reduce the impact on the conductance pathway within the MJ. An interesting next step for these molecules would be to use an enhanced backbone in place of the largely insulating alkyl chain. This would enable manipulation of the head and backbone groups of the monolayer to give the best electron transport through those elements.

## 6.3 Tetrapodal Molecules

### 6.3.1 Introduction

Large, planar molecules have been investigated extensively within the field of molecular electronics.<sup>[162]</sup> They have either been found to bond to the substrate via van der Waals forces<sup>[163]</sup> or by covalent bonding.<sup>[164]</sup> Though these did result in monolayers, they decomposed quickly and did not always arrange in space as desired.<sup>[165]</sup> As a result, multipodal structures were proposed in an attempt to control special arrangement and longevity.<sup>[166]</sup> It has also been suggested that contacts between molecule and substrate both mechanically and electrically are key considerations when designing molecular electronic devices.<sup>[167]</sup> Hence, tripodal molecules have been previously studied, for improving the mechanical interaction with gold substrates.<sup>[168-173]</sup> In these works it is theorised that it is possible to decouple anchor groups from the conductive backbone of the molecule, allowing for highly conductive groups to be investigated on gold substrates, regardless of their affinity for arranging on it. Electrons are expected to tunnel from the base of the conductive backbone to the substrate, bypassing the anchor groups.

Developing from this, four anchor groups have been proposed to create an even stronger tetrapodal base for the molecular layers. In this instance, conjugation between the anchors and backbone will be broken allowing for fewer electron pathways along the molecule and, therefore, minimising quantum interference.<sup>[174]</sup> In this particular work, it was demonstrated via charge transport calculations that the anchor groups (modified carbazole, in this instance) had negligible influence over electronic coupling to the substrate. It was noted, however, that the electrical conductance of these structures was similar to that of the base molecule rather than improved. It was suggested that this electronic coupling could be improved by altering functional groups, enabling greater conductance.<sup>[174]</sup>

### 6.3.2 Molecular Design

In this research, four anchor groups have again been employed as in the aforementioned paper,<sup>[174]</sup> however, the molecules tested were modified with the addition of different pendant, or 'tail', groups to alter the electron tunnelling between the conductive backbone ('neck') and the substrate, different anchor group to investigate the interaction with the substrate, or the top contact ('head' group) was altered. The tail groups are expected to also influence the tilt angle of the overall molecule, which would allow for higher packing density in monolayers. See Figure 6.6 for a depiction of the different regions referenced.

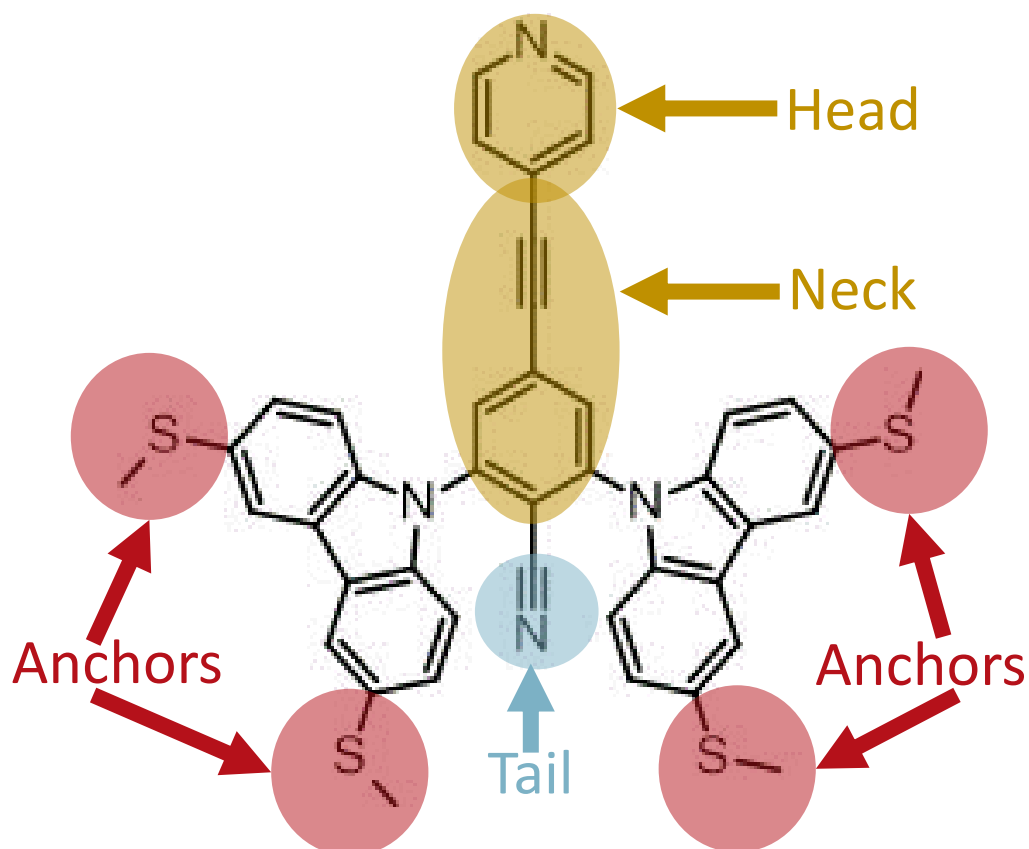


Figure 6.6 Naming convention of sections of tetrapodal molecules. The gold segment is divided into a head and neck portion, with the aromatic ring forming the head in this instance. The anchors are shown in red. The tail group is shown here in blue.

The series of tetrapods used in this research was based on the structure given at the top of Figure 6.7.<sup>[174]</sup> This was designed to have a conductive backbone that was not hybridised with the anchors, due to there being interrupting single bonds and, therefore, no conjugation. For the head of the molecule, a pyridine group was selected because it has delocalised electrons across the ring, creating conjugation. The lone pair associated with the nitrogen is not part of the hybridisation and is, therefore, free to bind with a probe.

In the first instance, the top contact to the probe was changed from a pyridine group to a ferrocene (Figure 6.7a). This was expected to create better contact with the probe due to being larger and flatter, creating a greater area for the probe to come into contact with.

Following this, three structures were studied that utilised different pendant groups on the bottom of the conductive backbone. The first of these pendants (Figure 6.7b) was an  $\text{NH}_2$  group, for which the theory was that this would be a relatively small but conductive group, which may covalently bond directly to the substrate material, in effect creating a fifth anchor and subsequently coupling the conductive backbone to the substrate. The two following molecules also employed different pendant groups to see how different-

sized groups would influence the bonding of the anchors; a bigger pendant group may spread the anchors out further and straighten the tilt angle of the conductive backbone (Figure 6.7c & d). It is expected that straightening the conductive backbone will increase electrical conductivity, as when the backbone is at an angle it is less likely to contact the probe in the junction, therefore, resulting in poor electrical conductance.

Subsequently, the anchors were altered for the next molecule design to see if using a larger atom within the anchor (moving from sulphur to selenium) would create a better binding to the substrate (Figure 6.7e). Altering the anchor group to include Se in place of S also leads to a potentially larger space for the tail group, and thus more flexibility in the nature of this group. Furthermore, studies have shown that Se and Au bind together more strongly than S and Au, due to Au acting as a soft acid and Se as a soft base.<sup>[175, 176]</sup> This could be due to the electrons donated by Se being further from the nucleus and therefore more free to covalently bond with the Au.

A final molecule (Figure 6.7f) was tested which combined the most conductive of the pendant groups ( $\text{NO}_2$ ) with the bulkier anchor group (Se), to see if the combination of those two features resulted in better overall contact and conductivity.

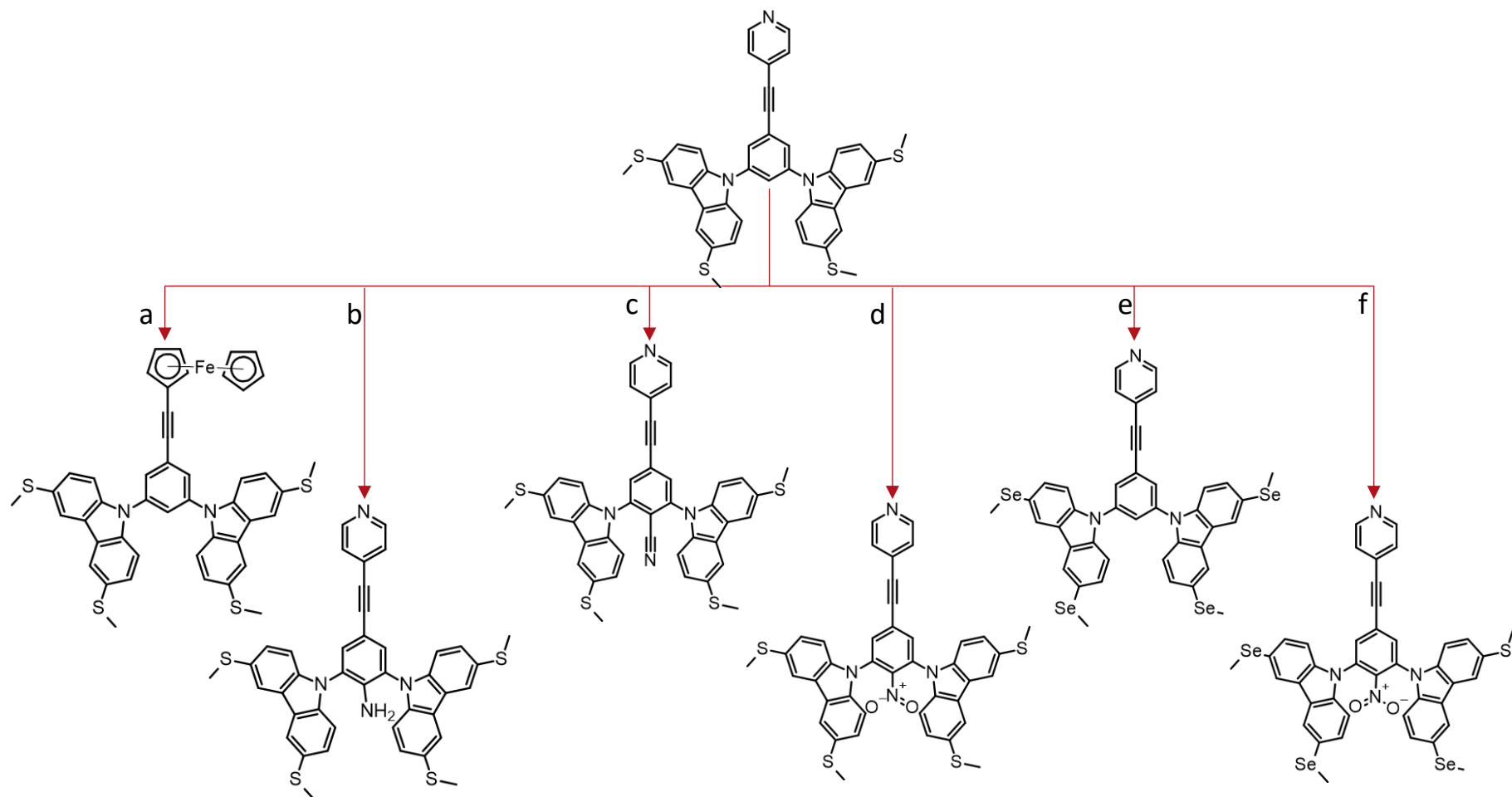


Figure 6.7 Tetrapodal molecule structures, based on previous research.<sup>[174]</sup> The parent molecule is from the original work whilst the remaining molecules have been altered to investigate the impact of different functional groups on the molecule's electrical conductance. The molecule at the top is the parent molecule, LJO-C-76; a is LJO-D-66; b is LJO-D-81; c is LJO-D-80; d is LJO-D-29; e is EK7a and f is LJO-D-127.

Further details of each tetrapod examined are given in Table 6.23.

Table 6.23 Details of the tetrapods investigated in this work. The numbering is consistent with Figure 6.7.

Ref.	Structure	Molecular Mass (g/mol)	Formula
<b>Parent</b>	LJO-C-76	693.96	C <sub>41</sub> H <sub>31</sub> N <sub>3</sub> S <sub>4</sub>
<b>a</b>	LJO-D-66	800.89	C <sub>46</sub> H <sub>36</sub> FeN <sub>2</sub> O <sub>4</sub> S <sub>4</sub>
<b>b</b>	LJO-D-81	708.98	C <sub>41</sub> H <sub>32</sub> N <sub>4</sub> O <sub>4</sub> S <sub>4</sub>
<b>c</b>	LJO-D-80	718.97	C <sub>42</sub> H <sub>30</sub> N <sub>4</sub> O <sub>4</sub> S <sub>4</sub>
<b>d</b>	LJO-D-29	738.96	C <sub>41</sub> H <sub>30</sub> N <sub>4</sub> O <sub>6</sub> S <sub>4</sub>
<b>e</b>	EK7A	881.55	C <sub>41</sub> H <sub>31</sub> N <sub>3</sub> O <sub>4</sub> Se <sub>4</sub>
<b>f</b>	LJO-D-127	990.54	C <sub>41</sub> H <sub>30</sub> N <sub>4</sub> O <sub>6</sub> Se <sub>4</sub>

### 6.3.3 Molecular Area

QCM was employed to investigate packing density, by determining the area per molecule deposited via self-assembly. As described in Chapter 5.3, crystals were placed in solutions containing the relevant tetrapods for set periods ranging from 30 seconds to 30 minutes, before being rinsed in ethanol and toluene and placed into the Open QCM Q<sup>-1</sup> for measurement of frequency. The lengths of time required were determined through trial and improvement. The solutions used were 1 mMol in concentration and were dissolved in a ratio of 1:5 ethanol: toluene. Before taking the initial base measurement, crystals underwent rigorous cleaning, per Chapter 5.3. All solvents used were as bought from Sigma Aldrich, and were 96- 99% purity. Examples of the results of this process for each tetrapod can be seen in Figure 6.8.



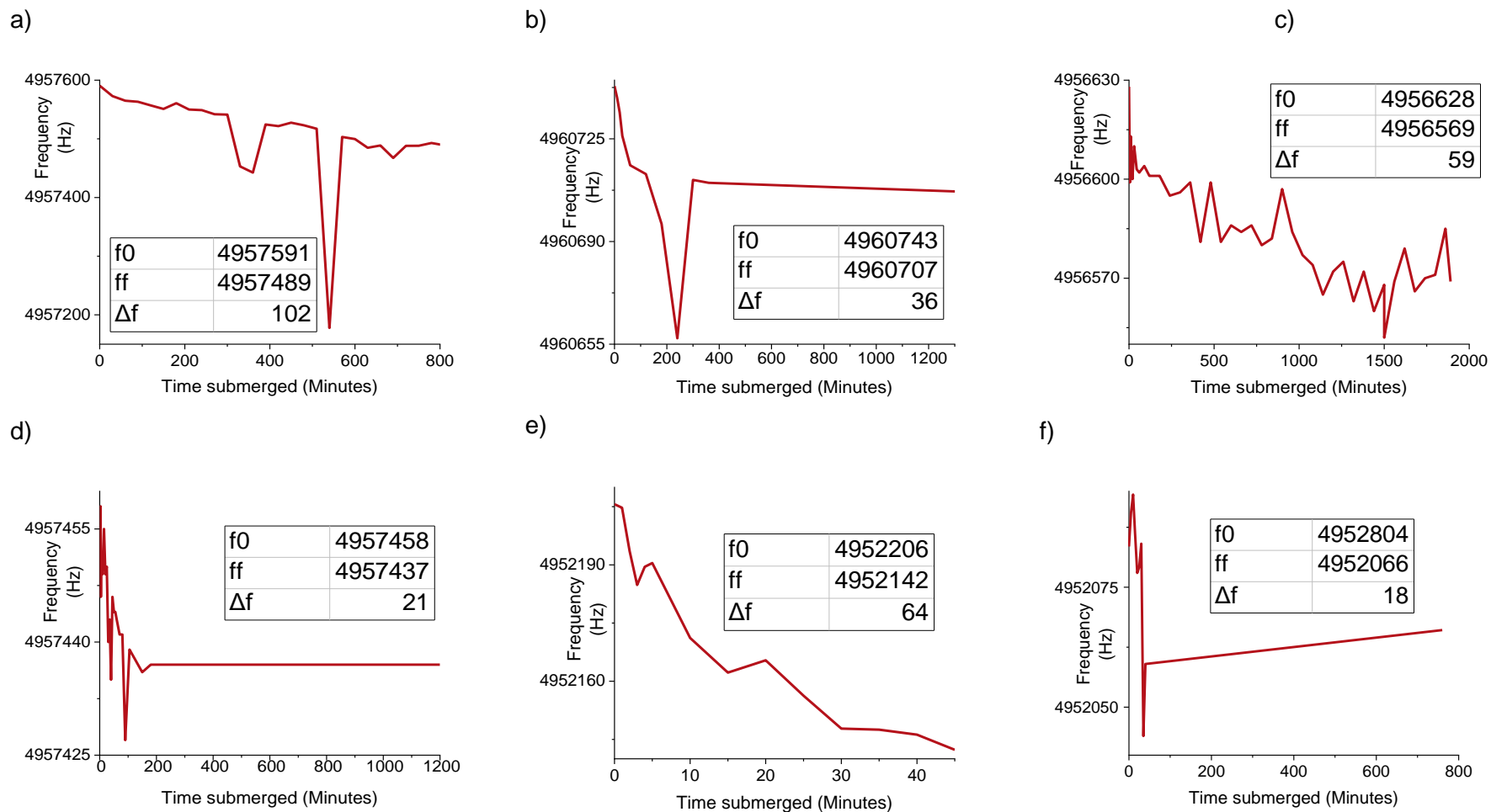
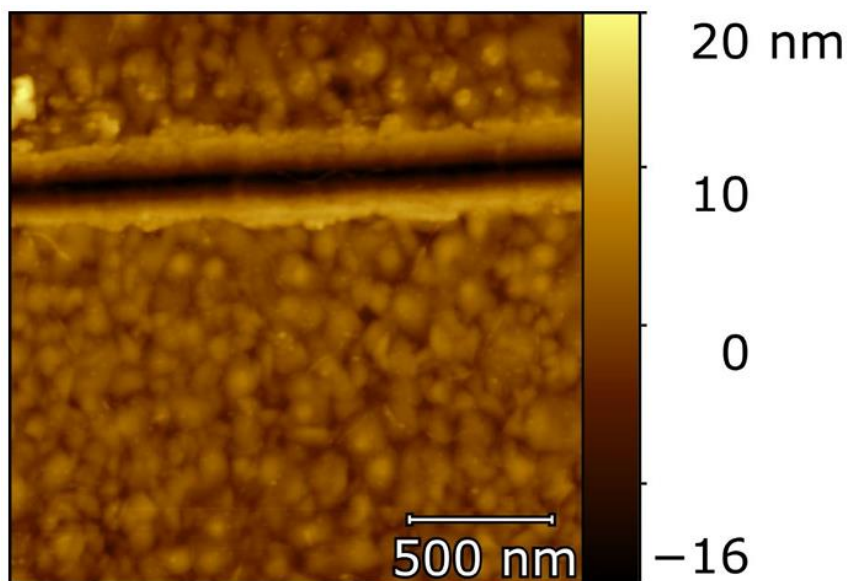


Figure 6.8 QCM results for tetrapodal molecules. The tables inlaid into each graph give the initial frequency ( $f_0$ ), final frequency ( $f_f$ ) and change in frequency ( $\Delta f$ ) measured for each molecule. The order of molecules shown is as follows: a) LJO-D-66; b) LJO-D-81; c) LJO-D-80; d) LJO-D-29; e) EK7A; and f) LJO-D-127. All frequencies shown are in Hz.

The frequency changes and subsequent calculated molecular area for each tetrapod can be observed in Table 6.24; the value for the parent molecule is from <sup>[174]</sup>. The large ranges are due to the roughness of gold on QCM crystals, which is typically far greater than for the template-stripped gold used in AFM experiments. For these tetrapodal molecules, the four anchors exacerbate this issue; the molecules are unable to properly bind to the surface unless all four anchors have the space to do so, which is not the case in the deep scratches that are typical of QCM crystals, see Figure 6.9.



*Figure 6.9 Topographical AFM image of the gold substrate on a QCM crystal as acquired by Lamantia.<sup>[17]</sup> Due to the roughness of the gold, it is difficult for multipodal molecules to bind to the surface with all anchors.*

Furthermore, issues with the deposition were aggravated when an improperly cleaned crystal was employed for the deposition. This occasionally left residue on the gold surface, or small particulates, both of which increased the roughness of the gold further still. This worsened the molecules' ability to adhere to the surface as they were unable to contact all four anchors, making the binding weaker than intended.

Table 6.24 Frequency changes attained for tetrapods via QCM measurements. Molecular areas, calculated via the Sauerbrey equation, are also shown

Ref.	Structure	Range of $\Delta f$ measured via QCM (Hz)	Standard Deviation (Hz)	Area per molecule of middlemost result ( $\text{\AA}^2$ )
Parent	LJO-C-76	-	-	187
a	LJO-D-66	-11 to -102	43	35
b	LJO-D-81	-36 to -70	24	18
c	LJO-D-80	-18 to -71	24	30
d	LJO-D-29	-9 to -21	8	33
e	EK7A	-17 to -178	89	5
f	LJO-D-127	-12 to -29	9	54

In the previous work, it was found that the tetrapodal anchors lay almost flat against the substrate material, even when nitrogen was added as an anchor group to the bottom of the conductive backbone. The thiomethoxy groups bond directly to the substrate and the backbone was then held at an acute angle above the surface.<sup>[174]</sup> Using these assumptions, the volume of space beneath the conductive backbone can be determined by assuming it forms a square-based pyramid shape. This is shown graphically in Figure 6.10, with dimensions for each tetrapod given in Table 6.25.

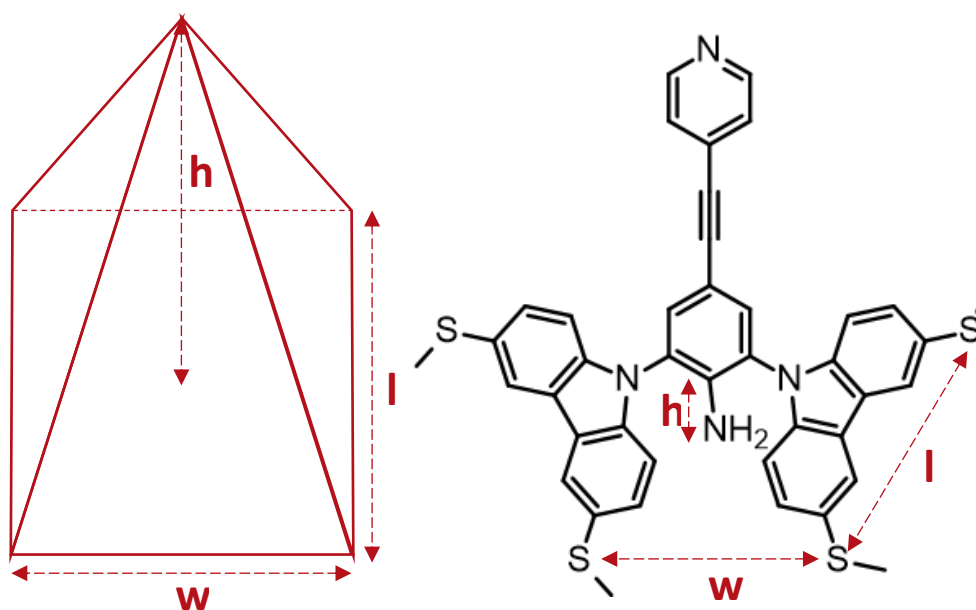


Figure 6.10 The diagram on the left shows the assumed shape of tetrapodal molecules.  $l$  is the distance between anchors in one direction;  $w$  is the distance between anchors in the other direction;  $h$  is the distance between the lowest carbon atom in the conductive backbone and the substrate (the length of the pendant bonds). This is given in terms of a tetrapodal molecule on the right.

The volume of each space beneath the conductive backbone, in between the tetrapodal anchors, was calculated using Equation 6.2; the volume of a square-based pyramid. The notation is consistent with that given in Figure 6.10.

$$V = \frac{l \times w \times h}{3}$$

Equation 6.2

The distances used in these calculations were determined by drawing each molecule using ChemSketch and then using the “bond length” function.

*Table 6.25 Dimensions for the assumed pyramidal volume in the base of the tetrapods, including calculated area and volume. The error associated with the ChemSketch “bond length” function is unknown.*

Ref.	Structure	l (Å)	w (Å)	h (Å)	Area (Å <sup>2</sup> )	Volume (Å <sup>3</sup> )
a	LJO-D-66	11.9	9.97	1.00	118.60	119.08
b	LJO-D-81	11.9	9.97	2.72	118.60	322.13
c	LJO-D-80	11.9	9.97	3.10	118.60	367.20
d	LJO-D-29	11.9	9.97	2.68	118.60	317.50
e	EK7A	12.0	14.41	1.00	172.90	173.59
f	LJO-D-127	12.0	14.41	2.68	172.90	462.86

As the anchors for all but the final two tetrapods are the same, the molecular areas as predicted by measuring bond lengths are also the same for the first four tetrapods in the series (see Table 6.25). However, this does not align with the molecular areas obtained from QCM measurements (see Table 6.24). QCM leads us to believe that the areas occupied by the molecules are far smaller than those predicted. This implies that either the anchors are standing much more upright than previously observed, or the average molecule does not have all four anchors contacting the substrate.

From this disparity, and the spread of data obtained for each molecule per Table 6.24, it was determined that reductive desorption would be a more reliable way to obtain molecular area and subsequently the tilt angle between the head group and substrate. This is suggested as further work as it is beyond the scope of this research.

Using the bond length function in ChemSketch, the length of the neck + head group (see Figure 6.6 for naming convention) for all of the molecules besides that with the ferrocene head was c. 1.1 nm. The length of the molecule with the ferrocene head was c. 0.9 nm. Figure 6.11 below shows how the head and neck tend towards the substrate due to  $\pi$ -interactions. This image shows the tetrapodal anchors in parallel with the substrate, as that was the arrangement concluded from theoretical modelling in the previous research.<sup>[174]</sup>

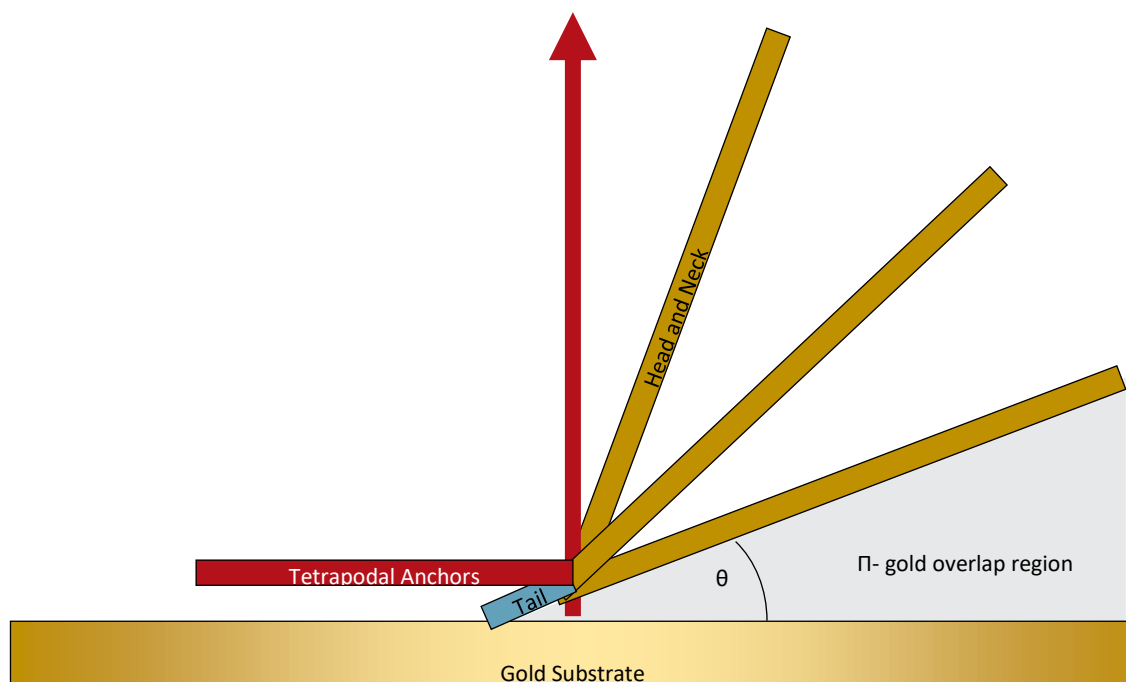
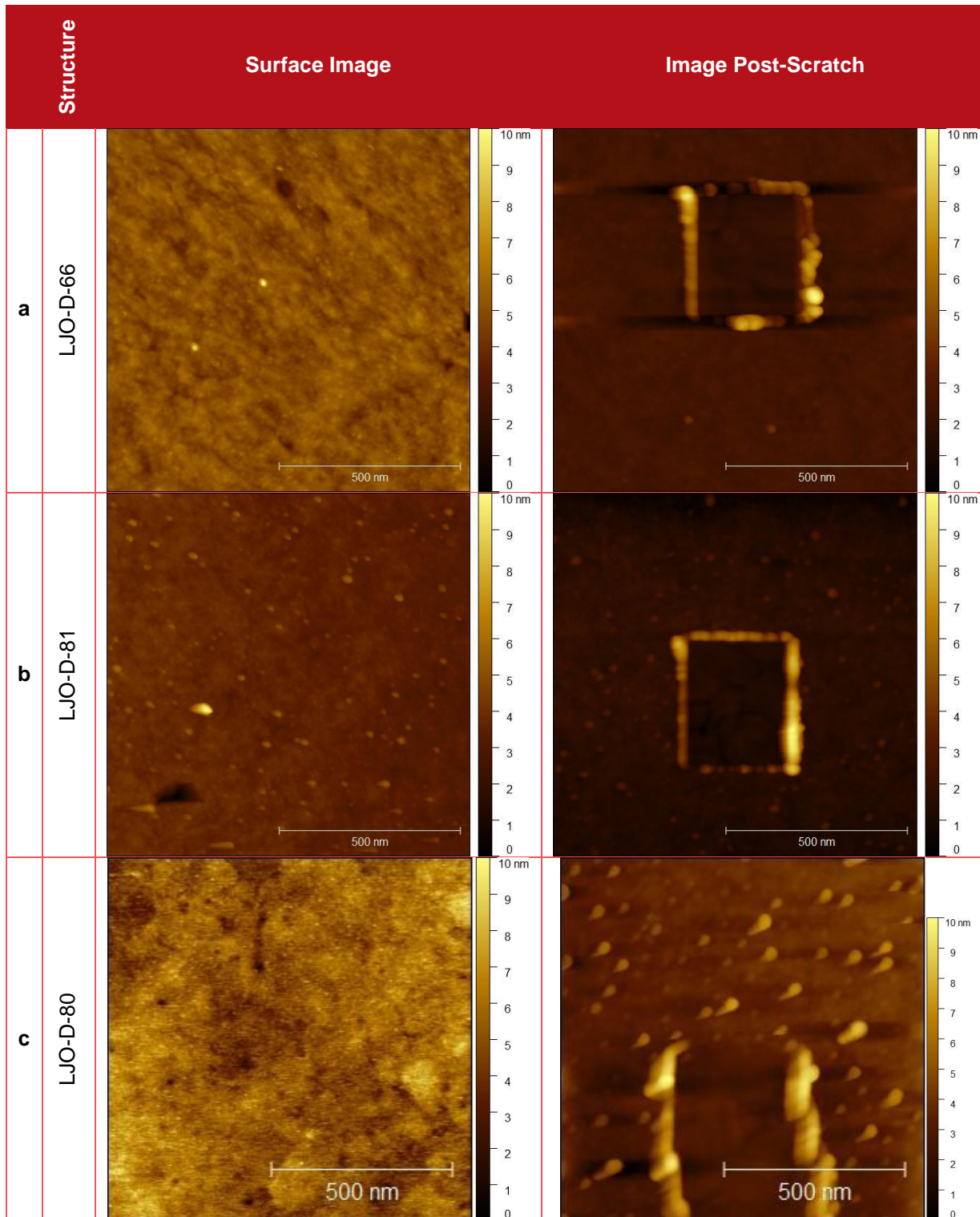


Figure 6.11 Schematic of how the head & neck groups of tetrapodal molecules tilt towards the substrate due to  $\pi$  interactions with the surface.  $\theta$  is referred to as the 'tilt angle'.

The results from carrying out nanoscratches for this work, per Table 6.26, did not enable the calculation of the tilt angle. This was due to the height profiles of all of the molecules being around the same as, or slightly greater than, the  $\sim 1$  nm anticipated for each. It is suspected that the larger tail groups featured in these molecules than those studied initially have caused the tetrapodal anchors to lift somewhat, rather than lying parallel to the substrate as they did previously. The results do, however, confirm that monolayers of the molecules are forming, as none of the heights are in the region of double the height expected.

Table 6.26 Nanoscratch test results for tetrapodal molecules. AFM was used to remove the monolayer from the surface and subsequently measure the height difference between where the molecule remained and where it had been scratched away. Each image is 1  $\mu\text{m}$  x 1  $\mu\text{m}$  and has a z scale from 0-10 nm. The scale bars are 500nm.



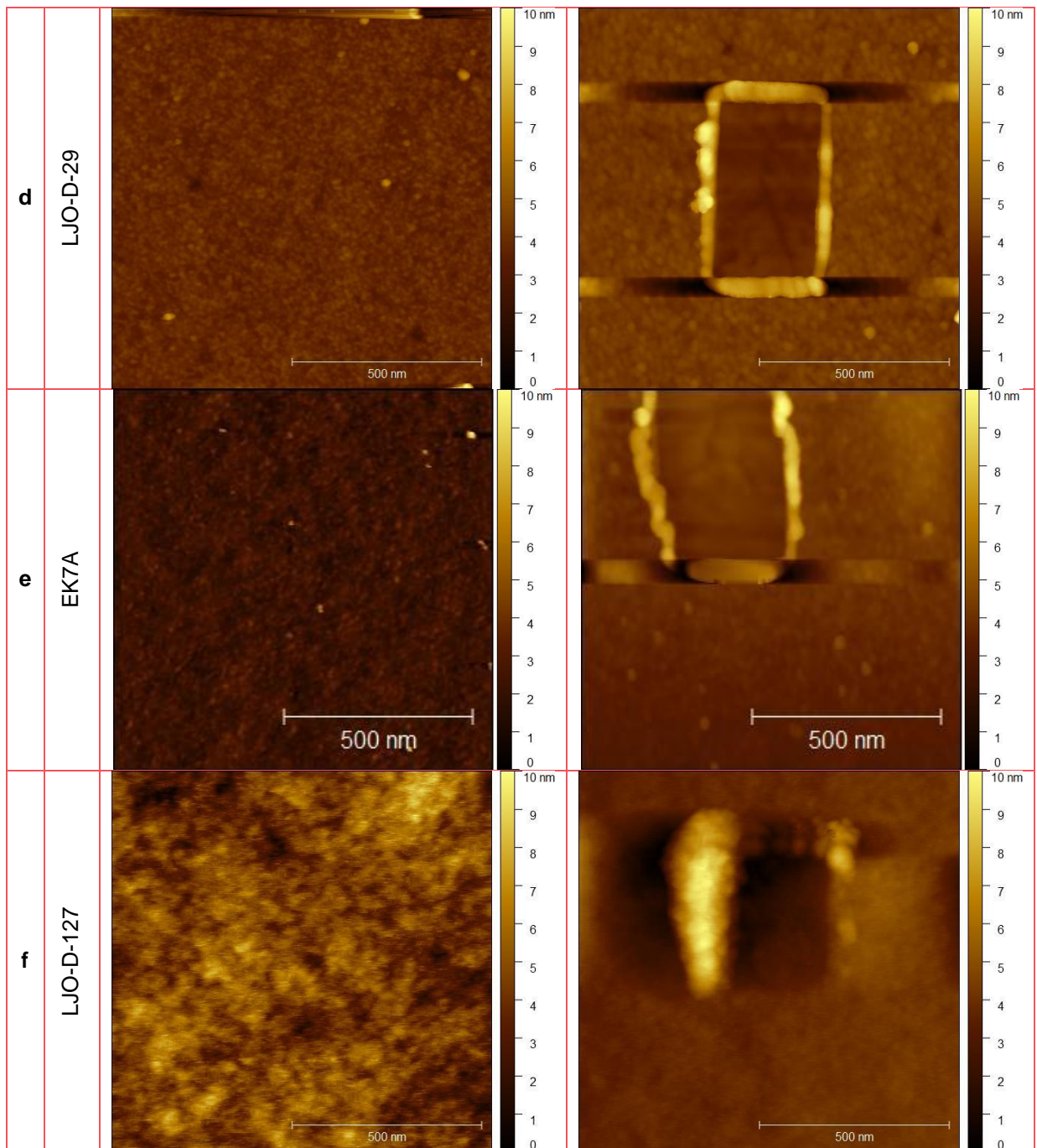
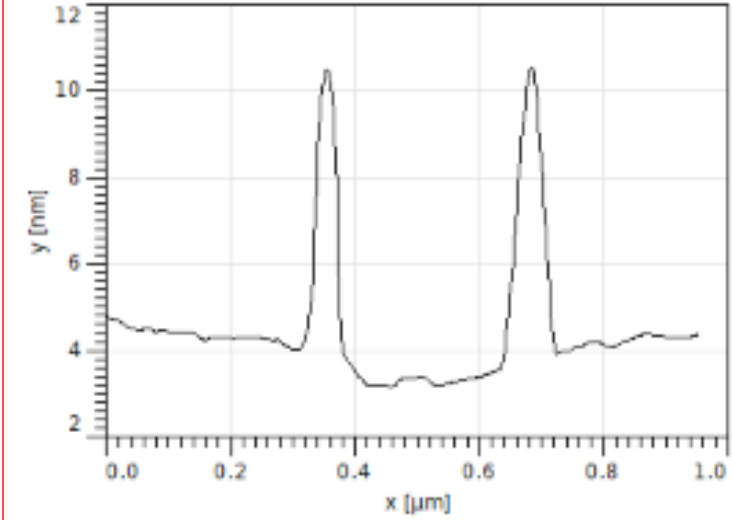
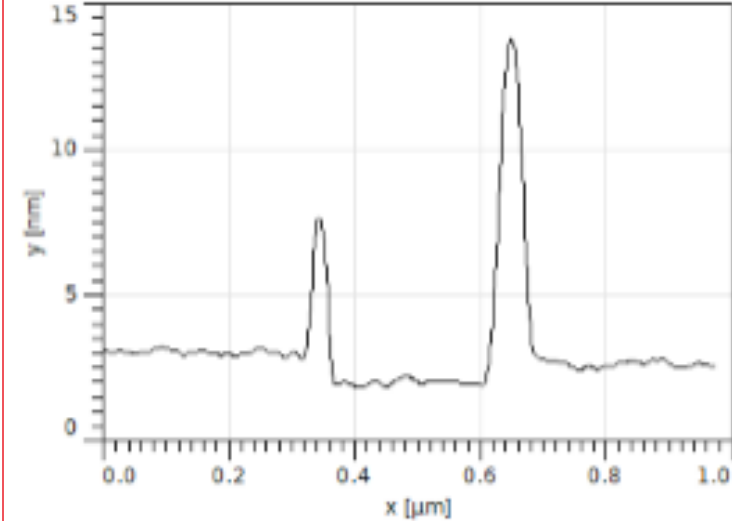
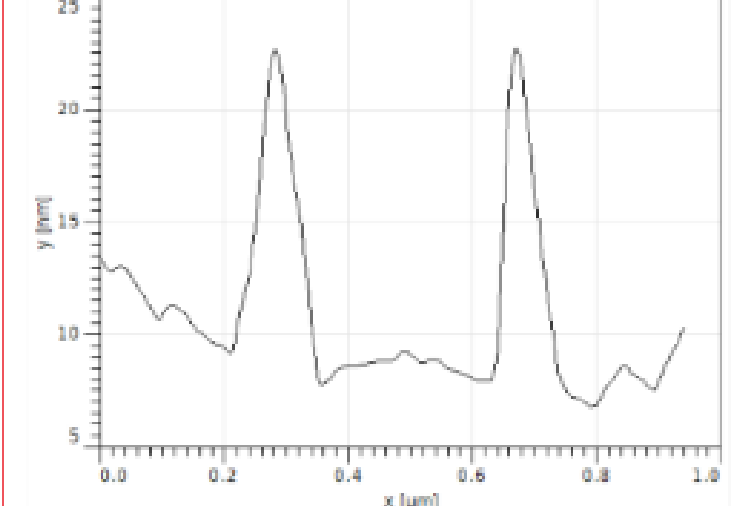
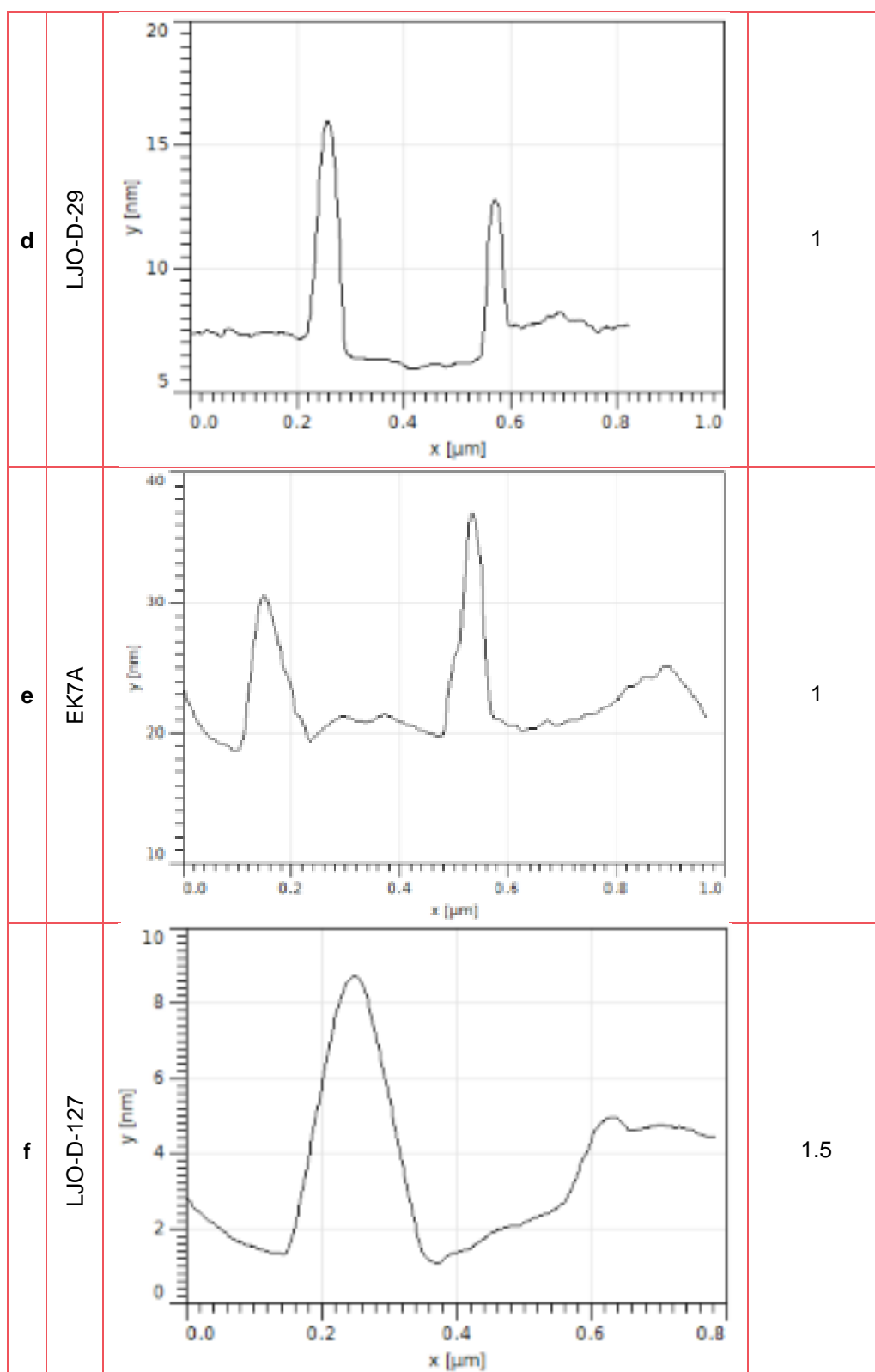


Table 6.27 Nanoscratch test results for tetrapodal molecules; scratch profiles and height difference observed. AFM was used to remove the monolayer from the surface and subsequently measure the height difference between where the molecule remained and where it had been scratched away.

Structure	Scratch Profile	Height Difference Observed (nm)
a LJO-D-66	 <p>The graph shows the scratch profile for LJO-D-66. The x-axis represents distance in micrometers (μm) from 0.0 to 1.0, and the y-axis represents height in nanometers (nm) from 2 to 12. The profile shows a baseline at approximately 4 nm with two distinct peaks at approximately 0.35 μm and 0.7 μm, both reaching a height of about 10.5 nm. The height difference between the peaks and the baseline is 1 nm.</p>	1
b LJO-D-81	 <p>The graph shows the scratch profile for LJO-D-81. The x-axis represents distance in micrometers (μm) from 0.0 to 1.0, and the y-axis represents height in nanometers (nm) from 0 to 15. The profile shows a baseline at approximately 3 nm with two distinct peaks at approximately 0.35 μm and 0.7 μm, reaching heights of about 8 nm and 14 nm respectively. The height difference between the peaks and the baseline is 1 nm.</p>	1
c LJO-D-80	 <p>The graph shows the scratch profile for LJO-D-80. The x-axis represents distance in micrometers (μm) from 0.0 to 1.0, and the y-axis represents height in nanometers (nm) from 5 to 25. The profile shows a baseline that fluctuates between 7 and 14 nm. Two distinct peaks are observed at approximately 0.3 μm and 0.9 μm, reaching heights of about 23 nm and 23.5 nm respectively. The height difference between the peaks and the baseline is 1.5 nm.</p>	1.5





Density functional theory (DFT) models performed by Ali Ismael and Colin Lambert allowed estimates of the tilt angles for each molecule. It was concluded that a neck group being tilted further towards the substrate would demonstrate greater electrical conductance due to  $\pi$ -interaction between the molecule's neck and head groups, and the gold surface due to bypassing the non-conductive anchors.

#### 6.3.4 Electrical Conductivity

Once packing density was determined, this could be used alongside cAFM to determine the electrical conductivity of each tetrapod.

The method described in Chapter 5.5.2 was employed for measuring the conductivity of the thin films created. The I/V trace histograms are given in Figure 6.12 to Figure 6.17; these show the typical sigmoidal shape expected of semiconductors. The red line depicted is the average trace; this is shown more clearly in the electrical conductance plots. The final histograms depict the spread of conductance values. The average value is subsequently presented in Table 6.28 where the values are compared between standard cAFM, and that carried out using graphene-coated probes.

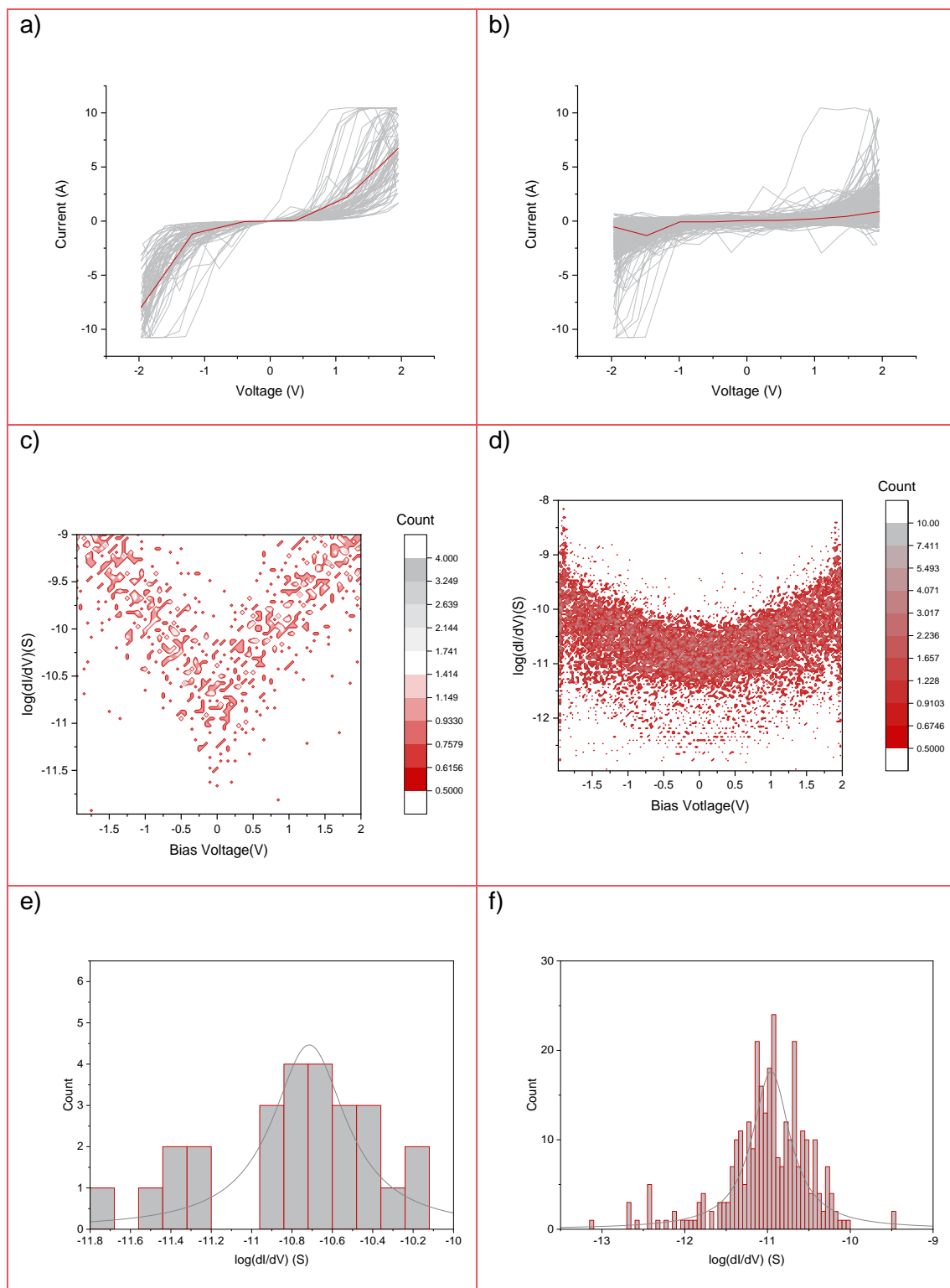


Figure 6.12  $I(V)$  data collated for tetrapod series using standard conductive probes. a and b show the statistical  $I(V)$  curves for tetrapodal molecules. c and dI show the  $\log(dI/dV)$  electrical conductance plots for the same results. e and f are the distributions for electrical conductance for the same data. The order of molecules remains the same down the columns, and along the rows, as follows: a) LJO-D-66 and b) LJO-D-81.

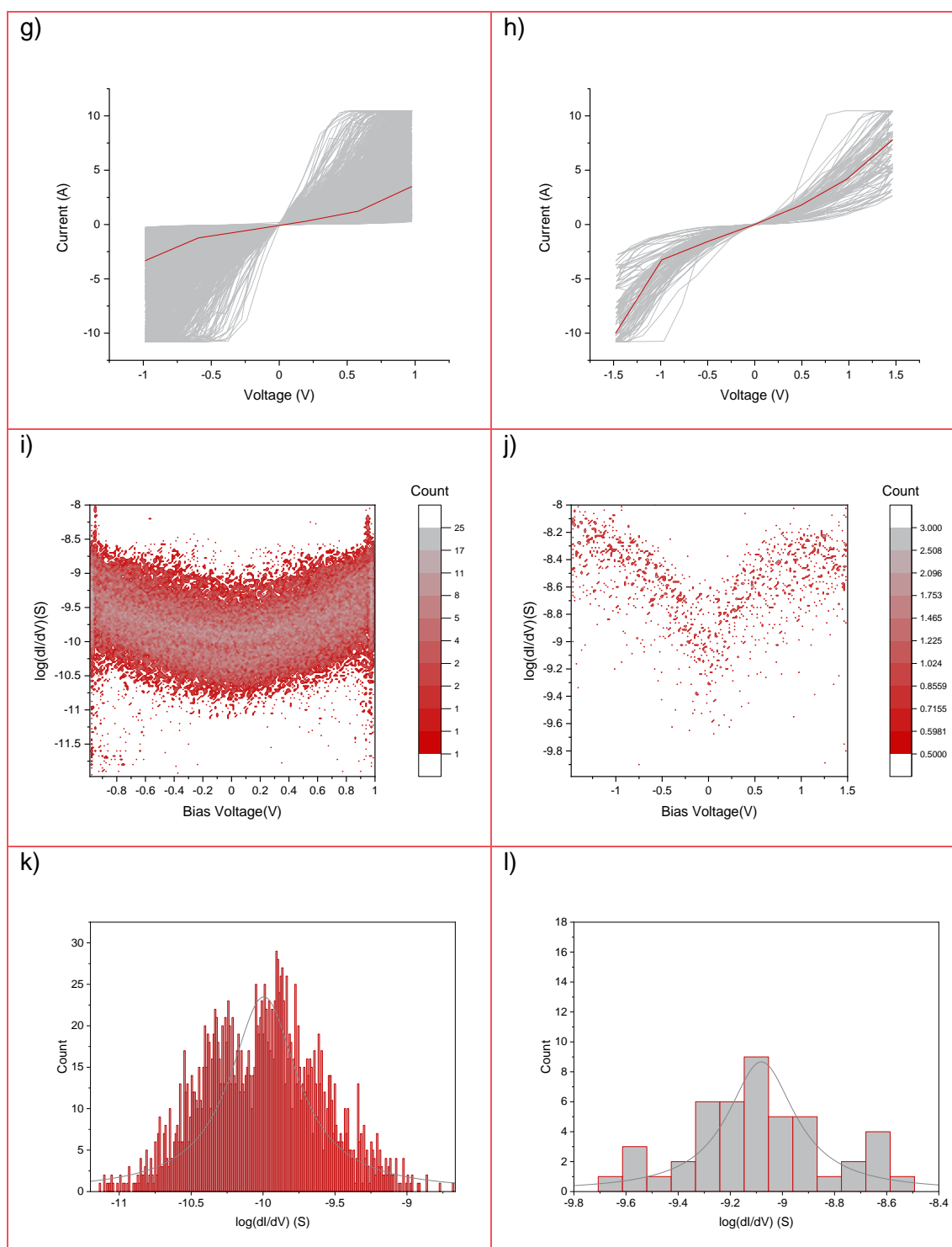


Figure 6.13  $I(V)$  data collated for tetrapod series using standard conductive probes. *g* and *h* show the statistical  $I(V)$  curves for tetrapodal molecules. *i* and *j* show the  $\log(dI/dV)$  electrical conductance plots for the same results. *k* and *l* are the distributions for electrical conductance for the same data. The order of molecules remains the same down the columns, and along the rows, as follows: *g*) LJO-D-80 and *h*) LJO-D-29.

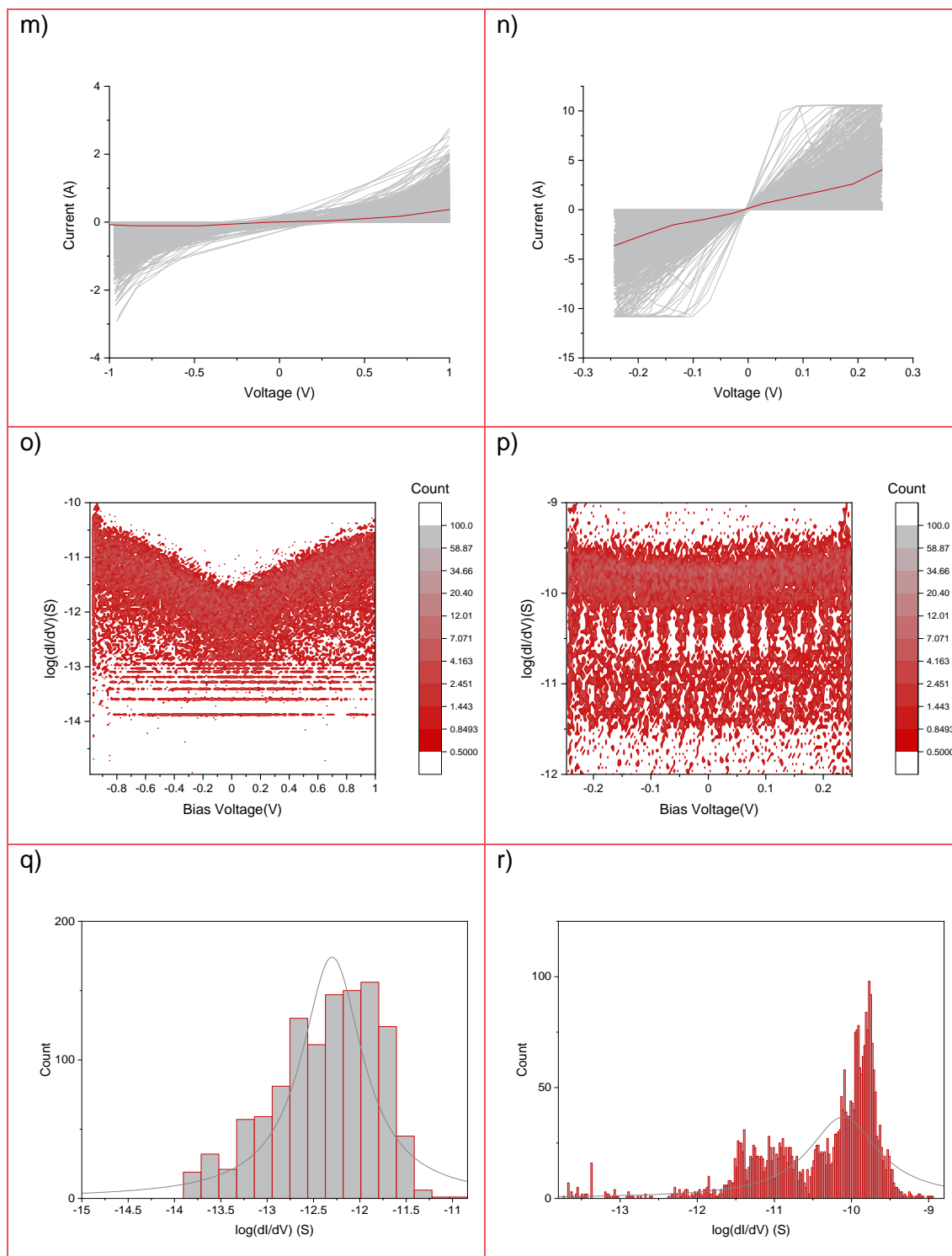


Figure 6.14  $I(V)$  data collated for tetrapod series using standard conductive probes. *m* and *n* show the statistical  $I(V)$  curves for tetrapodal molecules. *o* and *p* show the  $\log(dI/dV)$  electrical conductance plots for the same results. *q* and *r* are the distributions for electrical conductance for the same data. The order of molecules remains the same down the columns, and along the rows, as follows: *m*) EK7A and *n*) LJO-D-127.

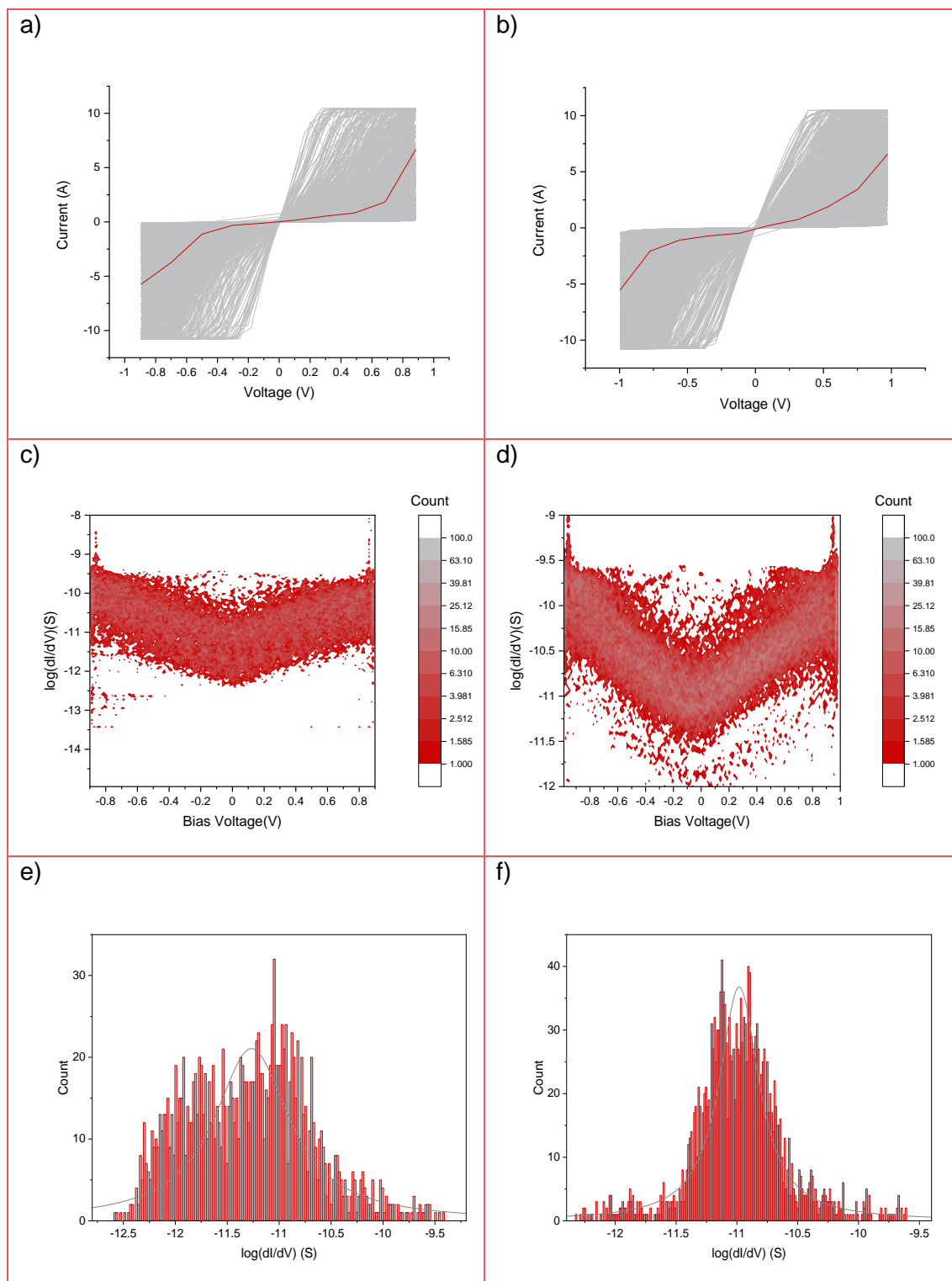


Figure 6.15  $I(V)$  data collated for tetrapod series using graphene-coated conductive probes. *a* and *b* show the statistical  $I(V)$  curves for tetrapodal molecules. *c* and *d* show the  $\log(dI/dV)$  electrical conductance plots for the same results. *e* and *f* are the distributions for electrical conductance for the same data. The order of molecules remains the same down the columns, and along the rows, as follows: *a*) LJO-D-66 and *b*) LJO-D-81.

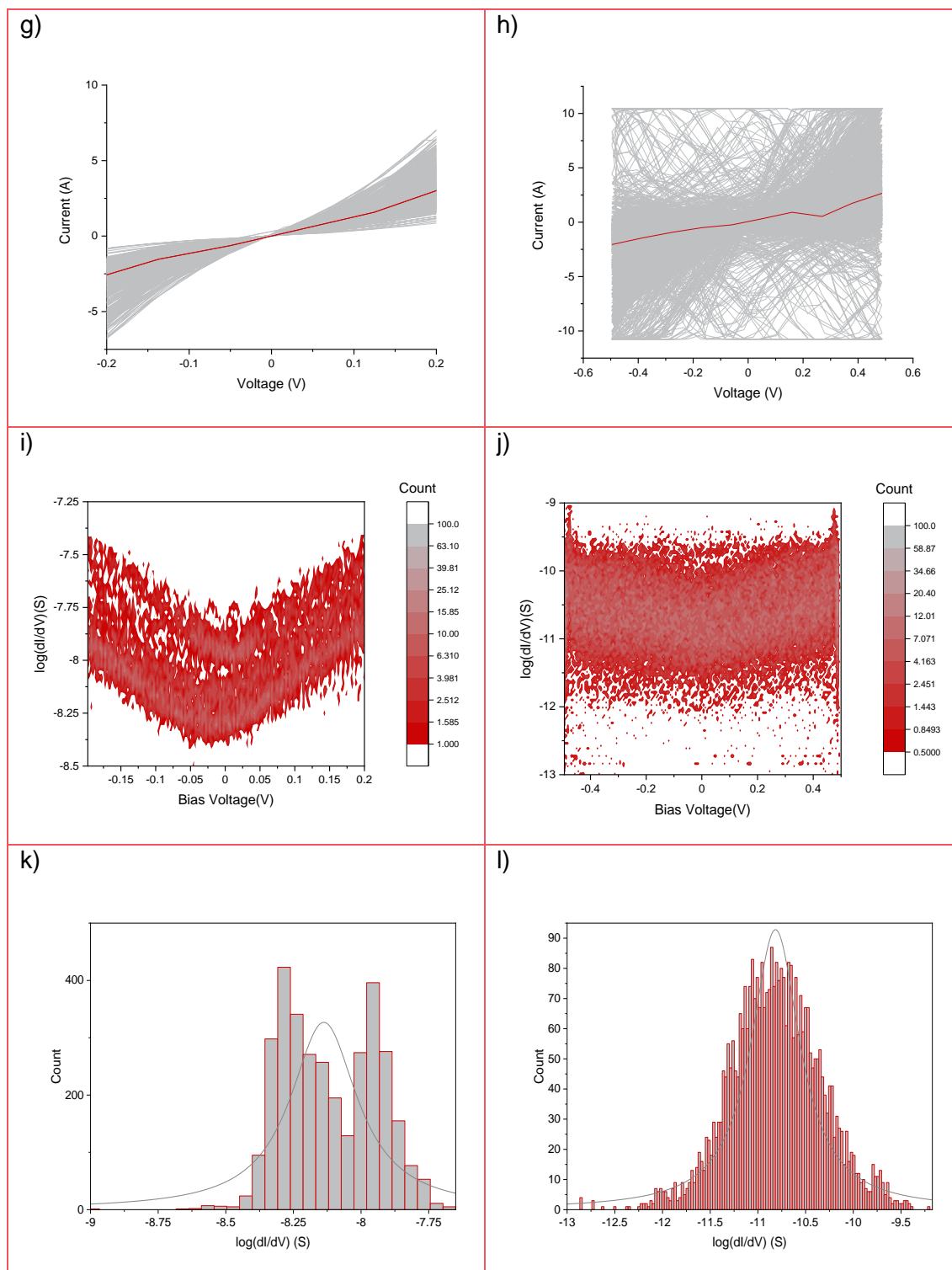


Figure 6.16  $I(V)$  data collated for tetrapod series using graphene-coated conductive probes. *g* and *h* show the statistical  $I(V)$  curves for tetrapodal molecules. *i* and *j* show the  $\log(dI/dV)$  electrical conductance plots for the same results. *k* and *l* are the distributions for electrical conductance for the same data. The order of molecules remains the same down the columns, and along the rows, as follows: *g*) LJO-D-80 and *h*) LJO-D-29.

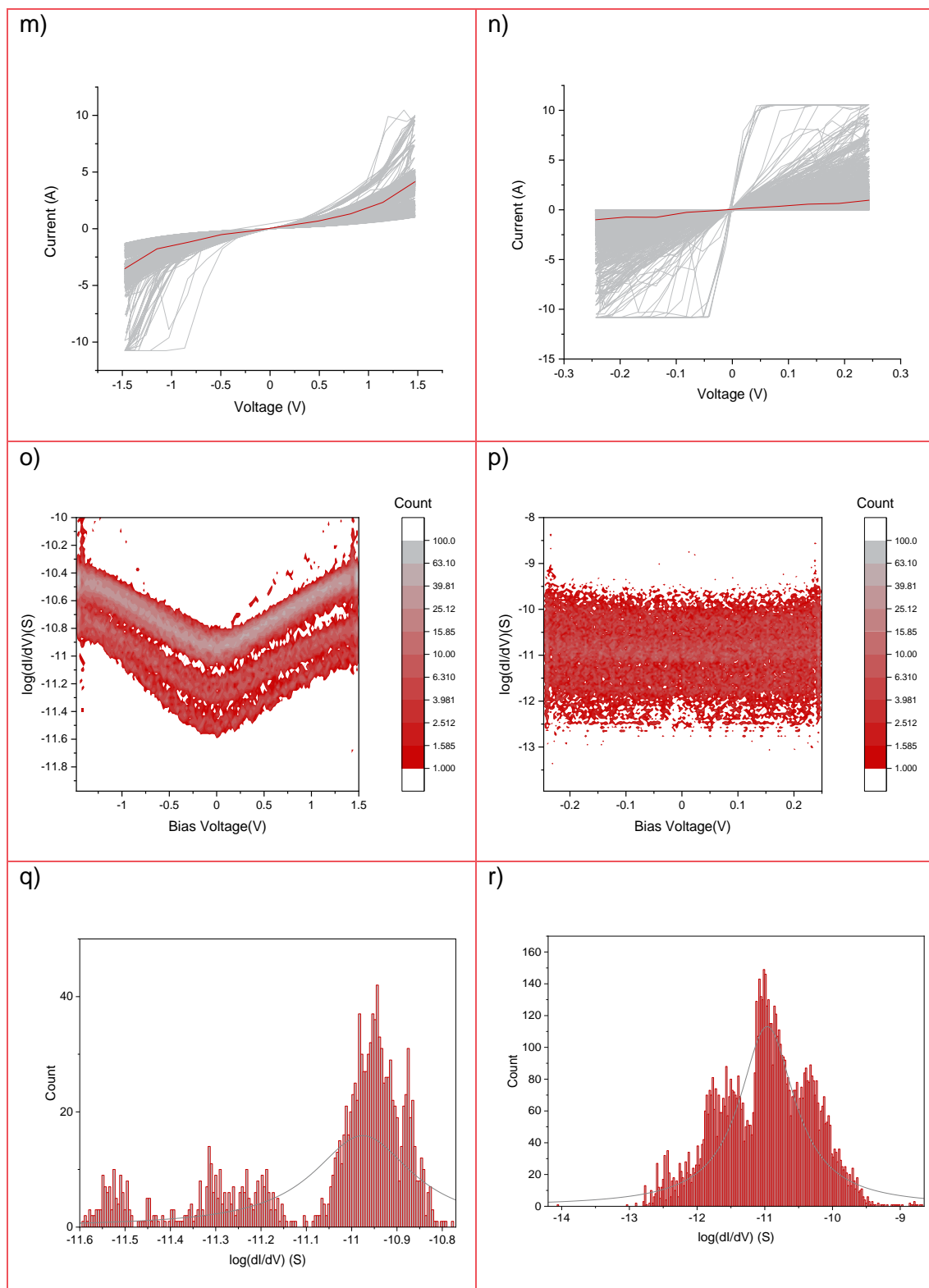


Figure 6.17  $I(V)$  data collated for tetrapod series using graphene-coated conductive probes. *m* and *n* show the statistical  $I(V)$  curves for tetrapodal molecules. *o* and *p* show the  $\log(dI/dV)$  electrical conductance plots for the same results. *q* and *r* are the distributions for electrical conductance for the same data. The order of molecules remains the same down the columns, and along the rows, as follows: *m*) EK7A and *n*) LJO-D-127.



The results were duplicated for each molecule but with graphene-coated probes. Figure 6.15 to Figure 6.17 show the  $I/V$  curves and conductance histograms for this, with the molecules ordered as previously.

As with the previous results, these data were manipulated as described in Chapter 5.5.2 to gain  $\log(G/G_0)$ . Table 6.28 gives the values of this for the tetrapodal molecules, using standard conductive probes and graphene-coated probes.

Table 6.28  $\log(G/G_0)$  values for tetrapods collated via AFM using both graphene-coated and uncoated probes. Results from the parent molecule are as published in<sup>[174]</sup>. The errors for the parent molecule are unknown.

Molecule	$\log(G/G_0)$ (standard probe)	$\log(G/G_0)$ (graphene-coated probe)
Parent	-4.44	-3.95
LJO-D-66	-6.46±0.64	-6.73±0.33
LJO-D-81	-6.05±0.64	-6.19±1.59
LJO-D-80	-5.68±0.08	-3.93±0.21
LJO-D-29	-4.71±1.14	-6.51±0.38
EK7A	-7.38±0.83	-7.04±0.77
LJO-D-127	-6.33±0.42	-6.50±0.60

Table 6.28 shows that in some cases, electrical conductance is improved by using a graphene-coated probe in the molecular junction, however, in most cases this has not been observed. It is expected that this is due to whether conductance is driven by  $\pi$ -interactions between the probe and molecule, or if the molecule is acting more as a molecular wire, similar to in a molecular break junction.

Ali Ismael and Colin Lambert have carried out Density Functional Theory (DFT) calculations to estimate the electrical conductance of the tetrapodal molecules, and the parent molecule shown in Figure 6.7. The angles referenced are the optimal positions of the head and neck group with the gold substrate; see Figure 6.6. as can be seen in Figure 6.18 there is very good agreement between the theory predictions and experimental results for electrical conductance. This implies that the molecules are forming SAMs that behave in a manner consistent with the single molecule junctions that have been modelled. It has therefore been concluded that the tail group for the tetrapods acts largely to determine the tilt angle and thus greatly controls electrical conductance.

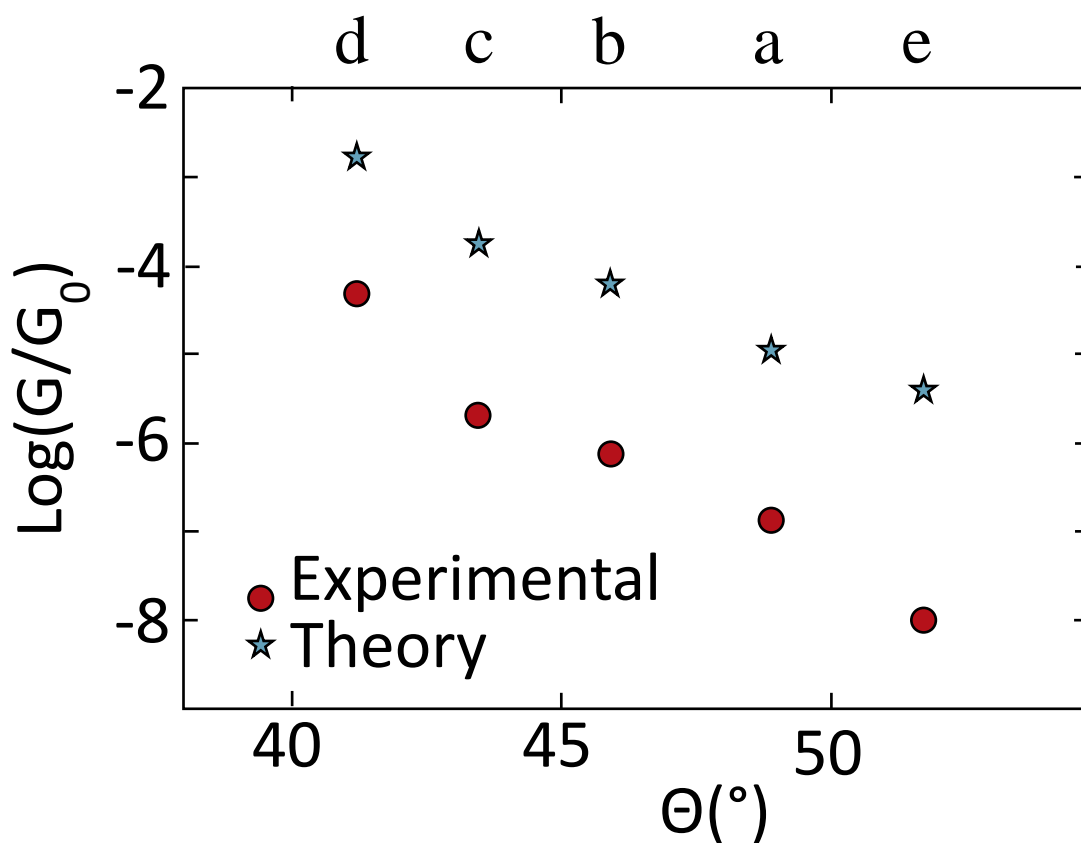


Figure 6.18 Graph comparing the theoretical electrical conductance values for the tetrapodal molecules with the experimental results. These values are for the standard molecular junctions, not with the graphene-coated probes. Density Functional Theory (DFT) was employed for the theoretical calculations; LJO-D-127 was not included in the theory calculations hence it is not included in this graph. The molecules are numbered as in Table 6.28. The angles given are for the optimised tilt angle for the molecule with the substrate, per Figure 6.11.

### 6.3.5 X-ray Photoelectron Spectroscopy

The addition of the tail groups into these molecules compared with those from the previous paper<sup>[174]</sup> led to the question of them forming pentapods rather than tetrapods, with the tail group acting as a fifth anchor. It was determined that XPS was the best method for finding if this was the case. Measurements were carried out per Chapter 5.6.

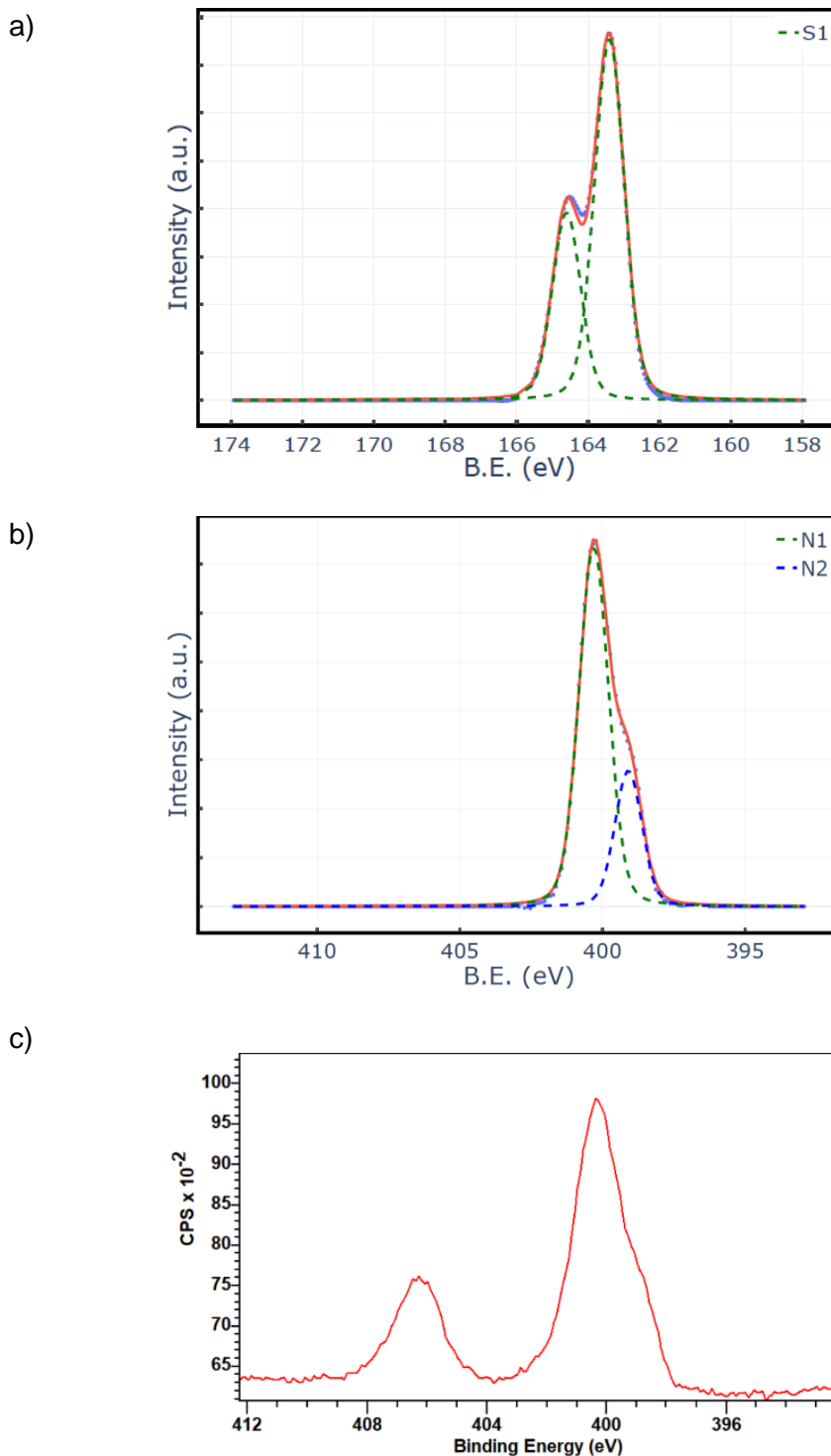


Figure 6.19 XPS spectra for tetrapods in powder form: a) sulphur in LJO-D-81, b) nitrogen in LJO-D-81 and c) nitrogen in LJO-D-29. The large sulphur peak at around 163 eV is assumed to correspond to unbound sulphur. Likewise, the large nitrogen peak at around 401 eV is assumed to correspond to unbound nitrogen.

Figure 6.19 depicts the sulphur and nitrogen spectra for the powder samples of LJO-D-81 and the nitrogen spectrum of LJO-D-29. The sulphur spectrum can be used as the reference for where the unbound sulphur peaks will be in all of the samples, as this is

the only sulphur peak present in the powder samples; it appears at around 163 eV. Sulphur bound to gold in S2p 3/2 is generally agreed to appear at around 162.1 eV; shown in blue in Figure 6.20. The nitrogen spectrum for LJO-D-81 is indicative of there being two nitrogen groups present which are expected to be the nitrogen within the tetrapodal structure and that of the tail group. This is discussed further later.

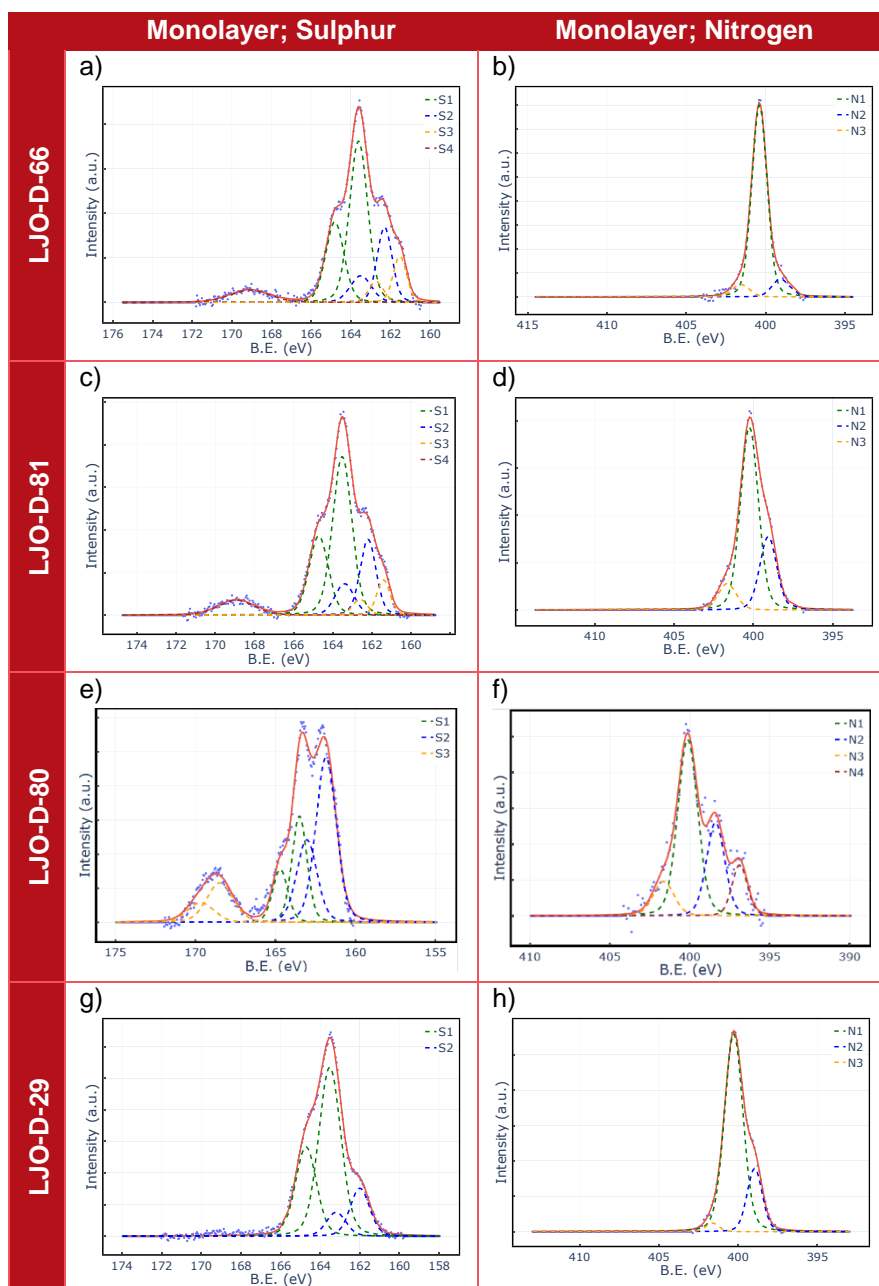


Figure 6.20 Sulphur and nitrogen focussed XPS results for a selection of tetrapods. The missing monolayers were contaminated so the results were not clear. The sulphur peak at around 163 eV is assumed to depict unbound sulphur whilst the remaining peaks correspond to bound sulphur; some where multiple anchors appear to be binding. Similarly, the peak in the nitrogen spectra at around 401 eV is considered to be unbound nitrogen whilst the remaining peaks depict bound nitrogen states.

Initial tests were carried out via XPS for all six tetrapods, however, selenium from the two selenium-anchored molecules appears to have contaminated all the samples (see

Figure 6.20 for the sulphur spectrum of LJO-D-80). New spectra were obtained for LJO-D-66, LJO-D-81 and LJO-D-29. Further testing is required to obtain clean data for LJO-D-80, EK7A and LJO-D-127. Due to EK7A and LJO-D-127 containing selenium, their spectra are unusable as it's not possible to determine if the peaks recorded are associated with the samples themselves or with the contamination.

With the sulphur spectra included in Figure 6.20, it is evident that there are two sulphur doublets for each molecule, indicating two sulphur states; each is split into two peaks per the S2p 3/2 and S2p 1/2 orbitals. These are likely bound to gold and unbound, meaning that a significant portion of the anchors are not binding to the substrate in each case. Using the powder spectra for comparison, the unbound sulphur is that which peaks at 163.6 eV (shown in dark green). For each of LJO-D-66, LJO-D-81 and LJO-29, the unbound sulphur peak is significantly larger than the bound sulphur, meaning that fewer anchors are binding to the surface than anticipated. It appears that around half of the anchors are binding to the surface, whilst the excess unbound sulphurs may be due to molecules that have physisorbed to the surface and have not been sufficiently washed off in the SAM preparation. Alternatively, the anchors could be binding to either top sites or hollow sites within the gold substrate which would lead to shifted XPS peaks however, further study would be required to determine this in more detail; typically it is assumed that sulphur binds to three-fold hollow sites.<sup>[177]</sup> For LJO-D-80, it appears that all of the anchors are binding correctly, with some molecules again physisorbed to the surface. These can be seen in the AFM images obtained of the samples, shown in Table 6.25, creating the islands of more material. It is noted that the spectra for LJO-D-80 for both nitrogen and sulphur seem to show contamination from selenium, in the form of the yellow peaks to the left.

Regarding the nitrogen spectra, the larger peak in each at around 401 eV looks to be the nitrogen in the tetrapodal structure between the anchors and the neck group as this is still significant in the LJO-D-66 spectrum. The blue peak to the right is likely indicative of the tail groups for the other molecules, as it's significantly reduced in the LJO-D-66 spectrum. It would have been expected to see another nitrogen peak for the LJO-D-29 molecule due to it having nitrogen bound to oxygen. However, as can be seen in Figure 6.19 this peak was present in the powder nitrogen spectrum for this molecule, at around 406 eV, but when comparing this to the nitrogen spectrum in Figure 6.20 for the same molecule, the peak is no longer present. This may be a result of the oxygen splitting off from the nitrogen due to the interaction of NO<sub>2</sub> with gold, where steps and kinks in the gold surface reduce the NO<sub>2</sub>.<sup>[178, 179]</sup>

Furthermore, it is particularly worthy of note that for the molecule LJO-D-80, there appears to be a third nitrogen peak, shown in maroon at 396 eV, which looks to be the nitrogen bound to the gold substrate. This is very significant as combined with the sulphur spectrum it appears to show that all four anchors are contacting the gold surface, and the tail group for this molecule is acting as a fifth anchor and creating a pentapod. This implies that the nitrogen tail group featured in this molecule is binding strongly enough to the gold substrate to overcome the resistance of the additional anchors binding.

### 6.3.6 Conclusions

As described in Chapter 2 this research intended to produce SAMs of specifically designed molecules with enhanced electrical conductance, achieved through manipulation of quantum interference effects. This was in line with literature suggestions that multipodal molecules could be a means to improve the lifetime of SAMs produced for enhanced electrical conductivity. In this study, molecules with four anchors (tetrapods) were designed to have anchors that were decoupled from the conductive backbone, allowing for the alignment of typically conductive molecules onto gold despite their lack of affinity for it. The design of the overall molecule also aimed to promote conductive quantum interference by using conjugation between the anchors and backbone. These designs were developed building on work previously carried out that concluded simply decoupling the anchors was insufficient in improving the molecules' conductance.<sup>[174]</sup> As such, 'tail' groups were also included in this series of molecules, in an attempt to improve conductance by forming a quasi-fifth anchor and enabling electron tunnelling.

An AFM was used to obtain electrical conductance results for the tetrapodal molecules and concluded that they vary in conductance as expected from DFT calculations. Results were also gained using graphene-coated probes; this concluded that largely electrical conductance worsened with graphene coverage, however in the case of two molecules it was improved. This was theorised to be due to  $\pi$ -interactions driving the conductance in these junctions.

XPS results indicated that most of the molecules were not binding all four anchors to the substrate, however, for the molecule with the triple bonded nitrogen tail group, the tail group does appear to be acting as a quasi-fifth anchor.

It is suggested that further work is carried out on this series of molecules, namely re-attempting the XPS experiments for the molecules containing selenium, but with minimising the risk of contamination. Further to this, reductive desorption could pose an interesting alternative to QCM for determining the area per molecule of the series, and

thus altering the electrical conductances as these are inherently linked through the methodology employed in this research. Finally, to gain insight into the FOM use of this series and therefore find how the materials compare to others being used in TEGs, Seebeck coefficients should be obtained.

Real-world benefits of these conclusions include more efficient harnessing of waste heat and conversion into electricity, as well as potentially greater lifetimes of devices that employ such techniques, due to the greater stability of these films.

## 6.4 Dithiolenate Molecules

### 6.4.1 Introduction

As studied within this research, multipodal molecules have been investigated as one method for improving the coupling between molecular layers and electrodes in electrode|molecule|electrode junctions.<sup>[174]</sup> Tripodal molecules have previously been designed to form ordered LB-deposited films; either end of the molecules included ethyl(thiomethyl) terminal groups with pyridyl-based anchors. Having the same anchors at either end enabled easy formation of the monolayer. It was concluded that just one end of the molecule was binding to the gold substrate, and homogeneous monolayers were formed.<sup>[116]</sup> Molecules with four anchors have also been investigated to find the impact of such structures on molecular stability when deposited onto a substrate. The molecules in one study (per Chapter 5) were designed such that the anchors did not interfere with the conductive pathway of the core molecular wire, by decoupling the anchors from the backbone. Phenyl or pyridyl head groups were used to ensure good binding to the top electrode within the junction. As a result of these planar head groups, conductance with graphene-coated top electrodes was shown to be better than the uncoated Pt counterparts. DFT binding energy calculations concluded that having more anchors did indeed improve the stability of the molecules.<sup>[174]</sup> Furthermore, an extensive study has been carried out, into the impact of using multipodal molecules over those with single anchor points. They concluded that in each case studied, the extra anchors did result in greater stability when deposited. However, other properties of the molecules varied wildly given they were designed for different purposes. For example, molecules of greater electronic coupling displayed improved electrical conductance which is ideal for electrical devices but the same design feature quenches the excited state for labelling applications.<sup>[165]</sup>

As was discussed in Chapter 6, amending the electrode has also been tested, for instance, by coating it in graphene or ITO. In one example, molecules were designed with planar head groups to bind well with graphene-coated AFM probes, to improve

conductance through the junction. It was proven that molecules with planar head groups indeed demonstrated improved conductance with graphene-coated probes compared to uncoated Pt probes. However, it was also found that more aromatic rings within these head groups do not lead to greater conductance; the opposite is true. Tilting of the rings about the electrode causes the junction to elongate and therefore reduces electrical conductance.<sup>[1]</sup>

Regarding ITO, the key advantage of it is that it is transparent whilst remaining conductive. However, molecules contacting such substrates previously needed to be terminated by a carboxylic acid group to bind properly to the surface. Research has trialled carboxylic acid, cyanoacrylic acid and pyridinium-squarate terminal groups for suitability. It was concluded that pyridinium-squarate bound well to ITO but not to gold, enabling orientational control over the molecule when using a gold| molecule| ITO junction.<sup>[180]</sup>

For this section of work, the proposition for improving conductance through a junction was achieved by using an anchor group with a dithiolenate moiety. This functional group acts as an alkene with two thiols substituted into the cis positions. Such groups have previously been used for ligands due to their affinity for transition metals, however, little research has been done into their applications in molecular wires.<sup>[181-183]</sup>



## 6.4.2 Molecular Design

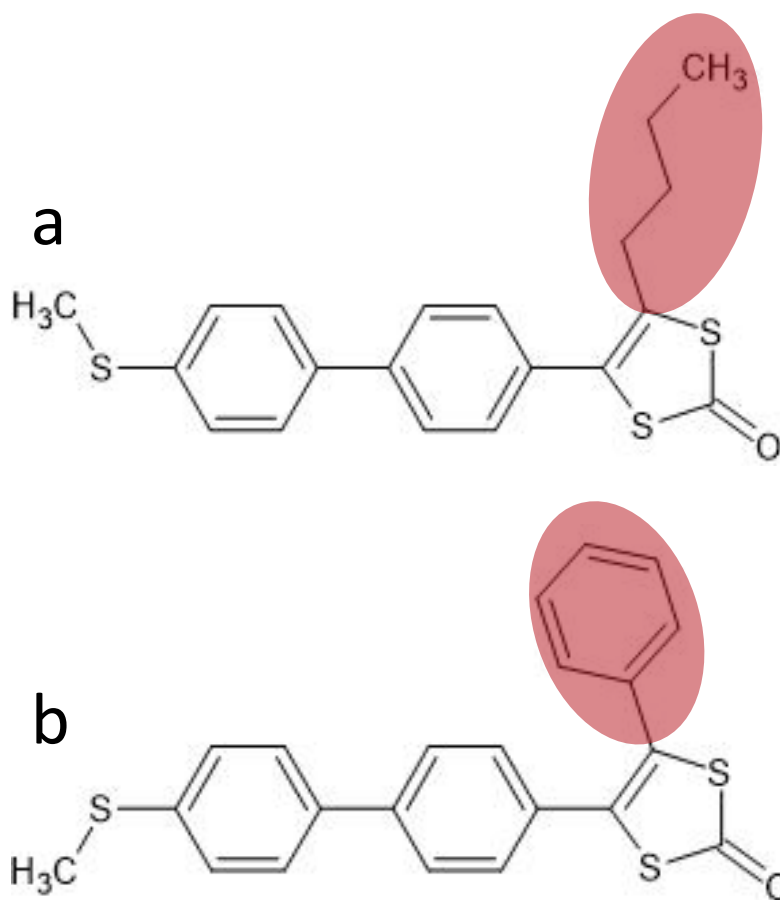


Figure 6.21a depicts the dithiolenone molecule labelled RJD2114. b is RJD2163. the functional group is highlighted in red, and both are later referred to as 'R'. This depiction of the molecules is the protected form.

Two molecules were designed for this series; however, both could be configured as protected and deprotected. The structures for the two molecules with their protection are given in Figure 6.21, wherein the highlighted groups are later referred to as 'R'. Figure 6.22 depicts the anticipated difference in binding to the substrate for the protected and deprotected molecules. a shows the binding of the protected molecule; b gives that of the deprotected form.

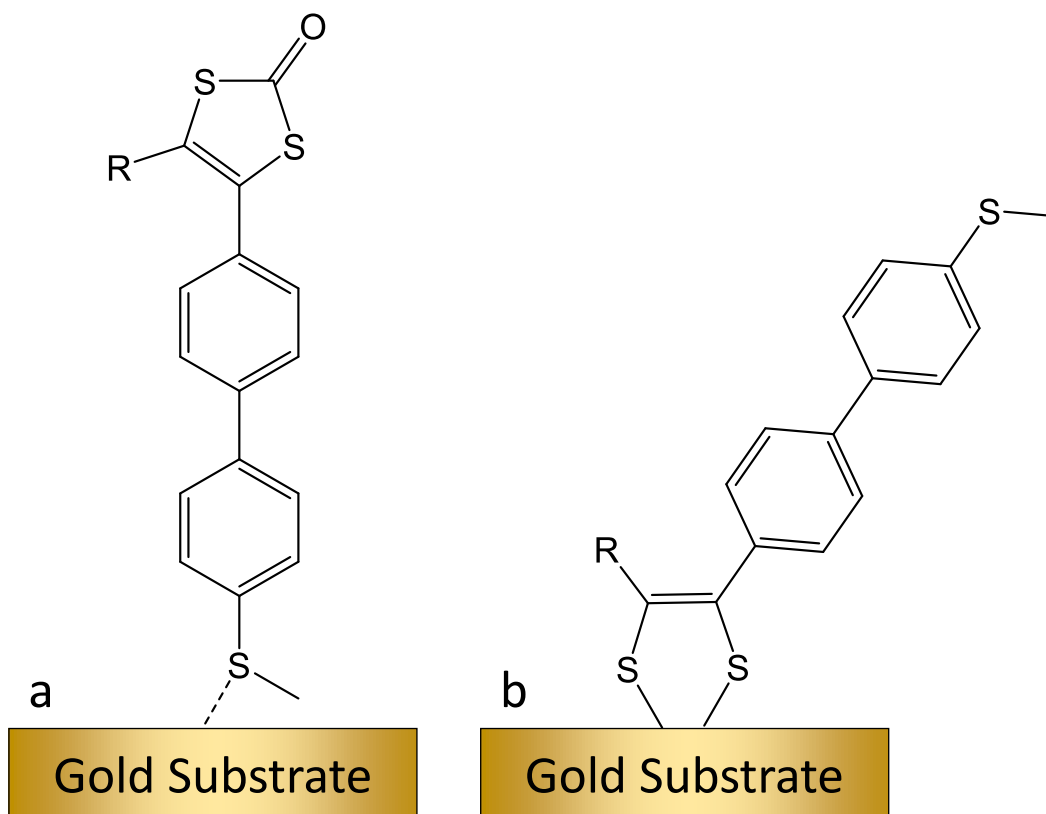


Figure 6.22 a gives the binding of the protected dithiolenate molecule in its general form and b the deprotected. R is the functional group for each molecule, per Figure 6.21.

The deprotection was carried out by adding a 2.5 molar equivalent of NaOMe to the molecular solution (containing the molecule at 1 mMol using the solvent THF). The solution was subsequently sonicated for 1 hour before adding a sample of template-stripped gold (see Chapter 5.4) for self-assembly.

### 6.4.3 Molecular Area

As in Chapter 6.3.3, the method for QCM outlined in Chapter 5.3 was employed; using the Open QCM Q<sup>-1</sup> device. All crystals were cleaned before their use, as in Chapter 5.3. Initial baseline measurements were obtained for each crystal, with each subsequently being submerged in solution overnight. Each solution was of 1 mmol concentration, with THF as the solvent. For the deprotected molecules, NaOMe was used for the deprotection, as described previously. The deprotected samples were additionally rinsed with methanol to remove NaOMe.

Once XPS analysis determined the deprotection was insufficient (see Chapter 6.4.5), the crystals onto which the deprotected monolayers had been deposited were also annealed for 1 hour at 100 °C to ensure the deprotection had occurred. At least three measurements were taken for each of the six molecules. For each sample, an initial

measurement was recorded as a control and a final measurement was recorded after the crystal had been submerged in solution overnight. See Table 6.29 for these results.

*Table 6.29 Frequency changes attained for dithiolenates via QCM measurements after the monolayer formed. Molecular areas, calculated via the Sauerbrey equation, are also shown.*

Structure	Range of $\Delta f$ measured via QCM (Hz)	Standard Deviation (Hz)	Average area per molecule ( $\text{\AA}^2$ )
RJD2114, Protected	-39 to -206	66	5
RJD2114, Deprotected	-3 to -28	11	13
RJD2114, Deprotected, Annealed	8 to -5	-1	69
RJD2163, Protected	-5 to -85	25	16
RJD2163, Deprotected	-27 to -105	39	6
RJD2163, Deprotected, Annealed	19 to -17	19	33

These results appear to show that the properly deprotected molecules occupy greater space. This is as expected, given the structure of the protected and deprotected molecules given in Figure 6.22; due to there being two sulphurs to bond with the gold, the molecule tilts slightly, meaning that fewer molecules would be able to pack in next to one another, therefore, increasing the area occupied by one molecule.

#### 6.4.4 Electrical Conductance

Initially, cAFM measurements were executed on the samples with and without deprotection. It was expected that the deprotected molecules would bind to the substrate as demonstrated in Figure 6.22b, whereas the protected molecules were projected to bind as in Figure 6.22a. The electrical conductance results can be seen in Figure 6.23 and Figure 6.24.

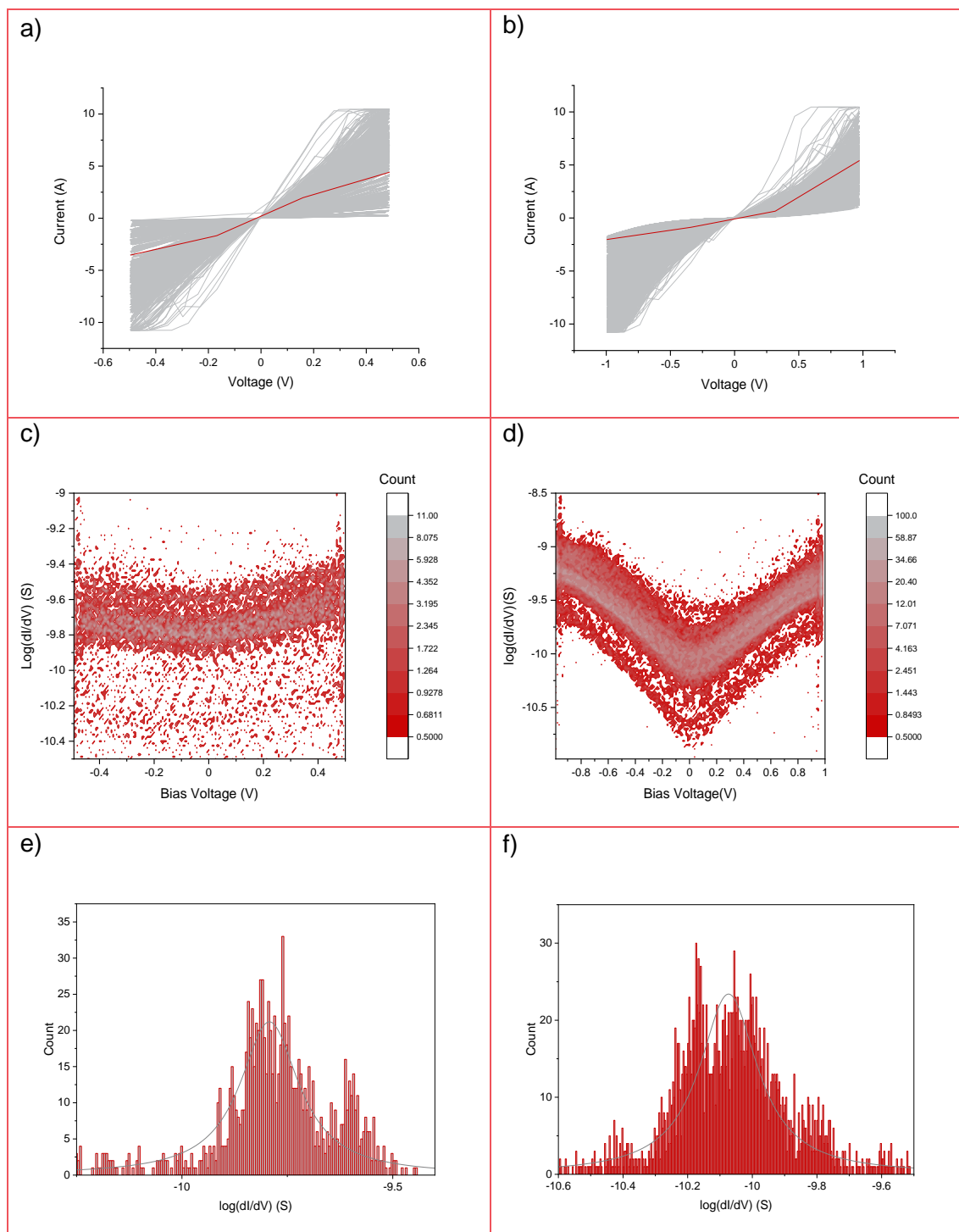


Figure 6.23  $I(V)$  data collated for RJD2114 in the dithiolene series using standard conductive probes. a and b show the statistical  $I(V)$  curves; c and d show the  $\log(dI/dV)$  electrical conductance plots; e and f are the distributions for electrical conductance. The order of molecules remains the same down the columns, and along the rows: a) RJD2114, protected and b) RJD2114, deprotected.

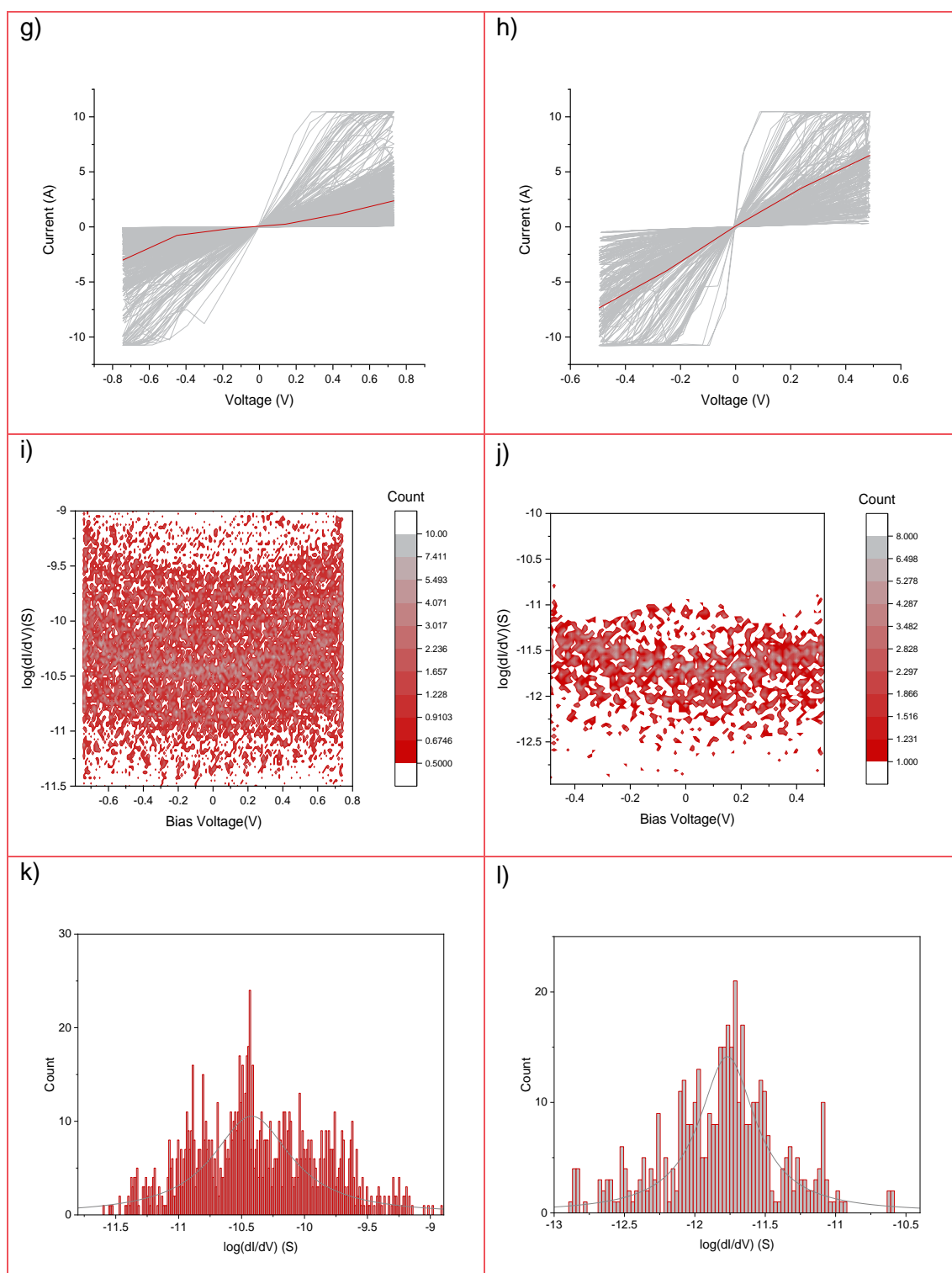


Figure 6.24  $I(V)$  data collated for RJD2163 in the dithiolenate series using standard conductive probes. *g* and *h* show the statistical  $I(V)$  curves; *i* and *j* show the  $\log(dI/dV)$  electrical conductance plots; *k* and *l* are the distributions for electrical conductance. The order of molecules remains the same down the columns, and along the rows: a) RJD2163, protected and b) RJD2163, deprotected.

As with the series of tetrapodal molecules, these results were repeated with graphene-coated conductive probes (see Chapters 4 and 5); see Figure 6.26 and Figure 6.27.

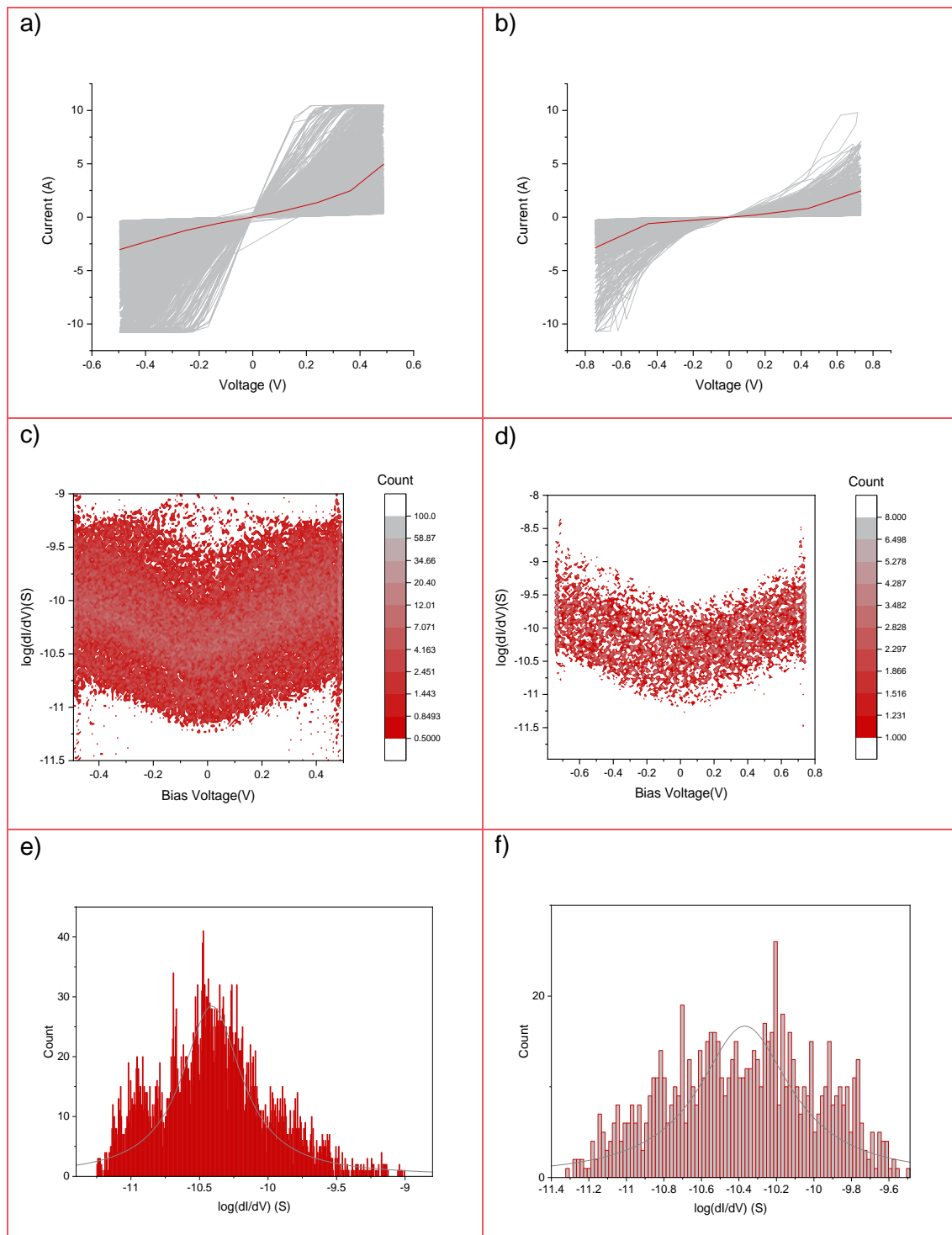


Figure 6.25  $I(V)$  data collated for RJD2114 in the dithiolenate series using graphene-coated conductive probes. a and b show the statistical  $I(V)$  curves; c and d show the  $\log(dI/dV)$  electrical conductance plots; e and f are the distributions for electrical conductance. The order of molecules remains the same down the columns, and along the rows: a) RJD2114, protected and b) RJD2114.

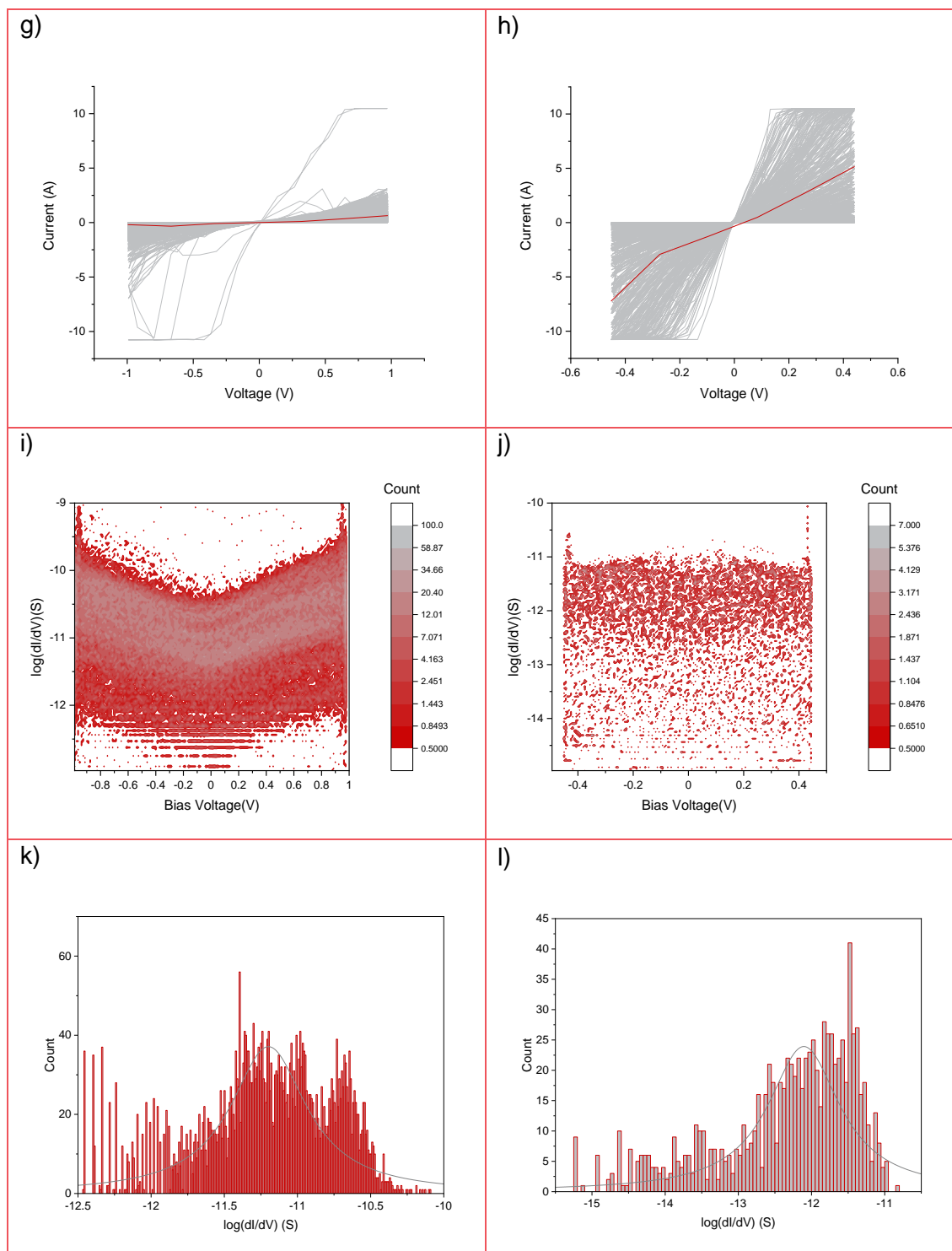


Figure 6.26  $I(V)$  data collated for RJD2163 in the dithiolenate series using graphene-coated conductive probes. g and h show the statistical  $I(V)$  curves; i and j show the  $\log(dI/dV)$  electrical conductance plots; k and l are the distributions for electrical conductance. The order of molecules remains the same down the columns, and along the rows: a) RJD2163, protected and b) RJD2163.

The comparison of conductive results is given in Table 6.30. As evidenced by these results, there is little difference observed in the conductance values gained for the protected and deprotected species though in both cases, the protected conductance is slightly better than the deprotected species. This is the opposite of what was anticipated.

Furthermore, in each case, it appears that the values obtained using graphene-coated probes were worse than those using standard, uncoated, conductive probes. This was as expected, as there were no planar aromatic rings on the end of the molecules expected to be in contact with the graphene-coated electrode.

*Table 6.30 Log(G/G<sub>0</sub>) values for dithiolenates obtained via cAFM. Results are given for graphene-coated and uncoated probes used in the junction.*

Molecule	Log(G/G <sub>0</sub> ) (standard probe)	Log(G/G <sub>0</sub> ) (graphene-coated probe)
<b>RJD2114, Protected</b>	-5.55±0.86	-6.15±0.63
<b>RJD2114, Deprotected</b>	-5.94±0.88	-6.76±1.00
<b>RJD2163, Protected</b>	-5.93±0.85	-6.07±0.64
<b>RJD2163, Deprotected</b>	-7.18±1.42	-7.58±0.92

After XPS analysis (see Chapter 6.4.5) it was evident that the deprotected molecules weren't binding as they had been designed to; the deprotection method used hadn't been successful. To overcome this the samples were heated to 100 °C and measurements were taken again. The conductive results for the annealed, deprotected samples are given in Figure 6.27.



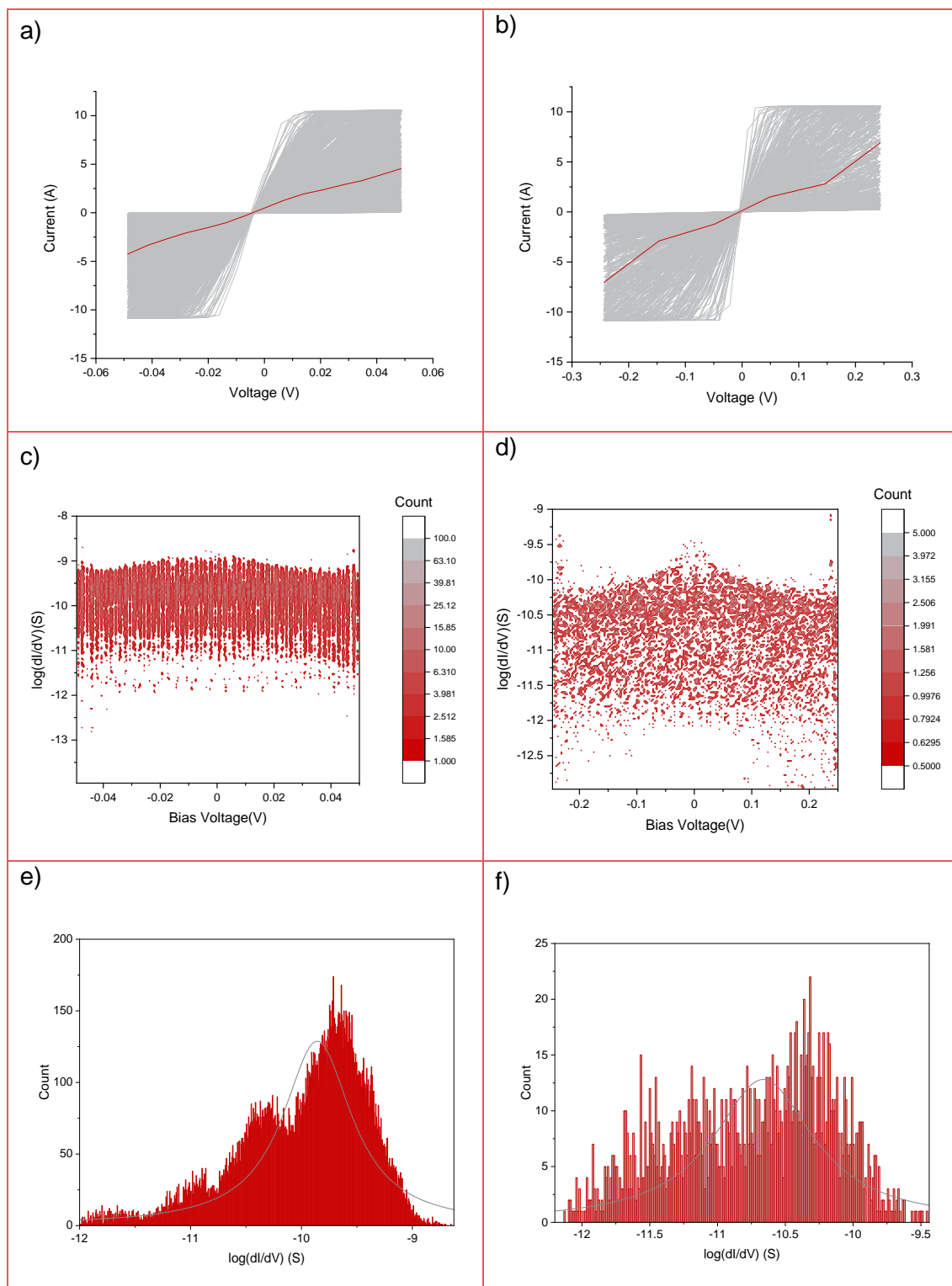


Figure 6.27  $I(V)$  data collated for dithiolenates series using conductive probes. *a* and *b* show the statistical  $I(V)$ ; *c* and *d* show the  $\log(dI/dV)$  electrical conductance; *e* and *f* are the distributions for electrical conductance. The first column depicts results for RJD2114 deprotected and annealed; the right-hand column gives those for RJD2163 deprotected and annealed.

The average conductance ( $\text{Log}(G/G_0)$ ) for annealed and deprotected RJD2114 (-5.63) and RJD2163 (-6.41) were both better than their deprotected but unannealed counterparts from Table 6.30. This confirms the results gathered from XPS; the initial

deprotection was insufficient however, annealing the samples activated the deprotection and subsequent molecule alignment. Contrastingly, neither annealed sample showed greater electrical conductance than the protected samples. This could be related to the molecular packing on the gold surface, as mentioned in Chapter 6.4.3; as the protected molecules can pack closer together, more molecules contact the probe in the junction therefore causing an increase in electrical conductivity. It is also possible that the annealed and deprotected SAMs are suffering from destructive quantum interference effects.

#### **6.4.5 X-ray Photoelectron Spectroscopy**

The samples from above were also subjected to XPS analysis, see Figure 6.28. In the monolayer results (c-h) the peaks at around 163.5 eV binding energy (B.E.) appear to depict a single sulphur bound to gold; those at 162.2 eV unbound sulphur and those at 161 eV double sulphur bound to gold.

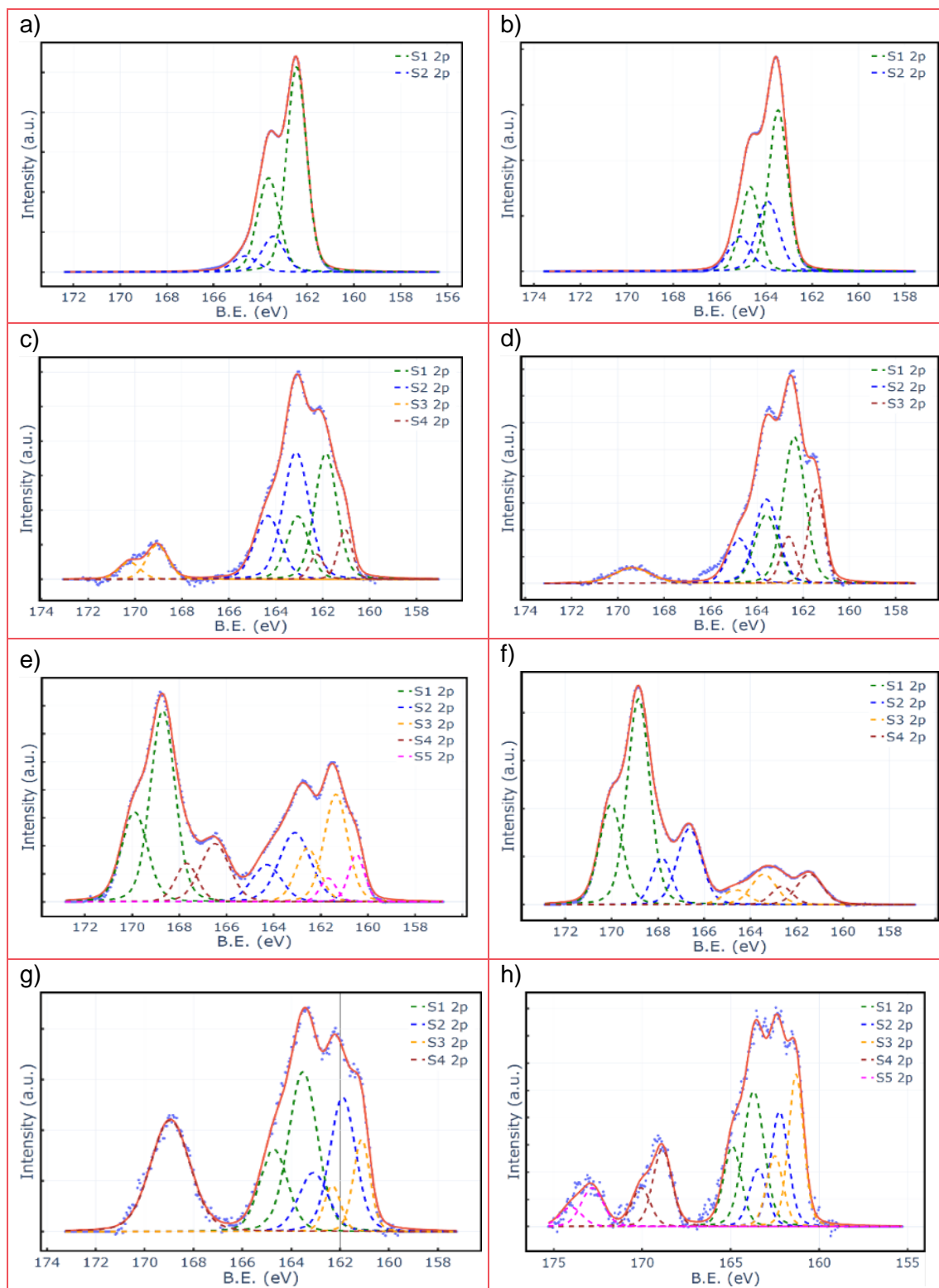


Figure 6.28 XPS spectra for molecules RJD2114 (left column) and RJD2163 (right column). The first row (a and b) shows the spectra for the powder form, row two (c and d) gives the protected results, row three (e and f) the deprotected room temperature results, and the final row shows the results for the samples that have been both deprotected and annealed at 100°C (g and h).

Both the powder and deposited forms of the samples were run through XPS. As can be seen from Figure 6.28, there is no sodium peak present in the powder samples (*a* and *b*), however, when looking at the deprotected samples (*e* and *f*) a large series of peaks on the left-hand side of the spectra appears, which seem to be sodium and oxygen. It was concluded that this must be a result of the NaOMe that was added to the solution in an attempt to deprotect the molecules. It appears that some of this contamination carried over into the protected samples, perhaps due to there being sodium present on the tweezers used for transference, or within the XPS.

To mitigate this presence of sodium, the samples were heated steadily to 100 °C; resultantly, it appeared that the sodium peaks became more limited upon heating, with the peaks on the left-hand side of the spectra significantly reducing. The peaks assigned to unbound sulphur at around 162.2 eV also appear to have reduced, implying there is greater binding of the sulphur to the gold surface. Furthermore, the double sulphur-to-gold bond at c. 161 eV appears to have increased. It was therefore concluded that the initial deprotection using NaOMe didn't have the desired effect on its own, however, raising the temperature of the sample to 100 °C caused the deprotection to activate. Further cAFM tests were attempted on the new samples, post-heating; these are presented in Figure 6.27, in the previous section.

#### 6.4.6 Conclusions

It was expressed at the beginning of this thesis that this work intended to study a second series of SAMs using two thiol groups in an attempt to create SAMs with desirable electrical conductance and improved stability; in a similar manner to the tetrapodal series. Four molecules were designed in this work, two with different functional groups and the protected and deprotected structures of both. It was further found that annealing was required in order to truly deprotect the molecules. It was concluded that the truly deprotected samples occupied greater area per molecule, which was speculated to be a result of the molecule tilting and thus limiting how closely they could pack together when forming a monolayer.

Moreover, the electrical conductance results showed improved conductance for the truly deprotected SAMs in comparison to their deprotected and unannealed counterparts. This could be a result of greater coupling to the substrate and therefore stronger electron transport through the junction. However, the protected monolayers displayed the best electrical conductance; this may be a result of destructive quantum interference with regard to the deprotected annealed samples. Furthermore, the protected monolayers

may pack more closely together thus resulting in increased conductance from more molecules contacting the probe in the junction.

Interesting further work would utilise the dithiolenate moiety whilst designing the molecular backbone to exhibit constructive quantum interference. It would also potentially be interesting to gain a more accurate understanding of the area per molecule through use of reductive desorption.

As with the tetrapodal series, the results from this series of molecules and their monolayers demonstrate that SAMs can present a successful method for forming thin films with desirable thermoelectric characteristics. Once again, Seebeck measurements would be an important next step with subsequent FOM calculation.

## 7. Conclusions

This research intended to demonstrate how molecular design can use bottom-up techniques to lead to thin films with improved thermoelectric properties that integrate well into practical devices for sustainable applications. It has been proven that self-assembly in particular can lead to monolayers of material with promising electrical conductance, and the potential for enhanced figure of merit.

Within this research, the benefit of molecular design for improving monolayer properties has been displayed thoroughly. It has been demonstrated that each element of molecular junction design is heavily influential when creating highly electrically conductive molecular junctions and thermoelectric devices. This can be broken down into the top contact and its coating, the head group contacting this, the conductive backbone that comprises the bulk of the monolayer, the anchor groups and how they interact with both the molecule and monolayer themselves, and with the substrate material.

Firstly, Langmuir Schaefer (LS) deposition was employed for coating non-conductive Atomic Force Microscope (AFM) probes with graphene, per Chapter 6. The objective of this research was to examine if such a coating would prolong the lifetime of the probes, acting as the top electrode for thermoelectric devices. The probes were subjected to AFM tests in multiple phases. Primarily, pairs of coated and uncoated probes underwent extensive AFM scanning to observe the result of long-time use in different AFM modes. This demonstrated that ScanAssyst mode, and contact mode when pressing with higher force, had the greatest destructive effect on the probes, with the graphene-coated probes looking to be less affected.

From this investigation it was concluded that the next phase would involve further SEM images, to see how graphene-coating and wear-testing impacted the probes' tip apexes. It appeared that in the graphene-coating stage for these tests, the graphene may have formed multilayers over the probes rather than monolayers, with larger graphene flakes adhering to the tip apexes. In most cases, this caused a vast increase in the tip apex, which would be undesirable for practical applications. Nevertheless, this testing revealed that there is likely a correlation between having the graphene coating and minimising the difference between the initial tip apex and the final tip apex. Further testing is required to clarify this; however, the results were promising. It is also suggested that similar investigations are carried out on conductive probes, to understand if graphene-coated probes couple better to monolayers.

A small part of the research, Chapter 6.2, focussed on a study of BOC8 molecules, examining whether changing the terminal group on an alkyl chain or altering the length of the chain would affect the molecule's electrical conductance when in contact with graphene-coated and uncoated conductive AFM probes. This work determined that due to the aromatic groups being coplanar to the graphene-coated probes, increasing the size of the aromatic head group decreased the resulting conductance as the electron pathway was extended. In the case for which the aromatic head group was expanded in width rather than length, the same was not observed. In this case, as the number of aromatic head groups ( $n$ ) increased, the conductance ratio of uncoated conductive probe: graphene-coated probe broadly followed the relationship  $n+1$  with wider head groups coupling better to graphene-coated probes. It was therefore concluded that graphene-coated probes couple well to molecules with aromatic heads, due to  $\pi$ - $\pi$  interactions between the two.

Regarding the alkyl chain length variation, it was predicted that the relationship  $G \propto e^{-\beta L}$  would be followed, in which  $G$  is electrical conductance,  $\beta$  is the tunnelling decay constant and  $L$  is the molecular length determined via DFT calculations. For the uncoated conductive probes,  $\beta$  was concluded to be  $5.6 \text{ nm}^{-1}$  which is slightly lower than that seen in literature, whereas for the graphene-coated probes,  $\beta$  was  $3.5 \text{ nm}^{-1}$  which is in line with literature values.

In Chapter 6.3 a series of tetrapodal molecules with different tail groups were studied, with the intention of decoupling the conductive backbone from the tetrapodal anchors. This would allow the avoidance of destructive quantum interference effects and therefore improve electrical conductivity, whilst maintaining a stable monolayer. The same core structure was used for each molecule, but with varying groups within the confines of the anchors, to observe the impact of this on electrical conductance.

The monolayers studied acted as expected from Density Functional Theory (DFT) calculations carried out, following the trend very closely. This showed that molecules, in which the head and neck groups tended towards the substrate, would exhibit greater conductance due to bypassing the anchors. cAFM tests were also executed using graphene-coated conductive probes, with the majority of monolayers exhibiting worse conductance in conjunction with these.

Finally, X-ray Photoelectron Spectroscopy (XPS) was used to see how different atoms within the molecules were binding to the substrate, to conclude whether all four anchors were contacting the surface. This found that in most cases, it appeared that only one or

two of the anchors were binding, however, in one example a pentapod may have been forming wherein the tail group between the four anchors was acting as a fifth anchor.

Similar to the tetrapods and how their multiple anchors cause greater film stability on the substrate surface, dithiolenates were investigated with two thiol groups on one anchor, as seen in Chapter 6.3. Two molecules were included in the study; however, both had protected and deprotected forms. It was expected that the deprotected forms would present better electrical conductance values. Initially, NaOMe was used to deprotect the samples and AFM analysis was carried out for the monolayers. The results for electrical conductance showed that the protected samples performed better than the deprotected samples, which was opposite to the hypothesis.

XPS was subsequently used to determine how the molecules were binding to the substrate. This revealed that the deprotection via NaOMe was insufficient. The samples were annealed in an attempt to cause the deprotection to occur; annealing to 100 °C appeared to trigger it. New AFM measurements were carried out on the annealed samples, with their electrical conductance proving worse than the protected samples. This was speculated to be a result of destructive quantum interference influencing the conductance of the deprotected samples. Further work was suggested to design molecules with the dithiolenate moiety which considered quantum interference effects.

Overall, the conclusions gained from this research provide a strong starting point for further work in fine-tuning the design of molecules and their deposition to create effective thermoelectric devices, with efficient monolayers and connections into their electrical circuits. The graphene-coated top contacts demonstrated improved coupling to molecules with planar aromatic head groups. The tetrapodal molecules exhibited that using a conductive backbone designed with constructive quantum interference in mind was critical to getting good electrical conductance results. Both the tetrapods and dithiolenate molecules showed the importance of decoupling multipodal anchors from their conductive backbone for enhanced electron transport.



## References

1. O'Driscoll, L.J., et al., *Planar aromatic anchors control the electrical conductance of gold|molecule|graphene junctions*. *Nanoscale Advances*, 2023. **5**(8): p. 2299-2306.
2. Feynman, R.P., *There's plenty of room at the bottom [data storage]*. *Journal of microelectromechanical systems*, 1992. **1**(1): p. 60-66.
3. Lindsay, S., *Introduction to Nanoscience*. 1 ed. 2010, New York: OUP Oxford.
4. Colson, P., C. Henrist, and R. Cloots, *Nanosphere Lithography: A Powerful Method for the Controlled Manufacturing of Nanomaterials*. *Journal of Nanomaterials*, 2013. **2013**: p. 948510.
5. Moore, G.E., *Cramming more components onto integrated circuits*. *Proceedings of the IEEE*, 1965. **86**(1): p. 82-85.
6. Petty, M.C., *Organic and molecular electronics: from principles to practice*. 2 ed. 2019, USA: John Wiley & Sons.
7. Bentley, P., *The end of Moore's Law: what happens next?*, in *BBC Science Focus Magazine*. 2018, BBC Focus: UK.
8. Change, I.P.o.C., *Climate Change 2023: Synthesis Report*. 2023, IPCC: Geneva, Switzerland. p. 35-115.
9. Feng, J.-j., W. Zhu, and Y. Deng, *An overview of thermoelectric films: Fabrication techniques, classification, and regulation methods*. *Chinese Physics B*, 2018. **27**(4): p. 047210.
10. Harman, T.C., et al., *Quantum Dot Superlattice Thermoelectric Materials and Devices*. *Science*, 2002. **297**(5590): p. 2229-2232.
11. Kraemer, D., et al., *Photovoltaic-thermoelectric hybrid systems: A general optimization methodology*. *Applied Physics Letters*, 2008. **92**(24).
12. Siah Chehreh Ghadikolaei, S., *Solar photovoltaic cells performance improvement by cooling technology: An overall review*. *International Journal of Hydrogen Energy*, 2021. **46**(18): p. 10939-10972.
13. Xiang, D., et al., *Molecular-Scale Electronics: From Concept to Function*. *Chemical Reviews*, 2016. **116**(7): p. 4318-4440.
14. Kelsall, R., I.W. Hamley, and M. Geoghegan, *Nanoscale science and technology*. 2005: John Wiley & Sons.
15. Lambert, C.J., *Quantum transport in nanostructures and molecules*. 1 ed. 2021, UK: IOP Publishing.
16. Aggarwal, A., V. Kaliginedi, and P.K. Maiti, *Quantum Circuit Rules for Molecular Electronic Systems: Where Are We Headed Based on the Current Understanding of Quantum Interference, Thermoelectric, and Molecular Spintronics Phenomena?* *Nano Letters*, 2021. **21**(20): p. 8532-8544.
17. Lamantia, A., *Thermoelectric properties of ultra-thin films formed by molecular self assembly and Langmuir-Blodgett deposition*, in *Department of Physics*. 2020, Lancaster University: Lancaster. p. 235.
18. Cuevas, J.C. and E. Scheer, *Molecular electronics: an introduction to theory and experiment*. 2010: World Scientific.
19. Kittel, C., *Solid state physics*. 19 ed. Vol. 19. 1976, New York: Wiley.

20. Magoga, M. and C. Joachim, *Conductance of molecular wires connected or bonded in parallel*. Physical Review B, 1999. **59**(24): p. 16011-16021.
21. Liao, K.-C., et al., *Molecular Series-Tunneling Junctions*. Journal of the American Chemical Society, 2015. **137**(18): p. 5948-5954.
22. Price, S.H. *The Peltier Effect and Thermoelectric Cooling*. 2007.
23. Cusack, N. and P. Kendall, *The Absolute Scale of Thermoelectric Power at High Temperature*. 1958.
24. Gaurav, K. and S.K. Pandey, *Efficiency calculation of a thermoelectric generator for investigating the applicability of various thermoelectric materials*. Journal of Renewable and Sustainable Energy, 2017. **9**(1): p. 014701.
25. Snyder, J. *Thermoelectrics*. 2022 [cited 2022 18th May]; Available from: <http://thermoelectrics.matsci.northwestern.edu/thermoelectrics/index.html>.
26. Goldsmid, H.J., *Introduction to thermoelectricity*. 2 ed. Vol. 121. 2010, Berlin: Springer.
27. Rowe, D.M., *CRC handbook of thermoelectrics*. 2018: CRC press.
28. Wang, X., et al., *Enhanced thermoelectric figure of merit in nanostructured n-type silicon germanium bulk alloy*. Applied Physics Letters, 2008. **93**(19): p. 193121.
29. Joshi, G., et al., *Enhanced thermoelectric figure-of-merit in nanostructured p-type silicon germanium bulk alloys*. Nano letters, 2008. **8**(12): p. 4670-4674.
30. Henry, A.S. and G. Chen, *Spectral phonon transport properties of silicon based on molecular dynamics simulations and lattice dynamics*. Journal of Computational and Theoretical Nanoscience, 2008. **5**(2): p. 141-152.
31. Ashcroft, N.W. and N.D. Mermin, *Solid state physics [by] Neil W. Ashcroft [and] N. David Mermin*, 1976.
32. García-Suárez, V.M., et al., *Redox control of thermopower and figure of merit in phase-coherent molecular wires*. Nanotechnology, 2014. **25**(20): p. 205402.
33. Maslyuk, V.V., S. Achilles, and I. Mertig, *Spin-polarized transport and thermopower of organometallic nanocontacts*. Solid State Communications, 2010. **150**(11-12): p. 505-509.
34. Al-Galiby, Q.H., et al., *Tuning the thermoelectric properties of metallo-porphyrins*. Nanoscale, 2016. **8**(4): p. 2428-2433.
35. Claughton, N. and C. Lambert, *Thermoelectric properties of mesoscopic superconductors*. Physical review b, 1996. **53**(10): p. 6605.
36. Bergfield, J.P., M.A. Solis, and C.A. Stafford, *Giant thermoelectric effect from transmission supernodes*. ACS nano, 2010. **4**(9): p. 5314-5320.
37. Evangeli, C., et al., *Engineering the thermopower of C60 molecular junctions*. Nano letters, 2013. **13**(5): p. 2141-2145.
38. Paulsson, M. and S. Datta, *Thermoelectric effect in molecular electronics*. Physical Review B, 2003. **67**(24): p. 241403.
39. Pierret, R., *Semiconductor Device Fundamentals, Addison-Wesley*. 1 ed. 1996, Reading, Massachusetts: Pearson.
40. Yee, S.K., et al., *Thermoelectricity in fullerene-metal heterojunctions*. Nano letters, 2011. **11**(10): p. 4089-4094.
41. Reddy, P., et al., *Thermoelectricity in molecular junctions*. Science, 2007. **315**(5818): p. 1568-1571.

42. Mann, B. and H. Kuhn, *Tunneling through Fatty Acid Salt Monolayers*. Journal of Applied Physics, 2003. **42**(11): p. 4398-4405.
43. Aviram, A. and M.A. Ratner, *Molecular rectifiers*. Chemical Physics Letters, 1974. **29**(2): p. 277-283.
44. Ratner, M., *A brief history of molecular electronics*. Nature Nanotechnology, 2013. **8**(6): p. 378-381.
45. Reed, M.A., et al., *Conductance of a Molecular Junction*. Science, 1997. **278**(5336): p. 252-254.
46. Datta, S., *Overview*, in *Lessons from Nanoelectronics*. 2018, World Scientific. p. 1-18.
47. Cuniberti, G., G. Fagas, and K. Richter, *Introducing Molecular Electronics: A Brief Overview*, in *Introducing Molecular Electronics*, G. Cuniberti, K. Richter, and G. Fagas, Editors. 2005, Springer Berlin Heidelberg: Berlin, Heidelberg. p. 1-10.
48. *The birth of molecular electronics*, in *Molecular Electronics*. p. 3-18.
49. Mayor, M., et al., *Electric Current through a Molecular Rod—Relevance of the Position of the Anchor Groups*. Angewandte Chemie International Edition, 2003. **42**(47): p. 5834-5838.
50. Pochettino, A. and G.G. Trabacchi, *Stil modo di comportarsi del selenio rispetto alle correnti alternanti*. Il Nuovo Cimento (1901-1910), 1906. **12**(1): p. 335-346.
51. Eley, D.D., *Phthalocyanines as semiconductors*. Nature, 1948. **162**(4125): p. 819-819.
52. Akamatu, H., H. Inokuchi, and Y. Matsunaga, *Electrical conductivity of the perylene–bromine complex*. Nature, 1954. **173**(4395): p. 168-169.
53. Deng, L., et al., *Organic Thermoelectric Materials: Niche Harvester of Thermal Energy*. Advanced Functional Materials, 2023. **33**(3): p. 2210770.
54. Tanaka, Y., *Metal Complex Molecular Junctions as Thermoelectric Devices*. Chemistry – A European Journal, 2023. **29**(29): p. e202300472.
55. Bennett, T.L., et al., *Multi-component self-assembled molecular-electronic films: towards new high-performance thermoelectric systems*. Chemical Science, 2022. **13**(18): p. 5176-5185.
56. Liu, S.-X., et al., *Signatures of Room-Temperature Quantum Interference in Molecular Junctions*. Accounts of Chemical Research, 2023. **56**(3): p. 322-331.
57. Tan, S., et al., *The effect of side substitution and quantum interference on the performance of molecular thermoelectric devices: a brief review*. Journal of Physics: Condensed Matter, 2023. **35**.
58. Okayama, K., et al., *Giant Seebeck effect in an undoped single crystal of 2,5,8-triphenylbenzo[1,2-b:3,4-b':5,6-b'']trifuran*. Chemistry Letters, 2023. **53**(2).
59. Xue, D.-J., et al., *Regulating strain in perovskite thin films through charge-transport layers*. Nature Communications, 2020. **11**(1): p. 1514.
60. MacManus-Driscoll, J.L., et al., *New approaches for achieving more perfect transition metal oxide thin films*. APL Materials, 2020. **8**(4): p. 040904.
61. Crivello, C., et al., *Advanced technologies for the fabrication of MOF thin films*. Materials Horizons, 2021. **8**(1): p. 168-178.
62. Liang, C., et al., *Two-dimensional Ruddlesden–Popper layered perovskite solar cells based on phase-pure thin films*. Nature Energy, 2021. **6**(1): p. 38-45.

63. Tang, R., et al., *Hydrothermal deposition of antimony selenosulfide thin films enables solar cells with 10% efficiency*. *Nature Energy*, 2020. **5**(8): p. 587-595.
64. Rasheed, M., S. Shihab, and O.W. Sabah, *An investigation of the Structural, Electrical and Optical Properties of Graphene-Oxide Thin Films Using Different Solvents*. *Journal of Physics: Conference Series*, 2021. **1795**(1): p. 012052.
65. Xin, B., et al., *Growth and optical properties of CaxCoO2 thin films*. *Materials & Design*, 2021. **210**: p. 110033.
66. Yao, F.-Z., et al., *Multiscale structural engineering of dielectric ceramics for energy storage applications: from bulk to thin films*. *Nanoscale*, 2020. **12**(33): p. 17165-17184.
67. Costa, M.J.d.S., et al., *Transition metal tungstates AWO4 (A2+ = Fe, Co, Ni, and Cu) thin films and their photoelectrochemical behavior as photoanode for photocatalytic applications*. *Journal of Applied Electrochemistry*, 2023. **53**(7): p. 1349-1367.
68. Yu, J., et al., *Green and edible cyclodextrin metal-organic frameworks modified polyamide thin film nanocomposite nanofiltration membranes for efficient desalination*. *Journal of Membrane Science*, 2023. **679**: p. 121714.
69. Shi, Z., et al., *MXene-Based Materials for Solar Cell Applications*. *Nanomaterials*, 2021. **11**(12): p. 3170.
70. Olabi, A.G., et al., *Application of graphene in energy storage device – A review*. *Renewable and Sustainable Energy Reviews*, 2021. **135**: p. 110026.
71. Novoselov, K.S., et al., *Electric field effect in atomically thin carbon films*. *Science*, 2004. **306**(5696): p. 666-9.
72. Yu, W., et al., *Progress in the functional modification of graphene/graphene oxide: A review*. *RSC Advances*, 2020. **10**(26): p. 15328-15345.
73. C. M. Rodrigues, D., et al., *Exploring the enhancement of the thermoelectric properties of bilayer graphyne nanoribbons*. *Physical Chemistry Chemical Physics*, 2022. **24**(16): p. 9324-9332.
74. Dai, H., *Carbon nanotubes: opportunities and challenges*. *Surface Science*, 2002. **500**(1): p. 218-241.
75. Mabrook, M.F., et al., *The morphology, electrical conductivity and vapour sensing ability of inkjet-printed thin films of single-wall carbon nanotubes*. *Carbon*, 2009. **47**(3): p. 752-757.
76. Gao, C., et al., *Surface modification methods and mechanisms in carbon nanotubes dispersion*. *Carbon*, 2023. **212**: p. 118133.
77. Li, F., et al., *Recent Advances in SnSe Nanostructures beyond Thermoelectricity*. *Advanced Functional Materials*, 2022. **32**(26): p. 2200516.
78. Kogo, G., et al., *A thin film efficient pn-junction thermoelectric device fabricated by self-align shadow mask*. *Scientific Reports*, 2020. **10**(1): p. 1067.
79. Park, S., J. Jang, and H.J. Yoon, *Validating the Mott Formula with Self-Assembled Monolayer (SAM)-Based Large-Area Junctions: Effect of Length, Backbone, Spacer, Substituent, and Electrode on the Thermopower of SAMs*. *The Journal of Physical Chemistry C*, 2021. **125**(36): p. 20035-20047.
80. Petsagkourakis, I., et al., *Correlating the Seebeck coefficient of thermoelectric polymer thin films to their charge transport mechanism*. *Organic Electronics*, 2018. **52**: p. 335-341.

81. Cougnon, F.G. and D. Depla, *The Seebeck Coefficient of Sputter Deposited Metallic Thin Films: The Role of Process Conditions*. Coatings, 2019. **9**(5): p. 299.
82. Singh, S., S. Jindal, and S.K. Tripathi, *High Seebeck coefficient in thermally evaporated Sb-In co-alloyed bismuth telluride thin film*. Journal of Applied Physics, 2020. **127**(5): p. 055103.
83. Usop, R., et al., *Seebeck coefficient of synthesized Titanium Dioxide thin film on FTO glass substrate*. IOP Conference Series: Materials Science and Engineering, 2018. **342**: p. 012051.
84. Mikami, M. and K. Ozaki, *Thermoelectric properties of nitrogen-doped TiO<sub>2</sub>-xcompounds*. Journal of Physics: Conference Series, 2012. **379**: p. 012006.
85. Kitagawa, H., et al., *Effect of boron-doping on thermoelectric properties of rutile-type titanium dioxide sintered materials*. Journal of Alloys and Compounds, 2010. **508**(2): p. 582-586.
86. Dekkiche, H., et al., *Electronic conductance and thermopower of single-molecule junctions of oligo(phenyleneethynylene) derivatives*. Nanoscale, 2020. **12**(36): p. 18908-18917.
87. Wang, X., et al., *Scale-Up of Room-Temperature Constructive Quantum Interference from Single Molecules to Self-Assembled Molecular-Electronic Films*. Journal of the American Chemical Society, 2020. **142**(19): p. 8555-8560.
88. Isotta, E., et al., *Towards Low Cost and Sustainable Thin Film Thermoelectric Devices Based on Quaternary Chalcogenides*. Advanced Functional Materials, 2022. **32**(32): p. 2202157.
89. Hong, M.-H., et al., *Ti doping effects on the Seebeck coefficient and electrical conductivity of mesoporous ZnO thin film*. Materials Chemistry and Physics, 2019. **235**: p. 121757.
90. Delime-Codrin, K., et al., *Large figure of merit ZT = 1.88 at 873 K achieved with nanostructured Si<sub>0.55</sub>Ge<sub>0.35</sub>(P<sub>0.10</sub>Fe<sub>0.01</sub>)*. Applied Physics Express, 2019. **12**(4): p. 045507.
91. Kanno, T., et al., *Enhancement of average thermoelectric figure of merit by increasing the grain-size of Mg<sub>3.2</sub>Sb<sub>1.5</sub>Bi<sub>0.49</sub>Te<sub>0.01</sub>*. Applied Physics Letters, 2018. **112**(3): p. 033903.
92. Barnes, G. and I. Gentle, *Interfacial science: an introduction*. 2011: Oxford university press.
93. Cea, P., L.M. Ballesteros, and S. Martín, *Nanofabrication techniques of highly organized monolayers sandwiched between two electrodes for molecular electronics*. 2014.
94. Schwartz, D.K., *MECHANISMS AND KINETICS OF SELF-ASSEMBLED MONOLAYER FORMATION*. Annual Review of Physical Chemistry, 2001. **52**(1): p. 107-137.
95. Laidler, K.J., *The development of the Arrhenius equation*. Journal of Chemical Education, 1984. **61**(6): p. 494.
96. Bigelow, W.C., D.L. Pickett, and W.A. Zisman, *Oleophobic monolayers: I. Films adsorbed from solution in non-polar liquids*. Journal of Colloid Science, 1946. **1**(6): p. 513-538.
97. Colorado Jr, R. and T. Lee, *Thiol-based Self-assembled Monolayers: Formation and Organization*. 2001.

98. Nuzzo, R.G. and D.L. Allara, *Adsorption of bifunctional organic disulfides on gold surfaces*. Journal of the American Chemical Society, 1983. **105**(13): p. 4481-4483.
99. Porter, M.D., et al., *Structural characterization of n-alkyl thiol monolayers on gold by optical ellipsometry, infrared spectroscopy, and electrochemistry*. Journal of American Chemical Society, 1987. **109**: p. 3559-3568.
100. Laibinis, P., et al., *The synthesis of organothiols and their assembly into monolayers on gold*. THIN FILMS-NEW YORK-ACADEMIC PRESS-, 1998. **24**: p. 2-43.
101. Varatharajan, S., S. Berchmans, and V. Yegnaraman, *Tailoring self-assembled monolayers at the electrochemical interface*. Journal of Chemical Sciences, 2009. **121**(5): p. 665-674.
102. Tachibana, M., et al., *Sulfur–Gold Orbital Interactions which Determine the Structure of Alkanethiolate/Au(111) Self-Assembled Monolayer Systems*. The Journal of Physical Chemistry B, 2002. **106**(49): p. 12727-12736.
103. Ulman, A., *Formation and Structure of Self-Assembled Monolayers*. Chemical Reviews, 1996. **96**(4): p. 1533-1554.
104. Lee, W.H. and Y.D. Park, *Tuning Electrical Properties of 2D Materials by Self-Assembled Monolayers*. Advanced Materials Interfaces, 2018. **5**(1): p. 1700316.
105. Gautam, R.P. and C.J. Barile, *Preparation and Electron-Transfer Properties of Self-Assembled Monolayers of Ferrocene on Carbon Electrodes*. The Journal of Physical Chemistry C, 2021. **125**(15): p. 8177-8184.
106. Liu, J., et al., *Self-Assembly and Regrowth of Metal Halide Perovskite Nanocrystals for Optoelectronic Applications*. Accounts of Chemical Research, 2022. **55**(3): p. 262-274.
107. Chen, T., et al., *Self-assembly of PDINH/TiO<sub>2</sub>/Bi<sub>2</sub>WO<sub>6</sub> nanocomposites for improved photocatalytic activity based on a rapid electron transfer channel*. Applied Surface Science, 2022. **584**: p. 152667.
108. Franklin, B., *From Benjamin Frankline to William Brownrigg, 7 November 1773*, W. Brownrigg, Editor. 1773.
109. Partridge, M. *What is a Langmuir Monolayer?* Errant Science, 2014.
110. Langmuir, I., *Surface chemistry*. Chemical reviews, 1933. **13**(2): p. 147-191.
111. Langmuir, I., *The mechanism of the surface phenomena of flotation*. Transactions of the Faraday Society, 1920. **15**(June): p. 62-74.
112. Blodgett, K.B., *Films built by depositing successive monomolecular layers on a solid surface*. Journal of the American Chemical Society, 1935. **57**(6): p. 1007-1022.
113. Martin, P. and M. Szablewski, *Tensiometers and Langmuir-Blodgett Throughs Operating Manual*. Cranfield University Milton Keynes, England: Nima, 1995.
114. Petty, M.C., *Langmuir-Blodgett Films*. 1996.
115. Herrer, L., et al., *pH control of conductance in a pyrazolyl Langmuir–Blodgett monolayer*. Journal of Materials Chemistry C, 2021. **9**(8): p. 2882-2889.
116. Escorihuela, E., et al., *Towards the design of effective multipodal contacts for use in the construction of Langmuir–Blodgett films and molecular junctions*. Journal of Materials Chemistry C, 2020. **8**(2): p. 672-682.

117. Gabaji, M., et al., *From Langmuir–Blodgett to Grafted Films*. Langmuir, 2020. **36**(10): p. 2534-2542.
118. Divagar, M., N. Ponpandian, and C. Viswanathan, *Langmuir-Blodgett deposited Na<sub>3</sub>V<sub>2</sub>(PO<sub>4</sub>)<sub>3</sub>-MnO<sub>2</sub> nanocomposite thin film electrodes for hybrid energy storage application*. Materials Science and Engineering: B, 2021. **270**: p. 115229.
119. da Rocha Rodrigues, R., et al., *Conjugated polymers as Langmuir and Langmuir-Blodgett films: Challenges and applications in nanostructured devices*. Advances in Colloid and Interface Science, 2020. **285**: p. 102277.
120. Liu, H., et al., *Lead halide perovskite nanowires stabilized by block copolymers for Langmuir-Blodgett assembly*. Nano Research, 2020. **13**(5): p. 1453-1458.
121. Rugar, D. and P. Hansma, *Atomic force microscopy*. Physics today, 1990. **43**(10): p. 23-30.
122. Eaton, P. and P. West, *Atomic Force Microscopy*. 1 ed. 2010, United States: OUP Oxford.
123. Bennett, I.D., et al., *Lipidated DNA Nanostructures Target and Rupture Bacterial Membranes*. Small. **n/a**(n/a): p. 2207585.
124. Ku, B., et al., *AFM-Based Hamaker Constant Determination with Blind Tip Reconstruction*. Advanced Materials Technologies, 2023. **8**(1): p. 2200411.
125. Quate, C.F., *The AFM as a tool for surface imaging*. Surface Science, 1994. **299-300**: p. 980-995.
126. Wang, X., et al., *Determination of electric and thermoelectric properties of molecular junctions by AFM in peak force tapping mode*. Nanotechnology, 2023. **34**(38): p. 385704.
127. Ted Limpoco, F. and D.E. Beck, *How to Choose the Right AFM Probe for Your Experiment*. Microscopy Today, 2023. **31**(4): p. 22-27.
128. Ltd, N. *NuNano AFM Probes*. [Web Page] 2024 [cited 2024 14th June 2024]; Available from: <https://www.nunano.com/store>.
129. Milczarek, M., et al., *Novel paradigm in AFM probe fabrication: Broadened range of stiffness, materials, and tip shapes*. Tribology International, 2023. **180**: p. 108308.
130. Palacio, M. and B. Bhushan, *Nanomechanical and nanotribological characterization of noble metal-coated AFM tips for probe-based ferroelectric data recording*. Nanotechnology, 2008. **19**(10): p. 105705.
131. Briggs, D. and M.P. Seah, *Practical Surface Analysis, Auger and X-ray Photoelectron Spectroscopy*. 1996: Wiley.
132. Lee, M.H. and W. Wu, *2D Materials for Wearable Energy Harvesting*. Advanced Materials Technologies, 2022. **7**(9): p. 2101623.
133. Assawaworrarit, S., Z. Omair, and S. Fan, *Nighttime electric power generation at a density of 50 mW/m<sup>2</sup> via radiative cooling of a photovoltaic cell*. Applied Physics Letters, 2022. **120**(14): p. 143901.
134. Eid, A.F., et al., *Hybrid cooling techniques to improve the performance of solar photovoltaic modules*. Solar Energy, 2022. **245**: p. 254-264.
135. Chowdhary, A.K., V.A. Reddy, and D. Sikdar, *Selective thermal emitters for high-performance all-day radiative cooling*. Journal of Physics D: Applied Physics, 2021. **55**(8): p. 085504.

136. Wang, C.-H., et al., *Design and experimental validation of an all-day passive thermoelectric system via radiative cooling and greenhouse effects*. Energy, 2023. **263**: p. 125735.
137. Bianchi, C., et al., *Near infrared photothermoelectric effect in transparent AZO/ITO/Ag/ITO thin films*. Scientific Reports, 2021. **11**(1): p. 24313.
138. Wen, D.-L., et al., *Wearable multi-sensing double-chain thermoelectric generator*. Microsystems & Nanoengineering, 2020. **6**(1): p. 68.
139. Singh, M., N. Kaur, and E. Comini, *The role of self-assembled monolayers in electronic devices*. Journal of Materials Chemistry C, 2020. **8**(12): p. 3938-3955.
140. Sauerbrey, G., *Verwendung von Schwingquarzen zur Wägung dünner Schichten und zur Mikrowägung*. Zeitschrift für Physik, 1959. **155**(2): p. 206-222.
141. Scientific, B. *QCM-D Measurements*. 2022 [cited 2022 25th May]; Available from: <https://www.biolinscientific.com/measurements/qcm-d#how-does-qcm-d-work>.
142. Kim, J., et al., *Interfacial structure of atomically flat polycrystalline Pt electrodes and modified Sauerbrey equation*. Physical Chemistry Chemical Physics, 2017. **19**(33): p. 21955-21963.
143. Banner, L.T., A. Richter, and E. Pinkhassik, *Pinhole-free large-grained atomically smooth Au (111) substrates prepared by flame-annealed template stripping*. Surface and Interface Analysis: An International Journal devoted to the development and application of techniques for the analysis of surfaces, interfaces and thin films, 2009. **41**(1): p. 49-55.
144. Weiss, E.A., et al., *Si/SiO<sub>2</sub>-templated formation of ultraflat metal surfaces on glass, polymer, and solder supports: Their use as substrates for self-assembled monolayers*. Langmuir, 2007. **23**(19): p. 9686-9694.
145. Gwyddion. *Gwyddion User guide*. 2022 [cited 2022 22nd July]; Available from: <http://gwyddion.net/documentation/user-guide-en/>.
146. Lanza, M., et al., *Graphene-Coated Atomic Force Microscope Tips for Reliable Nanoscale Electrical Characterization*. Advanced Materials, 2013. **25**(10): p. 1440-1444.
147. Hui, F., et al., *Graphene coated nanopropes: A review*. Crystals, 2017. **7**(9): p. 269.
148. Fruhman, J.M., et al., *High-yield parallel fabrication of quantum-dot monolayer single-electron devices displaying Coulomb staircase, contacted by graphene*. Nature Communications, 2021. **12**(1): p. 4307.
149. Wang, G., et al., *A New Approach for Molecular Electronic Junctions with a Multilayer Graphene Electrode*. Advanced Materials, 2011. **23**(6): p. 755-760.
150. Wen, Y., et al., *Multilayer Graphene-Coated Atomic Force Microscopy Tips for Molecular Junctions*. Advanced Materials, 2012. **24**(26): p. 3482-3485.
151. Martin-Olmos, C., et al., *Graphene MEMS: AFM Probe Performance Improvement*. ACS Nano, 2013. **7**(5): p. 4164-4170.
152. Lanza, M., et al., *Nanogap based graphene coated AFM tips with high spatial resolution, conductivity and durability*. Nanoscale, 2013. **5**(22): p. 10816-10823.
153. Shim, W., et al., *Multifunctional cantilever-free scanning probe arrays coated with multilayer graphene*. Proceedings of the National Academy of Sciences, 2012. **109**(45): p. 18312-18317.



154. Hui, F., et al., *Moving graphene devices from lab to market: advanced graphene-coated nanoprobes*. *Nanoscale*, 2016. **8**(16): p. 8466-8473.
155. Hybertsen, M.S. and L. Venkataraman, *Structure–Property Relationships in Atomic-Scale Junctions: Histograms and Beyond*. *Accounts of Chemical Research*, 2016. **49**(3): p. 452-460.
156. Limburg, B., et al., *Anchor Groups for Graphene-Porphyrin Single-Molecule Transistors*. *Advanced Functional Materials*, 2018. **28**(45): p. 1803629.
157. Bailey, S., et al., *A study of planar anchor groups for graphene-based single-molecule electronics*. *The Journal of Chemical Physics*, 2014. **140**(5): p. 054708.
158. Zhao, S., et al., *Cross-plane transport in a single-molecule two-dimensional van der Waals heterojunction*. *Science Advances*, 2020. **6**(22): p. eaba6714.
159. Tan, Z., et al., *Atomically defined angstrom-scale all-carbon junctions*. *Nature Communications*, 2019. **10**(1): p. 1748.
160. Engelkes, V.B., J.M. Beebe, and C.D. Frisbie, *Length-Dependent Transport in Molecular Junctions Based on SAMs of Alkanethiols and Alkanedithiols: Effect of Metal Work Function and Applied Bias on Tunneling Efficiency and Contact Resistance*. *Journal of the American Chemical Society*, 2004. **126**(43): p. 14287-14296.
161. Zhang, Q., et al., *Graphene as a Promising Electrode for Low-Current Attenuation in Nonsymmetric Molecular Junctions*. *Nano Letters*, 2016. **16**(10): p. 6534-6540.
162. Mathew, P.T. and F. Fang, *Advances in Molecular Electronics: A Brief Review*. *Engineering*, 2018. **4**(6): p. 760-771.
163. Gao, H.-Y., et al., *In-plane Van der Waals interactions of molecular self-assembly monolayer*. *Applied Physics Letters*, 2015. **106**(8).
164. Ziogos, O.G., I. Blanco, and J. Blumberger, *Ultrathin porphyrin and tetra-indole covalent organic frameworks for organic electronics applications*. *The Journal of Chemical Physics*, 2020. **153**(4).
165. Valášek, M., M. Lindner, and M. Mayor, *Rigid multipodal platforms for metal surfaces*. *Beilstein Journal of Nanotechnology*, 2016. **7**: p. 374-405.
166. Valášek, M. and M. Mayor, *Spatial and Lateral Control of Functionality by Rigid Molecular Platforms*. *Chemistry – A European Journal*, 2017. **23**(55): p. 13538-13548.
167. Xin, N., et al., *Concepts in the design and engineering of single-molecule electronic devices*. *Nature Reviews Physics*, 2019. **1**(3): p. 211-230.
168. Davidson, R.J., et al., *Conductance of 'bare-bones' tripodal molecular wires*. *RSC advances*, 2018. **8**(42): p. 23585-23590.
169. Je, Y., et al., *Nature of Electron Transport by Pyridine-Based Tripodal Anchors: Potential for Robust and Conductive Single-Molecule Junctions with Gold Electrodes*. *Journal of the American Chemical Society*, 2011. **133**(9): p. 3014-3022.
170. Kolivoška, V., et al., *Probabilistic mapping of single molecule junction configurations as a tool to achieve the desired geometry of asymmetric tripodal molecules*. *Chemical Communications*, 2019. **55**(23): p. 3351-3354.
171. Pijper, T.C., et al., *Position and Orientation Control of a Photo- and Electrochromic Dithienylethene Using a Tripodal Anchor on Gold Surfaces*. *The Journal of Physical Chemistry C*, 2015. **119**(7): p. 3648-3657.

172. Valášek, M., et al., *Synthesis of Molecular Tripods Based on a Rigid 9,9'-Spirobifluorene Scaffold*. The Journal of Organic Chemistry, 2014. **79**(16): p. 7342-7357.
173. Wei, Z., et al., *Triazatriangulene as Binding Group for Molecular Electronics*. Langmuir, 2014. **30**(49): p. 14868-14876.
174. O'Driscoll, L.J., et al., *Carbazole-Based Tetrapodal Anchor Groups for Gold Surfaces: Synthesis and Conductance Properties*. Angewandte Chemie International Edition, 2020. **59**(2): p. 882-889.
175. Howell, J.A.S., *DFT investigation of the interaction between gold(I) complexes and the active site of thioredoxin reductase*. Journal of Organometallic Chemistry, 2009. **694**(6): p. 868-873.
176. Bernabeu de Maria, M., et al., *Selenol (-SeH) as a target for mercury and gold in biological systems: Contributions of mass spectrometry and atomic spectroscopy*. Coordination Chemistry Reviews, 2023. **474**: p. 214836.
177. Yang, Y.W. and L.J. Fan, *High-Resolution XPS Study of Decanethiol on Au(111): Single Sulfur-Gold Bonding Interaction*. Langmuir, 2002. **18**(4): p. 1157-1164.
178. Abbasi, A. and J.J. Sardroodi, *A novel nitrogen dioxide gas sensor based on TiO<sub>2</sub>-supported Au nanoparticles: a van der Waals corrected DFT study*. Journal of Nanostructure in Chemistry, 2017. **7**(2): p. 121-132.
179. Bukhtiyarov, A.V., et al., *In-situ XPS investigation of nitric oxide adsorption on (111), (310), and (533) gold single crystal faces*. Surface Science, 2012. **606**(3): p. 559-563.
180. Planje, I.J., et al., *Selective Anchoring Groups for Molecular Electronic Junctions with ITO Electrodes*. ACS Sensors, 2021. **6**(2): p. 530-537.
181. Kato, R., *Development of  $\pi$ -Electron Systems Based on [M (dmit)<sub>2</sub>](M= Ni and Pd; dmit: 1, 3-dithiole-2-thione-4, 5-dithiolate) Anion Radicals*. Bulletin of the Chemical Society of Japan, 2014. **87**(3): p. 355-374.
182. Prignot, E., et al., *Divergent Behavior in the Chemistry of Metal-Bis(dithiolene) Complexes Appended with Peripheral Aliphatic Butyl Chains*. European Journal of Inorganic Chemistry, 2023. **26**(6): p. e202200591.
183. Rabaça, S., et al., *Complexes based on asymmetrically substituted pyridine-dithiolene ligands [M(4-pedt)<sub>2</sub>] (M=Au, Cu, Ni; 4-pedt=1-(pyridin-4-yl)-ethylene-1,2-dithiolate): Synthesis, structure and physical properties*. Polyhedron, 2009. **28**(6): p. 1069-1078.